

INVESTIGATION OF ELECTROMAGNETIC WELDING

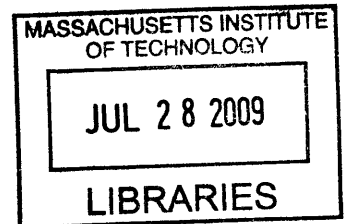
by
Daniel G. Pressl

Diploma Engineer Materials Science
Montanuniversity of Leoben, 2004

SUBMITTED TO THE DEPARTMENT OF MATERIALS SCIENCE AND ENGINEERING IN
PARTIAL
FULFILLMENT OF THE REQUIREMENTS FOR THE DEGREE OF
DOCTORAL DEGREE IN STRUCTURAL AND ENVIRONMENTAL ENGINEERING
AT THE
MASSACHUSETTS INSTITUTE OF TECHNOLOGY

JUNE 2009

© 2009 Massachusetts Institute of Technology. All rights reserved.



ARCHIVES

Signature of Author: _____
Department of Materials Science and Engineering
27th of April, 2009

Certified by: _____
Thomas W. Eagar
Professor of Materials Science and Engineering
Thesis Supervisor

Accepted by: _____
Christine Ortiz
Chair, Departmental Committee on Graduate Students

ABSTRACT

We propose several methodologies to study and optimize the electromagnetic process for Electromagnetic Forming (EMF) and Welding (EMW), thereby lowering the necessary process energy up to a factor of three and lengthening the life-time of EMW compression coils.

We present a new theoretical approach to calculate a so-called critical kinetic energy to achieve a proper EMW joint, which is related to the volume of the accelerated mass and the Vicker's Hardness of the material. Using this novel approach, welding windows for several materials are presented.

Studying the circuit theory, the current discharge pulse can be optimized to the needs of the EMW process, when opting for a critically damped RLC circuit. We present MultiSIM and MATLAB models that prove the proposed optimization and reflect the experimental EMW setup and parameters. Using the models, unknown parameters, such as machine inductance and resistance can be extrapolated for EMF and EMW machinery. Furthermore, the MATLAB model can calculate the optimal gap between the outer and inner workpiece for the outer workpiece to reach the maximum velocity at impact. Good correlation was found with regards to the High-Speed Videography used to study the EMF process in further detail measuring velocities between 50 m/s and 100 m/s.

Studying the mechanical properties of the outer workpiece we propose an EMF-EMW setup that would decrease the strength of the outer workpiece by introducing a controlled amount of wrinkles through an EMF step with a mandrel inside the outer workpiece, followed by a lower critical energy EMW step.

Through a failure study, accompanied by a metallurgical analysis, of an Aluminum Bronze Bitter coil we present a materials selection of other possible coil materials, as well as a new method called Electromagnetic Fatigue (EMFA) Analysis to study the crack initiation and propagation in electromagnetic high-current applications.

Finally, through two sets of EMW experiments tubular lap joints that were stronger than the base material could be produced and the EMW process parameters of increased cleanliness, gap, wall thickness and a lower taper angle, for the case of our setup, showed to increase the final joint strength.

I WOULD LIKE TO THANK

my Family and Friends,

my Advisor Thomas W. Eagar,

my Visiting Students Peter Wagner and Laura Droessler,

my UROPs Bernard Arnest, Yun Lan, Jacob Levinso, Diego

A. Melani Barreiro, Joe Pokora, Chris Liu, Sadik Antwi-
Boampong and Nicole D Teague,

David Bono,

Donald Galler, Harold Larsen,

Andy Sherman, Sergey Golovashchenko,

Victor Shribman, Pierre L'Eplattenier,

Robert O' Handley, Krystyn J. Van Vliet,

Sergio Tavares, Yu Watanabe, Brian Hohmann, David Fischer,

Kathleen R. Farrell, Angelita Mireles and Jerilyn Hill

TABLE OF CONTENTS

ABSTRACT	2
ACKNOWLEDGMENTS	3
TABLE OF CONTENTS	4
1. INTRODUCTION	7
1.1 Literature Review	
1.1.1 Basic Research Needs for Vehicles of the Future	
1.1.1.1 Materials Choice and Challenges	
1.1.1.2 Joining and Processing	
1.1.2 Electromagnetic Forming and Welding	
1.1.2.1 Electromagnetic Forming	
1.1.2.2 Electromagnetic Welding	
1.1.2.3 Mechanics of the Electromagnetic Welding Process	
1.1.2.4 Necessary Limiting Conditions for Electromagnetic Welding	
1.2 State of the Art in Electromagnetic Welding	
1.2.1 Who is researching High Energy Joining Technologies	
1.2.2 Materials Combinations and Applications	
1.3 FORD – MIT Alliance; Scientific Objects and Tasks of this thesis	
1.3.1 FORD – MIT Alliance	
1.3.2 Scientific Objects asked to be investigated by FORD in this study	
2. ELECTROMAGNETIC FORMING	63
2.1. Introduction	
2.2 Background	

2.3 EMF Machinery and Experimental Setup

2.3.1 EMF MAGNEFORM Machine at MIT

2.3.2 A Priori Calculations

2.4 EMF Simulation Effort

2.4.1 Electrical Circuit Approximations

2.4.2 Optimization of the EMW Process through the Process Parameters

2.4.3 Workpiece Acceleration and Velocity Calculations

2.4.4 LS-DYNA Simulation Effort

2.5 High Speed Videography Studies

2.6 Buckling Studies

2.7 Deformation Studies with a Fieldshaper and an Inner Workpiece

3. TOOL FATIGUE AND MATERIALS SELECTION

116

3.1. Introduction

3.2. Failure Study of an Aluminum Bronze Bitter Coil

3.2.1 A Priori Calculations

3.2.2 Optical Microscopy (OM)

3.2.3 Metallurgical Analysis

3.2.4 Discussion

3.3 Electromagnetic Fatigue (EMFA) or Fracture

3.3.1 Design Changes of the Crack tip to weaken EMFA Effects

3.3.2 High Speed Video Analysis of EMFA Experiments

3.3.3 ABAQUS Analysis of the EMFA crack behavior

3.3.4 Discussion

3.4 Materials Selection for the EMF and EMW Tooling Equipment

4. PULSED ELECTROMAGNETIC WELDING	153
4.1 Introduction	
4.2 Background	
4.3 Hypothesis to Optimize the EMW Process using a Threshold Kinetic Energy Approach	
4.4 EMW Experiments	
4.4.1 Design of Experiment	
4.3.2 Experimental Setup	
4.3.3 EMW Specimen Evaluation	
4.4.3.1 Metallurgical Analysis	
4.4.3.2 Optical Microscopy and SEM	
4.4.3.3 Chemical analysis- EDS	
4.4.3.4 Tensile Tests	
4.4 Conclusions	
5. CONCLUSIONS AND FUTURE WORK	193
APPENDIX	205

1 Introduction

During the past decade the amount of Aluminum alloys used in automotive vehicles has increased significantly. This trend has spurred the development of new forming and joining methods applicable to Aluminum (Section 1.1.1: Basic Research Needs for Vehicles of the Future).

Pulsed Electromagnetic Welding is a joining method, which has been applied to the production of drive shafts [1] and may be attractive in the manufacture of vehicle frames [2]. The advantage of Electromagnetic Welding (EMW) compared to traditional Metal Inert Gas (MIG) welding is that a weld can be produced in less than a second for a round or rectangular tube instead of requiring a welding head attached to a robot to traverse the entire length of the joint, i.e. move around the perimeter of the tube. In addition, as a solid state joining process, EM welding does not produce the heat-affected zone and/or porosity, which are typical of a conventional fusion welding processes. For heat treated Aluminum alloys, this means that joints of 100 percent efficiency can be produced.

These advantages have motivated efforts to verify whether EMW is applicable to materials used in automotive production and to define the process parameters for EMW, which will help to formulate tooling requirements and provide joints having sufficient durability for high volume production.

A design challenge is the high energy involved in the process, which limits the process to small dimensions, as well as a low life span of the coils, which are used to generate the magnetic field around the work. In comparison to the very similar process called Electromagnetic Forming (EMF), much higher energies are needed in EMW to achieve a weld at the joint of the two workpieces, instead of just forming the workpieces upon each other, or forming the workpiece upon a die (Section 1.1.2: High Energy Forming and Welding).

The literature does not give proper suggestions for the design of a coil or the workpieces depending on the workpiece material or dimensions. In this chapter, we present an overview of the parameters that affect the EMW process (Section 1.1.2.2: Electromagnetic Welding).

The low life span of the coils is one of the main reasons why EMW is not used today in the automotive industry even though the end-product could show very favorable advantages over today's standards (Section 1.2 gives an overview of current state of the art joining methods).

The goal of my research in this FORD-MIT Alliance project (Section 1.3) is the study of EMF and EMW, their parameters and outcome, which affect the final joint and the energy needed to achieve a proper EMW joint. Using the observations made in this study, we propose several methodologies to optimize the process, thereby lowering the necessary process energy and lengthening the life-time of the tooling equipment.

The hope is that EMW can be verified as a high volume automotive welding process, in the future, which will enable greater use of Aluminum in low to moderate price vehicles, thereby improving fuel economy and other customer-perceived characteristics, such as performance, handling and corrosion resistance.

1.1 Literature Review

This chapter provides a brief overview of the work that has been done in the area of high energy joining, which tries to overcome deficiencies in current joining methods and provide new ways for the technological needs of vehicles of the future.

1.1.1 Basic Research Needs for Vehicles of the Future

Low-cost, light-weight materials are major, ongoing industry needs, due to improved fuel economy and reduced CO₂ vehicle emission resulting in environmental benefits.

Reducing vehicle mass (“curb weight”) is a major objective for the so called Partnership for a New Generation of Vehicles (PNGV). The fuel economy of a vehicle varies inversely with the primary vehicle mass, to a first approximation. Each pound saved on primary mass saves an additional 0.5-0.75 pounds of secondary mass (engine, brakes,...) [3]. The identified research challenges are: material cost and performance, processing, joining, durability and recycling.

1.1.1.1 Materials Choice and Challenges

Many materials could be considered, but two material types are outstanding in their potential to displace Steel automotive body structures: light metals (especially Aluminum and Magnesium) and polymer matrix fiber composites (PMCs). It is estimated that these materials can produce a 50% weight reduction relative to Steel. A great example is FORD’s fleet of Aluminum Intensive Vehicles (AIV) with a 47% weight reduction in body structure relative to a comparable Steel production vehicle (ex.: Mercury Sable).

Low volume aerospace applications use superplastic forming processes for Aluminum, which are too slow and expensive for manufacturing automotive components at high volumes. For this reason, new and less expensive alloys are needed that can be superplastically formed at 10-100 times the current rates. Besides superplastic behavior, corrosion resistance and improved toughness are required. These properties require alloy material optimization through control of grain size, microstructure, grain boundary and interfacial chemistry, thermomechanical processing, and alloy composition. Aluminum and Magnesium are the most likely candidates. Following are short descriptions of the other challenges:

Material Cost and Performance

Today, plastic components already take up 14% of the total weight of a car. As far as metallic materials are concerned, research challenges include less expensive primary processing of Aluminum ores, as cast and wrought Aluminum are roughly 2-5 times more expensive than Steel, on a weight basis. On a functional basis, Aluminum is about 50% more expensive than Steel.

Durability

Material property changes that would affect vehicle function and passenger safety are of primary concern. Corrosion, wear and metal fatigue are metallurgical-based phenomena and the experimental data must reflect a wide spectrum of expected operating conditions, such as arctic and tropical temperatures, high humidity, high-salt and high-dust environments.

Recycling

Wrought and cast Aluminum require different processing conditions, implying the need of optimized in situ segregation of Aluminum alloys during auto shredding. Furthermore, efficient procedures for purifying Aluminum once it has been contaminated with other elements are important (ex.: fractional crystallization of Aluminum) [3].

1.1.1.2 Joining and Processing

Improved joining and forming processes are essential to increased Aluminum use in automobiles. Furthermore, validated computer models are desirable for all available forming processes, such as cold, warm, superplastic and hyperplastic forming. Successful low-cost improvements of super- and hyperplastic forming would lead to their use in low production volumes on niche vehicles.

As far as joining is concerned, welding and adhesive bonding are the principal low-cost methods for joining Aluminum. For resistance welding, major challenges include monitoring and modeling heat generation and heat transfer in the weld-fusion zone. Another welding option is laser welding, where joint porosity, material loss and plume control while welding complex parts are the challenges. Further state of the art Joining processes are discussed Chapter 1.2.3. [3]

1.1.2 Electromagnetic Forming and Welding

The physics of Electromagnetic Forming (EMF) process are quite the same as for Electromagnetic Welding (EMW), until the point of contact of the two work pieces, after which they are either formed against each other or joined, creating a solid state joint.

It is helpful to the process into events that happen inside the work tool and those that happen inside the work pieces. Figure 1 gives an understanding of this division and lists the important processes:

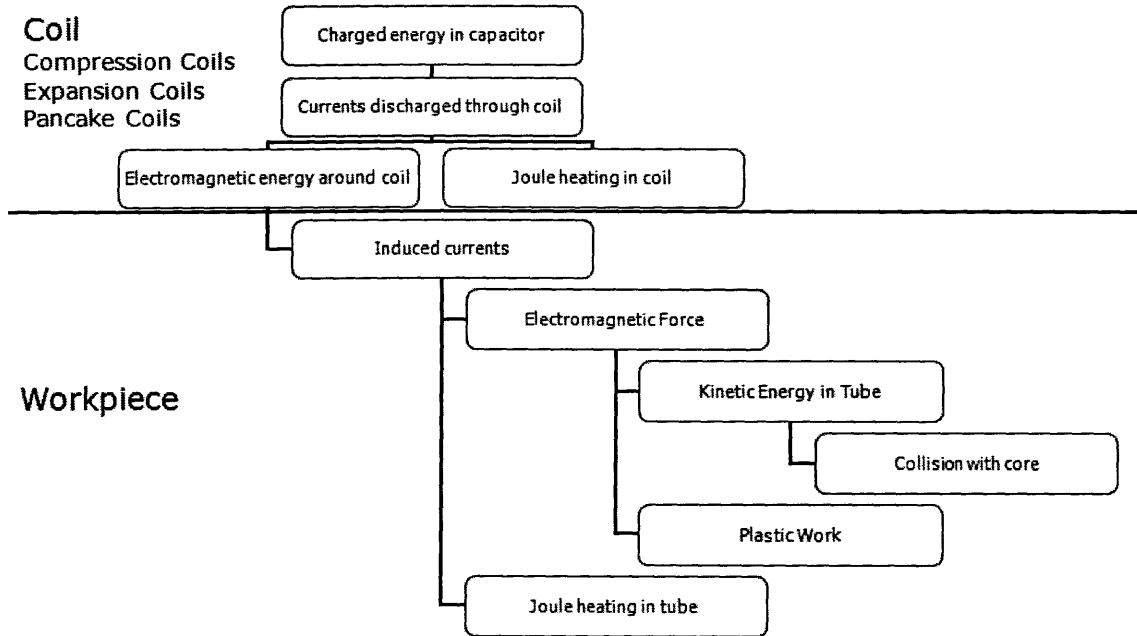


Figure 1: Division of the processes into two systems the work tool “coil” and the workpiece.

During the last point in Figure 1, called “Collision with Core” (“core” for a compression coil setup), a critical minimum velocity of the accelerated workpiece can be calculated, which determines if EMW occurs, otherwise the process will be an EMF process. Therefore, I will describe the physics up to this point in Chapter 1.1.2.1 and will then describe the calculations and aspects of the critical velocity, which lead to an EMW weld and its properties in the following chapter (Chapter 1.1.2.2).

1.1.2.1 Electromagnetic Forming

To describe the different processes in more detail, I categorize the processes into groups described by different physical theories: Circuit Theory, Deformation Theory and Energy Theory. Figure 2 shows the categorization of the different processes into groups with similar physical behavior:

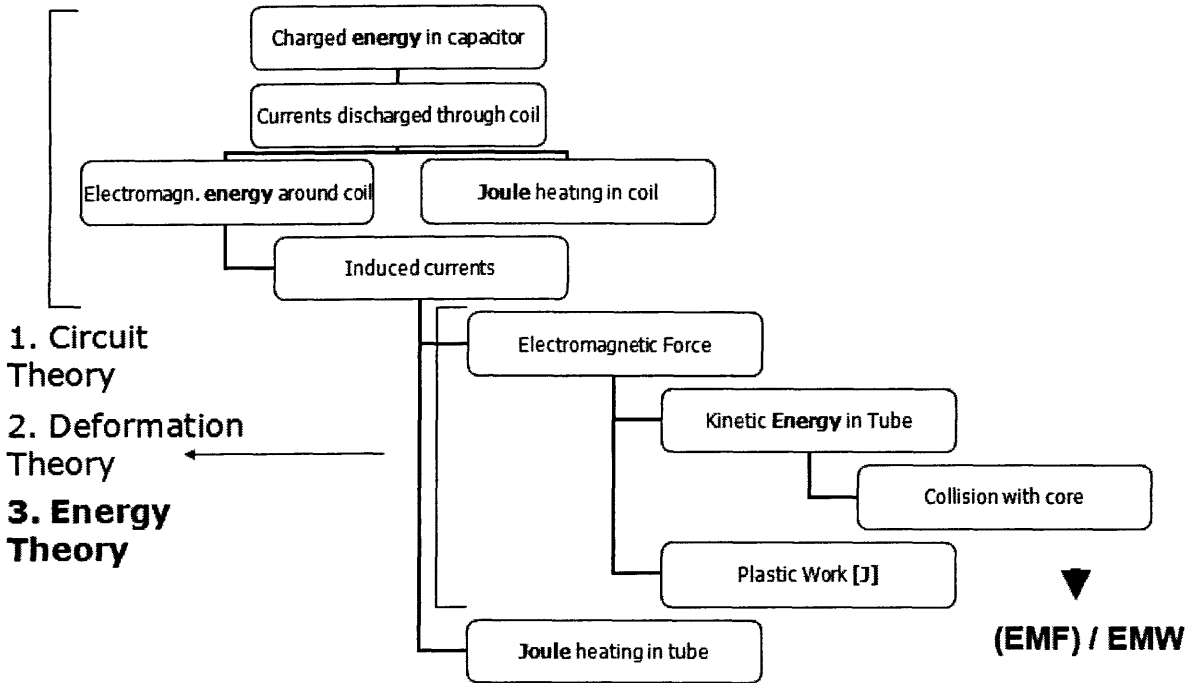


Figure 2: Categorization of the processes into different theories describing the physical phenomena and properties of the processes. Orange highlighted text stands for an energy theory property of the process.

1. Circuit theory speaks about the currents inside the tool, as well as the induced currents in the work pieces. Furthermore, the nature of the magnetic field which causes the induced currents is discussed, as well as the electrical components which are necessary to build up the large currents observed in the process.
2. Deformation theory speaks about the electromagnetic forces acting on the workpieces and the kinetic energy and plastic work acting on the accelerated workpiece. Also, the point of collision is discussed here.
3. The energy theory overshadows both circuit theory and deformation theory and is inherent in almost all individual processes. Electromagnetic energy around the coil, as well as the kinetic energy and the plastic work caused during the deformation of the workpieces, but also the joule heating of the coil and the work pieces are discussed here. An energy balance is performed after introducing the circuit theory.

1. Circuit Theory

Figure 3 shows a cross-section of the setup used in the EMF and EMW process. The process begins at the capacitor which gets charged to a certain voltage. Consequently, the capacitor is discharged and a large current runs through the attached coil. The circulating current in the coil creates a changing magnetic flux, which in turn creates an induced current in the outer workpiece (inner workpiece is not depicted in Figure 3), also described by Faraday's Law. The induced current opposes the primary current, as described by Lenz's Law. Now, the two opposing currents lead to a magnetic force which compresses the workpiece inwards (Lorentz's Law).

Figure 4a shows another graphic of the setup, where the coil and workpieces are drawn in 3D. In this case both "core" (the stationary part or so-called inner workpiece), and the "tube" (the accelerated part or so called outer workpiece) are depicted. Figure 4b shows a cross-section of the entire workpiece setup. One can see that the core has a turned down diameter in the area, where the tube will be colliding with the core. In this case the core is a full cylinder, but it could also be possible to have another tube as the core, with another stabilizing core on the inside, if necessary, to reduce the deformation of the inner tube during impact.

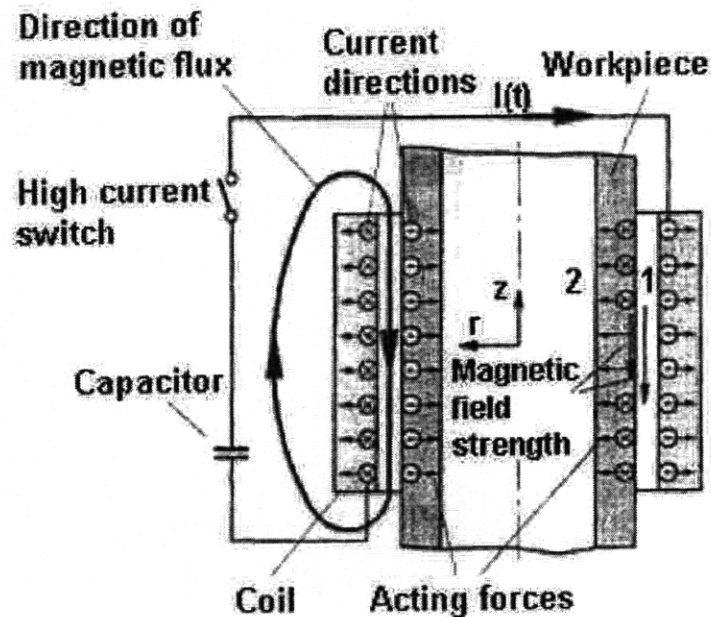


Figure 3: Cross-section of a graphic depicting the coil and the outer workpiece (the inner workpiece is not depicted in this case), as well as the circuit, the magnetic flux, the direction of the currents and the acting forces [4].

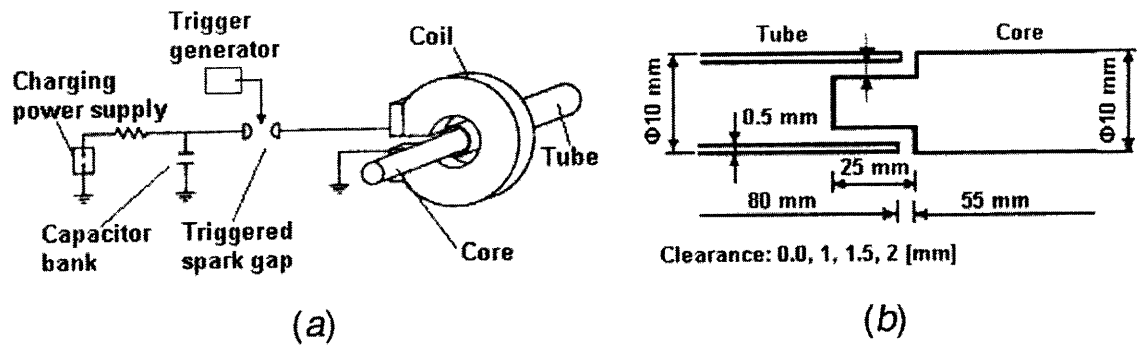


Figure 4: a) Shows another view of the circuit attached to a 3D graphic of the coil and workpiece setup. b) Shows a cross-section of the two workpieces the “tube” (accelerated workpiece) and the “core” (stationary workpiece) [5].

The circuit can be modeled as an RLC (Resistance, Inductance and Capacitance) circuit with a secondary circuit for the tube coupled through a mutual inductance. This can be further simplified as an RLC circuit with lumped equivalent parameter, see Figure 5.

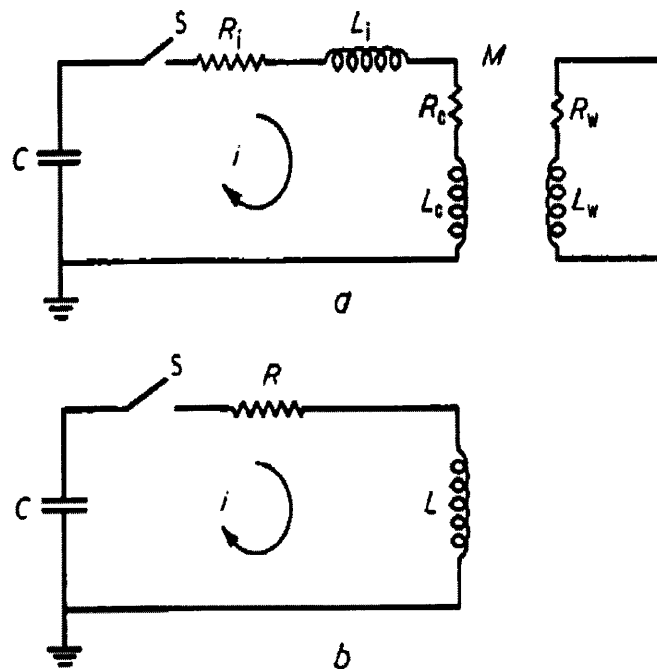


Figure 5: a) Model of the circuit where the left side resembles the coil and the right part the workpiece. (C is the capacitor, R_i is the inner resistance of the machine, L_i is the inner inductance of the machine, R_c is the resistance of the coil, L_c is the inductance of the coil, R_w is the resistance of the workpiece, L_w ... Inductance of the workpiece. b) This circuit model is a simplification of the model in a) where the two circuits are lumped together. (R and L are the resistance and inductance of the entire system) [6].

Again, the circuit setup is the same for EMW and EMF. It is important to mention that the parameters R , L and C in the presented equivalent circuit are functions of time, thereby making the real analysis much more complex.

As stated above, when the capacitor is discharged it leads to an induced current (“secondary current”) in the workpiece, thereby creating a force which compresses the workpiece inside the coil. However, at the same time the induced current also creates a magnetic field itself, which in turn induces a current in the coil in the opposite direction to the primary current, thereby recharging the capacitor. The capacitor discharges again and induces an opposite secondary current in the workpiece and so forth. The resulting discharge current can be calculated by the following formula:

$$I = \frac{V}{L\omega} e(-\beta t) \sin(\omega t), \tag{1.1}$$

where β is the damping coefficient and can be calculated by $\beta = R/2L$, V is the charge voltage of the capacitor. Increasing resistance causes more damping; increasing inductance causes the angular frequency ω to decrease ($\omega = 10\text{-}100$ kHz for typical EMW operations) [6].

This leads to a damped sinusoidal waveform of the discharge current, which was calculated and measured in my experiments (see Chapter 2). Figure 6 shows a theoretical graphic of the resulting waveform of the discharge current I_1 , as well as the induced current in the outer workpiece I_2 :

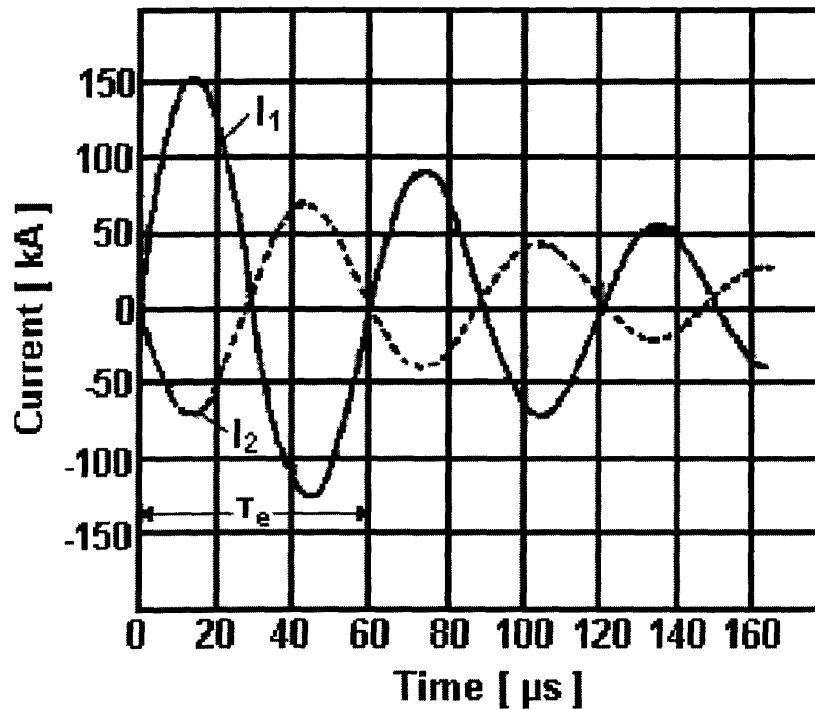


Figure 6: Graphic of the discharge current (primary current) in the coil and the induced current in the workpiece, neglecting the phase shift. T_e is the electric current period in seconds. [7].

The induced current (I_2) in the workpiece flows in the opposite direction of the coil's current, (Lenz's Law) and is smaller than the primary current because of coupling losses. It is not possible to measure the induced current because no measuring devices can be attached to the workpiece inside the coil.

Now, having found that this is an AC current operating at a high frequency, the current only penetrates to a so called "skin depth":

$$\delta = \sqrt{\frac{2\rho_e}{\mu\omega_d}}, \quad 1.2$$

where ρ_e is the electrical resistivity and ω is the angular frequency and

$$\mu = \mu_0\mu_r, \quad 1.3$$

where μ_0 is $4\pi \times 10^{-7}$ H/m and μ_r is the magnetic permeability of the material [7]. The skin depth was calculated for several possible coil materials (see Chapter 3). Furthermore, metallurgical analysis of a coil was performed to see if the Joule heating in the skin depth had an effect on the metallurgical structure and properties of the material (see Chapter 3).

From equation 1.1, resulting from the lumped system in Figure 5b, one can see that the systems of coil and workpiece, as described in Figure 1 are very much coupled, especially when one considers more than one peak of the sinusoidal curve depicted in Figure 6. However, for EMW the joining process only takes place during the first current peak, after that the two workpieces are connected through a solid state joint. On the other hand the forces created through the following current peaks could already cause cracks to form at the EMW joint.

Energy Balance

The behavior of the workpiece is governed by the parameters of the circuit shown in Figure 5. Looking at the equivalent circuit model we arrive at the first energy term, the magnetic energy of the coil:

$$E_M = \frac{1}{2}LI_1^2 - M \cdot I_1 \cdot I_2 \quad 1.4$$

The first term is the energy in the coil, the second term is the coupling energy loss from the mutual inductance M ; I_1 and I_2 are the primary and secondary current (induced current in the workpiece), respectively. The second term in Equ. 1.4 can be neglected in our calculations as the system's electrical parameters R , L and C are lumped in a single RLC circuit (see Figure 5b). However, with a fieldshaper (see Chapter 1.1.2.2 and Chapter 2) in the circuit, the second term can account for coupling losses between the coil and the fieldshaper. This magnetic energy in the coil is then converted into plastic work and collision energy [6,7].

The second term in our energy balance is of course the energy created by the capacitor ($E_C=CV^2/2$), but for our energy balance we will use

$$E_M = \frac{q^2}{2C}, \quad 1.5$$

where q is the charge on the capacitor.

Before dealing with the deformation theory, there are two more energy terms which need to be discussed. First, the Joule Heat in skin depth, which can be calculated using the following formula:

$$E_J = \int_0^t [(R_i + R_c) * I_1^2 + R_w * I_2^2] * dt \quad 1.6$$

or just

$$E_J = \int_0^t R * I^2 dt \quad 1.7$$

in our equivalent circuit. The temperature rise due to Joule heating can be calculated with

$$\Delta T_J = \frac{\rho_{el}}{(\rho \cdot c_p)} \cdot \int_0^t j^2(t) \cdot dt, \quad 1.8$$

where ρ_{el} , ρ , c_p , and j_w are the electrical resistivity, the density, the heat capacity and the current density of the material, respectively. The respective temperature rise due to deformation is

$$\Delta T_D = 0.9 \cdot (\rho \cdot c_p) \cdot \int_0^{\varepsilon_f} \sigma \cdot d\varepsilon, \quad 1.9$$

where σ is the stress and $d\varepsilon$ is the change in strain applied to the material during the process. Certainly the temperature rises due to joule heating and deformation cause thermal fatigue, which was also found in our experiments causing failure in the EMW tool equipment (discussed in Chapter 3) [7].

The second energy term in our energy balance is the mechanical work W performed on the circuit (workpiece and coil).

Having taken account for all energies, we can write the energy balance at a random moment t during the process:

$$\frac{d}{dt} \left(\frac{1}{2} LI^2 + \frac{q}{2C} \right) + I^2 R + \dot{W} = 0. \quad 1.10$$

The voltage balance equation in the circuit is

$$\frac{d}{dt} (LI) + \frac{q}{C} + IR = 0 \quad 1.11$$

Which combines with Equ. 1.10 to give

$$\dot{W} = \frac{I^2}{2} \frac{dL}{dt} \quad 1.12$$

Equ. 1.12 can now be used to get the necessary magnetic pressure to deform the workpiece. This will be discussed in the following deformation theory.

2. Deformation Theory

For a workpiece of length l and radius r , moving with a radial velocity v under pressure P , the rate of work done is

$$\dot{W} = 2\pi r l P v. \quad 1.13$$

Therefore, combining Equ. 1.13 with Equ. 1.12 and setting

$$v = \frac{dr}{dt} \quad 1.14$$

we get

$$P = \frac{I^2 L_c}{2\pi r_c^2 l}. \quad 1.15$$

where r_c is the radius of the coil and L_c is the inductance of the coil given by

$$L_c = \frac{k\mu(\pi r_c^2)N^2}{l_c} \quad 1.16$$

where, k is the Nagaoka's constant (indicating the rate of magnetic flux leakage and l_c is the length of the coil [10]).

Thus, combining the discharge current given in Equ. 1.1 with the pressure given in Equ. 1.15 and the formula for the inductance (Equ. 1.16) we get the formula for the magnetic pressure causing the deformation of the workpiece, which is created by the high current flowing in the coil:

$$P = P_0 e^{-2\beta t} \sin^2 \omega t, \quad 1.17$$

where

$$P_0 = \frac{\mu_0 N^2 E_c}{L}, \quad 1.18$$

where E_c is the charged energy in the capacitor and L is the equivalent inductance [6]. Therefore, P is a time varying pressure which is graphically depicted in Figure 7:

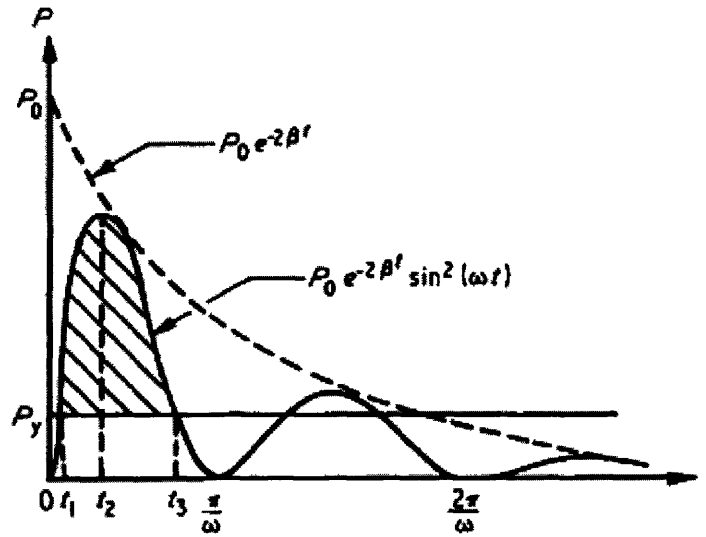


Figure 7: Time varying magnetic pressure curve for an EMF/EMW process. The shaded area underneath the curve marks the time and necessary pressure to cause plastic deformation of the workpiece [6].

Figure 7 shows a shaded area underneath the curve, which is cut off on the bottom by a minimum pressure called P_y . P_y is the yield stress, i.e. the minimum magnetic pressure necessary to cause plastic deformation described by

$$P_y = \frac{\bar{\sigma} h}{r}, \quad 1.19$$

where h is the thickness of the workpiece and $\bar{\sigma}$ is the average representative stress over 10-20 percent strain.

Having described P_y , it becomes clear that the shaded area underneath the time-varying pressure curve, shown in Figure 7, describes the only time and pressure, where actual deformation of the workpiece occurs. Furthermore, in this case we speak of radial unperturbed motion, which means that the possible creation of wrinkles (buckling and bending of the tube) is ignored [6]. In Chapter 2 (Section 2.7) we introduce wrinkles on purpose to reduce the mechanical strength of the outer workpiece and thereby reduce the necessary energy to create an EMW joint. Then the calculations need to be changed to a system of buckled (perturbed) motion.

Therefore, it is important to point out that Equ. 1.19 is a result of the equation of pure (no buckling) radial motion of the workpiece under the magnetic pressure P , which is

$$P + \frac{F_\theta}{r} = \rho h a, \quad 1.20$$

where a is the acceleration of the radial motion and F_θ is the hoop force given by

$$F_\theta = -\frac{(2-k)h\bar{\sigma}}{K_2}, \quad 1.21$$

Where k and K_2 are constants, depending upon the length/diameter ratio of the workpiece. Furthermore,

$$P_y = -\frac{F_\theta}{r} \quad 1.22$$

and in the case of a ring $k=0.5$ and $K_2=1.5$ giving Equ. 1.19. for the collapse pressure.

Now, to conclude deformation theory, we present two methods to calculate the velocity of the workpiece. First, the simple method just uses the basic kinematic equation ($v^2=a*x$), then

$$v^2 = \left(\frac{B^2}{2\mu_0} \frac{1}{h\rho}\right) \cdot x, \quad 1.23$$

where

$$P = \frac{B^2}{2\mu_0}, \quad 1.24$$

which is another way to calculate the magnetic pressure through the magnetic field B . This formula holds when the wall-thickness of the specimen is larger than the skin depth.

The second method arrives at the final result for the velocity by integrating Equ. 1.20 and neglecting the change in h , k , K_2 and $\bar{\sigma}$. Subtracting the collapse pressure, P_y multiplied with the time t gives

$$\int_0^t P dt - P_y t = \rho h (v(t) - v(0)) \quad 1.25$$

and finally with $v(0)=0$, because the workpiece starts from rest we get

$$v = \frac{1}{\rho h} \left(\int_0^t P dt - P_y t \right) \quad [6,7]. \quad 1.26$$

The kinetic energy can then simply be calculated by measuring the accelerated mass and equating $E_k = m \cdot v^2 \cdot 1/2$. The accelerated mass is just the volume of material of the workpiece that gets accelerated during the EMW process. However, we are not taking into account that some of the accelerated mass of the workpiece material is actually constrained, by either the non-accelerated part of the workpiece or by a workpiece holding fixture.

Taking into account that the kinetic energy of the tube at impact with the core is simply converted into collision energy, we can simply say that the collision energy $E_{coll} = E_k$ (while estimating that the velocity is the maximum value at collision (optimum) and not taking into account the effect of the tapered angle of the core in most EMW operations).

As stated above the physics up to this point are the same for EMF and EMW. In the next chapter, I will go into detail summarizing the available literature and theory on EMW.

1.1.2.2 Electromagnetic Welding

The physics of Electromagnetic Forming (EMF) process (Chapter 1.1.2.1) is quite the same as for Electromagnetic Welding (EMW), until the point of contact of the two work pieces, after which they are either formed upon each other or joined. At the point of collision if the velocity of the accelerated workpiece goes beyond a certain critical velocity EMW is observed.

The literature states several design factors and limiting conditions that need to be taken into account for to reach EMW at lower energies or at all, in addition to the necessary critical velocity. These will be discussed in detail.

First, to summarize the processes up to this point, Figure 8 gives an overview of the individual processes described in chapter 1.1.2.1, which are the same for EMF and EMW:

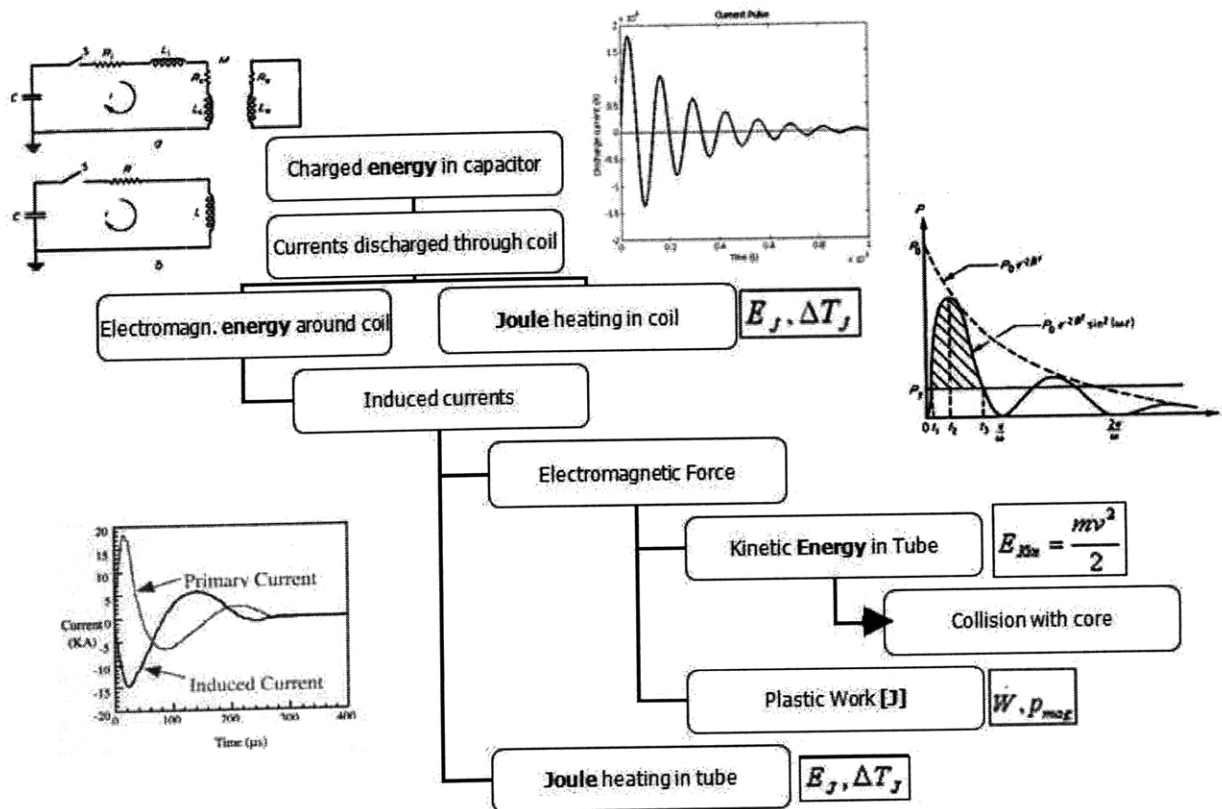


Figure 8: Summary of the processes described in Chapter 1.1.2.2, which are the same for either EMF or EMW.

As stated above, at the point of the collision a necessary critical velocity of the accelerated workpiece determines if EMW occurs. This critical velocity can be calculated by two formulas stated in the literature:

$$v_c' = k' * \sqrt{\frac{2 * H_v}{\rho}} \text{ and} \quad 1.27$$

$$v_c'' = 2.25 \sqrt{\frac{H_v}{\rho}}, \quad 1.28$$

where $k' \sim 1$ (dimensionless constant), H_v is the materials' Vickers hardness and ρ is its density. For the first formula a minimum tapered angle of 3-12 degrees is necessary [8, 9].

One can see that the speed needed depends in a major way on material properties of the workpieces. From Equations 1.17 and 1.18 we can see that there is a strong relation between the Vicker's Hardness of the material and the critical threshold velocity. Figure 9 shows a graph in which the welded length ratio R was plotted against the Vicker's Hardness of the material to be welded. Table 1 shows the necessary critical velocities for several materials.

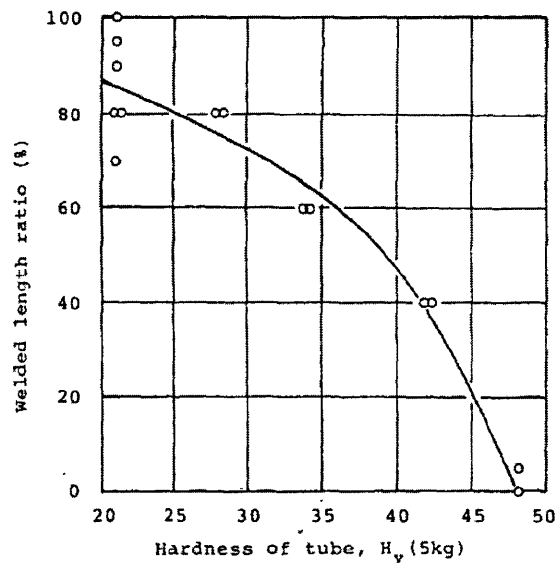


Figure 9: Variation of the welded length ratio with the hardness of the outer workpiece [18].

Alloy	H_v [Pa]	ρ [kg/m ³]	v_c' [m/s]	v_c'' [m/s]
Al (pure)	$1.47 * 10^8$	2698.9	330	530
Al 3005-H18	$7.36 * 10^8$	2730	730	1170
Al 6061-T6	$1.05 * 10^9$	2700	880	1400

Table 1: Calculations of critical threshold velocities for several materials.

The strong dependence of the critical velocity on the Vickers Hardness of the material is particularly important, as we can see that there are material properties that could be fine-tuned to lower the necessary critical velocity and thereby the necessary high energy that needs to be put into the process. Calculations and first order optimization approximations are performed in Chapter 4.

Now, I would like to describe the different observations made in the EMW literature by grouping them into different physical categories, again: Circuit Theory and Deformation Theory. One will see that the changes made in Circuit Theory are mainly for increasing the energy put into the system, which is then converted to kinetic energy of the accelerated workpiece. The Deformation Theory on the other hand deals mainly with changes in the design of the workpieces to maximize the energy and velocity of the deformed section of the workpiece exactly at the point of impact. Certainly, the deformability of the workpiece material also affects the final velocity at impact and will therefore be discussed.

1. Circuit Theory

As stated previously, the necessary critical velocity mandates large energies to be put into the process, which also leads to a strong need in optimizing the parameters described in the circuit theory of EMF in Chapter 1.1.2.1, such as the inductance of the coil. Many papers in the literature state empirical observations of optimized electrical parameters. Figure 10 shows an example of an optimized inductance, which was observed for the particular experimental setup (dimensions of the workpiece,...). Figure 11 shows an optical image of a specimen depicting a measure for goodness of a joint, the welded length ratio R , which can be calculated by

$$R = l/l_0 * 100\% \tag{1.29}$$

where, l_0 is the total length of circumference at tube-core interface after welding and l is the length of the welded portion along the circumference of the interface [10].

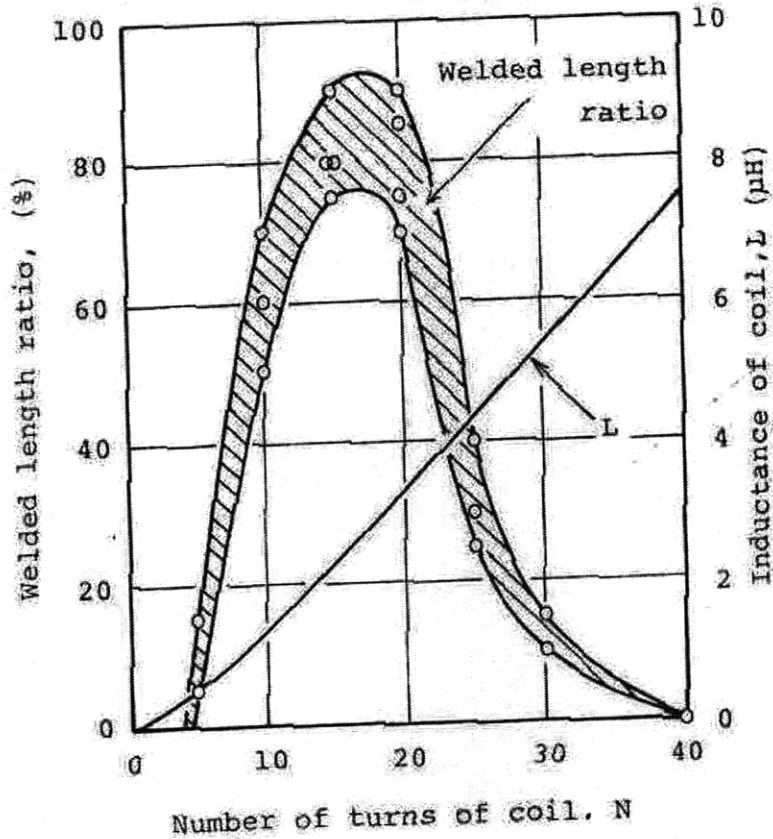


Figure 10: Effect of inductance L on the welded length ratio (in %) [10].

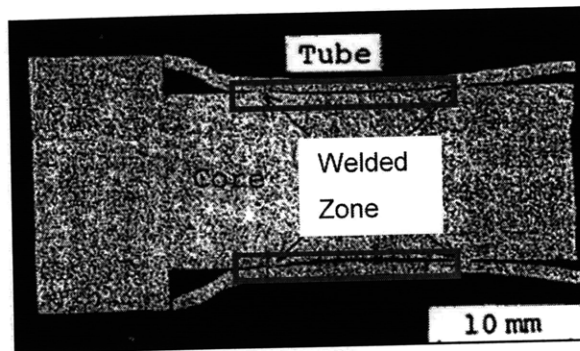


Figure 11: Optical micrograph depicting length of the welded portion along the circumference of the interface, which can then be used to calculate the welded length ratio R [10].

Figure 10 shows how the welded length ratio (in %) is empirically optimized by changing the number of turns in the coil and thereby changing the coil's inductance. One can see that for a particular current and piece dimensions there will be an optimal inductance, which is approximately $3 \mu\text{H}$ in this case.

The results here can certainly be very helpful, however it needs to be stated that the experiments were performed using a crucible coil, which means that the turns of the coil were just wire wrapped around the outer workpiece (with an insulation layer in-between). The wires would practically

evaporate during each experiment due to the high currents. Certainly, such crucible coils are not useful for the automotive industry. Bigger coils are necessary to withstand the high energy in the process and to weld larger workpieces. This brings the difficulty with it that such large coils are very expensive, especially when they tend to fail after a few EMW shots have been performed.

So, the circuit theory optimizations and literature for EMW deals mostly with the design of longer lasting tools and energy or magnetic field concentrators.

There is also the idea of optimizing the circuit by optimizing the resulting waveform of the discharge current. PULSAR, an EMW technology company, situated in Israel (see Chapter 1.2.1) has patented magnetic pulse welding technology incorporating switching capability able to transfer as much as 2 million amps in less than 100 microseconds [11]. However, other than the technology from PULSAR nothing in that category can be found in the literature.

Process Parameter: Coil Design and Field shapers

One can say that the design of the coil is the base to the electrical circuit of the process. It holds the necessary inductance, as well as the dimensions of the workpiece. In fact, the design of the workpiece dimensions is limited by the necessary tool design of the coil to withstand the high stresses during the process. However, some design suggestions are given in Chapter 3 (Tool Fatigue) to possibly increase the life of the coil.

Basically, there are different coils for different applications such as compression coils, expansion coils, where the workpiece is compressed or expanded, respectively. In the case of our applications a compression coil is more suitable, because it surrounds the workpiece, can therefore be larger and withhold higher stresses. There are also other coils for non-tubular workpieces, for example to accelerate a metal plate upon another metal plate or a die. These are usually called pancake coils.

Another very important part of the EMF equipment is the field shaper or field intensifier [12]. A field intensifier is a current carrying conductor, inductively coupled to the forming coil and used to concentrate the magnetic pressure at the point at which forming is desired. Field intensifiers are especially important for EMW, as here the magnetic pressure needs to be very high over a certain area to achieve high enough velocities of the tube [13]. This study features a self-built fieldshaper for the EMF setup at MIT, which is described in further detail in Chapter 2.

2. Deformation Theory

As stated above, the deformation theory deals mainly with changes in the design of the workpieces to maximize the energy and velocity of the deformed section of the workpiece exactly at the point of impact. Figure 12 shows a graphic depicting all important design parameters: the tapered angle of the core, the gap between workpiece and core and the workpiece wall thickness, as well as the outer diameters of the workpiece and the core.

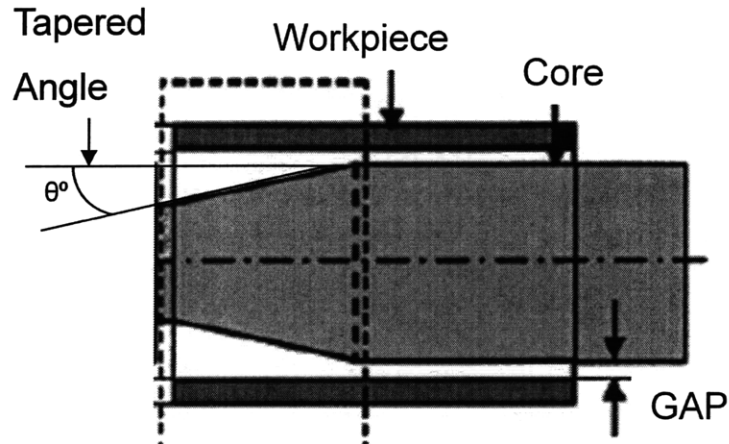


Figure 12: Design of an EMW workpiece and core setup depicting the important design parameters [9].

There is also another process parameter for the EMW setup (not depicted in Figure 12, see Figure 3, for example), which is the gap between the workpiece and the inner coil surface. This gap needs to be designed as low as possible to create good coupling between the coil and the workpiece, thereby maximizing the magnetic pressure compressing the outer workpiece. In fact the magnetic pressure coincides with the magnetic energy density in the gap between the coil and the workpiece [7].

Process Parameter: Tapered Angle

Figure 13 shows a series of experiments optimizing the tapered angle of the core (performed by the same group that investigated the change of inductance, described in Figure 10). For this particular setup an optimal tapered angle of 8 degrees was found. Kojima finds that when the inner workpiece is tapered, an impact point moves along the tapered surface.

Then, due to the high strain rates at impact, the tube and the core materials behave like high-viscosity fluids; as a result a small surface layer is ejected, which is also sometimes called “jet” in the literature, see Figure 14. This causes the contaminated layers of the core and workpiece surfaces to be removed and upon further pressure on each other are welded together [14]. In Section 1.1.2.3 we will go into further detail regarding the necessity of the jet to form for welding to occur in the EMW process and we will discuss the mechanics of the jet-formation based on the observations that have been made in the Explosive Welding literature.

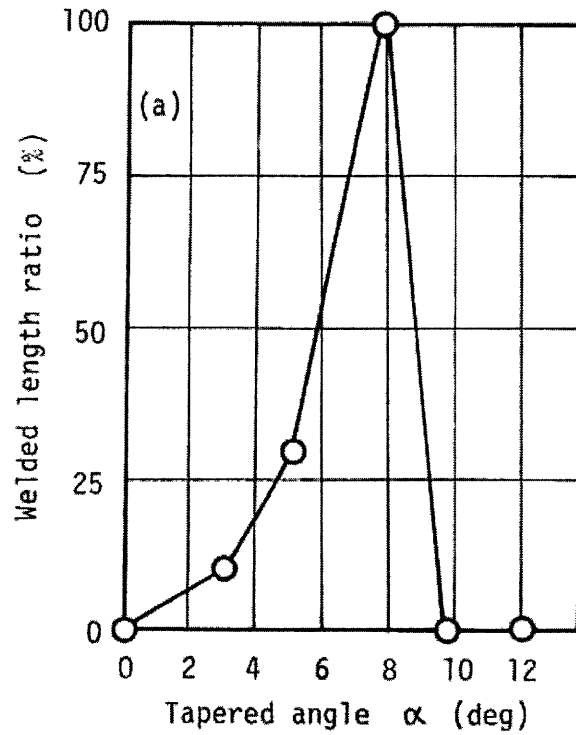


Figure 13: Effect of the tapered angle of core on the welded length ratio. (Note: Al specimen of $t = 0.6$ mm for tapered core; $t = 1$ mm for straight core, discharge current = 60 kA) [14]

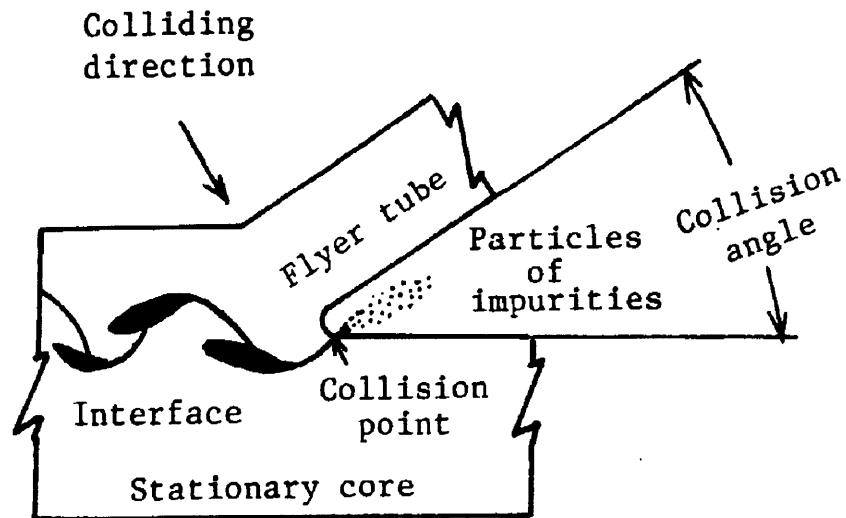


Figure 14: Graphic of the so called "jet" that develops during the impact of the workpiece ("Flyer Tube") and the core [14].

Figure 15 shows an optical micrograph of the typically observed wavy interface that is formed between the workpiece and the core surfaces, in this example between an Aluminum workpiece and a Copper core:

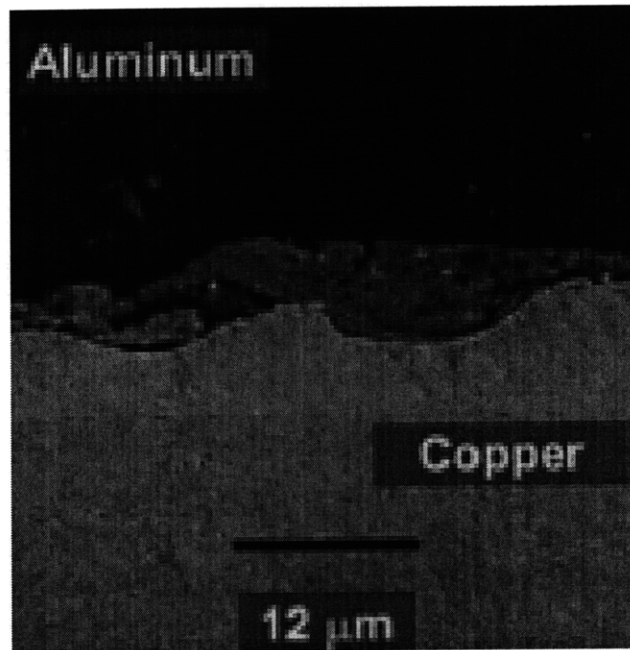


Figure 15: Typically observed wavy interface of an EMW joint. In this case between an Aluminum workpiece and a Copper core [9].

Section 1.1.2.3 will describe the formation of the wavy interface that is formed during the EMW process, see Figure 15.

Process Parameter: Gap

Figure 16 shows a study interrelating the gap between the workpiece and the core with the tapered angle and the resulting weld length ratio R (see Equ. 1.29). The tapered core, compared to the non-tapered core shows better weld length ratios for lower gaps, but at higher gaps than 1.5 mm drops back down to $R=0$, where the straight core still shows an R of 100%. The optimum gap for both, tapered and straight core was found to be 1.5 mm in this setup.

The conclusions are that the tube does not have enough time to gain velocity, if the gap is too small and if the gap is too large the kinetic energy of the tube is converted into deformation rather than into collision energy. Furthermore, the authors of this study (Kojima et al.) found that the effect of the gap was interrelated with the current frequency. In fact, they found that the time to impact should lie between $\frac{1}{4}$ and $\frac{1}{2}$ of the current period (when the magnetic pressure is maximized and falls almost to zero, respectively).

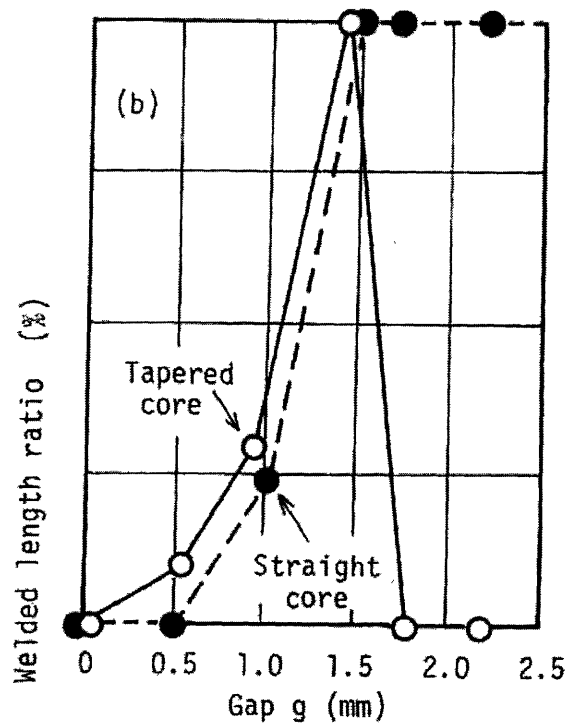


Figure 16: Effect of the gap between tube and core on the welded length ratio. (Note: Al specimen of $t = 0.6$ mm for tapered core; $t = 1$ mm for straight core, discharge current = 60 kA) [14]

Process parameter: Diameter and Wall Thickness of the Tube

Figure 17 shows a study of the effect of the wall thickness of the workpiece. The obvious result was that when the tube wall thickness decreased it was easier to achieve an EMW joint, due to its lower mechanical strength [15]. Certainly, a wall thickness that is too small, can cause failure of the tube, as was the case for a wall thickness of 0.5 mm in this case.

Figure 18 shows an experiment of the same study, which was performed to show the effect of the diameter of the tube on the final welded length ratio R . As the diameter of the workpiece is changed, so is the inner diameter of the coil and therefore the inductance, see Equ. 1.16.

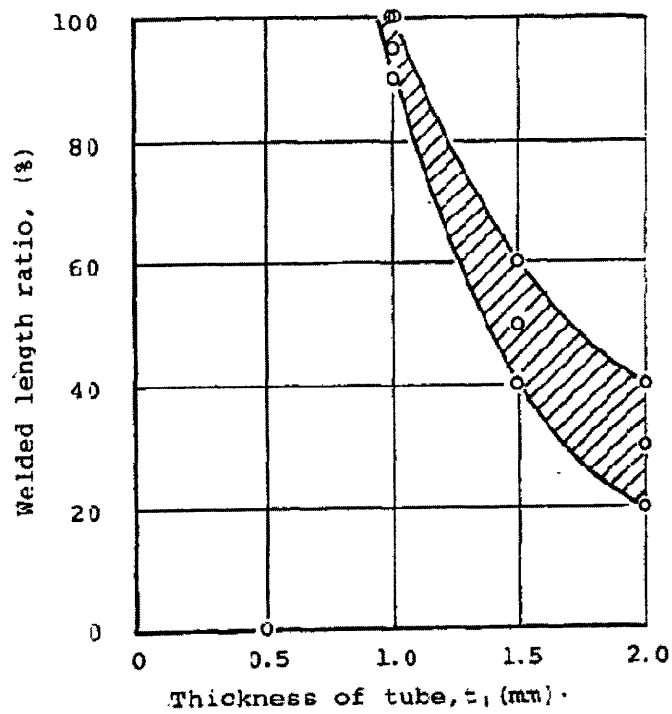


Figure 17: Effect of the wall-thickness of the workpiece on the welded length ratio R [10].

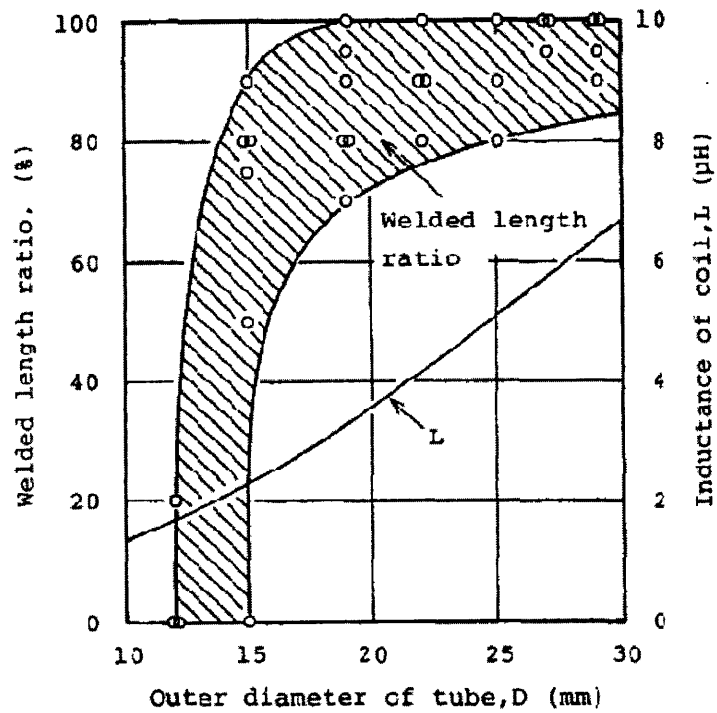


Figure 18: Effect of the outer diameter D of the workpiece. L is the inductance of the coil, which also changes due to the change of the inner diameter of the coil [10].

The mechanical strength of a tube decreases as its wall-thickness decreased, the same effect occurs when increasing the diameter of the tube. For diameters larger than 20 mm in this case, welded length ratios of 100% were always found for in this study [10, 15].

Process parameter: Weld length

Ring height in this case is nothing else than the length over which the workpiece is formed upon the core in the case of EMW. Figure 19 depicts the set of Al 6061 T4 rings that was tested in the EMF study of Tamhane:

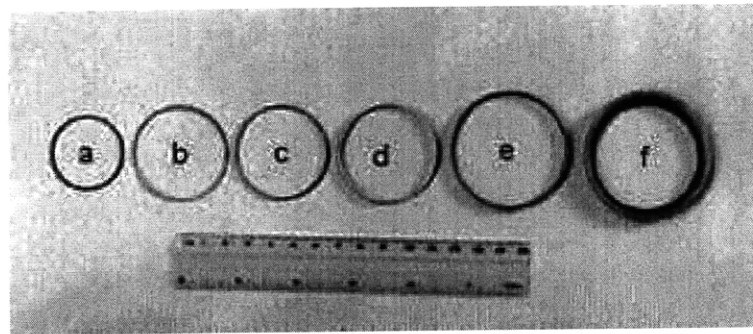


Figure 19: Ring expansion experiment specimens [16].

Tamhane has found that the height of the specimen rings has an effect on the ductility during ring expansion experiments. He found that the maximum deformation that can be obtained without failure is seen to increase with increasing ring height [16].

Additionally, these factors (workpiece wall thickness and diameter and strain rate sensitivity) are just as important for EMF processes, because they decrease the necessary energy needed to deform the workpiece.

At high strain rates, some Aluminum alloys are strain dependant, which brings us to the next process parameter, called strain rate sensitivity.

Process parameter: Strain Rate Sensitivity

Strain rate sensitivity decreases with decreasing purity and the increase of alloy strength. Figure 20 depicts a set of different Aluminum alloys and strain rate experiments plotting the Rate Sensitivity Parameter against the alloy's strength.

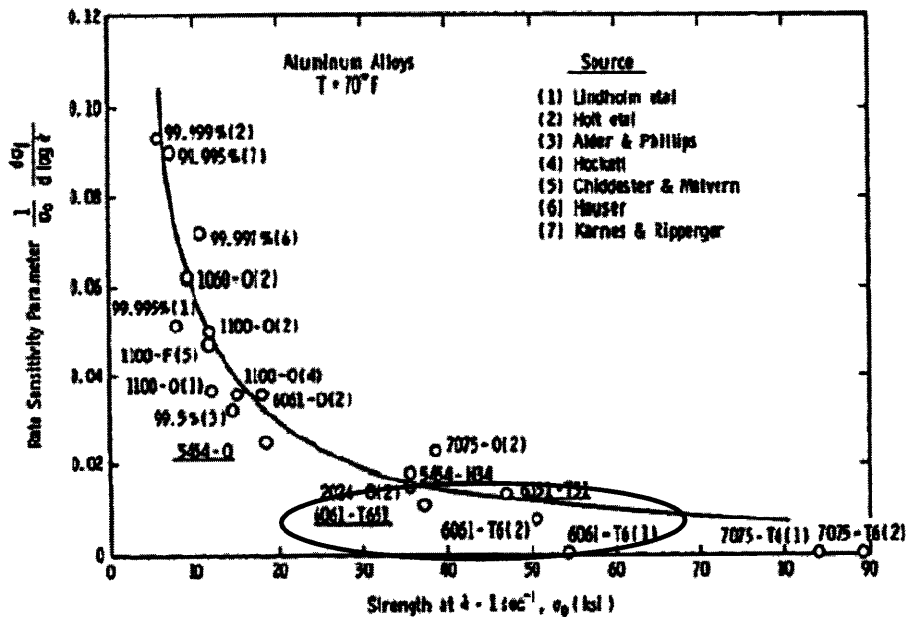


Figure 20: Graph of rate sensitivity parameter versus the strength of several Aluminum alloys [17].

The summary of experiments shown in Figure 20, clearly states that Al6061-T6 falls into the family of Aluminum alloys, which observe a lower strain rate sensitivity. That is good for high speed forming and joining processes, because in general at higher strain rates, strain hardening is increased, which leads to less formability of the material.

Al6061-T6 has a further advantage as far as formability is concerned, because it holds a mechanical property at such high strain rates, which is called hyperplasticity. We will deal with this property now.

Process Parameter: Formability of the Workpiece Material

Hyperplasticity extends the ductility of a material in high velocity conditions. Materials with this behavior can be stretched to much higher strains at high velocity compared to what is available in conventional quasi-static stretching. A category of materials with this behavior is low strain rate sensitivity materials (for example: Aluminum alloys with high strength, see Figure 20). Hyperplasticity results from inertial stabilization of material failure modes and permits dramatic increases in strain to failure. Figure 21 shows an example of a major and minor strain plot for direct force quenching (DFQ) Steel and Al6061-T4, which were conventionally stretched and Al6061-T4, which was stretched by EMF.

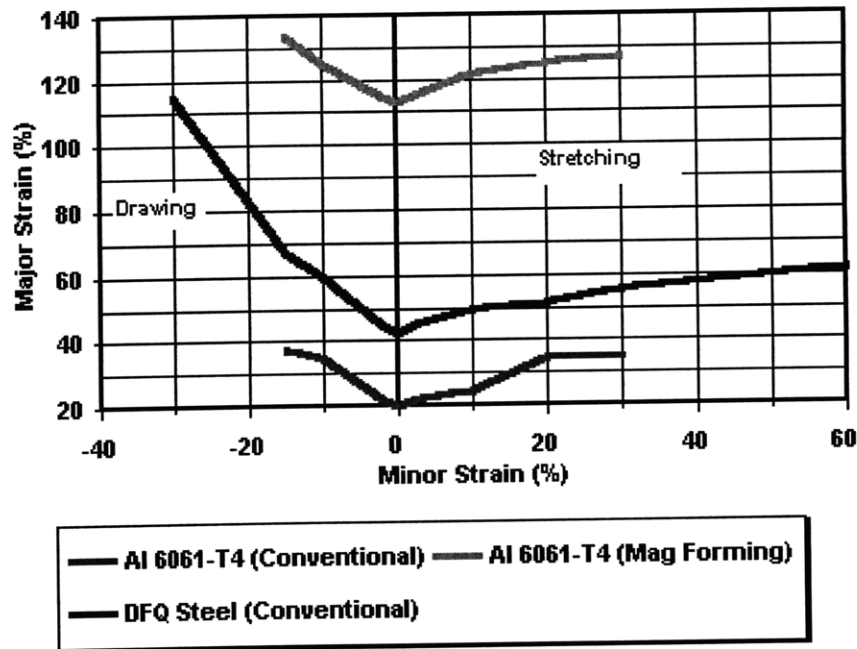


Figure 21: Major Strain and Minor Strain plot for Al6061-T6 and DFQ Steel. The Aluminum alloy was stretched using both methods: conventional and EMF stretching [18].

One can see, in Figure 21, that the values observed for major strain in the EMF stretching experiment were up to 5 times higher than compared to conventional stretching experiment, for Al6061-T4.

Some reasons that are thought to be major for the observed results caused by Hyperplasticity are:

- a. Inertial stabilization of necks¹: This is described by a uniform major strain distribution and a deformation diffused along the workpiece instead of concentrated in the necking region (“diffuse neck development”).
- b. Elimination of frictional contact: the tool does not touch the workpiece during the operation.
- c. “Inertial Ironing”: This is a common effect observed in conventional sheet metal forming processes, where due to impact a large through thickness compressive stress is formed. This can also produce lateral extension of the material [18].

¹ **necking** is a mode of tensile deformation where relatively large amounts of strain localize disproportionately in a small region of the material. The resulting prominent decrease in local cross-sectional area provides the basis for the name "neck" [[http://en.wikipedia.org/wiki/Necking_\(engineering\)](http://en.wikipedia.org/wiki/Necking_(engineering))].

1.1.2.3 Mechanics of the EMW Process

It is generally accepted by many investigators that the well known phenomenon of jet formation (see Chapter 1) at the collision point is an essential condition for high energy rate welding [19].

During the process of jet formation, a chemically clean surface of the outer and inner workpieces is produced, free of films and contaminants. Therefore, the bare surface atoms of the two materials can meet at interatomic distances. Furthermore, the interfacial pressure during the collision can reach values of the order of magnitude of 10^2 Mbar, which renders the materials to act like fluids. Therefore, using fluid mechanics Cowan and Holtzman, among others, have shown the importance of a critical collision angle, for jetting to occur [20]. Figure 22 shows a diagram illustrating the important parameters during the impact of the outer workpiece with the inner workpiece:

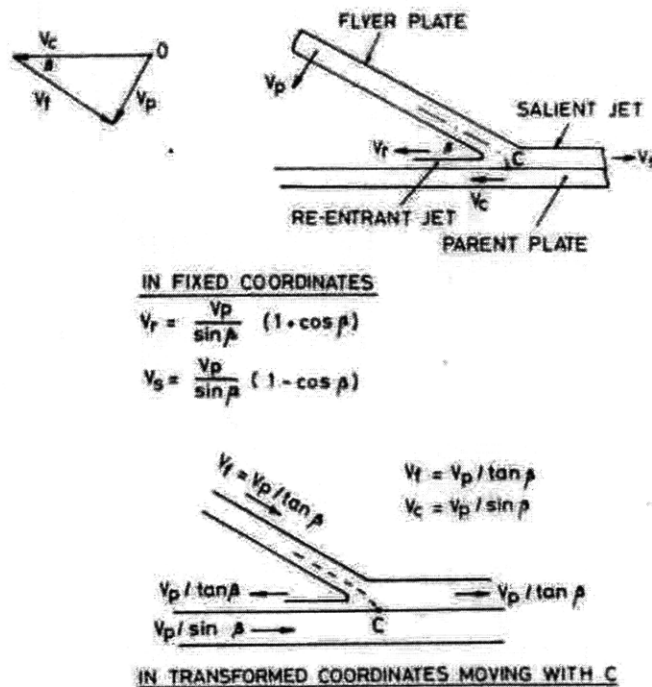


Figure 22: Welding velocity diagram [19].

One can see from Figure 22 that the critical collision angle can be calculated by

$$\beta = \sin^{-1}(v_p / v_c). \tag{1.30}$$

Figure 23 shows this critical collision angle as a function of the collision velocity, for a selection of materials.

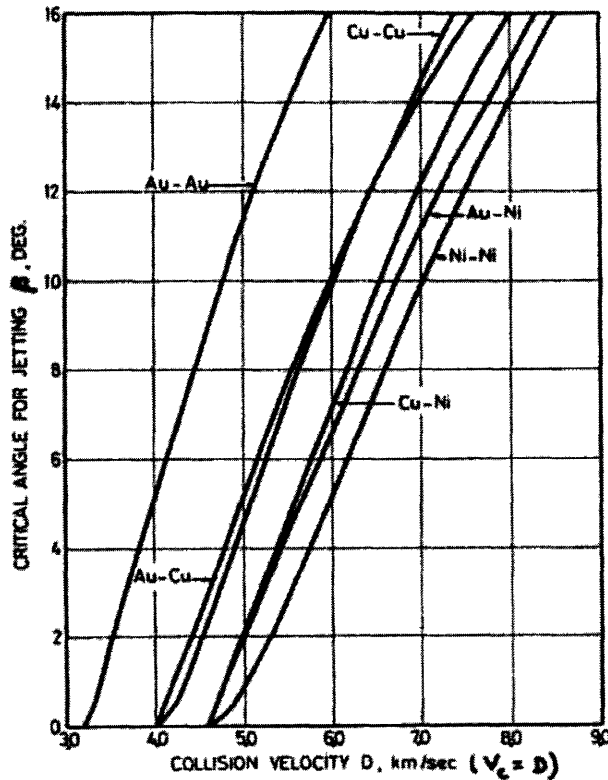


Figure 23: Relationship between the calculated values of β and the collision point velocity for initially parallel plates [20].

We will now go into further detail of the fluid mechanics that describe the process of wave formation, which is observed at the interface of the inner and outer workpiece.

Interfacial Wave Formation

The Explosive Welding literature presents a good deal of information on the description of the formation of the observed interfacial waves [19]. Figure 24 shows an example of three types of waves, which were observed in the Explosive Welding literature. The result depicted in Figure 24a is caused by a large rotation, without any melting of either of the materials. Figure 24b shows an example of a multilayer Cu-Brass-stainless Steel wire reinforced composite. The large wave is categorized by a front vortex, but no back vortex. Furthermore, at the crest of the wave and at the front vortex phase changes can be observed. Figure 24c is an example of another multilayer interface. Here, front and back vortices are observed, as well as plane interfaces and a large asymmetry.

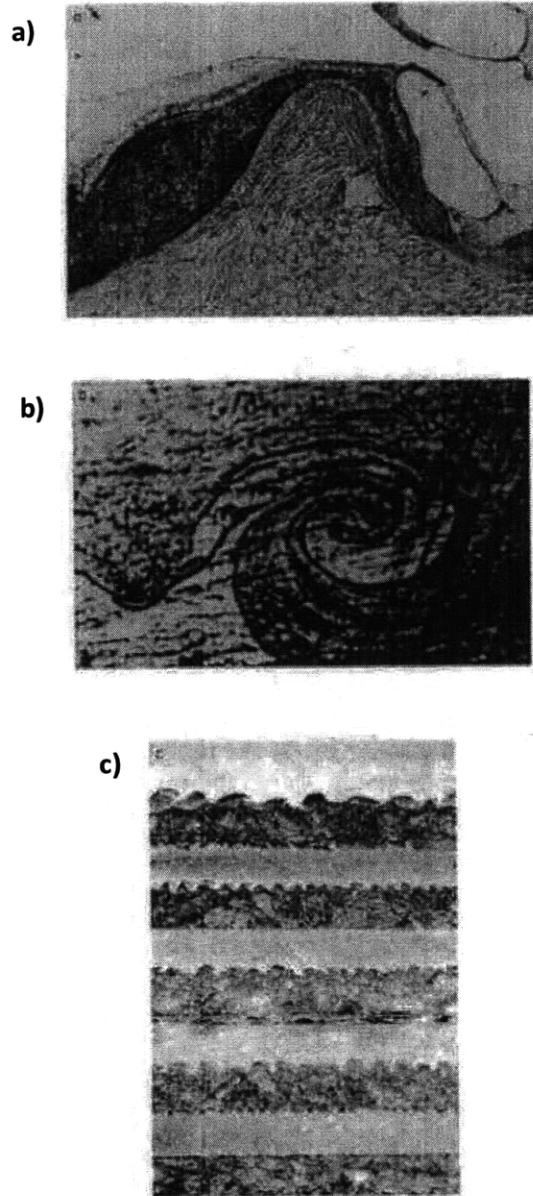


Figure 24: Types of welding waves. a) Rotation without appreciable melting, b) large wave with front vortex only, c) multiple interface waves [19].

H. El-Sobky presents a brief review of the existing mechanisms, which can be classified into four groups:

i) Jet Indentation Mechanism

This mechanism is described by two postulates and depicted in Figure 25. First that the wave forms because of the salient jet (see also Figure 22) indenting into the base plate and the periodic release of the hump formed ahead of the collision point by the material removed by the indentation. Then, the

salient jet overtakes the hump and the process continues [21]. Second that the indentation happens due to the re-entrant jet and the formation of vortices, where re-entrant jet material is trapped between the hump and the salient jet [22].

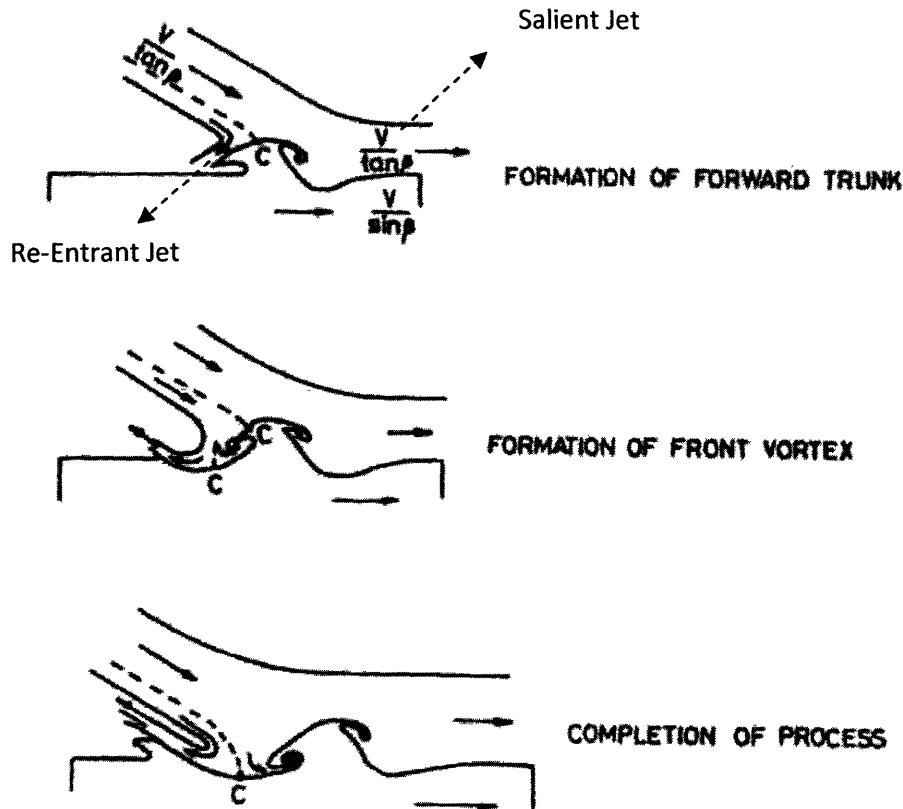


Figure 25: Diagram of the jet indentation mechanism causing the waveform that is observed at Explosive Welding and EMW material interfaces [22].

ii) Flow Instability Mechanism

This mechanism suggests that the waves are formed ahead or behind the collision point, due to a velocity discontinuity across the interface involving the re-entrant jet and salient jet respectively. Some important aspects of this mechanism are:

- Process of wave formation is treated as a Helmholtz Instability.

This can occur when velocity shear is present within a continuous fluid or, when there is sufficient velocity difference across the interface between two fluids [23-25]. Figure 26 shows an example of such instability.



Figure 26: Wave clouds forming over Mount Duval, NSW [26].

- The discontinuity is a sharp one.
- The re-entrant jet is necessary for wave formation.
- The re-entrant jet must remain in contact with the parent plate.
- The fluid behavior does not extend to the salient jet [27].

Robinson, however states through calculations that the salient jet still behaves like a fluid, due to the high strain rates and that the velocity profile across the interface has one or two inflection points. Robinson computed the surface of the deformation as a surface of constant velocity. The result was a wave with a rolling up crest [28-30].

iii) Vortex Shedding Mechanism

This mechanism is believed to be analogous to a von Karman vortex street. Figure 27 an example of the formation of a von Karman vortex street. Waves are formed due to a vortex shedding mechanism initiated at the stagnation point and continuing to grow behind the collision zone. It is suggested that the stagnation point acts as a solid obstacle, once a steady state has been established [19, 31]. Figure 28 shows a schematic of the mechanism.

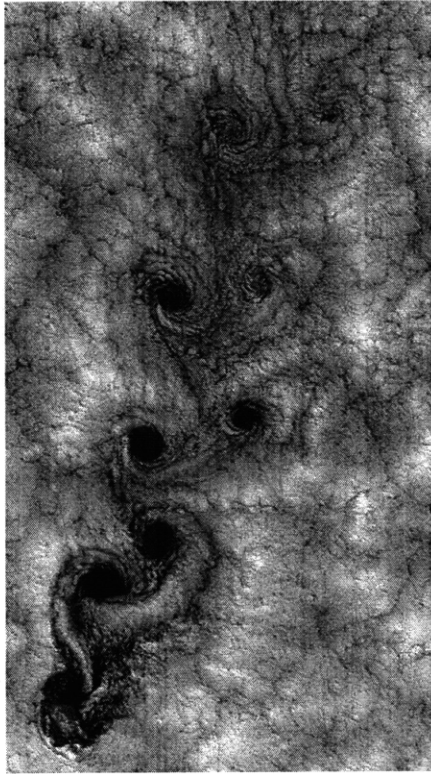


Figure 27: Image of clouds off the Chilean coast near the Juan Fernandez Islands (also known as the Robinson Crusoe Islands) on September 15, 1999 showing a unique pattern also called a von Kármán vortex street [32].

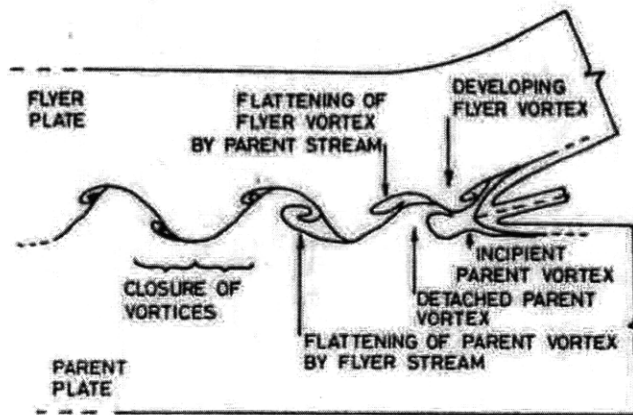


Figure 28: Schematic of the vortex shedding mechanism [31].

1.1.2.4 Necessary limiting conditions for EMW

In addition to what has been observed in the remaining EMW and Explosive Welding literature and summarizing what has been stated so far we can state a collection of necessary limiting conditions for EMW [7, 19]:

1. As stated above, a minimum collision angle must be exceeded, for jetting to occur. For a given metal the value of such an angle is a function of the collision velocity (see Figure 1).

2. It is beneficial if the collision velocity v_c and the plate velocity v_p are less than the velocity of sound in either the inner or outer workpiece. This condition, which was found experimentally, expresses the need for the dynamic pressure to be held for a sufficient length of time to observe interatomic diffusion and equilibrium within the collision region. In addition, otherwise the reflected stress waves can interfere with the incident wave at the collision point [19]. However the next condition will show that much higher velocities are needed to achieve an EMW joint for certain materials.

3. A minimum outer workpiece velocity must be exceeded (and hence a minimum impact pressure). The empirical formulas for the minimum velocity to achieve a weld during EMW have been empirically established and presented (see above). The author presents an approach to optimize the EMW process based on this observation by introducing a new formula to calculate a threshold kinetic energy. The formula makes it possible to easily create plots showing the weldability of certain materials based on their Vicker's Hardness and the necessary threshold kinetic energy.

Furthermore, it is suggested that the impact energy required is related to the strain energy and to the dynamic yield strength of the outer workpiece material [33]. Certainly, also an upper limit for the energy is required to avoid excess heating and possibly melting of the materials.

4. The gap between the inner and outer workpiece needs to be sufficiently large so that the outer workpiece can accelerate to the required threshold velocity. For Explosive Welding this value lies between 0.5 to 1.0 times the thickness of the outer workpiece [33].

5. If possible the outer workpiece (in the case of a compression coil setup) should have a higher electrical conductivity than the inner workpiece. This will lower the Joule heating effect of the outer workpiece, as well as provide a higher possible magnetic pressure for the workpiece deformation. Furthermore, it has been reported that induced currents in the inner workpiece can cause the outer workpiece to be repelled into the opposite direction, creating a so-called "cushioning effect" [7].

From this summary of limiting conditions for EMW and as stated many times, it can be seen that it is difficult to separate the respective efforts completely. In Appendix A, the author presents additional possible limiting conditions, based on the EMW, the Explosive Welding and the Cold-Welding literature.

With the presented literature analysis and the summary of further observations in the Cold-Welding, Explosive Welding and EMW literature (see Appendix A), the following factors could be of importance in addition to the first five limiting conditions for EMW.

VI. Metal to Metal-Oxide Hardness Ratio

Material combinations that observe a large difference between their metal and metal-oxide hardness ratios are more easily welded through Cold-Welding [35,36]. We have stated before that the hardness of the materials of the inner and outer workpiece play an important role in the EMW process. The author thinks it is important to also look at the hardness of the oxide and compare it to the hardness of the metal itself.

VII. Surface Preparations

For Cold-Welding it is observed that a surface preparation using scratch-brushing, and/or the use of Heptane are most beneficial, reducing the necessary deformation to create proper weld [35,36].

VIII. Crystal Structure of the Metal Combination

Looking at the material combinations that have been electromagnetically welded at this point, it can be observed that materials with similar crystal structures (besides similar metal combinations) are more favorable. Furthermore, one finds that hexagonal materials are not favored for Explosive Welding or EMW and can sometimes not even be welded autogenously (with the exception of Zr and Mg). Fcc crystal structures are reported to be best weldable, followed by bcc and fcc-bcc combinations, such as Brass and Steel [34,41].

IX. Crystal Orientation

For cold-welded joints it is observed that an optimized texture orientation of the individual parts can improve the strength of the welded joint [35,36].

X. Post Heat Treatment

Post heat treatment has been reported to be beneficial for dissimilar metal combinations of cold-welded joints, as it has a positive effect towards the formation of brittle intermetallics [35,36].

The next chapter will give an overview, where EMW is currently used in the industry and who is studying it.

1.2 State of the Art in Electromagnetic Welding

This chapter will give a brief introduction of the OEMs (1.2.1), scientific centers and universities that are currently involved with work and research regarding Electromagnetic Welding. Furthermore, an overview of the current joining possibilities, as far as different material combinations and their current applications are concerned, is given (1.2.2). Finally, a summary of state of the art joining methods used in the automotive industry and to join Aluminum is presented (1.2.3).

1.1.3 Who is researching High Energy Joining Technologies

a. OEMs

DANA

The Advanced Technology Program's (ATP) Focused Program, Motor Vehicle Manufacturing Technology, provided Dana Corporation with the necessary funding to develop technology to bond Aluminum to Steel without depositing additional metal at the weld site. Dana Corporation developed a functional magnetic pulse welding machine prototype to manufacture automobile parts that are two-thirds lighter. Once installed into vehicles, these lighter parts would result in increased fuel efficiency of 8 to 10 percent. Since the project ended in 1998, automakers have contacted Dana Corporation about using magnetic pulse welded materials in their vehicles. [44]

Driveshafts have been prototyped and developed initially for 89 - 102 mm tube diameters with 2.1-mm wall thickness. The current equipment can be tooled for up to 150 mm diameter thin walled tubes for light-duty and medium-duty applications. [45]

PULSAR

Pulsar's patented magnetic pulse welding technology incorporates switching capability able to transfer as much as 2 million amps in less than 100 microseconds. It can be applied to any two materials, as long as one of them is a good electrical conductor. The other could even be plastic or ceramic. The company has been contracted by General Motors to produce test samples of welded tube for delivery in early 2000. The samples include an all-Aluminum tube as well as a combined Steel/Aluminum tube.

The company has also won a contract from Federal Mogul to develop a welded aluminium/ Steel part, and has installed its first magnetic pulse welding machine at the US Edison Welding Institute. [11]

MAGNEFORM

MAGNEFORM has been an Electromagnetic Forming supplier since 1961. Their technologies are installed in over 500 systems worldwide, as well as in industrial installations in 19 countries. Welding Dissimilar Materials*, etc. They have been first in Electromagnetic Welding in U.S.A, 1967. [46]

b. Universities and Scientific Centers

Through the Pulsar Research & Education Program, which PULSAR established to promote magnetic pulse technology and facilitate the communication of know-how and experience between major magnetic pulse research centers worldwide, selected institutes like the University of Waterloo in Canada, RIST in South Korea and MIRDC in Taiwan, to name a few, collaborate and conduct further research on this technology with the aim of making it an additional technology of choice for manufacturing industries worldwide [47].

Here, is a list of some of the strong players working on Electromagnetic Welding research and accompanying technologies and sciences, such as Electromagnetic Forming and Hyperplasticity.

Waterloo University

The University of Waterloo in Ontario, Canada, known for being one of the most innovative universities in Canada, has been researching electromagnetic forming for the past six years. The current research focuses on the formability of electromagnetically-formed automotive grade Aluminum alloy sheets and the simulation of the electromagnetic forming process. In collaboration with PULSAR and using their system they are expected to significantly improve the University's capabilities in this field. [48]

Edison Welding Institute (EWI)

The EWI owns 15- to 90-kJ MAGNEFORM power supplies with coil systems for various sizes (compression coils and expansion coils, as well as open coils (“split”). Furthermore, they have a process parameter optimization/prediction system [49].

IAP Research

IAP Research has its own manufacturing capability through MAGNEPRESS Products, LLC. This is a joint venture between IAP and Select Industries Corporation of Dayton, OH. MAGNEPRESS Products, LLC can produce prototype to medium run quantities of parts using various magnetic pressing technologies.

This capability includes the production of net powder metal components and electromagnetic forming operations to include, sheet forming, tube expansion, tube reduction, and pulse welding of Aluminum, copper and low alloy Steel materials [50].

Ohio State (Group of Prof. Glenn S. Daehn)

Recent work in Daehn's group has shown that high velocity sheet metal forming can dramatically improve material formability (the amount of stretch available without tearing) and wrinkling can be greatly suppressed. Electromagnetic forming is a very convenient way of flexibly producing very high velocity deformation (see example at right of non-contact launch of an Aluminum sheet). Presently Daehn's group is working with automotive, Aluminum and aerospace companies and the National Science Foundation to develop this process. Details are available at www.osu.edu/hyperplasticity [51].

Livermore Software Technology Corporation (LSTC)

LSTC, in California has developed a new electromagnetism module in LS-DYNA for coupled mechanical/thermal/electromagnetic simulations. One of the main applications of this module is Electromagnetic Metal Forming. LSTC has published a paper on the module in collaboration with Glenn Daehn. [52,53]

1.2.2 Materials Combinations and Applications

a. Materials

EMW can work on any material that is conductive. The more conductive the part, the less energy is required to achieve a weld. The easiest materials to weld are Aluminum and copper—they can be welded to almost anything.

EMW has been successful in welding Aluminum to Steel. Other dissimilar and similar metals that have been welded can be found in Table 2 and Appendix A.

		Inner tube rod												
		Alumi. 1xxx	Alumi. 3xxx	Alumi. 5xxx	Alumi. 6xxx	Alumi. 7xxx	Cast Alumi.	Cu	Brass (C360)	Steel 10xx	SS (304)	Ni	Mg	Ti
O u t e r t u b e	Alumi. 1xxx	U	U	U	U	U	U	U	U	U	U		U	
	Alumi. 3xxx	U	U	U	U	U	U	U	U	U	U			
	Alumi. 5xxx	U	U	U	U	U	U	U	U	U	U		U	
	Alumi. 6xxx		U	U	U	U	U	U	U	U	U			
	Alumi. 7xxx				U	U	U							
	Cast Alumi.													
	Copper						U	U	U	U	U			
	Brass (C360)						U			U				
	Steel 10xx									U	U			
	SS (304)										U			
	Ni										U		U	U
	Mg													
	Ti													

Table 2: Metal combinations that have been successfully welded [34].

Magnetic pulse technology also can be used for joining or crimping parts that do not necessarily need a metallurgical bond, such as a metal to a nonmetallic part. It can create a mechanical lock on ceramics, polymers, rubber, and composites, so adhesives, sealants, and mechanical crimps are not necessary. With the process, metal is basically shrink-wrapped over the components.

b. State of the Art Applications of Electromagnetic Welding

Fuel filters (Automotive; PULSAR)

Materials: Aluminum - Aluminum

Dimensions: Up to \varnothing 100 mm

Recommended machine: MPW 25/9

To assure leak-free filters, manufacturers have developed special manufacturing processes, some based on laser welding. To achieve good results with laser welding, the welded parts should have precise dimensions, tight tolerances and a very clean surface. Some car makers require that the parts are machined to their final dimension before they are welded.

Electromagnetically welded fuel filters have a lower investment in equipment and manufacturing costs, parts that could be less accurate, with lower tolerances and with no special pre-weld preparation.

An advantage that is very particular to EMW is that the filters can have smaller dimensions as there is no need to keep a distance between the welding area and the filter elements made from paper to prevent burning. Figure 29 shows two photographs of the manufactured fuel filters using EMW at PULSAR:

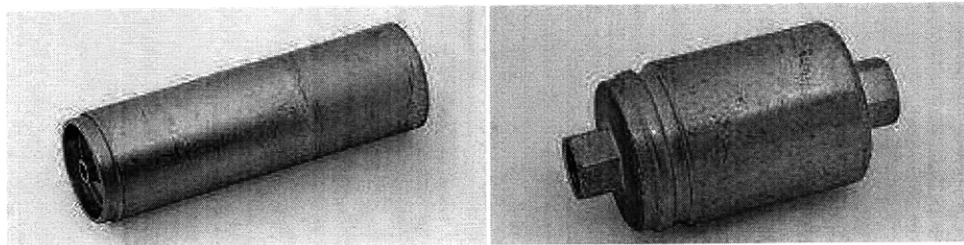


Figure 29: Photograph of two fuel filters electromagnetically welded at PULSAR [54].

Driveshafts (Automotive; PULSAR)

Materials: Tube: Al-6061 or similar; Yoke: Al-6061 or similar; or low-carbon Steel

Dimensions: Up to \varnothing 110mm; Tube's wall thickness up to 2.2 mm

Recommended machine: MPW 100/25

Driveshafts are large and relatively heavy parts made of Steel or stainless Steel. Aluminum alloys are not used due to the inability of conventional welding methods to weld dissimilar metals, and due to the heat which is generated during the welding process, causing the formation of intermetallics.

Using conventional welding techniques, the tubes used for driveshafts must be thicker than required to compensate for the reduction in mechanical properties in the welding area due to heating.

Driveshafts welded with EMW, showed twice the torque strength compared to conventional welding, with the same tube dimensions. Furthermore, it is possible to weld Aluminum tubes to Steel yokes thus saving about 1kg per 1 meter of driveshaft length. Figure 30 shows the joint interface between Steel and Aluminum. The number of parts, which are required for dynamic balancing is reduced, by delivering a homogenous weld.

The process is environmentally friendly, with no gases, sparks, smoke or radiation. EMW welds also save consumables such as filler wire or shielding gases, and additional operations such as pre and post-weld cleaning and deburring.

Figure 31 shows the manufactured driveshaft using EMW, after a torsion test. It could be shown that the weld sustains the test and the tube material fails before the joint.

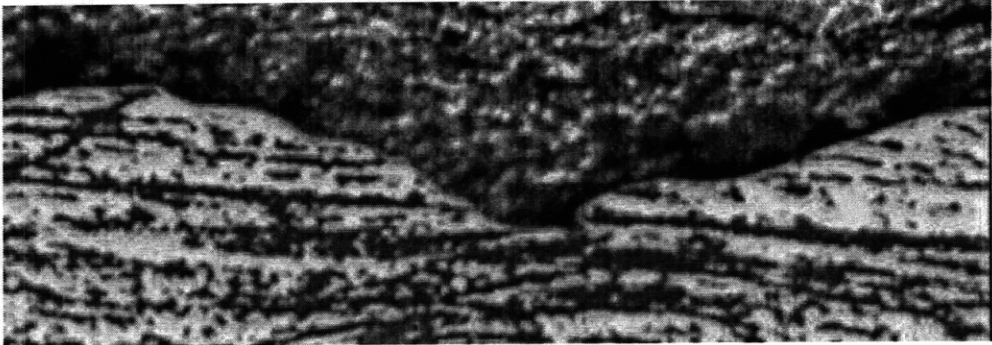


Figure 30: Micrograph of the Aluminum to Steel weld interface: no heat affected zone [54].

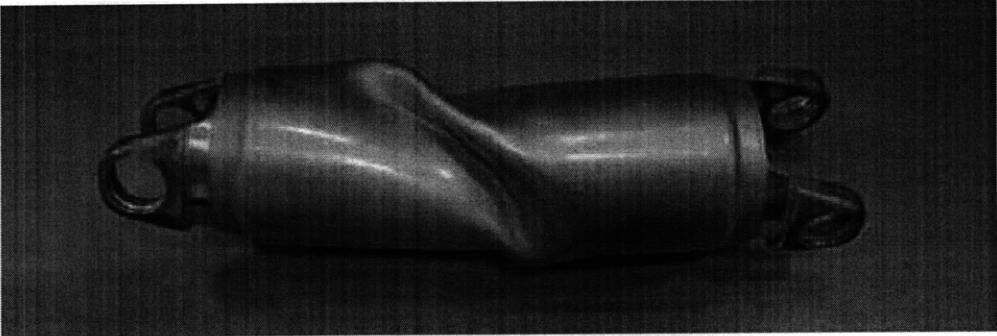


Figure 31: Photograph of the driveshaft, after a torsion test [54].

Power cables (Automotive; PULSAR)

Materials: Cable: Al, Cu; Lug: Al, Cu, Brass

Dimensions: Up to Ø 25 mm

Recommended machine: MPW 25

Today's cars require more electrical power than ever before. Electrical systems are becoming mission critical and must be completely reliable. This, together with hybrid cars and the trend of moving batteries to the back of the car, presents new challenges to design and production engineers.

To improve power/weight ratio, car makers are moving to Aluminum cables. However, Aluminum cables are more difficult than copper cables to tighten to the connectors, which are usually made of brass or Aluminum. Conventional methods such as brazing or crimping do not provide the required long-lasting conductivity and contact. In addition, these methods tend to develop corrosion in the connection area.

The EMW creates a reliable tight connection that sustains its high conductivity and high corrosion resistance even after tough vibrations and extreme temperature changes. Figure 32 shows the cable section after the EMW process. The micrograph shows that joining occurred between the individual wires of the cable.

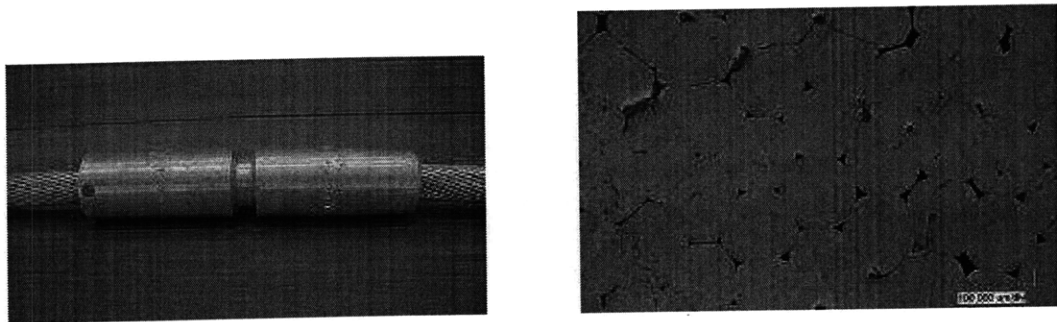


Figure 32: a) Photograph of the electromagnetically joint cable section.
b) A micrograph showing a cross-section of the individual wires of the [54].

Other (Automotive; PULSAR)

Welding of Body Construction elements (bumper support beams, welding of Aluminum interfaces to hydro formed Steel, and bi-metal earth connectors), Exhaust parts, Fuel pipes and Automotive Climate Control Elements [54].

HVAC (Heating, Ventilating and Air Conditioning) parts (Automotive and Other, PULSAR)

Approximately half a billion cooling system units, including refrigerators and air conditioners, are manufactured every year. These units contain gas that runs through tubes, valves and fittings each made of a different material such as copper, Aluminum, Steel or stainless Steel.

Conventional methods for joining dissimilar metals, such as brazing, bonding or mechanical locking have several limitations:

- High rate of leaks in mass production, leading to a significant amount of re-work
- Galvanic Currents leading to corrosion, which in turn causes leaks
- Dirty processes, leaving the joined area with poor aesthetic

PULSAR presents a variety of dissimilar EMW metals joints for HVAC, such as copper to Aluminum or copper to stainless Steel creating a solid-state cold weld (see Figure 33).

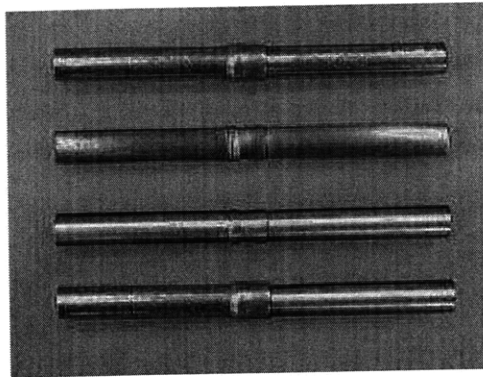


Figure 33: Photograph of HVAC piping of a variety of dissimilar material joints [54, 55].

Nuclear Industry (EWI, MAGNEFORM)

With nuclear power plants the choice of, and design for, refractory metal or refractory metal alloy, ceramic, or non-refractory metal alloy cladding and refractory or non-refractory metal core structural materials is strongly influenced by the feasibility of joining dissimilar metal joints. The challenge therefore is the avoidance of brittle intermetallics that can form when joining dissimilar metals.

Project Prometheus is an aggressive effort to develop nuclear/electric propulsion for deep-space exploration. The basic concepts under consideration include a compact fission reactor coupled with a Brayton cycle turbine. The turbine would then drive on-board generators, providing electrical power for both propulsion as well as other on-board systems. The design mandates the use of refractory metals in the areas of the power system and the Brayton cycle turbine, however, uses working fluid systems largely manufactured from Ni-based superalloys. Assembly of the system therefore requires joining

techniques capable of attaching these disparate materials. In this program inertia welding, electro-spark deposition (ESD) and Electromagnetic Welding were considered. [56]

Welding Nuclear Fuel Pins (MAGNEFORM)

MAGNEFORM built special production machines for the welding of the end closures of nuclear fuel pins [Weld Journal June 1978]. The first was for Westinghouse Hanford, the second for PNC, a Japanese nuclear fuel manufacturer. Figure 34 shows an electromagnetically welded nuclear fuel pin end closure:

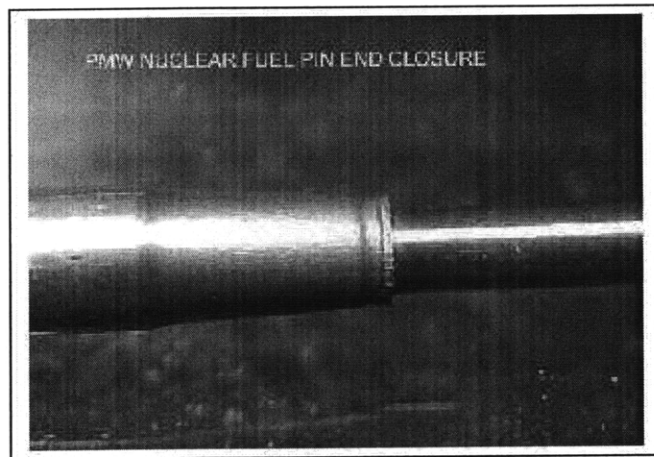


Figure 34: Photograph of an electromagnetically welded nuclear fuel pin end closure [57].

Various combinations of materials were welded including 316 Stainless Steel, Inconel 706, PE 16, and RA 330. Diameter of the outer tube was 0.230 inches. A mild Steel driver was used on the outside of the tube. Figure 35 shows a micrograph of an un-etched section of a welded fuel pin:

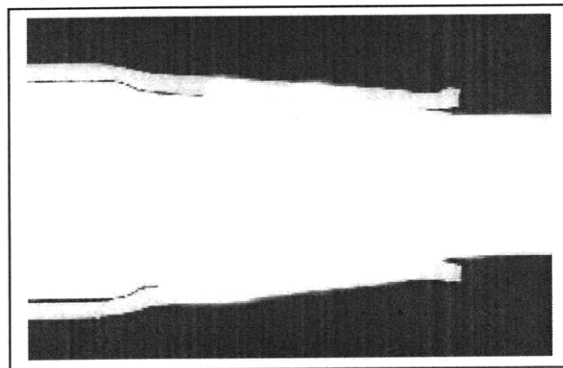


Figure 35: Micrograph of an un-etched section of a welded fuel pin [57].

In Figure 35, it can be seen in the cross-section that the two parts are firmly joint and welded. Figure 36 shows an electron-micrograph viewing the weld interface at a magnification of x1000:



Figure 36: Electron-micrograph showing the weld interface of the electromagnetically welded fuel pin end closure (magnification: x1000) [57].

Sealing of Aluminum Pressure Vessel (MAGNEFORM)

The requirement was to create a hermetically sealed pressure vessel using both mild Steel and Aluminum closures. The diameter was 2 inches. The body was Al6061-T6 and the closures Al6061-T6 and 1010 Steel. Figure 37 shows the pressure vessel before and after the EMW process:

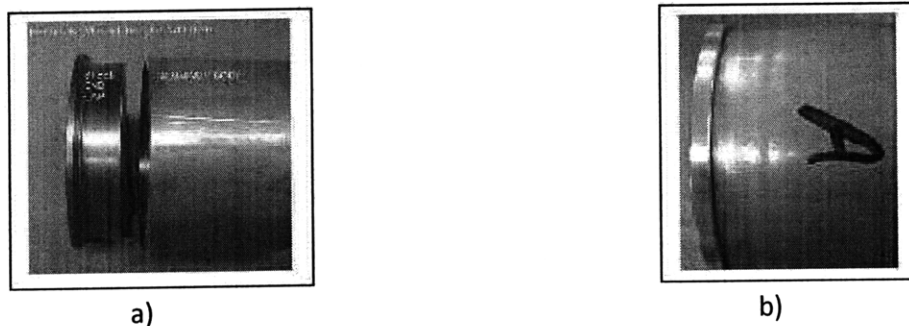


Figure 37: a) Photograph of the pressure vessel parts.

b) Photograph of the electromagnetically welded pressure vessel [57].

1.3 FORD – MIT Alliance; Scientific Objects and Tasks of this thesis

1.3.1 FORD – MIT Alliance

The Ford Motor Company and MIT are addressing an array of 21st century challenges that confront the automotive manufacturer through an innovative program begun in 1997. The Ford-MIT Alliance, renewed through 2008, has created a model for mutually beneficial university-corporate research and the alliance has grown beyond the initial focus areas of environmental science and policy, information technology in product development, virtual teams, and education. [58]

For this thesis, FORD would perform EMW experiments with their available EMW machinery, in Detroit. The experimental data and specimens would then be sent to MIT, through which the author was asked to study and optimize the process of EMW. In the following section, I will give an overview of the scientific objects that FORD asked to be investigated in this study. The particular points are highlighted in cursive italics.

1.3.2 Scientific Objects asked to be investigated by FORD in this study

1. *Validation of the EMW process simulation:*

- a. So that the process can be adopted or designed for other applications making prior experimental and empirical measurements unnecessary.
- b. The simulation should connect the EMF machine parameters, coil parameters, the initial geometry of the welded parts and the parameters of the weld.
- c. It will involve the combination of the separate models for the electromagnetic interactions, deformation of the blank and weld generation.
- d. The simulation should make it possible to optimize the parameters of the process and electrical circuit.

→ Simulation Effort of this study

In this study, theoretical calculations, a MultiSIM and a MATLAB model of the EMF process are provided. The author could not focus on the simulation of the EMW process, because the EMW experiments were not performed at FORD, in Detroit. Therefore, through this study, a collaboration with PULSAR had to be established first to perform the EMW experiments, in Israel. Furthermore, a collaboration was formed between MIT and LSTC, in California to help build an EMW simulation model in the future using the experimental data provided in this study (see Chapter 1.3.3).

PULSAR has also provided us with an in-company-built software that can calculate the outcome of the EMW experiments, based on the equations for EMW and EMF in the literature (see Appendix D).

2. Comparison of the weld performance vs. modeling result:

- a. Establishment of a welding window for which EMW is possible for different materials and dimensions.
- b. Demonstration of welded parts, which would verify the capability to produce a sound weld around the entire periphery of a circular weld or at least on four sides of a rectangular profile.
- c. Understanding of the maximum loads and types of loads that an EM weld can withstand to give an idea of loads that a particular part with EM welds can tolerate.

→ Materials to be electromagnetically welded

The appropriate work piece materials for EMF, as well as EMW are engineering materials which exhibit high electrical conductivity and low yield strength, such as Aluminum alloys, copper alloys, as well as certain Steels. In fact, high energy rate forming processes tend to overcome certain negative aspects of these materials, such as the low formability of Aluminum alloys in conventional (quasi-static) forming processes [59].

In the beginning, FORD has asked the Materials Welding and Joining Laboratory to investigate two materials: Steel DP600, as well as Aluminum alloy Al6061-T6 to be welded using EMW. Then, for my EMW experiments at PULSAR the material asked to be investigated was Al6061-T6.

FORD suggested future application for the use of EMW for one of their parts in their automotive production plants (see Appendix A). The material Al6061-T6 should be studied in detail *verifying the expected performance* of a part welded with EMW.

Furthermore, in this study a new method of calculating the critical kinetic energy of the process is presented, which can be used to create welding windows of EMW for several materials.

→ Electromagnetic Weld Evaluation

There are a number of ways that can be used to verify the quality of the weld that is obtained in this process. *We need to understand the maximum loads and types of loads that an EMW joint can withstand and tolerate. Furthermore, the demonstration of welded parts is necessary, showing a weld around the entire periphery of a circular weld or at least on four sides of a rectangular profile.*

The first method to evaluate the joint is a so called peel test on the welds similar to the verification process used in spot welds. An example of the result of this procedure is shown in Figure 38. It can be seen from this figure that the failure occurred in the base metal as opposed to the weld indicating a successful weld [60].

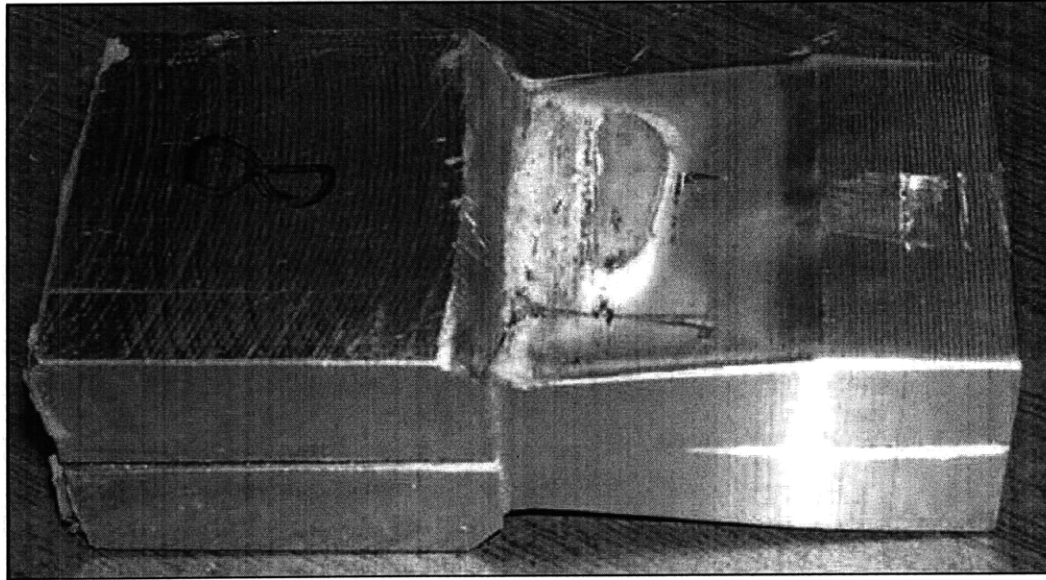


Figure 38: Results of a peel test performed on an electromagnetically welded specimen with rectangular cross-section, showing the base metal failure [60].

Another method is to analyze the microstructure of the weld material to verify the generation of welding waves at the weld zone interface. The absence of oxides at the weld interface indicates that there is a sufficient development of the cumulative jet, which cleans the workpiece surfaces during the welding process [37]. Figure 39 shows an example of a metallurgical analysis of an electromagnetically welded joint.

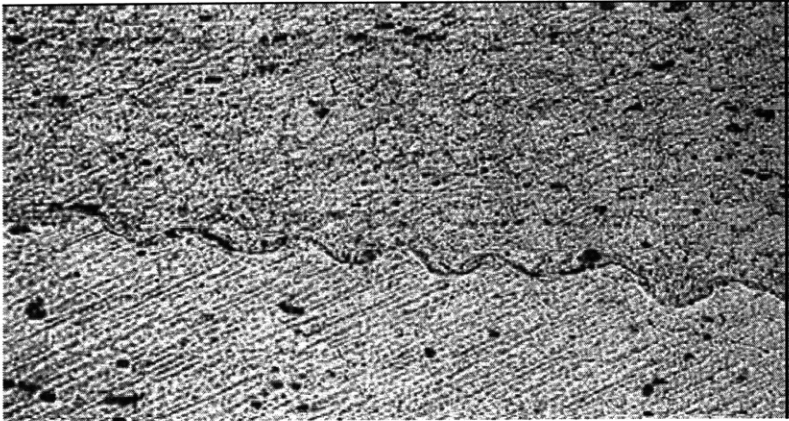


Figure 39: Microstructure of Al 6061 T6 that was electromagnetically joined. The image shows the typical wave interface [60].

The final analysis to determine weld quality can be the manufacturing of fatigue samples from the welded area and testing these samples, for example, in constant amplitude strain control. An example of such a sample is shown in Figure 40 [36]. The failure occurred outside the welded area in the base metal indicating the weld properties were as fatigue resistant as the base metal.

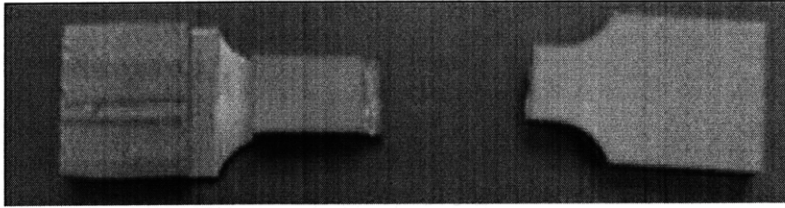


Figure 40: Failed electromagnetically welded sample, which was tested in a fatigue test under constant amplitude strain control [60]

In this study Optical Microscopy, SEM and EDS analysis were performed to study the weld zone interface in detail. Furthermore, tensile tests were performed, instead of peel tests, to verify the quality of the weld.

3. Development of the EMW process for high volume production:

- a. Proof that the process is robust, repeatable and capable of being scaled for high volume production.
- b. Design to make the process as low energy as possible, which would translate into reduced loads on the coil and thus increased life.
- c. Study of a new coil design, coil material or material combination that is able to endure the large stresses and strains.
- d. The design of multi-part coils, which could make it possible to manufacture EMW joints with complicated cross-sections.
- e. The investigation of issues such as dimensional tolerances and other process variations in an automotive industry environment studied.

→ Design of a low energy process

The EMW process must be robust, repeatable and capable of being scaled for high volume production. The process must be capable of operation at comparable lower energies in relation to other welding processes already in use. Furthermore, low energy transfers into reduced loads on the coil and an increased coil life.

Through a clear understanding of the process parameters, we must develop a set of parameters that are optimized to produce a proper weld with as low energy as possible, thereby, reducing the high stresses that are induced on the coil during the process.

First, this can be achieved by a pulsation of the magnetic field with the use of a transformer, setting the deformation at the right intervals of time and thereby forming the weld continuously using substantial lower amounts of energy. This technology was provided by partnering with PULSAR (company description: Chapter 1.2.1, collaboration overview for this study: Chapter: 1.3.3).

Secondly, the possibility of introducing a field intensifier along the axis of the coil inside the work, which is usually tubular, was studied.

A third way is the design optimization of the workpiece itself. Through optimized surface structures it might be possible to enhance the final mechanical properties of the electromagnetically welded joint [61]. In this study, we propose several ways how to optimize the material of the workpieces to lower the necessary energy of the EMW process.

Another study to be performed in the future could be to harness any later produced energy (after the first discharge current peak) and reuse it. This can be done by adjusting the electric circuit, yielding the highest energy output for a short initial period of time, during which the welding takes place, as well as recharging the capacitor and stopping the process.

4. Feasibility of the EMW process:

- a. Comparison to other welding techniques that are currently in use in the automotive industry.
- b. Balance of advantages and disadvantages of the process.
- c. Study of the possibility to make a final product that is superior to other joints made by other joining techniques.

→ Economical Feasibility Study of the Use of EMW in an Automotive Plant

For a new process to replace another process it must not necessarily, but in most cases should be superior in its energy consumption. It will be a challenge to design an EMW process to be part of an assembly line and be equally efficient as other welding processes in use, such as Laser Beam Welding, Spot welding or Seam Welding. Certainly, EMW has many advantages over the named processes, such as the possibility to weld a majority of metals, as well as join dissimilar metals. There are many other advantages, but in the end it will come down to the question, whether EMW can replace another process economically.

How to incorporate an EMW machine or robot into an automotive assembly line was not studied in this thesis, as well as other aspects such as tolerances issue and possible deviations from them (how precise the workpiece needs to be placed in the center of the coil / fieldshaper or if a movement of the workpiece during the process affects the reproducibility drastically).

However, the effect of cleanliness of the surface and a possible necessary surface preparation were studied for the use of EMW in an automotive industry environment.

1.3.3 Collaboration with LSTC and PULSAR

PULSAR

Through the course of the study, the author came across the company PULSAR, which already was described in proper detail [34]. A collaboration between MIT and PULSAR (Yoav Tomar, Victor Shribman) was established and initiated by the author starting in the fall of 2006. This collaboration was based on FORD employing PULSAR to develop their current EMW machinery in Detroit and PULSAR was very eager to collaborate again.

As stated, in Section 1.3.2, FORD would provide MIT with EMW samples manufactured with their machine, in Detroit, which should then be studied in detail. However, the machine at Detroit was never available for any EMW experiments and no specimens were delivered to MIT. Therefore, the author had to partner with PULSAR and go to Israel to perform the experiments himself. Finally, the collaboration with PULSAR led to our only EMW experiments that were performed in the summer and fall of 2007, at PULSAR, in Israel (see Chapter 4).

LSTC

Starting in the summer of 2006 the author traveled to California to visit LSCT California (company description in Chapter 1.2.1 and [52]). Through the LCTS-employed programmer Pierre L'Eplattenier, who has been collaborating with Glenn Deahn at the University of Waterloo to develop a model for EMF [53], a collaboration with the author was started to co-develop an EMW model, with LS-DYNA.

MIT would provide the experimental data that would then be used to optimize the EMW simulation model. LSTC has been very helpful in the process. The author provided LSTC with Solidworks [62] drawings of the coils and LSTC provided TrueGrid meshes of the Solidworks drawings [63]. However, this was done for the EMF coil at MIT only, because the collaboration and EMW experiments happened too late in the course of the study (see above and Chapter 2.4). Therefore, also no experimental EMW data could be delivered to LSTC, besides this thesis document.

The author hopes that the observations and experiments made in this study will lead to the final optimization of the EMW model, provided by LSTC and Pierre L'Eplattenier.

Bibliography – Chapter 1

- [1] Boris A. Yablochnikov, Method of Magnetic Pulse Welding an end fitting to a driveshaft tube of a vehicular driveshaft, US Patent No 5981921, 1999.
- [2] Robert L. Benoit, Bernard I. Rachowitz, Fabricating automotive spaceframes using electromagnetic forming or magnetic pulse welding.
- [3] Basic Research Needs for Vehicles of the Future
- [4] Beerwald C, Brosius A, Homberg W, Kleiner M, and Wellendorf A (1999), New aspects of electromagnetic forming, 6th ICTP Proc on Adv Tech of Plasticity, III, M Geiger (ed), Springer, 2471–2476.
- [5] Hokari H, Sato T, Kawauchi K, and Muto A (1998), Magnetic impulse welding of Aluminum tube and copper tube with various core materials, *Weld Int* 12.8., 619–626.
- [6] S. T. S. Al-Hassan, The Plastic Buckling of Thinwalled Tubes Subject to Magnetomotive Forces, *Journal Mechanical Engineering Science OIMechE* Vol 16 No 2 1914, 59-70.
- [7] Mamalis AG, Manolakos DE, Kladas AG, Koumoutsos AK, Electromagnetic forming and powder processing: Trends and development, *Appl Mech Rev* 57(4), 299-324.
- [8] Simonov, V.A., Building Criterion for Metals with Explosive Welding, Combustion, Explosion, and Shock Waves . Springer New York. Vol. 21, #1. January 1991. pgs. 1221-123.
- [9] M. Marya and S. Marya, Interfacial microstructures and temperatures in Aluminum-copper electromagnetic pulse welds, *Sci. Technol. Weld. Joining*, 2004, 6, 541-547.
- [10] K. Tamaki, M. Kojima. Factors Affecting the Result of Electromagnetic Welding of Aluminum Tube. *Transaction of the Japan Welding Society*, Vol 19, ?No. 1, April 1988.
- [11] <http://www.designnews.com/article/CA138008.html>
- [12] Wilson MN, and Srivastava KD (1965), Design of efficient flux concentrators for pulsed high magnetic fields, *Rev. Sci. Instrum.* 36(8), 1096-1100.
- [13] Powers HG (1967), Bonding of Aluminum by the capacitor discharge magnetic forming process, *Weld. J.* (Miami, FL,U. S.) 46(6), 507-510.
- [14] I. Masumoto, K. Tamaki, M. Kojima. Electromagnetic Welding of Aluminum Tube to Aluminum or Dissimilar Metal Cores. *Transaction of the Japan Welding Society*, Vol 16, No. 2, October 1985.
- [15] W. Beitz, K.-H. Grote, Taschenbuch fuer den Maschinenbau – Buckling of shells, p. C47.
- [16] A.A. Tamhane, M. Padmanabhan, G. Fenton, M. Altynova and G.S. Daehn. Opportunities in High-Velocity Forming of Sheet Metal.

- [17] J. Boyd. Increased Formability and the Effects of the Tool/Sheet Interaction in Electromagnetic Forming of Aluminum Alloy Sheet. M.S. Thesis. Waterloo, Ontario, Canada, 2005.
- [18] http://www.magnepress.com/qa_tube_forming.htm
- [19] T.Z. Blazynski. Explosive Welding, Forming and Compaction. Book, Applied Science Publishers LTD, 1983
- [20] G. R Cowan, A. H. Holtzman. J. Appl. Phys., **34** (1963), 928.
- [21] G. R. Abrahamson, J. Appl. Mech. (1961), 519-28.
- [22] A. S. Bahrani, T. J. Black, B. Crossland. Proc. Roy. Soc., **A296** (1976) 123-36.
- [23] http://en.wikipedia.org/wiki/Kelvin%E2%80%93Helmholtz_instability
- [24] Kelvin, Lord (William Thomson), "Hydrokinetic solutions and observations," *Philosophical Magazine*, vol. 42, pages 362–377 (1871).
- [25] Helmholtz, Hermann Ludwig Ferdinand von, "Über discontinuierliche Flüssigkeits-Bewegungen [On the discontinuous movements of fluids]," *Monatsberichte der Königlich Preussische Akademie der Wissenschaften zu Berlin* [Monthly Reports of the Royal Prussian Academy of Philosophy in Berlin], vol. 23, pages 215 ff (1868).
- [26] English Wikipedia <http://en.wikipedia.org/wiki/Image:Wavecloudsduval.jpg>
- [27] J. N. Hunt. Phil. Mag., **17** (1968) 669-80.
- [28] J.L. Robinson. Phil. Mag., **31** (1975), 587-97.
- [29] J.L. Robinson. Proc. 5th Australian Conf. on Hydraulics and Fluid Mechanics, 1974.
- [30] J.L. Robinson. Proc. 5th Int. Con. Of the Center for High energy Rate Forming, University of Denver, Colorado, (1975).
- [31] J.F. Kowalick, R. Hay. Proc. 2nd Int. Con. Of the Center for High Energy Rate Forming, University of Denver, Colorado (1969).
- [32] English Wikipedia <http://en.wikipedia.org/wiki/File:Vortex-street-1.jpg>
- [33] H. K. Wylie, P. E. G. Williams, B. Crossland. Proc. 3rd Int. Conf. of the Center for High Energy Rate Forming, University of Colorado (1971).
- [34] <http://www.pulsar.co.il>
- [35] R. F. Tylecote. The Solid Phase Welding of Metals. St. Martin's Press, New York (1968).

- [36] R. F. Tylecote. Investigations on Pressure Welding. Reports of the British Welding Research Association, March 1954.
- [37] J.P. Schaffer, A. Saxena, S.D. Antolovich, T.H. Sanders, S. B. Warner. The Science and Design of Engineering Materials. Book, McGraw-Hill (1999).
- [38] C. S. Smith. Interphase Interphases. Nature of Imperfections in Nearly Pure Crystals (Eds. W. Shockley et. Al, New York (1950), 377-401.
- [39] F. Erdmann-Jesnitzer, M. May. Z.Met. (1955), **46**(10), 756-764.
- [40] K. J. B. McEwan, D. R. Milner. Br. Weld. J. (1962), **9**, 406-420.
- [41] V. Shribmann, Y. Livshitz, O .Gafri. Magnetic pulse welding & joining: A new tool for the automotive industry. SAE Int and Messe Duesseldorf ATTCE Proc Vol 3: Manufacturing (2001), 131–146.
- [42] <http://materials.iisc.ernet.in/~kamanio/fig/sfig1.jpg>
- [43] H. Okamoto. Al-Ni (Aluminum-Nickel). Journal of Phase Equilibria and Diffusion, Volume 25, Number 4, Oktober 2004, 394.
- [44] <http://www.dana.com/technology/innovative/default.shtm> or
<http://statusreports.atp.nist.gov/reports/95-02-0055PDF.pdf>
- [45] <http://www.dana.com/technology/innovative/default.shtm>
- [46] <http://www.magneform.com/>
- [47] <http://www.pulsar.co.il/news/?nid=17>
- [48] Conference on the Explosion of New Processes; Aug. 14-15, 2007 • San Diego
(<http://www.aws.org/conferences/explosion.pdf>)
- [49] <http://www.ewi.org/capabilities/rssw.asp#magnetic>
- [50] <http://www.iap.com/index.html>
- [51] <http://www.mse.eng.ohio-state.edu/~daehn/>
- [52] <http://www.lstc.com>
- [53] P. L’Eplattenier, G. Cook, C. Ashcraft, M. Burger, A. Shapiro, Introduction of an Electromagnetism Module in LS-DYNA for Coupled Mechanical-Thermal-Electromagnetic Simulations, 9th International LS-DYNA Users Conference
- [54] <http://www.pulsar.co.il/industries/>
- [55] http://www.thefabricator.com/TubePipeFabrication/TubePipeFabrication_Article.cfm?ID=54

[56] Preliminary Investigations of Joining Technologies for Attaching Refractory Metals to Ni-Based Superalloys, Report, October 10, 2005, NASA Glenn Research Center, Edison Welding Institute

[57] <http://www.magneform.com/PulsedMagneticWelding.html>

[58] <http://web.mit.edu/ctpid/www/ford.html>

[59] Plum MM, and Maxwell Laboratories Inc (1996), Electromagnetic Forming, *Metals Handbook 9th Edition*, 14, ASM, Metals Park, Ohio.

[60] S. Golovashchenko, Vladimir V. Dmitriev and Al Krause, Electromagnetic Welding of 6061 Aluminum Alloy, TMS Letters (2005)

[61] Y.B. Park, H.Y. Kim, S.I. Oh, Design of axial/torque joint made by electromagnetic forming, Thin-Walled Structures 43 (2005) 826-844

[62] <http://solidworks.com>

[63] <http://TrueGrid.com/>

2 Electromagnetic Forming

2.1 Introduction

Explosive forming and electro-hydraulic forming are well known high energy rate forming (HERF) processes. An HERF process is characterized by the plastic work being transferred in a very short period of time to the workpiece, usually on a microsecond scale, which makes these processes high velocity forming processes [1, 2].

Electromagnetic forming (EMF) has been studied since the 1920's but the process itself mainly developed during the period 1955-1975. Nowadays, EMF has been studied again due to great interest from the automotive industry [3].

As described in detail in Chapter 1.1.2.1, Electromagnetic Forming (EMF) is the same process as Electromagnetic Welding up to the point of the collision of the workpieces. If at the point of collision the energy which was put into the process is converted into enough kinetic energy of the accelerated workpiece, which then reaches a critical velocity, EMW is observed. So, EMW is the same process as EMF up to the point of the collision with much faster time scales.

2.2 Background

It came to the author's attention that a large amount of money is spent for EMW research on manufacturing the EMW tools (coils), which undergo harsh work load conditions. FORD reported that sometimes the coil would break within a number of dozen trials. A broken EMW coil was sent to the author to study the failure mechanisms and optimize the tool design (this will be discussed in detail in Chapter 3).

Furthermore, the promised EMW experiments were not performed at FORD, in Detroit. In fact, it was not possible at all to find the proper EMW machinery in the first two years of this study. The FORD EMW machinery was tied up in other experiments and the planned EMW experiments could never be performed.

The importance of the fatigue of the coils and non-availability of EMW experiments and specimens were certainly the major reasons why the tool fatigue and EMF with the available MAGNEFORM EMF machinery at MIT (Section 2.3.1) were studied in detail first. Thereby, money could be saved and careful preparations could be made for the possibility of performing the proper EMW experiments at PULSAR, in Israel (see Collaboration with PULSAR, Section 1.3.3, Electromagnetic Welding, Chapter 4).

In fact, the author believes that the similarities between EMF and EMW should be used as an advantage to get a preliminary overview of the process and its limitations by studying and learning from the cheaper and less complicated process of EMF.

2.3 EMF Machinery and Experimental Setup

In EMF, as well as electromagnetic welding (EMW), a repulsive force is generated by opposite magnetic fields in adjacent conductors. There is a primary field, which is developed by the discharge of capacitors through a forming coil that surrounds the workpiece. The opposing field results from eddy currents that are generated (induced) in the workpiece. Figure 1 shows a cross-section of the setup used in the EMF and EMW process depicting the coil and the workpiece, as well as the circuit, the magnetic flux, the direction of the currents and the acting forces:

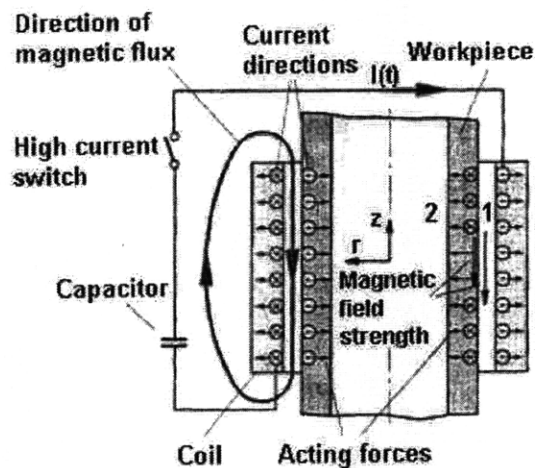


Figure 1: Operating principle of a compression coil [4].

The process begins at the capacitor which gets charged to a certain voltage. Consequently, the capacitor is discharged and a large current runs through the attached coil. The circulating current in the coil creates a magnetic flux, which in turn creates an induced current in the outer workpiece (inner workpiece is not depicted in Figure 1). The two opposing currents lead to a magnetic force which compresses the workpiece inwards.

In EMW the additional necessary process configuration is the compression of a tube collapsing onto an inside co-central mandrel rod, which is stationary. One of the critical parameters is the tube velocity, which needs to exceed a critical level causing the formation of a solid-state weld in the lap joint surfaces [5-8].

The most frequently employed coils in industrial applications are compression coils. They consist of an insulating structure and a metal casing, which provides mechanical support as well as pulse shielding. This pulse shielding reduces the magnetic field surrounding the coil to a very low level, thereby protecting personnel from its harmful consequences [9]. Further shielding suggestions such as a Faraday shield can be found in [10].

2.3.1 EMF MAGNEFORM Machine at MIT

Aspects of modern EMF equipment, equipment design and commercial data can be found in [11], [12] and [13], respectively. Figure 2 shows a schematic of the component locations of the EMF MAGNEFORM machine available in our laboratory [14].

Primarily, there is a so called charging unit, which is used to transform the plant current to a high voltage current and then to rectify it in order to charge the capacitor bank. In the case of the MAGNEFORM machine, available in our laboratory, the operator selects a proper energy level by setting the dial on the front panel. A voltage proportional to that applied to the capacitor bank is continuously compared with the regulated voltage set by the operator and applied across a reference resistor¹ [14]. The capacitor bank consists of smaller capacitors connected in parallel. Usually, the charging unit also includes the control unit of the equipment.

EMF equipment is supplied with short-circuit devices shunting the capacitor bank after the controlling signal appearance. Moreover, doors and panels are electrically interlocked to avoid unauthorized access to the high voltage component. These supplementary circuits constitute the *built-in safety* of the equipment [19, 12].

To close the RLC circuit, fast action switches are used, which are usually ignitrons. Ignitrons are tube like devices, which are filled with mercury. The mercury, when introduced to a small spark, causes ionization of the vapor above the liquid mercury. This breakdown can carry very large currents.

The capacitor bank (consisting of three 60 μF capacitors) is connected to the forming coil by current carrying conductors, which are either flat busbars or coaxial cable bars. Our system consists of flat busbars on the inside of the MAGNEFORM machine as well as coaxial cable bars on the outside [14].

To measure the current that runs through the coaxial cable bars, a PEARSON current monitor can be added to the set-up. A current monitor, consisting of a coil that runs around the coaxial cable bar, is a wide band current transformer that measures AC or pulse currents with an oscilloscope or other voltage-sensing instrument. By passing the current-carrying conductor or charged particle beam through the monitor opening, the monitor will sense the associated magnetic field and accurately measure the current without requiring a direct connection. Current monitors convert the primary current into a proportional voltage signal, which is then displayed on the scope or voltmeter (<http://www.ionphysics.com/monitors.html>).

¹ When the charging voltage exceeds the regulated voltage, relay K-104 is energized which de-energizes the dual-vacuum switch. This switch, in turn, opens the primary of the high-voltage transformer and completes the capacitor power supply return circuit, thus triggering the ignitron and allowing the capacitor bank to discharge through the coil [14].

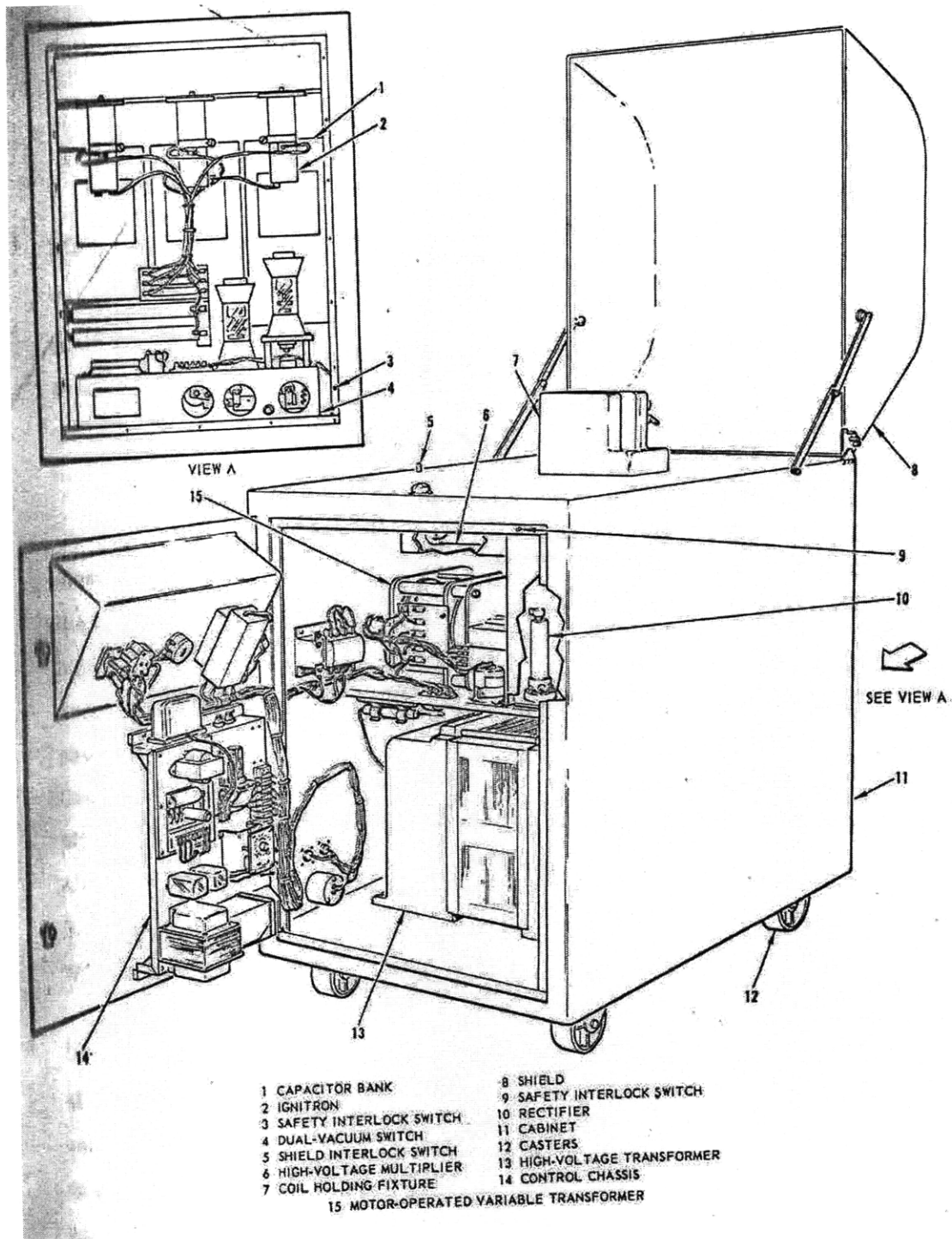


Figure 2: Schematic of the components locations of the MAGNEFORM machine available in our laboratory [14].

Figure 3 shows a construction scheme of a compression coil, which represents exactly the compression coil used in our experiments. It also presents how a fieldshaper could be placed inside the coil.

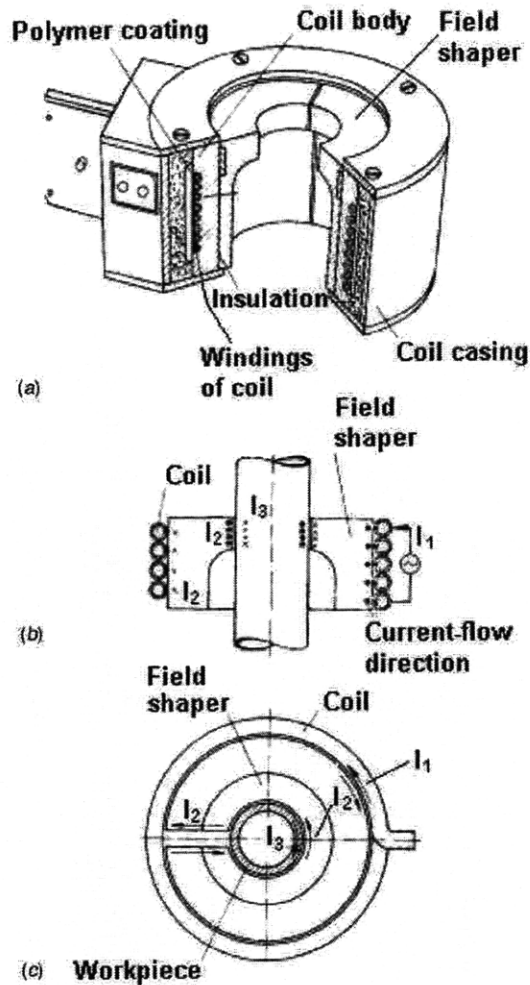


Figure 3: a) Scheme of the compression coil used at MIT.
 b) Cross-section of the coil and fieldshaper with a workpiece inside the fieldshaper. Also the primary current (I_1) in the coil, the secondary current (I_2) in the fieldshaper and the tertiary current (I_3) in the workpiece are displayed.
 c) Top-view of the coil depicted in a) and b) [2].

Figure 3 also shows how the fieldshaper is inserted into the coil and how the induced current (I_2) on the outer side of the fieldshaper is then directed to the inside of the fieldshaper. There, it induces a third current (I_3) in the workpiece. We will present the manufacturing of a fieldshaper for the presented compression coil, as well as experiments in Section 2.6.

Figure 4 shows the EMF setup with the coil and an Aluminum can that was cut to a tube on the inside.

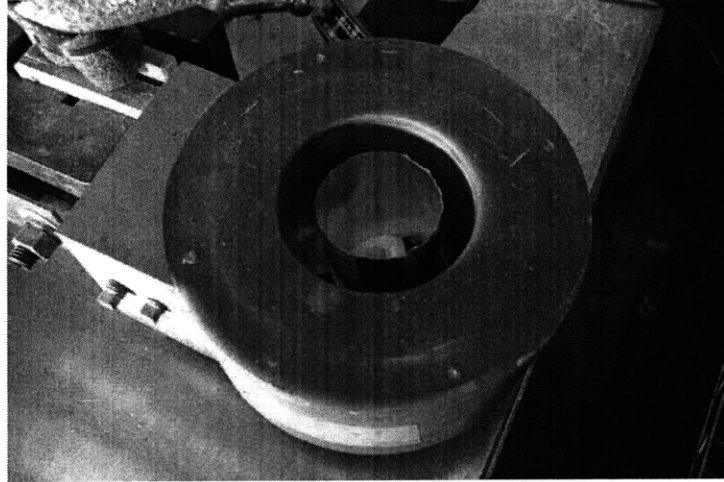


Figure 4: Top-view of the MAGNEFORM coil used at MIT at an early stage (without modifications) and an Aluminum can as the workpiece specimen.

Secondary equipment of EMF can consist of (from literature):

- A die to shape the workpiece [12]
- A vacuum pump and a vacuum chamber to avoid air constraints in high deformation velocities
- A high-speed camera
- An accelerometer

Secondary equipment added by the author:

- Oscilloscope HP Infinium 54810A (from MIT Strobe lab, Edgerton Center)
- Pearson Current Monitor
- High Voltage Probe
- High-Speed Camera Equipment
 - High-Speed Camera: Vision Research PHANTOM v7.1
 - Lowel DP 1000W Halogen Lamp
 - Camera: Nikon D70 (sn: 3057815)
 - Lenses:
 - Nikon 50mm lens (sn: 274653)
 - Nikon 18-70mm zoom lens (sn: US2118600)
- Transparent hood
- A workpiece “stopper”
- A workpiece “stage” (holder)
- A fieldshaper

Figure 3 shows the experimental installation that was available in our laboratory prior to all modifications made to the setup. For this MAGNEFORM machine, a Variac was connected to the machine to provide the necessary 230 V of operation (current of 9A).

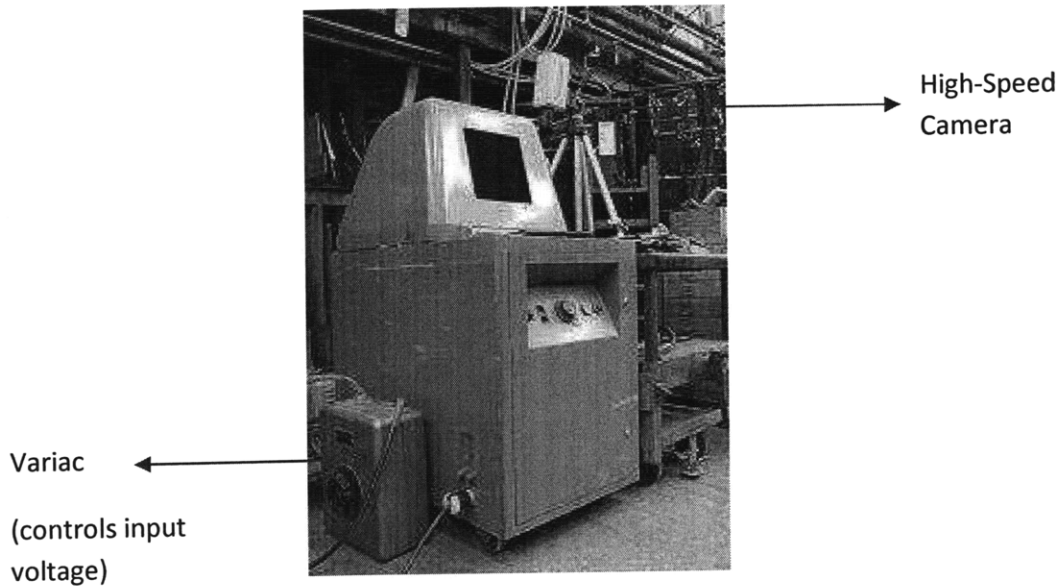


Figure 3: Experimental installation of the MAGNEFORMER machine available in our laboratory. The photograph shows the Variac on the left, as well as a High-Speed camera on the right.

Figure 4 shows the experimental installation that is available in our laboratory, after all modifications have been made:

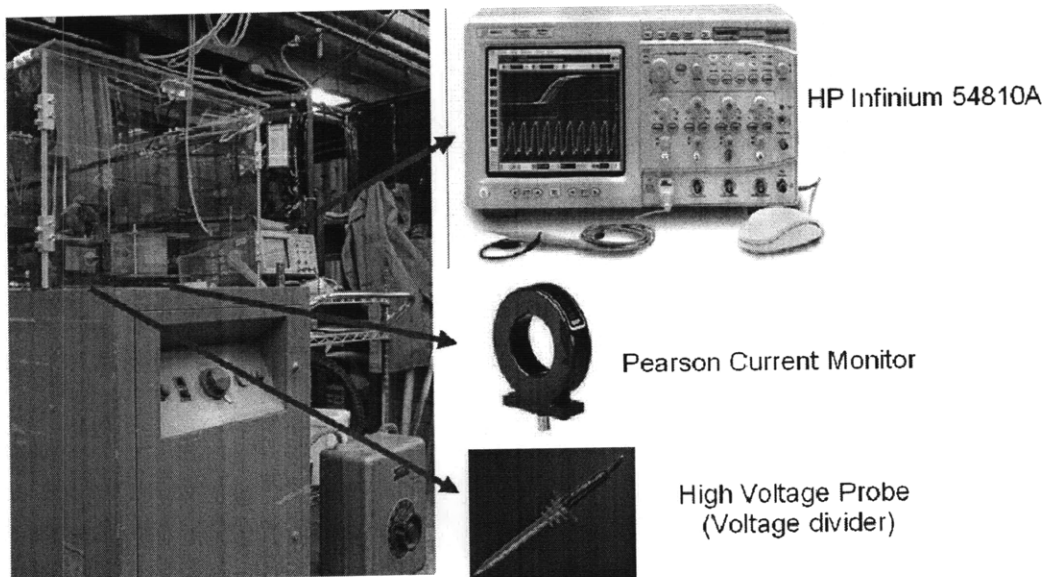


Figure 4: Experimental installation of the MAGNEFORM machine available in our laboratory. The photograph shows the Variac on the bottom right corner, as well as an oscilloscope, which was used to measure current (measured by the Pearson Current Monitor) and voltage (measured by the High Voltage Probe) that go through the coil.

Table 1 shows a summary of the characteristic parameters for EMF machinery in the literature and the MAGNEFORM EMF machine at MIT, in comparison with an EMW machine (EMW machine at FORD, in Detroit).

	EMF Literature	MAGNEFORMER at MIT	EMW machine in Detroit
Electric energy storage bank			
Energy per discharge E_c [KJ]	6-20	up to 6	100
Voltage V_o [kV]	2-20	up to 10	25
Capacity C [microF]	10-5000	220 (measured)	320
System Characteristics			
Electric pulse frequency f [KHz]	10-75	5-10	5-50
Maximum Coil Current I_1 [kA]	10-200	up to 40	1600
Forming Parameters			
Maximum Magnetic Pressure p_m [MPa] for Compression (outer) coils	up to 340	up to 350	depends upon the design
Duration of the first period of magnetic pressure pulse T_1 [microsecond]	10-100	10-20	25-100
Workpiece temperature increment ΔT [C]	30-150	up to 100	have not measured

Table 1: Summary of the characteristic parameters of the EMF process (from the literature), the MAGNEFORMER machine at MIT and the EMW machine in Detroit [4, 5, 9, 12, 13, 15-17].

By comparing the data given in Table 1, one can see that an EMW machine can be about five times more powerful than an EMF machine. In the following section and Section 2.4 we will go into more detail of the electrical parameters and why these parameters ultimately determine the difference between the EMF and the EMW process.

2.3.2 A Priori Calculations

A simplified circuit is shown in Fig. 2 [18]. When the switch S is closed, the capacitor is suddenly discharged through the coil of resistance R_c and inductance L_c . The internal resistance R_i and internal inductance L_i of the unit are shown separately. The workpiece is represented by a closed circuit of resistance R_w and inductance L_w . The equivalent circuit which includes the total lumped resistance and inductance is shown in Fig. 2b. Figure 5 shows a schematic of the RLC circuit:

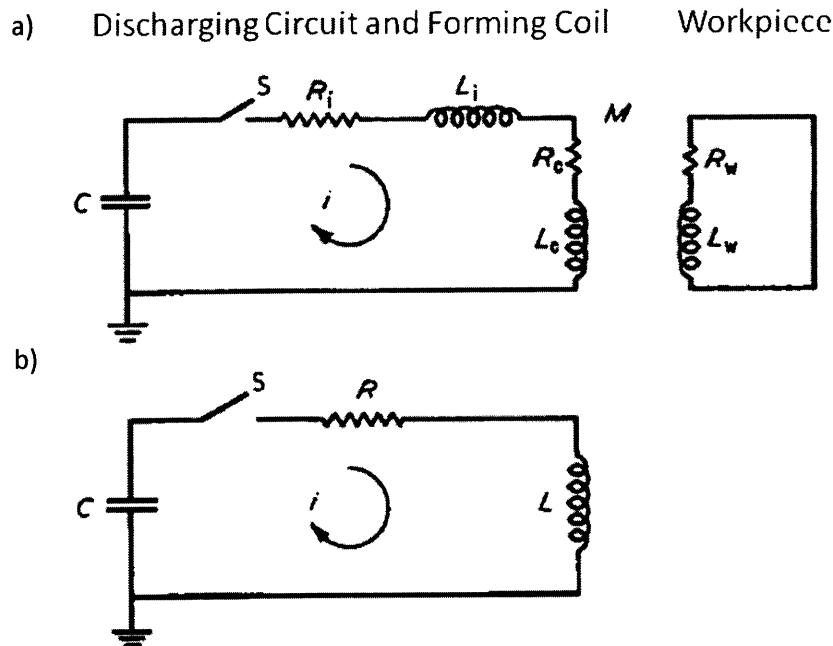


Figure 5: Simplified schematic of the RLC circuit.

a) Shows the tube as a secondary circuit, coupled with the primary through a mutual inductance M .

b) Shows an equivalent circuit with lumped parameters [18].

When the capacitor is discharged it leads to an induced current ("secondary current") in the workpiece, thereby creating a force which compresses the workpiece inside the coil. However, at the same time the induced current in the workpiece also creates a magnetic field itself, which in turn induces a current in the coil in the opposite direction to the primary current, thereby recharging the capacitor. The capacitor discharges again and induces an opposite secondary current in the workpiece and so forth. The resulting and so called discharge current can be calculated by the following formula:

$$i(t) = \frac{U}{\omega L} e^{-\beta t} \sin(\omega t), \quad 2.1$$

where U is the charge voltage at the capacitor, ω is the frequency and

$$\beta = \frac{R}{2L}, \quad 2.2$$

which is called the damping coefficient. $\omega = 10\text{-}100$ kHz for typical EMW operations [19]. Therefore, an increase in resistance creates more damping in the system and an increase in Inductance will reduce damping, but also reduce the current and the initial current, which is the first term in Equ. 2.1:

$$I_o = \frac{U}{\omega L}. \quad 2.3$$

The frequency ω can be calculated with

$$\omega = \sqrt{\frac{1}{LC} - \beta^2}. \quad 2.4$$

Looking at Equ. 2.1 for the current we can see that it consist of 2 parts, a sinusoidal term and an exponentially decaying term. The exponentially decaying term is due to the resistance of the circuit, i.e. the resistance of the coil. If there was no resistance present in the circuit, the circuit would reduce to an LC circuit and setting $R=0$ in Equ. 5 we get

$$\omega = \sqrt{\frac{1}{LC}}, \quad 2.5$$

which is just the frequency for an LC circuit.

Figure 6 shows schematic graph of the sinusoidal primary current wave as described with Equ. 2.1. The induced current (or secondary current) in the workpiece is also shown.

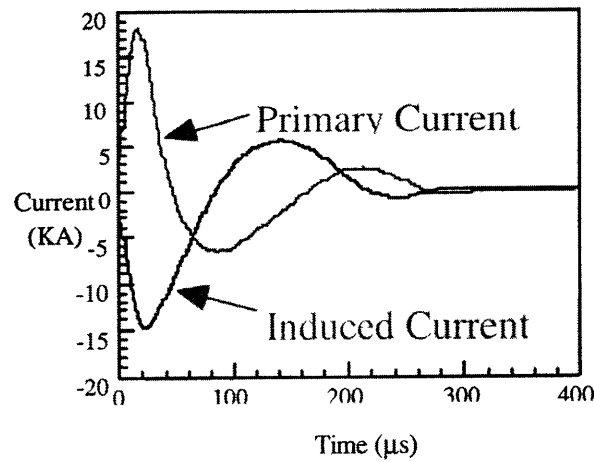


Figure 6: Graph of the primary current (I_1) in the coil and the induced current (I_2) in the workpiece [20].

In the EMF or EMW process, one pulse with a high amplitude and a short or optimum pulse time is favorable. During this first pulse the whole deformation of the workpiece takes place, whereas with more than one pulse, energy that is dissipated during later pulses is not sufficient in amplitude and can be regarded as loss. This leads us to the following theorem.

Theorem

In EMF, and even more critically in EMW, a short optimally timed pulse with large amplitude is desired. This behavior can, in electrical engineering terms, be described as *critically damped*. Figure 7 shows a graph for a critically damped current waveform.

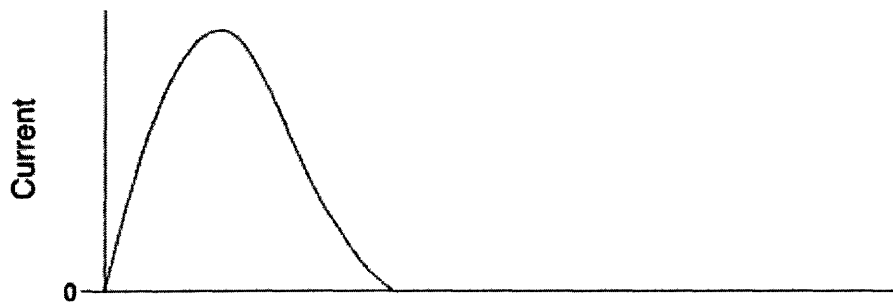


Figure 7: Current waveform for the critically damped case. There are no current reversals. The current rises with reasonably short rise time to its peak value and then falls over a somewhat longer period to zero and ceases [19].

There are two ways of achieving this behavior:

The first one is called “equality of plane LC circuit case with plane exponential decay case”.

The time for one pulse in the LC circuit is given by one half the inverse of ω , so

2.7

$$t = \frac{\frac{1}{2}}{\sqrt{\frac{1}{LC}}} \text{ or } t = \frac{\sqrt{LC}}{2} \tag{2.6}$$

Furthermore, the decay time for the exponential decay is given by the inverse of δ , see Equ.

2.2. When setting this time equal with the time given in Equ. 2.6 one gets

$$\frac{\sqrt{LC}}{2} = \frac{L}{R} \tag{2.7}$$

With the second approach one arrives at a simpler solution by just setting the frequency ω to zero. By setting $\omega=0$ in Equ. 2.4, one achieves the same result as shown in Equ. 2.9, which is usually shown as

$$R^2 = \frac{4L}{C}. \quad 2.8$$

This is the criterion for a critically damped circuit. Two other cases which will not be mentioned in further detail are the *overdamped* and *underdamped* waveform behavior for which

$$R^2 > \frac{4L}{C} \text{ and } R^2 < \frac{4L}{C}, \quad 2.9$$

hold, respectively. From the literature, we find that the pulse time can be calculated by

$$t_p = 3\sqrt{LC}. \quad 2.10$$

This pulse duration t_p is usually specified as the time between the points on the leading and trailing edges of the pulse at 10% of the peak amplitude [19].

Due to the fact that the capacitance needs to be as high as possible to give a large current amplitude, we need to decrease the value of the inductance to achieve a short pulse with a high current peak at the beginning of the process. The inductance of a coil is given by

$$L = \frac{k\mu(\pi r^2)N^2}{l}, \quad 2.11$$

where k is the Nagaoka constant equal to 0.77, r is the radius of the coil, l is the length of the coil and $\mu = \mu_0 \times \mu_r$, where μ_0 is $4\pi \times 10^{-7}$ H/m and μ_r is the magnetic permeability of the material [21]. The permeability is usually taken to be the permeability of the core, which in our case is air and therefore is just 1. Therefore, if one wants to reduce the inductance of the coil to reduce the pulse duration time, the number of turns N and the radius r need to be decreased and the length l can be increased, if possible. These necessities can be achieved by an introduction of a fieldshaper to the system (see Section 2.6).

Finally, it is most important to mention that in the case of the critically damped circuit a different formula for the discharge current needs to be used, as otherwise the current would just be zero ($\omega = 0$ and $\sin \omega = 0$):

$$I = \frac{U}{L} \cdot t \cdot \exp\left(\frac{-R \cdot t}{2L}\right). \quad 2.12$$

With the formula presented in Equ. 2.12 als a new magnetic pressure formula can be calculated for the case of a critically damped circuit, instead of the formula given in Equ. 1.19 in Chapter 1. The formula for the magnetic pressure is

$$P = \frac{1}{2} \cdot \mu_0 \cdot I^2 \cdot N^2, \quad 2.13$$

where μ_0 is $4\pi \times 10^{-7}$ H/m (magnetic permeability of vacuum), I is the current and N is the number of turns of the coil [18]. Equ. 2.13 combined with the new current formula given in Equ. 2.12 gives

$$P = \frac{1}{2} \cdot \mu_0 \cdot \left(\frac{U}{L} \cdot t \cdot \exp\left(\frac{-R \cdot t}{2L}\right) \right)^2 \cdot N^2 \quad 2.14$$

2.4 EMF Simulation Effort

With the presented setup in Section 2.3.1 and the A Priori calculations made in Section 2.3.2, it was clear that we had to understand and know all parameters given. For this matter the electrical circuit simulation software MultiSIM [22] was used to not only compare the measured results of the important process parameters to the calculated (MATLAB [23]) and simulated results, but even to find a view missing variables that were still unknown for the MAGNEFORM machine at MIT. These values were for example, the internal inductance and resistance of the machine.

2.4.1 Electrical Circuit Approximations

The following electrical circuit simulation shows how to approximate the RLC circuit by a model and by comparing the measured waveforms of current and voltage, one can estimate the values for R , L and C of the available EMF/EMW machinery.

Experiment and Simulation

Figure 8 shows the discharge current and the voltage that was measured at the experimental setup at MIT:

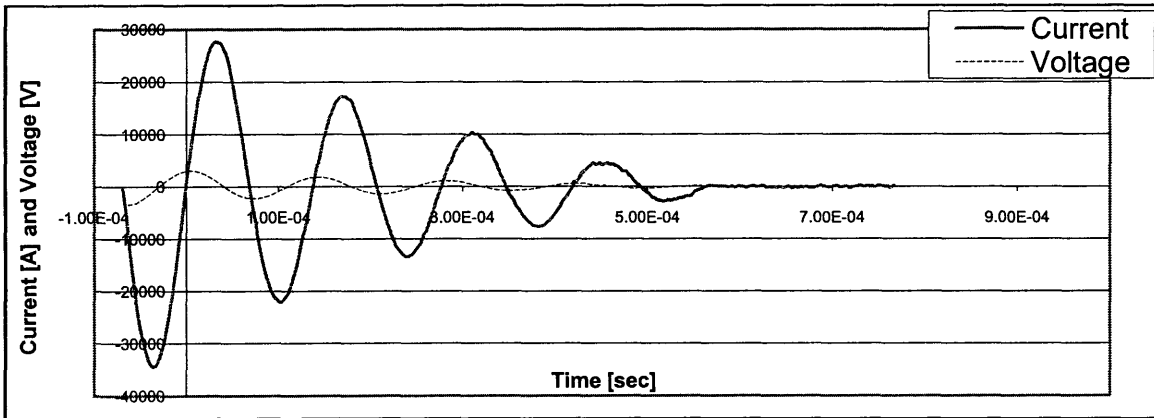


Figure 8: Measured discharge current and capacitor voltage at the EMF setup at MIT (MAGNEFORM power-setting of 50, input voltage = 4.44kV).

In Figure 8, voltage and current are depicted in a graph, which were measured by the voltage divider and the PEARSON current monitor, respectively. The peak values for voltage and current are -3.4 kV and -34.5 kA, respectively.

To be able to calculate the parameters presented in Section 2.3.1, more values than just the current waveform and the voltage waveform needed to be known. From the machine manual, the capacitance of the capacitor was given, which was three times 60 μF . The actual capacitance of the machine which we measured was 220 μF . However, the inductance and the resistance of either the coil or the machine were not known.

We were able to measure the inductance (L_c) and the resistance (R_c) of the coil at their operating frequency of 7KHz, giving us exact values of $2.5 \mu\text{H}$ and 0.017Ω , respectively.

Next, we created a MultiSIM simulation model which would identify the missing values by comparing the waveforms observed in the experiment with the waveforms from the simulation. Then, through proper tweaking of the system parameters and therefore, approximating the simulation to the measurement the machine values could be found. Figure 9 shows a MultiSIM simulation of the RLC circuit and the production of the sinusoidal damped current:

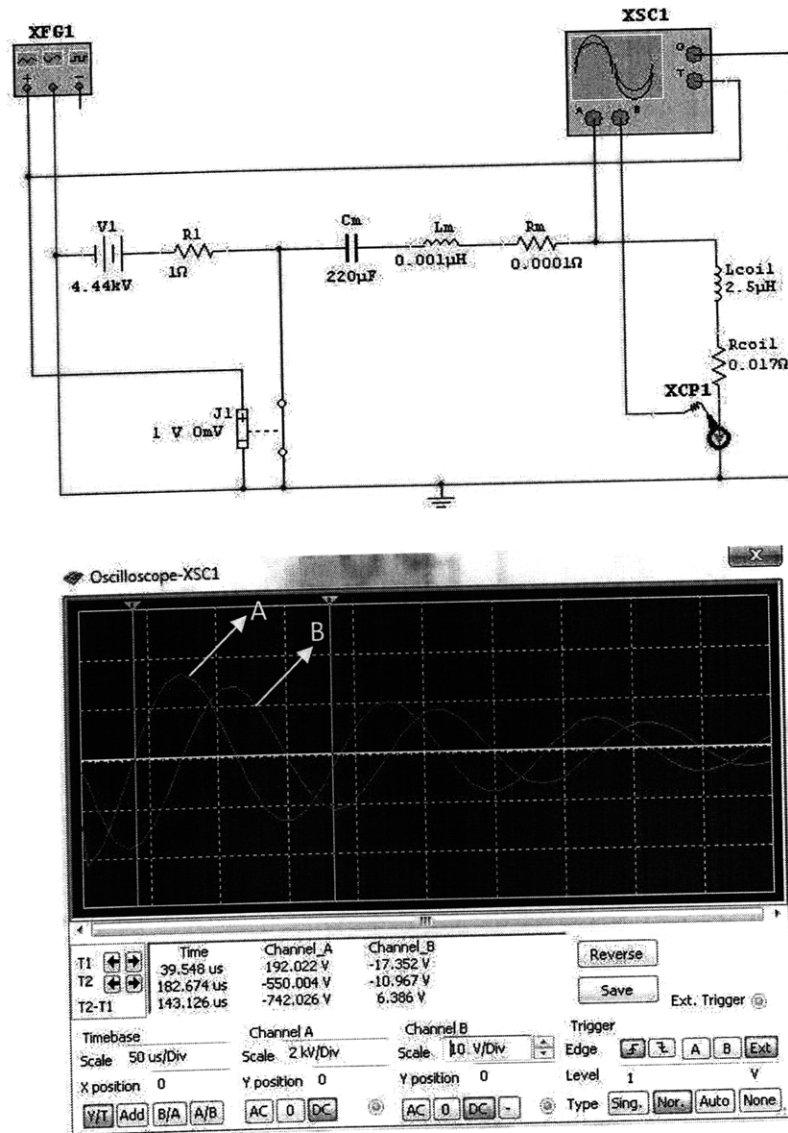


Figure 9: RLC circuit simulation obtained from the software MultiSIM. The Voltage is displayed by Channel A, whereas the current is displayed by Channel B (in V/div; can be converted to A by a multiplication of 2000A/V). R_{coil} and L_{coil} represent the resistance and inductance of the coil and R_m and L_m represent the resistance and inductance of the machine, respectively.

In the presented MultiSIM simulation the frequency generator XFG1 created a step function (Function Generator, see Figure 9), which would set off the modeled ignitron switch at a small voltage of 1V. Closing the switch would then discharge the charged capacitor into the machine and coil circuit. The capacitor was charged to a value of 4.44 kV (input voltage measured for a power setting of 50 on the MAGNEFORM machine) by the VARIAC, which is modeled by a battery (V_1 , R_1) in our simulation. Then the oscilloscope XSC1(Figure 9b) measures the sinusoidal damped current and the voltage of the coil. The current measurement is modeled by a current monitor just like we are using it in our lab. When the current monitor measures a voltage it is multiplied by a ratio of 2000A/1V to give the appropriate current.

The two cursors are then used to measure the time between the voltage and current peaks, as well as their amplitudes. Depicted for the measurement of the current in Figure 9b, we obtain values of -34700A and -22000A at the first current peak and the second current peak, respectively. The times between the peaks is measured to be 143 μ s. The measured values match exactly what we observed in our experimental observations (Figure 8). Additionally, see Table 2 for a summary for the comparison of the data and the simulation.

Figure 9 shows the simulation at one point, however to find the missing parameters the parameters of the circuit had to be adjusted until the same waveforms for voltage and current were observed, as seen on the oscilloscope in the experiment (see Figure 8). The presented model could be obtained by fine-tuning the machine resistance and inductance to the values of 0.001 μ H and 0.001 Ω , respectively, basically rendering them to zero.

Results

With the presented simulation we were able to find the internal inductance (L_i) and resistance (R_i) of the machine, which were 1 nH and 0.001 Ω , respectively. To summarize, the following holds true for the MAGNEFORM EMF machine circuit, at MIT:

- Equivalent resistance (resistance of the coil + resistance of the machine): $R_c + R_i = 0.018 \Omega$
- Equivalent inductance (inductance of the coil + inductance of the machine): $L_c + L_i = 2.501 \mu\text{H}$

Now, we can calculate the theoretical discharge current. Figure 9 shows the discharge current waveform, calculated in MATLAB, with a coil inductance L_c of 2.5 μ H and a coil resistance R_c of 0.018 Ω .

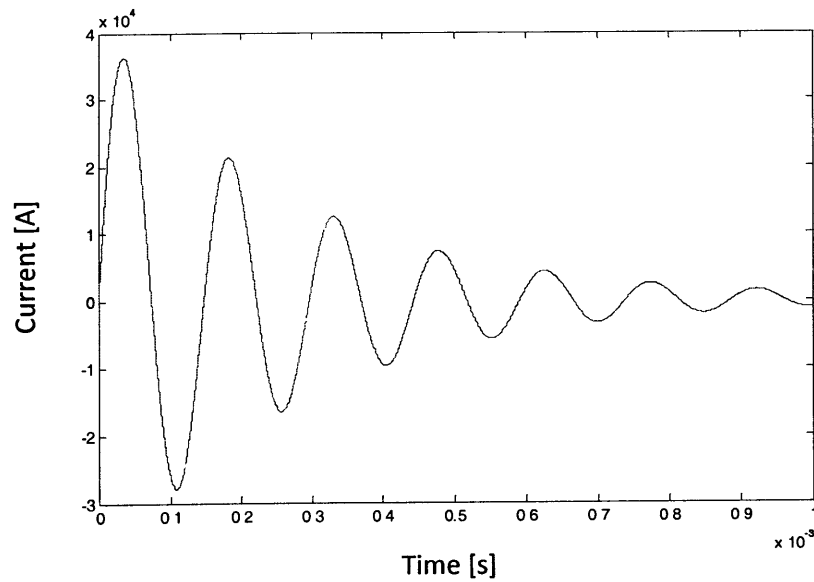


Figure 10: Calculated discharge current (MATLAB). $V = 4.4$ kV (measured input voltage at a power-setting of 50), $C = 220$ μ F (measured), $R = 0.018$ Ω , $L = 2.501$ μ H.

The respective MATLAB code for Figure 10 can be found in the Appendix B. Comparing Figure 9 and 10 with the experimental data (see Figure 8, for example), we can exact modeling and calculation of the measured data. All results are summarized in Table 2:

	Theory (MATLAB)	Experiment (EMF Setup)	Simulation (MultiSIM)
$1/\beta$ [sec]	2.77E-04	2.00E-04	2.00E-04
$f = \omega/2\pi$ [Hz]	6760	7407	6993
V_{peak} [V]	-	3.47E+03	3.7E+03
I_{peak} [A]	3.60E+04	3.45E+04	3.47E+04

Table 2: Summary of the results obtained through the presented theory, experimental data and simulation using $V = 4.4$ kV (measured input voltage at a power-setting of 50), $C = 220$ μ F (measured), $R = 0.018$ Ω and $L = 2.501$ μ H.

Looking at Table 2, the inverse of β is just the time it takes the current to drop from its peak value to a value of 69% (see Equ. 2.1). This was also measured in the calculated and simulated current wave forms. ω divided by 2π gives the frequency. This was measured from the simulated graphs as well as calculated from Equ. 2.4. V_{peak} and I_{peak} are the peak-voltage and -current, respectively.

From the comparison of theory, experiment and simulation, we can see that the experiment goes quite well with the trend of the theory. As far as the simulation is concerned, good agreement with the theory can be achieved for $1/\delta$, as well as $1/f$. The voltage values, however, seem to be a little bit off. Further tweaking of the circuit-model could result in closer agreement with the theory.

Based on the theory presented in our A Priori calculations in Section 2.3.2 we were able to calculate and compare the theoretical values (calculated with MATLAB) with the measured data from the experiment and the presented MultiSIM simulation. This is an important step, because parameters like the machine inductance and resistance are very important parameters in the RLC circuit and for the process. This becomes inherently clear when trying to optimize the RLC circuit to achieve higher discharge currents over shorter times, which would be an optimum outcome for the EMW process. The inductance of the circuit plays a large role and we will go into detail of this matter in the next section.

Furthermore, with the given MultiSIM model it is now possible to calculate any current or voltage in the EMF coil at MIT, for several values such as different coil inductance and resistance or different input voltages.

Now we are presenting the prove of the theorem stated in Section 2.3.2 that by using the theory of a critically damped RLC circuit optimum values can be calculated to achieve an optimum pulse profile of the EMW process.

2.4.2 Optimization of the EMW Process through the Process Parameters

In section 2.3.2 we stated that an optimal waveform of the discharge current would be the current behavior that is observed for a critically damped RLC circuit. In this section we present MATLAB calculations proving this theorem.

In the case of a critically damped circuit, Equ. 2.10 must hold. Knowing the capacitance and the resistance of the MAGNEFORM EMF setup at MIT and the EMW machine at FORD, in Detroit, we calculated the necessary inductance to fulfill the requirement given in Equ. 2.10. Table 3 shows the results of these calculations.

The resistances are 0.018 Ω and 0.01 Ω of the circuit at MIT and the circuit at FORD, respectively. The capacitances are 220 μF and 320 μF of the circuit at MIT and the circuit at FORD, respectively.

<i>R</i>	<i>L</i>	<i>C</i>
[Ohms]	[μHenry]	[μFarrad]
<i>MIT</i>		
0.21320072	2.5	220
0.06741999	0.25	220
0.02132007	0.025	220
0.006742	0.0025	220
<i>DETROIT</i>		
0.21794495	3.8	320
0.06892024	0.38	320
0.02179449	0.038	320
0.00689202	0.0038	320

Table 3: Examples of inductance calculations to fulfill the requirement of a critically damped RLC circuit, for the EMF setup at MIT and the EMW machine at FORD, in Detroit.

From Table 3 one can see that we calculated several values of R , while changing the inductance L by an order of magnitude, to finally get a resistance approximately on the order of the actual resistance in the circuit, while fulfilling the requirement for the critically damped circuit (Equ. 2.10).

Fortunately, for the FORD EMW machine setup the reported inductance is 38nH, which is on the right order to get close to a critically damped RLC circuit ($R = 0.02 \Omega$ and $C = 320 \mu\text{F}$). This could be achieved, for example, by a one-turn coil in the circuit made from Aluminum Bronze with 50 mm in length and a radius of 30 mm. Thereby, it is possible to achieve short enough current pulses with the right magnitude to achieve EMW.

Unfortunately, the MIT EMF coil inductance is 2.5 μH , which is 2 orders of magnitude too large to get in the range of the appropriate inductance (25nH) of a critically damped circuit, which only makes it possible to perform EMF operations using the MAGNEFORM machine at MIT.

We now show a couple of calculations of the respective current and magnetic pressure curves for the EMF circuit case, as well as the critically damped circuit case, which makes EMW possible. Figure 11 shows the critical damped circuit discharge current for the case of an inductance of $L=38\text{nH}$ (observed at the EMW machine at FORD, with a one-turn coil, such as described above), using Equ. 2.14:

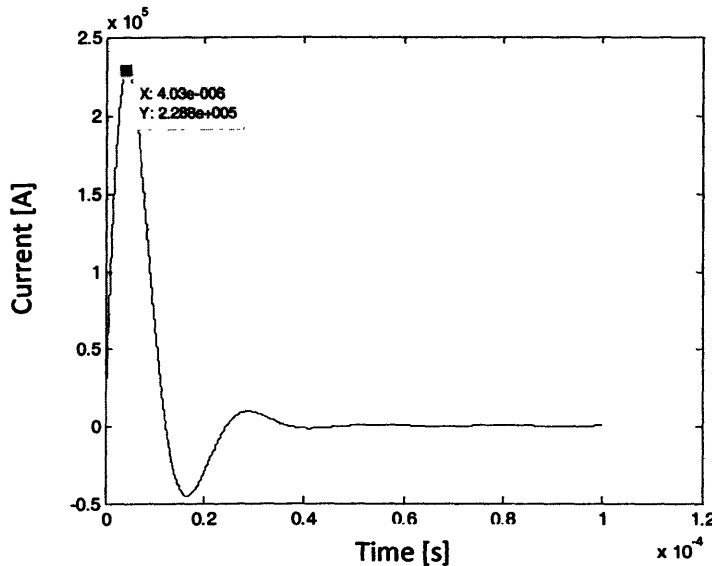


Figure 11: Calculated discharge current (MATLAB) for $V = 4.4 \text{ kV}$, $C = 320 \mu\text{F}$, $R = 0.01 \Omega$, $L = 38 \text{ nH}$.

In comparison to Figure 10 the peak current, for the settings observed for the $L = 38 \text{ nH}$ circuit, is 6 times larger. Furthermore, the peak current is already reached at a time of approximately 4 μs . The length of the pulse is approximately 40 μs . In this case the voltage was

taken to be 4.4 kV to compare the resulting current, while changing the inductance and the capacitance to the values observed at the EMW machine at FORD, in Detroit.

If now also the voltage is ramped up to 15 kV (as reported by FORD) we get a peak current of 800 kA, which is exactly the reported value by FORD. Also, the time length of the pulse duration is the same as the reported value of 40 μ s from FORD (see Chapter 3 for an example of a coil that was used at the EMW setup at FORD, with the mentioned parameters).

Calculating, the predicted optimum value for the resistance, from the critical damped circuit model, of 0.026 Ω for the resistance would lower the peak current to a value of 150 kA (using 4.4kV as an input voltage). Therefore, the chosen resistance of 0.01 Ω is an even better choice than predicted by the model. However, the critically damped circuit model can predict the order of magnitude for the necessary circuit parameters, such as the inductance (see before). Furthermore, as observed in Figure 11, the EMW machine at FORD, in Detroit almost behaves like a critically damped circuit.

Figure 12 shows the calculated magnetic pressure curve for the EMF setup at MIT using the formula for the magnetic pressure in Equ. 1.9, given in Chapter 1. Figure 13 shows the calculated magnetic pressure curve for the critically damped circuit case (Equ. 2.16), with $L = 38$ nH.

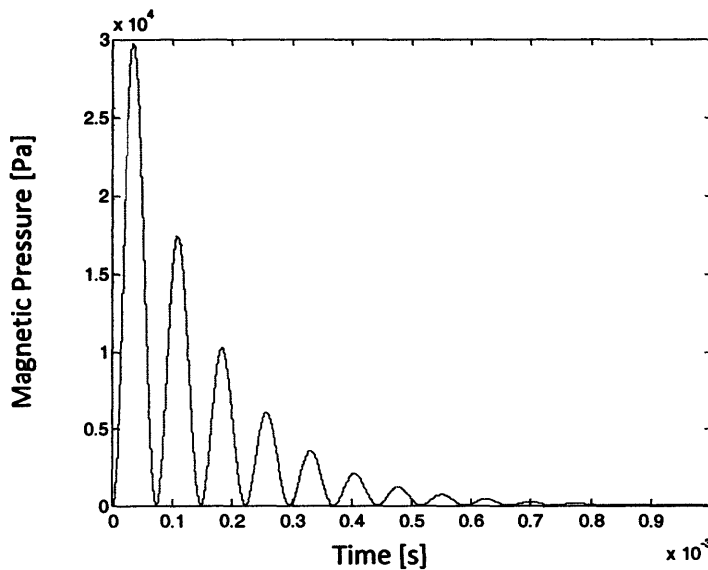


Figure 12: Calculated magnetic pressure curve for the EMF setup at MIT using $V = 4.4$ kV (measured), $C = 220$ μ F (from machine manual), $R = 0.018$ Ω , $N = 6$ Turns and $L = 2.501$ μ H.

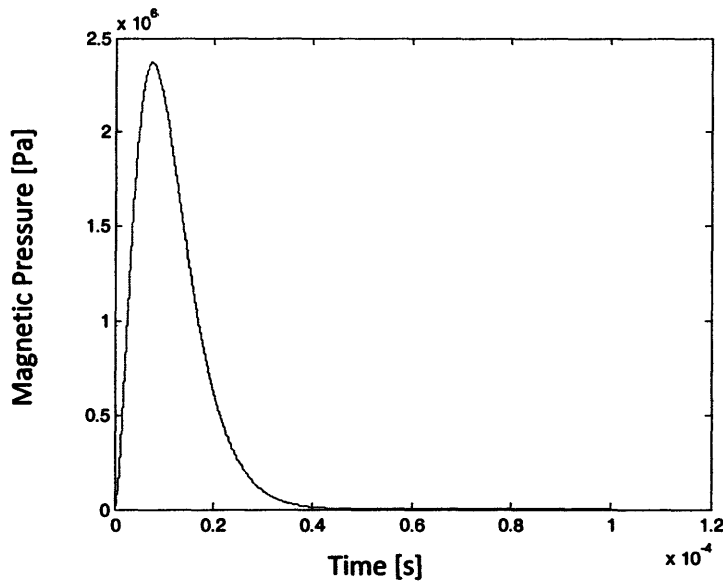


Figure 13: Calculated magnetic pressure curve for the EMW setup at FORD, in Detroit using $V = 4.4 \text{ kV}$, $C = 320 \text{ } \mu\text{F}$, $R = 0.01 \text{ } \Omega$, $N = 6 \text{ Turns}$ and $L = 38 \text{ nH}$.

In the critically damped circuit case (the EMW setup is almost a critical damped circuit, $L = 38 \text{ nH}$) the peak magnetic pressure is 2 orders of magnitude larger compared to the EMF machine case. Ramping up the voltage to 15 kV one gets 27 MPa of pressure at the magnetic pressure peak, after $7.8 \text{ } \mu\text{s}$.

Discussion

From the results presented above, one can see that it is absolutely necessary to have a low inductance in the RLC circuit to observe the optimal behavior needed for an EMW process.

When looking at the machine at FORD, we calculated that the necessary inductance would have to be on the order of 10^{-8} H and the inductance is 38 nH for the EMW machine at FORD, in Detroit. Thereby, from our calculations, the EMW machine at FORD represents an RLC circuit that is optimized to achieve a discharge current that is approximately critically damped and therefore the necessary magnetic pressure can be created to observe EMW.

Furthermore, we observed that although the circuit of the EMW machine in Detroit is not perfectly critically damped, it actually has a higher peak current at the first current peak. The current is not perfectly critically damped, i.e. shows another negative current peak, but having a higher peak current for the first current peak is more advantageous.

Finally, it is important to mention that the efficiency of the setup is dependent on the machine inductance. One can also calculate the efficiency of the machine, which is just given by

$$\eta = \frac{L_{Coil}}{L_{Coil} + L_{Machine}}, \quad 2.15$$

which has been reported to be larger than 0.9 for the EMW machine at FORD. A value close to $\eta = 1$ is optimal, which is the case for the EMF machine at MIT.

So, to conclude, if one would like optimize the circuit parameters for an EMF or EMW process, the process is as follows. Primarily, one should try to be close to the parameters that follow the presented theorem of a critically damped circuit. After having found these values one can always still optimize the circuit and maximize the discharge, by lowering the Resistance or the inductance (or increasing the capacitance).

2.4.3 Workpiece Acceleration and Velocity Calculations

This section presents further steps (other than the circuit parameters presented in the previous section) towards optimizing the EMF or later EMW setup. Here we present measures to optimize the setup of the workpieces inside the coil, by trying to optimize the gap between the two workpieces. We use the basic equations presented in Chapter 1 for the deformation of the workpiece.

Figure 12, in Section 2.4.2, showed the calculated magnetic pressure for the case of the EMF MAGNEFORM machine at MIT. In Chapter 1 we showed that the magnetic pressure (Equ. 1.9) needs to surpass a so called yield pressure P_y for deformation of the workpiece to occur (Equ. 1.12).

Figure 14 shows the magnetic pressure calculated for the MIT EMF machine case with the corresponding acceleration, velocity and position of the tube. Only during the time where the magnetic pressure is larger than P_y the workpiece accelerates to a certain velocity.

After the calculated magnetic pressure was multiplied by a factor of 10, the peak velocity observed in our calculations for the EMF machine case, at MIT, was on the order 50 m/s, which is close to what we observed in the High-Speed Videography study, presented in the next Section (2.5).

First, the factor of 10 accounts for the fact that there is a fieldshaper built into the EMF coil currently present at the EMF MAGNEFORM machine setup at MIT. An X-ray study was performed to show the inner structure of the EMF coil to make future simulation more accurate and is presented in the next section (2.4.4 LS-DYNA Simulation Effort).

Second, in Chapter 3 we will show that a non-perfect shape of the workpiece reduces its collapse pressure P_y , significantly. Small wrinkles introduced to the Aluminum tubing during

cutting would decrease P_y . This is accounted for in the factor of 10 increase in magnetic pressure (see also MATLAB code in Appendix B).

Using the calculations presented in Figure 13, we can calculate the optimum distance between the two workpieces, for the case of the EMF MAGNEFORM machine. When the acceleration becomes zero again, the workpiece has reached its maximum velocity, which is at a time of 56 μs , which corresponds to an outer workpiece position of 1 mm. At this distance the workpiece has achieved a velocity of approximately 50 m/s (maximum velocity). Therefore, to optimize the EMF workpiece setup, at MIT, the inner workpiece would have to have an outer diameter that is 2 mm smaller than the inner diameter of the outer workpiece.

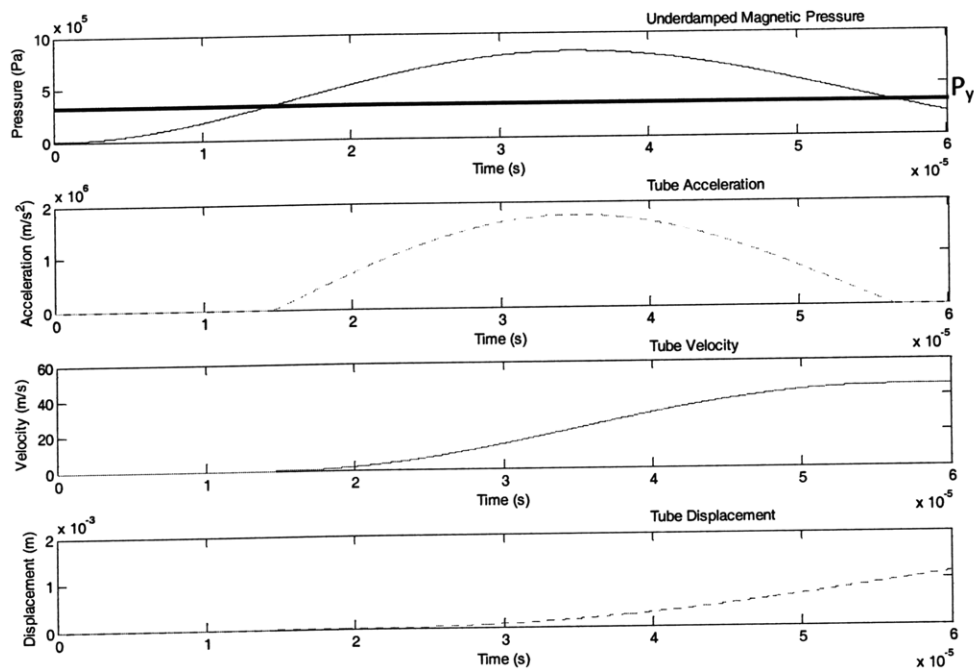


Figure 13: Calculation of the magnetic pressure, the tube acceleration and the resulting tube velocity (from top to bottom). The bold line in the first graph represents the value of the collapse pressure P_y . The values used were $V = 7.3$ kV (measured), $C = 220$ μF (measured), $R = 0.018$ Ω and $L = 2.501$ μH (further values can be found in the Appendix B). The workpiece was the Aluminium can body material (see Appendix B for dimensions and material properties).

The velocity can also be calculated using the impulse, which is calculated by integrating the pressure over time. Again, the factor of 10 in increasing the pressure had to be used to obtain the right values. The results for calculating the velocity using the impulse, as well as all MATLAB code can be found in Appendix B.

Now, we will present our efforts to simulate the process using LS-DYNA, as well as the X-ray study of the EMF coil of the MAGNEFORM machine, at MIT.

2.4.4 LS-DYNA Simulation Effort

FORD seeks a model that could connect the EMW machine parameters, coil parameters, field intensifier parameters (if applicable) and welded part initial geometry with the parameters of the weld. This will involve connection of the electromagnetic model, the deformation of the blank model and the weld generation model. LS-DYNA has proven to be a reliable software for the simulation of Electromagnetic Forming [24, 25]. Over the course of this thesis, I have been working closely with the software developers of LS-DYNA from LSTC, Livermore, CA.

Figure 14 shows the first approximate Solidworks Drawing with a TrueGrid mesh of the coil with a fieldshaper, an outer workpiece and an inner workpiece on the inside [26,27]. However, this was only an approximation and at this stage of our simulation efforts and LS-DYNA was not sophisticated enough yet, to actually provide a fine enough mesh.

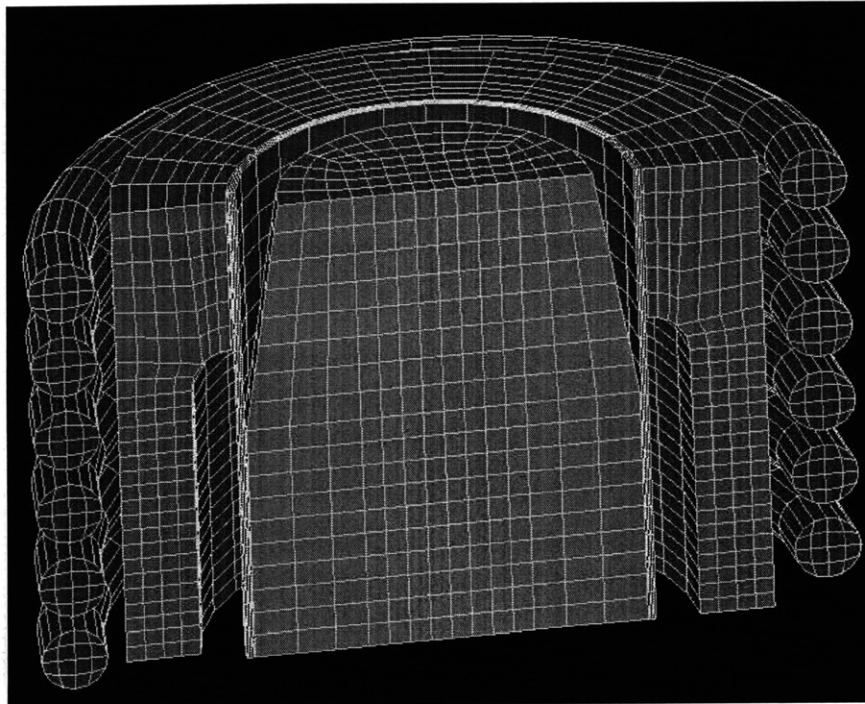


Figure 14: Preliminary mesh design (TrueGrid) representing the experimental setup at the MIT Welding and Joining Laboratory. On the outside is the coil with 6 turns, surrounding the field intensifier, which surrounds the outer and inner workpiece.

It was important to know the actual inner structure of the coil to be able to simulate the process with LS-DYNA. Therefore, X-rays need to be taken of the coil. Figure 15 and Figure 16 show a top-view and a front-view X-ray, respectively, of the compression coil used in all EMF experiments.

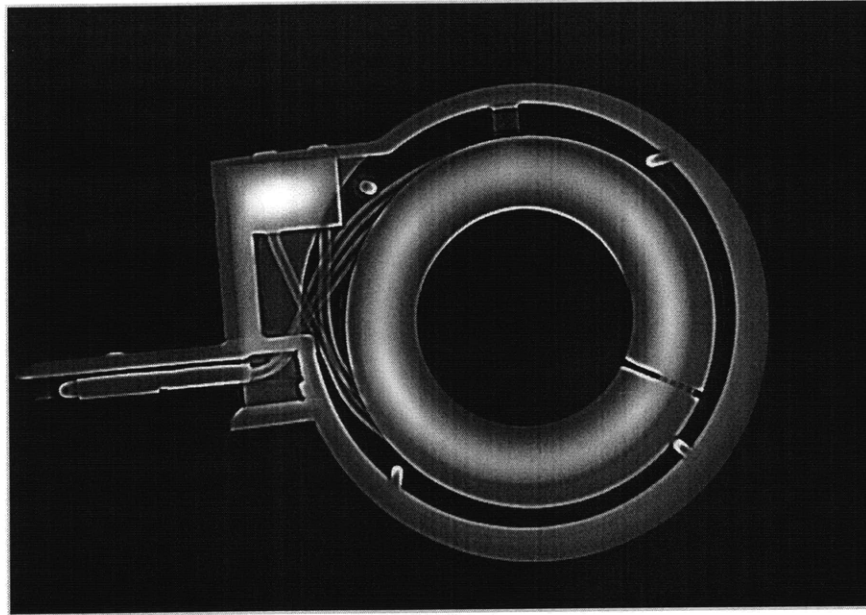


Figure 15: Top-view of the compression coil of the MAGNEFORM machine at MIT.

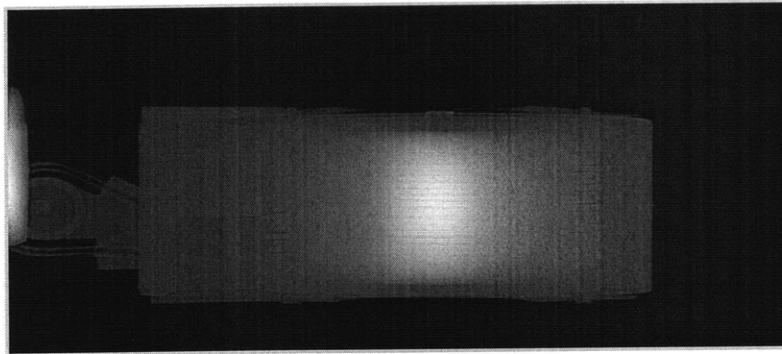


Figure 16: Front-view of the compression coil of the MAGNEFORM machine at MIT.

From the X-rays we were able to determine many key features of the coil. The most obvious was the use of a fieldshaper in the coil already. It appears to be used to take the magnetic field from a six turn solenoid and turns it into something that is more uniform as the inside wall of the fieldshaper is not tapered in any way.

The difficult part of the characterization process of the x-rays was to figure out how the wires were arranged inside the coil. After examining the X-rays from two separate imaging sessions, it was determined that there are two wires that run next to each other to make the solenoid in the coil. This presumably is to reduce the resistance of the coil while keeping up field strength. Another interesting observation was finding the wires to be hollow. This made theoretical sense considering the coil is used in an AC current where the current doesn't penetrate the entire wire.

After gathering the geometric information from a combination of digital and traditional X-rays we were able to construct a considerably accurate representation of our coil. From this

theoretical representation the team was able to construct a Solidworks model of the current coil shown in Figure 17:

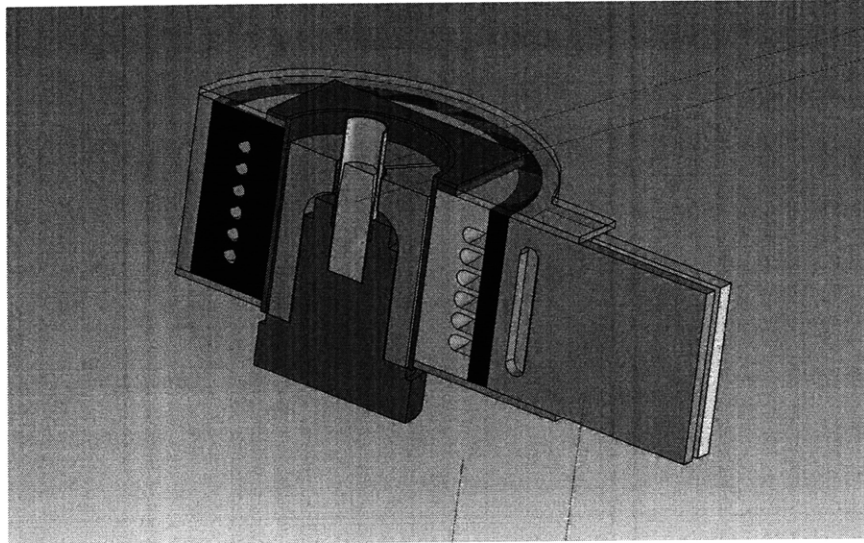


Figure17: Solidworks drawing of the compression coil used for the MAGENFORM machine at MIT [27].

At this stage of the simulation efforts and collaboration with LS-DYNA in California we are still in the process of providing a mesh for the acquired drawing, but LS-DYNA is ready to be used for the analysis of the magnetic field and force that is exerted on the workpieces as well as on the coil and field intensifier themselves.

Truegrid allows the user to parameterize all dimensions such as radii and length. This is particularly useful for optimization, when using another software package from LSTC, called LS-OPT [24]. Using LS-OPT, the researcher can optimize the dimensions as well as any other input parameters in the simulation to receive optimal values for certain desired parameters in the process, such as temperature increases on the surface. This analysis accompanied with experimental observations and measurements will make it possible to optimize the design of the setup and process parameters yielding optimum electromagnetically welded joints.

Unfortunately, we were not able to provide the drawings yet to LSTC for the EMW coils used for the EMW experiments at PULSAR, in Israel (see Chapter 4). However, the EMF and EMW data presented in this study can surely help improve the sophisticated new LS-DYNA model to simulate electromagnetic processes and make it possible to not only simulate the EMF process, but also the EMW process.

2.5 High-Speed Videography Studies

High-Speed Camera Equipment

The High-Speed camera used in the experiments was a Vision Research PHANTOM v7.1, borrowed from the Edgerton Center at MIT. For lighting we used a Lowel DP 1000W Halogen Lamp. The lenses were a Nikon 50mm lens (sn: 274653) and a Nikon 18-70mm zoom lens (sn: US2118600). A Nikon D70 (sn: 3057815) digital camera was used to take pictures of the setup. Figure 18 shows the final setup of the MAGNEFORM machine at MIT used for the EMF and High-Speed Video studies:

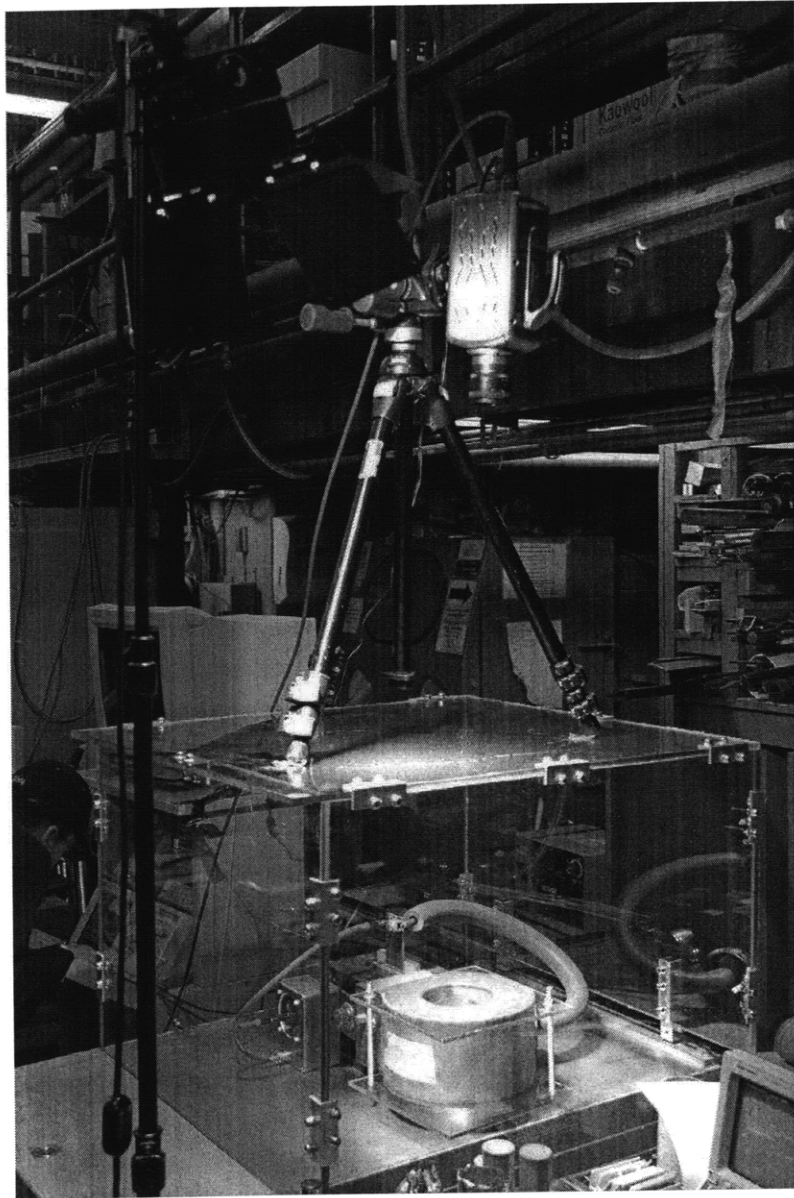


Figure 18: Final setup for the High-Speed Videography experiments.

Manufactured Transparent Hood

In order to capture the EMF process, we needed to focus the camera along the axis of the magnetic coil. However, the original hood of the MAGNEFORMER was opaque and we needed to build a transparent hood to allow us to map the process using the High-Speed Video. We manufactured the transparent hood from polycarbonate that had a thickness of 5/8". Figure 19 shows the completed transparent hood as it was mounted on the MAGNEFORMER.



Figure 19: A photograph of the transparent hood. On the lower left side is the original hood and covered in white sheet is the transparent polycarbonate hood as it sits on the MAGNEFORMER.

Manufactured Stopper

In addition to the transparent hood, we had to build a stopper. This was necessary to hold the workpiece in the right position and to stop it from flying out of the coil. This was due to the fact that the tubes got ejected from the coil, whenever a net upward force was exerted during the process (depending on workpiece position inside the coil). If the tube is placed asymmetrically in the coil, there can be a resulting upward force that causes the tube or can to fly out of the coil.

The stopper was constructed from polycarbonate with 1/4" thickness. It consisted of two plates that were held together by two screws at two opposite corners. We then placed the two plates on the top and bottom of the magnetic coil. Figure 20 shows the stopper as it was placed on the MAGNEFORMER during the experiment.

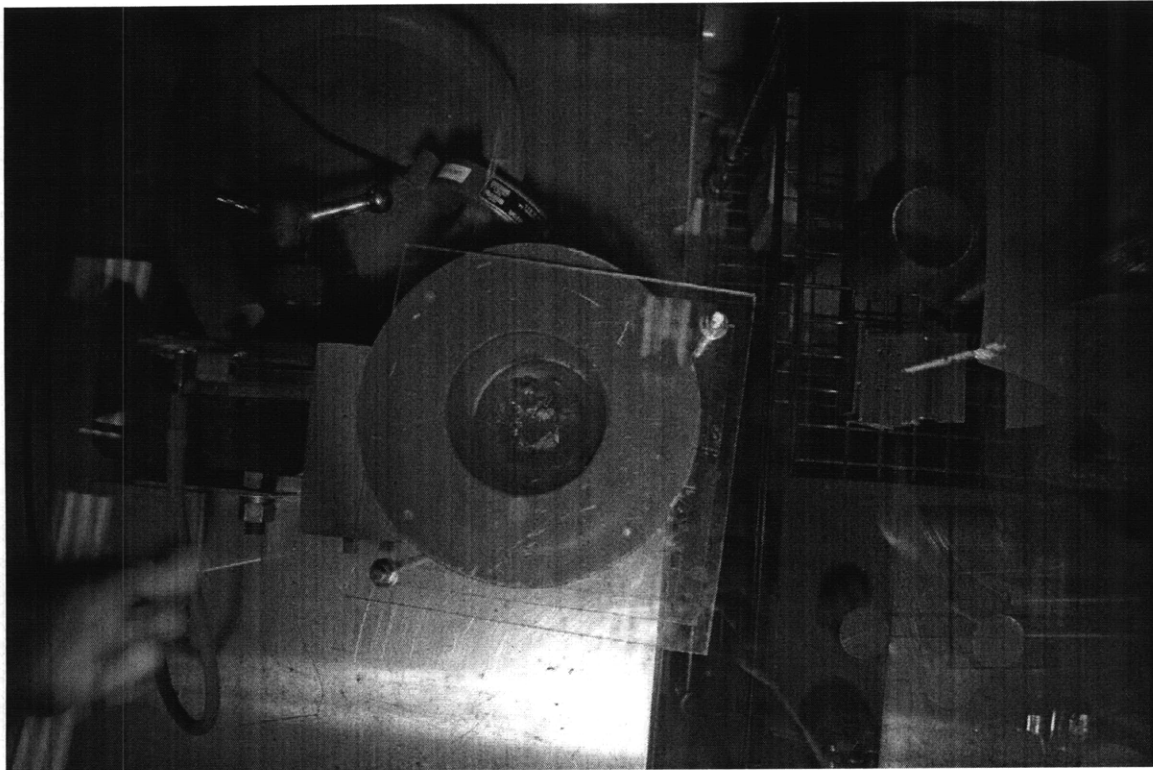


Figure 20: A photograph of the stopper as it is positioned on the coil.

High-Speed Videos of the tubes being accelerated upwards outside of the coil can be found on the DVD, enclosed in this study.

Manufactured Workpiece Stages

A workpiece holder was manufactured to hold the samples in place during the EMF process presented in this section. The same workpiece holder that was manufactured for the Electromagnetic Fatigue Experiments presented in Chapter 3.

Figure 21 shows the Solidworks Drawings of the 2nd workpiece holder which was used for the buckling studies, described in Section 2.7:

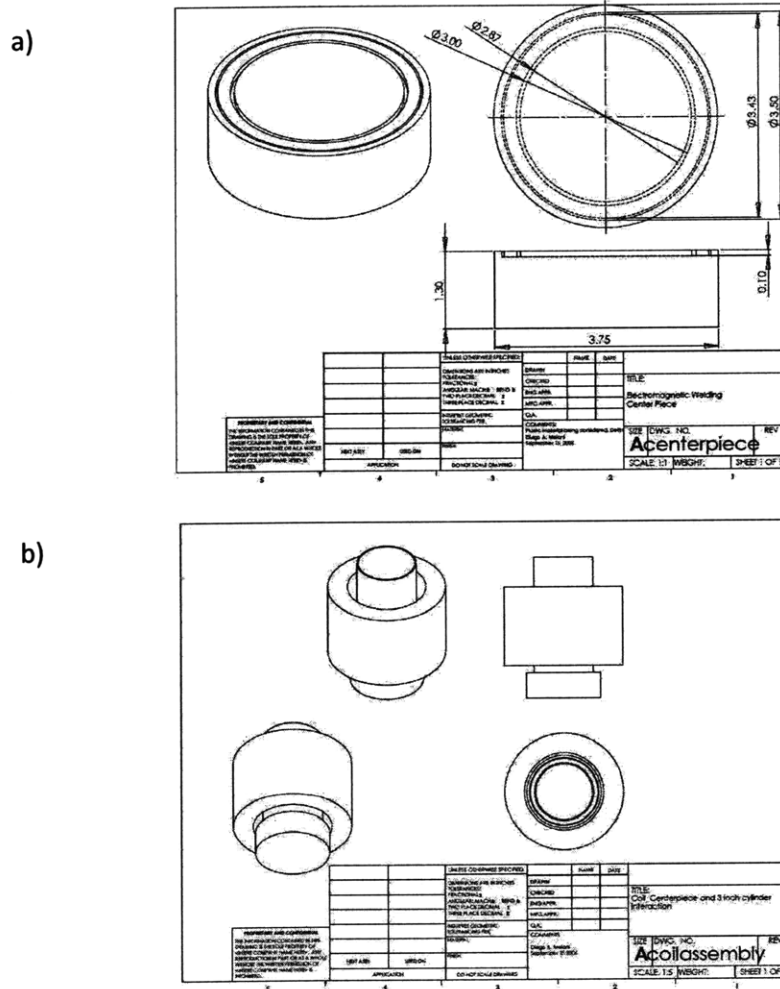


Figure 21a and 21b: Solidworks Drawing of the design of the manufactured workpiece holder and the assembly of the workpiece and the holder inside the coil.

A 3rd sample holder was designed to hold the samples which would be deformed with a fieldshaper (see Section 2.8 for a description of the sample holder for the fieldshaper experiments).

Materials and Specimens

Three different specimens were used in our experiments:

Aluminum cans were observed in our deformation studies. Aluminum cans are made of 3 different alloys. The tab and the top are made of Tab: AA5052 (Al-2.5%Mg) and AA5182 (Al-4.5%Mg), respectively, due to reasons of mechanical strength. The body is made of AA3004 (Al-1.2%Mg-1.0%Mn), which shows good formability. Thereby, we had a readily available source of an Aluminum alloy. So, for the first set of specimens, the material tested was the Aluminum alloy AA3004 and the tubes had an outer diameter of 2.6" and a wall thickness of 0.0047".

The next tests were performed on a high performance Aluminum alloy, Extra-Strength Aircraft-Grade Aluminum (Alloy 2024). Two kinds of specimens were tested, named Tubes I and Tubes II. Tubes I had an outside diameter of 2.5" and a wall thickness of 0.065". Tubes II had an outside diameter of 1.5" and a wall thickness of 0.035".

These tubes are certainly much stronger than the tubes cut from the Aluminum cans. For this reason, we chose tubing with the thinnest wall thickness, as well as largest diameter available on the market, because the mechanical strength of the tubes needed to be as low as possible to still observe plastic deformation of the tubes. Furthermore, an outer workpiece diameter as close as possible to the inner diameter of the coil needed to be chosen to enhance the coupling of the opposing currents during the EMF process.

Further properties of the tested materials are summarized in the Appendix. Figure 22 shows a digital photograph of all sample specimens:

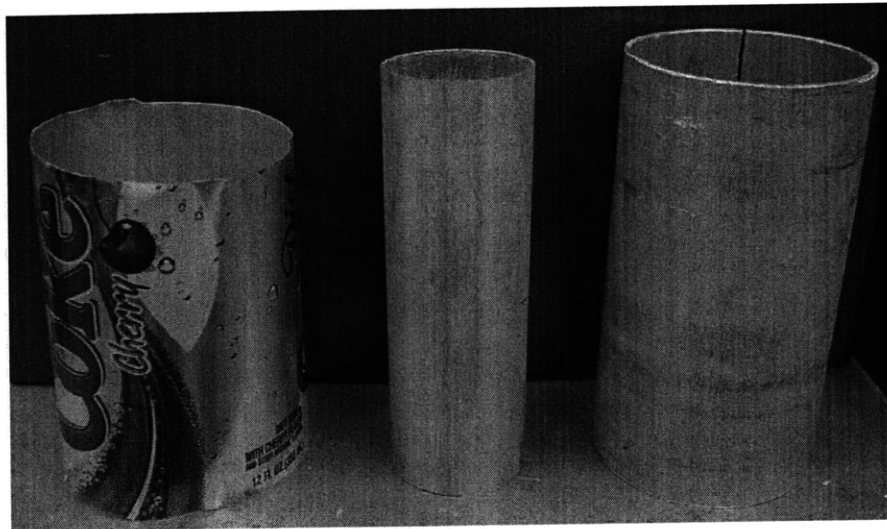


Figure 22: Digital Photograph (Sony DSC-S75) of the EMFA specimens. From left to right: The preliminary Aluminum alloy specimen (AA3004) and the two Extra-Strength Aircraft-Grade Aluminum (Alloy 2024) specimens Tube I and Tube II.

Experiment

Using box-cutters, the top and bottom aluminum discs were removed from all of the cans. The produced tubes were numbered can 6 (tube 1), can 7 (tube 2), can 8 (tube 3), can 9 (tube 4) and can 10 (tube 5). They were then placed in the center of the coil, and the stopper was put in place to both support the can from below and to prevent it from accelerating upwards. For tubes 1, 2, 3, and 4, the MAGNEFORMER dial was set to 50, 60, 70, and 80, respectively. Using a high voltage probe, the input voltages at these levels were measured to be 4.44 kV, 5.32 kV, 6.4 kV and 7.3 kV, respectively.

For each firing, the voltage and current through the coil was recorded on the oscilloscope. After the MAGNEFORMER had fully discharged its capacitor, the tube was removed from the coil, and its diameter was measured with calipers.

During each firing of the MAGNEFORMER, the HSV system and lamp were focused on the coil, through the top of the polycarbonate window that we constructed. A schematic of the exact locations of the lamp and camera relative to the coil are given in Figure 23 (Figure 18 is a photograph of the setup described in Figure 23).

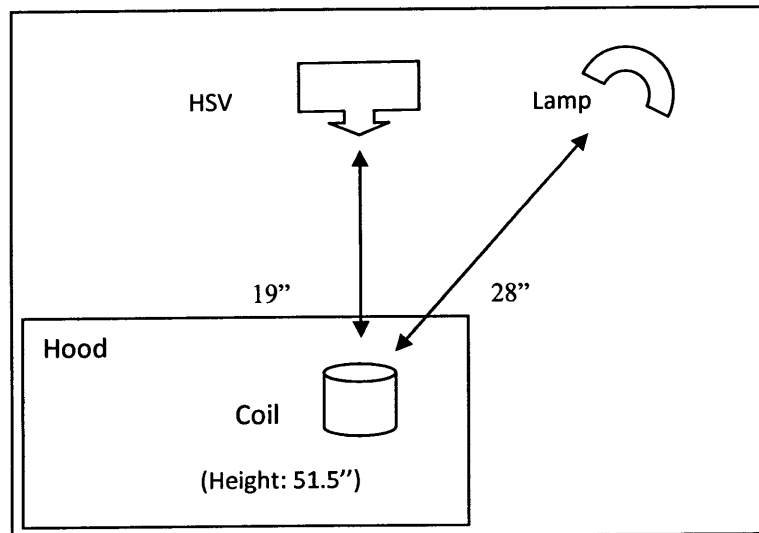


Figure 23: Relative placement of coil, HSV, and lamp for the videos of the tube compression.

For the videos, the HSV was recording at 20,000fps, with a $10\mu\text{s}$ exposure time and 0 EDR. The resolution was 320x240. The Nikon 50mm lens was used, with an aperture of f/1.8. After the four tubes had been compressed, the HSV was “dry-fired” without anything inside the coil. Again, this was done with power settings 50, 60, 70, and 80, and the current and voltage through the coil was recorded on the oscilloscope.

Tubes I and II could not be deformed with the MAGNEFORM machine available at MIT, because the MAGNEFORMER, which is present in our laboratory, cannot provide extremely high energies,

see Table 1. With these specimen dimensions, however, we had to go with a higher strength material (Extra-Strength Aircraft-Grade Aluminum Alloy 2024), which was the only available aluminum tubing, on the market.

Results

After being compressed in the MAGNEFORMER, the cans certainly had a much smaller diameter than before firing, due to plastic deformation. Recall that the initial diameter of our tubes was 2.6". Table 4 shows the final diameters of each of the cans, and the calculated percent change in diameter.

Tube	Power Setting [%]	Final Diameter [cm]	Diameter Change [%]
1	50	1.95	-25
2	60	1.58	-39.23076923
3	70	1.53	-41.15384615
4	80	1.31	-49.61538462

Table 4: The power setting, final diameter, and percent diameter change for each of the 4 tubes fired in the MAGNEFORMER.

Unsurprisingly, increasing the power setting on the MAGNEFORMER resulted in more compression of the tubes. As Table 4 shows, the MAGNEFORMER was able to reduce tube 4's diameter by nearly one half.

Now, we would like to present the results from the velocity measurements and calculations.

Velocity Measurements

The tubes fired in the MAGNEFORMER were compressed by the strong electromagnetic field induced between the tube and the coil wall. Figure 24 shows the High-Speed Video view of tube 1, 2, 3 and 4 at different times during the videos. The High-Speed Videos of the compression process can be found on the included DVD.

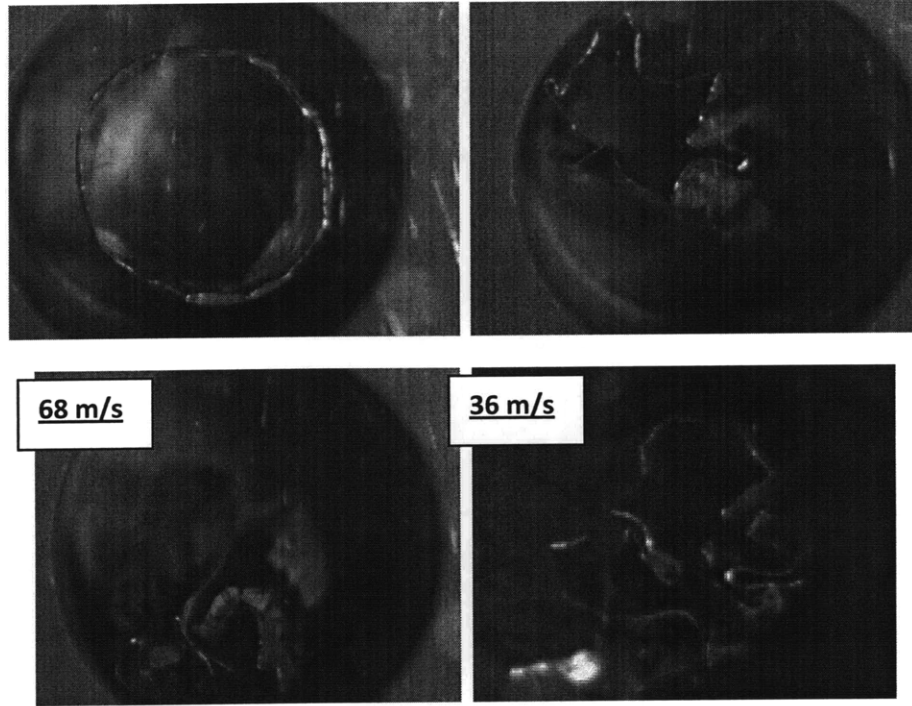


Figure 24: Tube 1, 2, 3 and 4, compressed in the MAGNEFORMER with power setting 50, 60, 70 and 80, respectively. The images are shown at different times during the video. Speeds could be measured for tube 3 and 4.

It was possible to measure the compression speeds for tube 3 and 4, which were 68 m/s and 36 m/s, respectively. The measurements could not be performed for tube 1 and 2, because their compression was too asymmetric. The deformation of tube 3 was very symmetrical, which must be the reason for the higher compression speed, in comparison to tube 4, which was compressed at a higher EMF energy setting.

Additionally, small cracks appeared in the tubes. Since these cracks are the subject of a fatigue study, we discuss possible causes of their formation in Chapter 3.

Because the deformation of the tubes was often highly irregular, we tracked various points on the cans being deformed as opposed to somehow measuring the area, which would have been considerably more difficult. By looking at the velocities for a few different points, we got a feel for the general linear deformation velocities of the tubes when using the MAGNEFORMER at various power settings. We tracked several points around the circumference of the tubes through the frames in the deformation videos. Figure 25 shows this study for tube #5 for one point on the circumference of the tube:

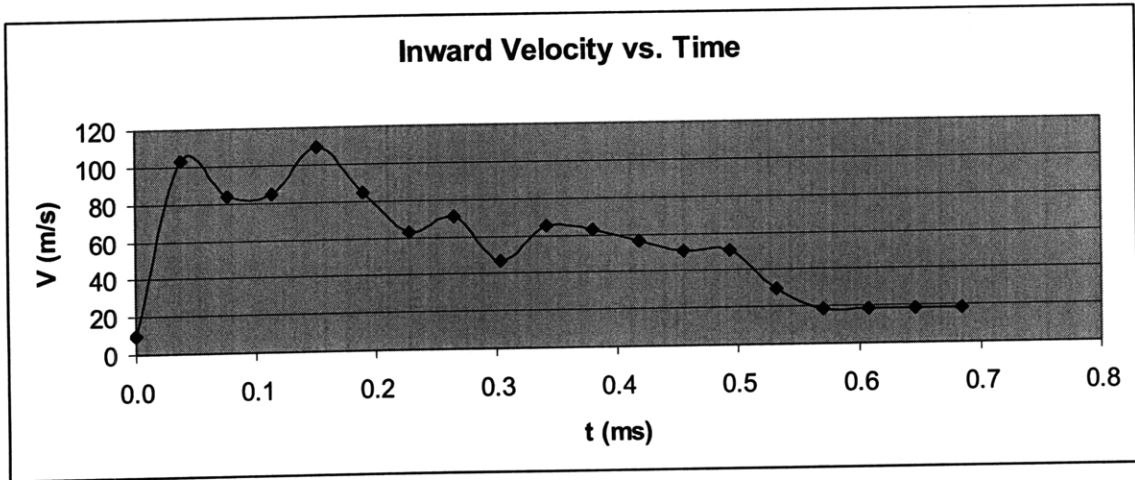


Figure 25: The average velocities of one point on the diameter of tube #5, tracked during successive frames.

Table 5 shows the results of the High-Speed Videography study and the study and measurements of the individual frames, with the resulting speeds of the individual points.

tube	Frame0	Frame1	Time t	x_0	y_0	x_1	y_1	dx	dy	v
5	-18145	-18138	0.000038	194	182	166	159	-28	23	47.2
5	-18145	-18131	0.000038	128	-33	111	130	-17	-97	64.2
5	-18145	-18138	0.000038	194	182	166	159	-28	23	47.2

Table 5: Linear velocities of points on the deformed tubes.

The average velocity for tube #5 was approximately 52.9 m/s. Further velocity measurements, where the average speed was calculated by measuring the speed of several points around the circumference of the tube, during the EMF process can be found in the Appendix B.

Table 6 gives an overview of the results observed in the High-Speed Video analysis, in comparison with the necessary critical velocity needed for EMW, as well as the calculated velocities from the theory.

	Threshold Velocity (for EMW) [m/s]		Measured Velocity [m/s]	Calculated Velocities [m/s]	
	$v_c'' = 2.25 \sqrt{\frac{H_v}{\rho}}$	$v_c' = k' * \sqrt{\frac{2 * H_v}{\rho}}$	<i>High Speed Video</i>	$v^2 = \left(\frac{B^2}{2\mu_0} \frac{1}{h \rho}\right) \cdot x$	$v = \frac{1}{\rho h} \left(\int_0^t P dt - P_y t\right)$
Al (cans)	1270	800	~50-100	86.1 (x = 2 mm)	45.3
A6061-T6	1400	882	n/a	86.4 (x = 2 mm)	57.5

Table 6: Summary of the threshold, the measured and the calculated velocities for the studied Aluminum can (Tube 5) and Al6061-T6 [18, 28, 29].

One can see, from Table 6 that the EMF MAGNEFORM machine is far away from achieving velocities large enough to successfully perform EMW. The theoretical calculations are in good agreement with the observed velocities in the High-Speed Videography studies (see Equ. 1.23 and Equ. 1.26, in Chapter 1, for the “calculated velocities”).

Power Measurements

As described above, we measured the voltage and the current during the EMF process, from which we were able to calculate the power by equating

$$P = IV . \quad 2.16$$

We now compare the power setting to the actual power in the process, as well as measure the change in diameter of the tubes 1, 2, 3 and 4. Figure 26 shows the calculated power curves (with and without tube 2 inside the coil), which were calculated from the measured current and voltage waveforms:

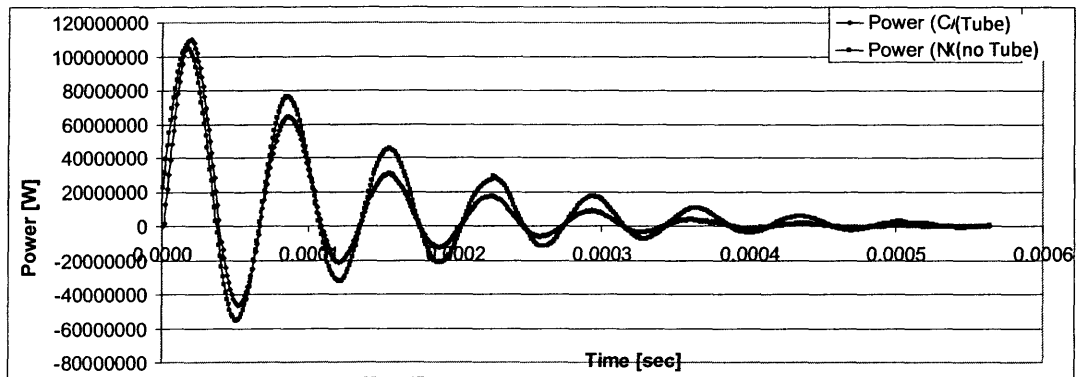


Figure 26: Power curve calculated from the current and voltage waveform, which were obtained for both cases, no tube inside the coil and with tube 2 inside the coil. The power setting was 60 for this case.

As stated above, we recorded the current and voltage through the coil as a function of time on the oscilloscope. This was also done for each MAGNEFORMER firing without a tube inside the coil and power settings of 50, 60, 70 and 80. Using Equ. 2.16 and

$$E = \int_0^t P dt \quad 2.17$$

we were able to calculate the electrical power and energy, respectively, inside the coil at the individual power settings. Figure 27 shows the calculated energy for each power settings.

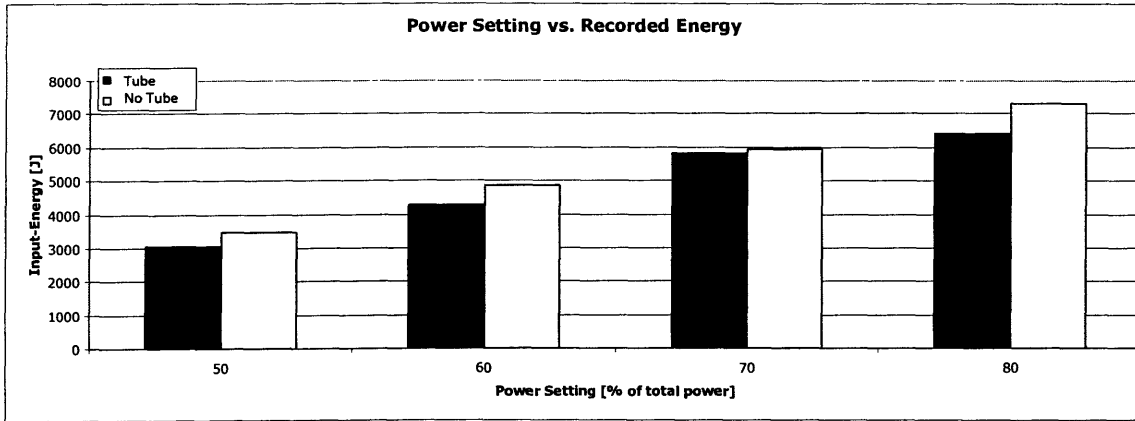


Figure 27: Recorded energy through the MAGNEFORMER coil as a function of power setting.

Notice that the amount of energy in the coil when no tube was inside is higher than the amount of energy when a tube was inside. This is due to the fact that the tube puts energy back into the coil by having its own induced current and creating its own electric and magnetic field. Alternatively, each workpiece can be thought of as a shield that blocks the magnetic field or as another impedance in the circuit. Thereby the current is lowered which in turn lowers the power (Equ. 2.16). We also observed this drop in the current peaks in our measurements.

The energy differentials are summarized in Table 7, along with the change in diameter for each tube. Figure 28 is an Excel graph representing the data in Table 7.

Input Power [%]	Energy shielded by the tube[J]	Diameter Change [%]
50	420	25
60	560	39
70	120	41
80	910	49

Table 7: The MAGNEFORMER power setting for each can firing, the energy absorbed by that can, and its % diameter change.

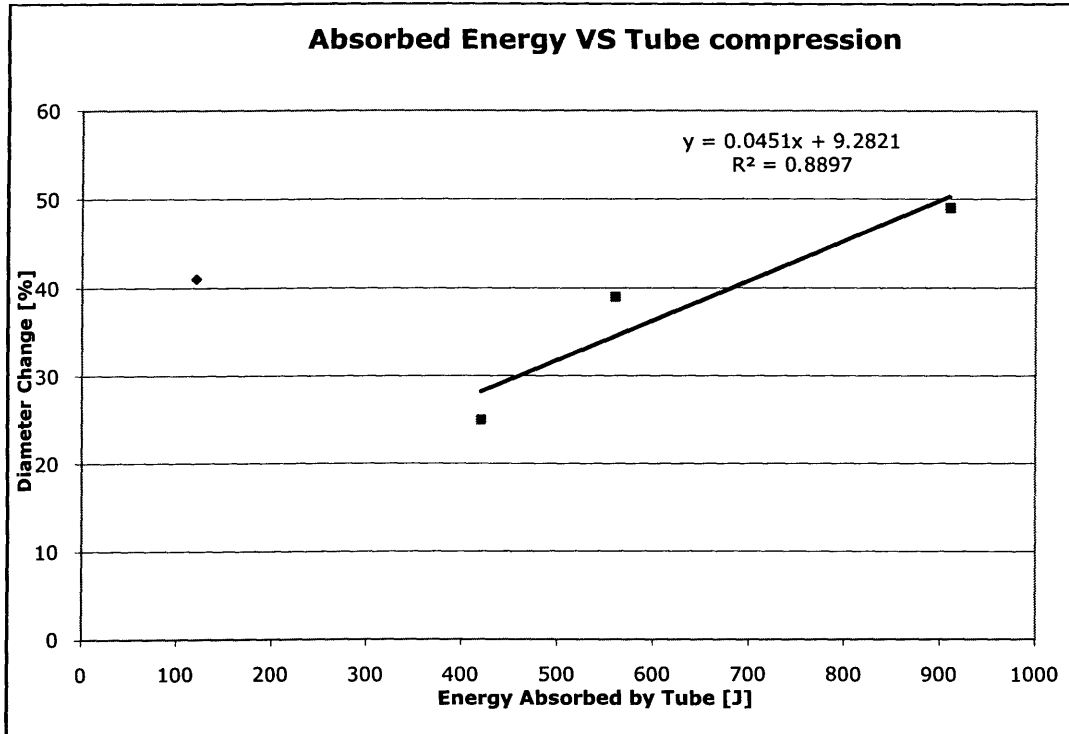


Figure 28: Chart showing the diameter change of each can as a function of the amount of energy it absorbed.

One might expect that there is a linear relationship between the amount of energy that the tube absorbs and the amount that its diameter changes. For the most part, our data supports this theory. The three pink points, representing tubes 1, 2 and 4, are oriented on a line of increasing slope. Interestingly tube 3, with the most symmetrical compression, does not fit this trend (see Figure 24 and High-Speed Video analysis of tube 3 on the enclosed DVD).

In the next section we propose a method to decrease the necessary energy for EMW by decreasing the mechanical strength of the outer workpiece by introducing an EMF step prior to the EMW step.

2.6 Buckling Studies

In this section we hypothesize that if a controlled EMF forming step would be performed prior to the EMW step to decrease the mechanical strength of the outer workpiece through the introduction of wrinkles a following EMW step would need a lot less energy.

We performed “wrinkling experiments” to show the decrease in mechanical strength of the specimens observed with increasing number of wrinkles around the circumference. Thereby, we tried to find a correlation between the number of wrinkles and the mechanical strength of the tube.

It needs to be emphasized that the EMF forming step needs to be controlled with a stable end-product, because the EMW step afterwards always needs to find the same workpiece geometry to properly create the needed coupling between the workpiece and the coil.

In this study we perform an approximation to control the EMF forming step by inserting a mandrel inside the outer workpiece. Thereby, the outer workpiece is deformed onto the mandrel in a controlled fashion during each pre-EMF-forming step. After that the EMW process would need to be performed, but with a much lower energy needed, because the mechanical strength of the specimen would be reduced.

Furthermore, we tried to find a critical number of wrinkles along the circumference, which will induce a much lower force needed to deform the specimen during the following step, which would then be the EMW step.

Background

In Chapter 1 we introduced the deformation theory of the EMF and EMW process through the description of pure (no buckling) motion. Now we need to move a step further by studying buckled (perturbed) motion. The mathematical and mechanical details for this theory are very complex and are presented in detail in [18]. We said that the collapse pressure P_y , which is the minimum pressure necessary for the workpiece to be deformed can be calculated by

$$P_y = -\frac{(2-k)h\bar{\sigma}}{rK_2}, \quad 2.18$$

where k and K_2 are constants (depending upon the length/diameter ratio of the workpiece), h is the wall-thickness of the workpiece, r is the radius of the workpiece and $\bar{\sigma}$ is the average representative stress over 10-20 percent strain [18]. Therefore, it can be seen that for smaller k the collapse pressure decreases. Figure 29 shows the change of the parameter k with increasing number of wrinkles n .

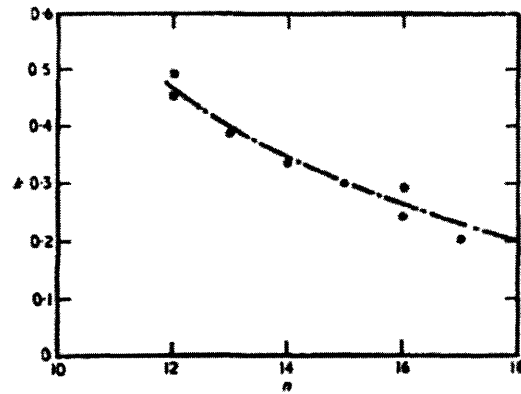


Figure 29: Variation of the constant k with the number of wrinkles, n , for Aluminum tubes of $r/h+16$, having different length/diameter ratios [18].

The number of wrinkles is affected by the axial restraints. Therefore, smaller values of k are observed for longer tubes, which buckle with a larger number of wrinkles. Figure 30 shows the dependence of the number of wrinkles n on the r/h ratio:

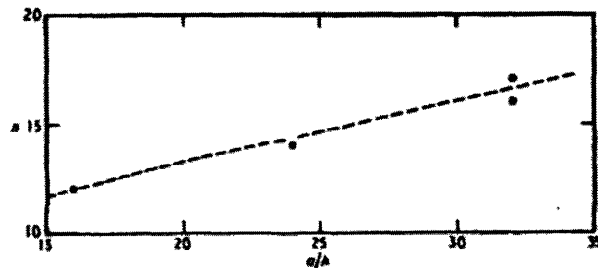


Figure 30: Variation of the number of wrinkles n , with the ratio r/h for a 4" outer diameter Aluminum workpiece with $k=0.45$ [18].

It is safe to say that by introducing wrinkles to the workpiece through an EMF step, we can lower the mechanical strength of the workpiece. If the EMF step introduces a number of wrinkles in a controlled fashion followed by an EMW step, we can say that we can decrease the necessary energy to deform the outer workpiece and accelerate it to the necessary threshold velocity to achieve an EMW joint.

Therefore, we will now study the effect of the number of wrinkles on the mechanical strength of Aluminum tubing being deformed in the EMF MAGNEFORM machine, at MIT. Further mathematical calculations, formulas for the numbers of wrinkles and more can be found in the literature, such as the piping literature, such as [30].

Specimens

The specimens for the buckling study were Al6061-T6 tubing with an outer diameter of 3.5" and a wall-thickness of 0.036". The mandrels that were used to deform the tubes onto were tubes with a wall-thickness of 0.066" and an outer diameter of 3".

Experiment and Results

The Aluminum 6061-T6 Tubes were placed inside the EMF coil of the MAGNEFORM machine at MIT. Then the EMF machine was fired for several times. The diameter changes and the number of wrinkles were measured, between the individual firings.

The bottoms of the tubes were held in place by the manufactured stage (see Figure 21). This needed to be done to not create an upwards acceleration of the tube. After each firing and measurement the tube could then be placed again inside the stage at the same position inside the stage, because the tube was not deformed on the bottom.

Figure 31 show two photographs after the tubes where compressed in the MAGNEFORM machine with three shots and four shots, respectively:

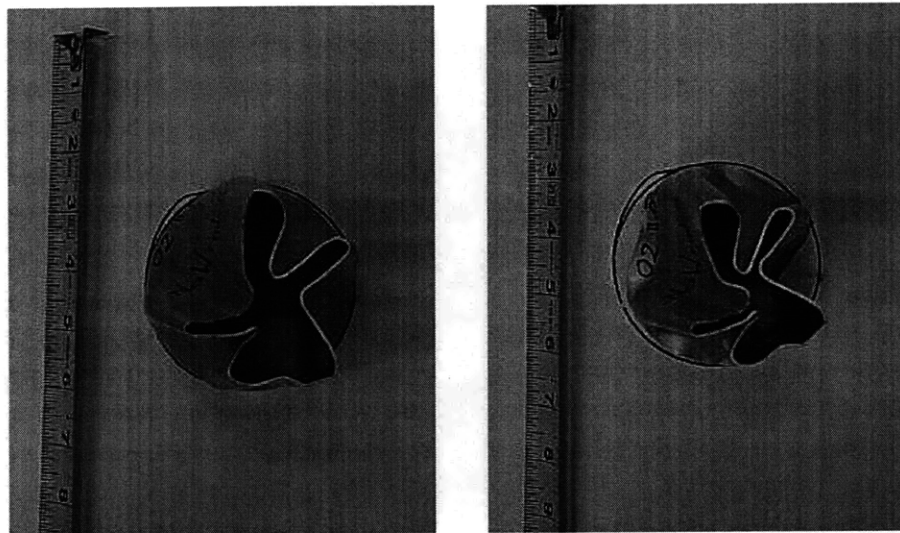


Figure 31: Aluminum tubes compressed after three and four EMF shots, respectively.

From Figure 31, one can see that the aluminum tube deforms in a quite uncontrollable fashion, which would be undesirable as it presents a non-repeatable process. To overcome this, a mandrel was inserted inside the tube and the MAGNEFORM machine was fired four times. After that, the mandrel was taken out and the machine was fired for one more time. Figure 32a and Figure 32b show photographs of the tube after four shots (with mandrel) and the 5th shot (without the mandrel), respectively:

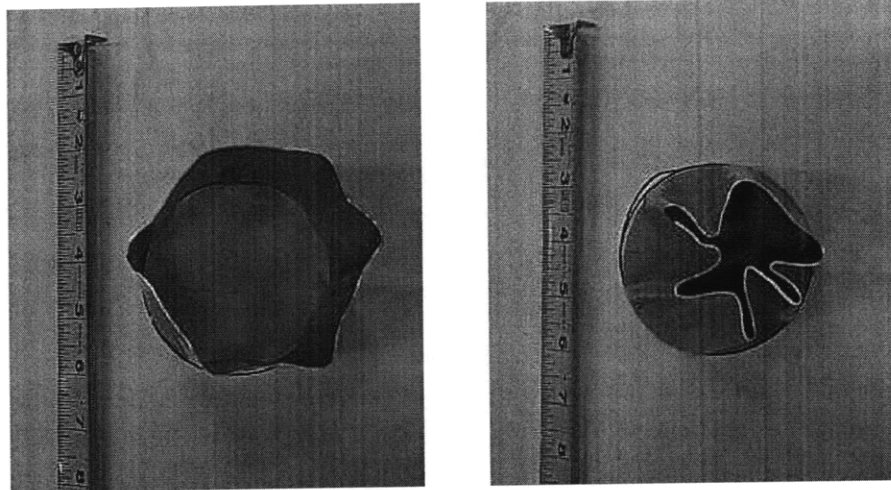


Figure 32: a) Photograph of the tube after 4 shots (with a mandrel on the inside of the tube) and b) after the 5th shot (without a mandrel).

Figure 33 shows a control experiment that the EMF step (with a mandrel) is very much repeatable. Here, two tubes were fired in the same manner and circumference, number of wrinkles, minimum and maximum diameter was noted.

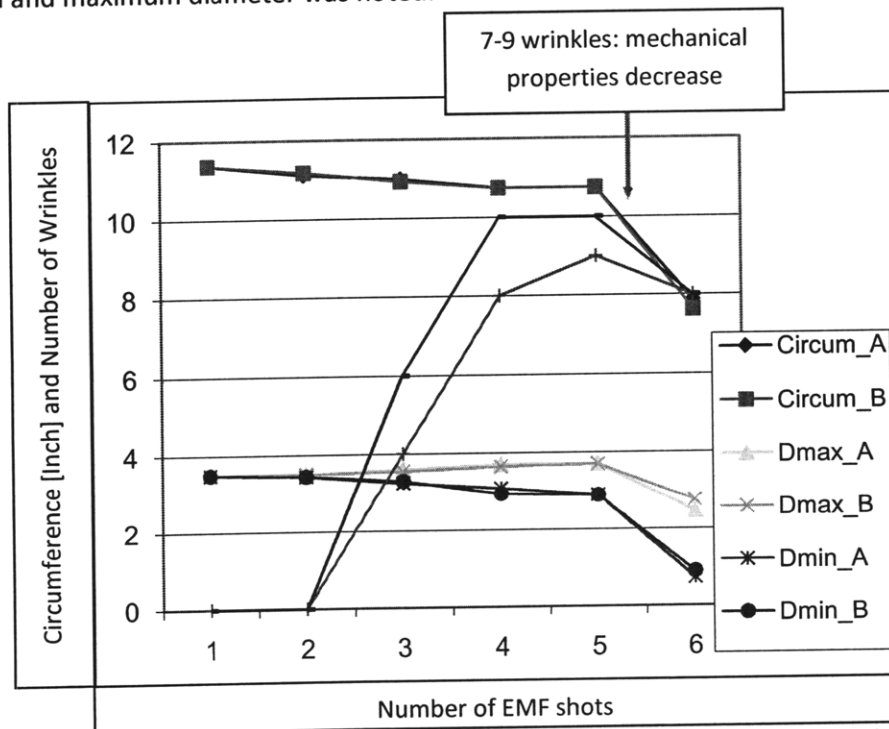


Figure 33: Control experiment comparing two tubes (A and B) being compressed with a mandrel. *Dmax* and *Dmin* are the maximum and minimum diameter measured, respectively. *Circum* is the measured circumference.

By looking at Figure 33, one can see that the critical number of Wrinkles necessary to suddenly see a large decrease in mechanical properties for this geometry, leading to much larger deformation

for the following EMF step, was between 7 and 9 Wrinkles. Figure 34 shows the comparison graph of a tube being compressed (without a mandrel) for four shots (*N*) and with a mandrel (*M*), which was removed after the 5th shot:

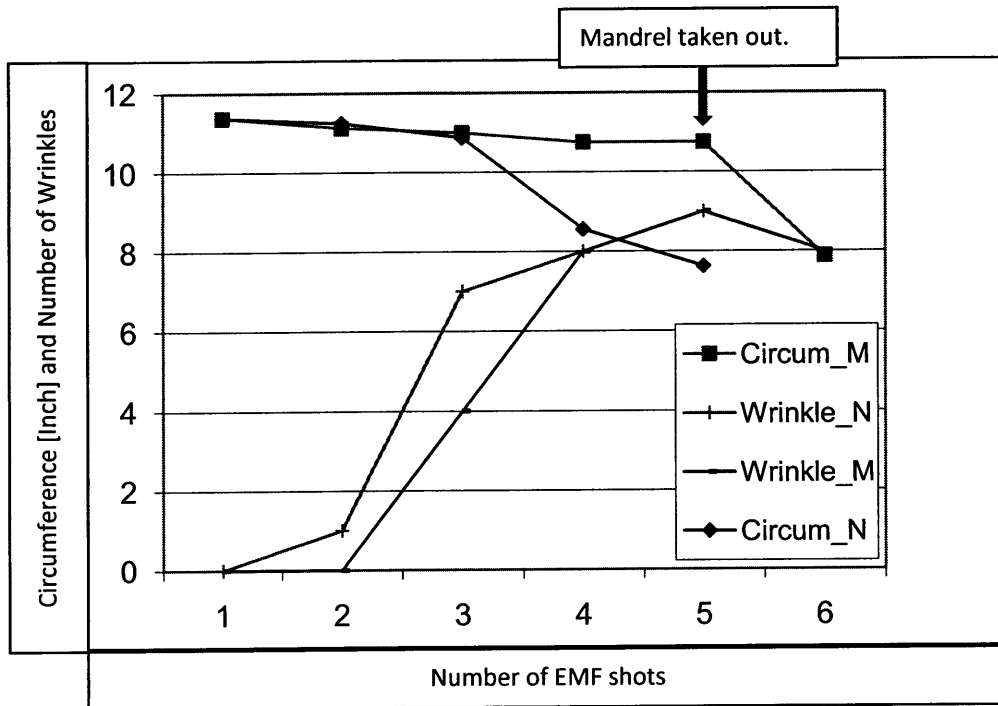


Figure 34: Comparison of two tubes being compressed. One without a mandrel for 5 shots (*N*) and one with a mandrel for 5 shots, which was then removed at the 6th shot (*M*). *Wrinkle* stands for the number of Wrinkles and *Circum* for the measured Circumference.

The measurements shown in Figure 34, show exactly what was already observed through visual observation in Figure 32: After the mandrel is taken out the possible compression and change in diameter of the EMF process is all of a sudden equally large as if the tube would have been compressed several times before this last shot or had a much lower collapse pressure.

Discussion

It could be shown that it was possible to deform the outer tube in a controlled fashion, while introducing a certain number of wrinkles. Thereby, the mechanical strength and necessary collapse pressure of the workpiece was decreased.

Through this pre-treatment of the workpiece one additional shot created a much larger deformation with the same energy.

In our proposed setting, the last shot would have had to be performed with EMW settings and the energy needed to accelerate the workpiece to the critical velocity needed for EMW would have been much lower. The EMW coil would have to get very close to the workpiece, which now has a perturbed surface, to avoid unnecessary coupling losses.

To summarize, one could think of a setup where, first, a mandrel is inserted into the outer workpiece and the outer workpiece is deformed onto the optimized outer surface of this mandrel. This is done by using a lower power setting and thereby achieving EMF only.

After that, the power setting is increased, however to a lower level that is usually much higher to achieve EMW. But, due to the decrease of mechanical strength in the prior preparation step the EMW step can now be achieved with a much lower energy necessary, thereby imposing lower stress on the coil and tools, which will increase their life.

2.7 Deformation Studies with a Fieldshaper and an Inner Workpiece

A fieldshaper was built from copper to perform further EMF experiments. Experiments with three different shapes (non-tapered, tapered and with a groove for adhesive) of the inner workpiece were performed. Unfortunately, no promising results could be obtained due to the lack of power of the EMF MAGNEFORM machine at MIT. However, the concept of a fieldshaper could be proven. The results from the experiments can be found in the Appendix B. Following, we describe the self-built fieldshaper as well as the new sample-holder that had to be built for the fieldshaper experiments.

Manufactured Fieldshaper

Fieldshapers, also known as flux concentrators (see also Figure 33 and [4, 19]) have been briefly introduced in the introduction of the circuit theory of EMW (Section 1.1.2.2). Now, we take a closer look at their properties as well as design.

The main feature of the fieldshapers is the radial slit, which has not been mentioned yet. Due to this slit, the outer induced eddy current is led from the outer to the inner periphery of the fieldshaper. Therefore, we now have another one-turn coil that surrounds the workpiece with a far lower radius. Thereby, we fulfill two of the requirements (see above) to reduce the inductance, which should therefore give a shorter pulse duration time. Figure 35 shows the principle of a fieldshaper:

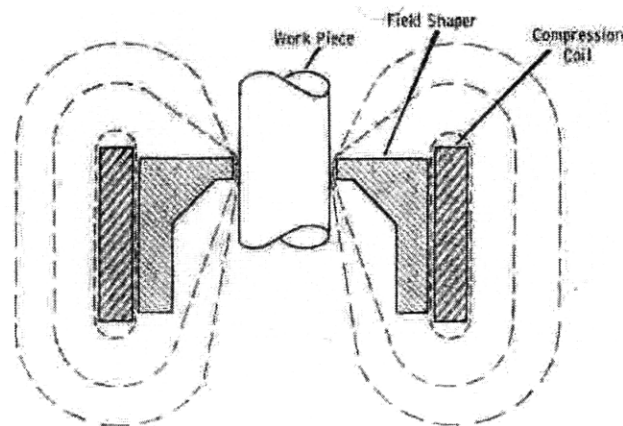


Figure 35: Principle of a fieldshaper. It can be seen that due to the fieldshaper the magnetic flux lines are concentrated around the workpiece at a certain position [5].

A concentration of the magnetic flux lines can be observed. However, other sources say that the term “flux concentrator” or “fieldshaper” is somewhat erroneous. In fact, it is stated that the only concentration happens in the axial direction at the inner periphery of the fieldshaper consisting of a secondary current density [31].

This current concentration leads to the production of high fields [32-34]. However, a principal drawback seems to be low energy transfer efficiency. The capacitor bank that is needed to produce a given volume of high field needs to be larger, when using a fieldshaper than using just a Bitter coil.

The energy losses can be divided into three types:

- a. Thermal losses – resistive dissipation
- b. Inductive energy losses – caused by poor coupling between the coil and the fieldshaper
- c. Inductive energy losses caused by the shape of the inner surface of the fieldshaper

First design steps against these energy losses are described in [31].

As stated above another sample holder to hold the samples inside the described manufactured fieldshaper had to be manufactured. Figure 36 shows a photograph of the sample holder. Figure 37 shows the Solidworks Drawings of the fieldshaper that was manufactured at MIT. Figure 38 shows a photograph of the manufactured fieldshaper.

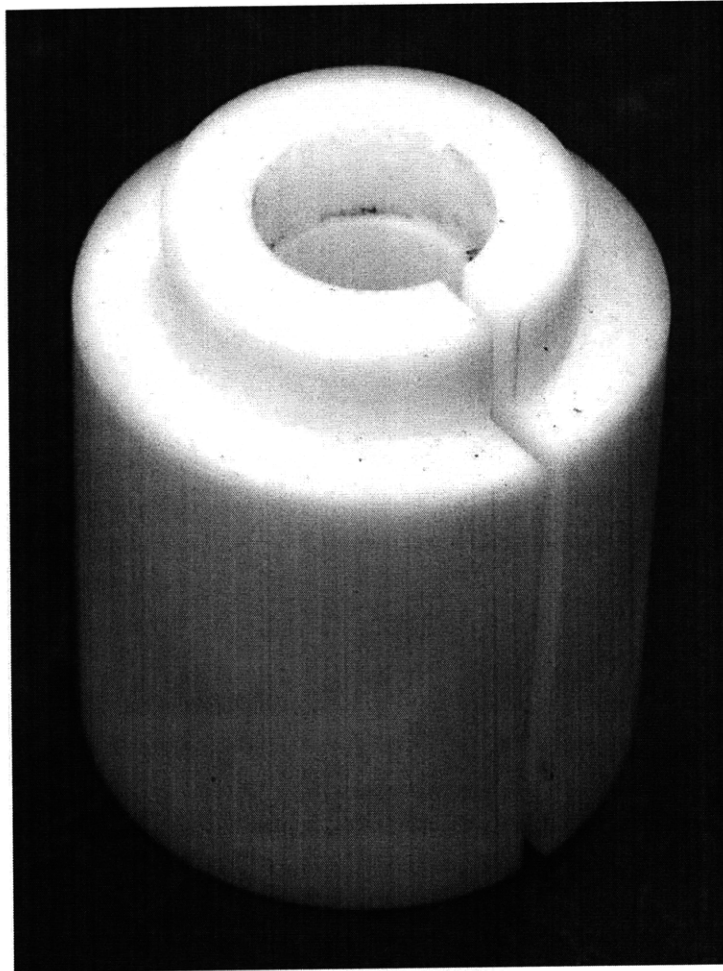


Figure 36: Sample holder that fit right inside the fieldshaper.

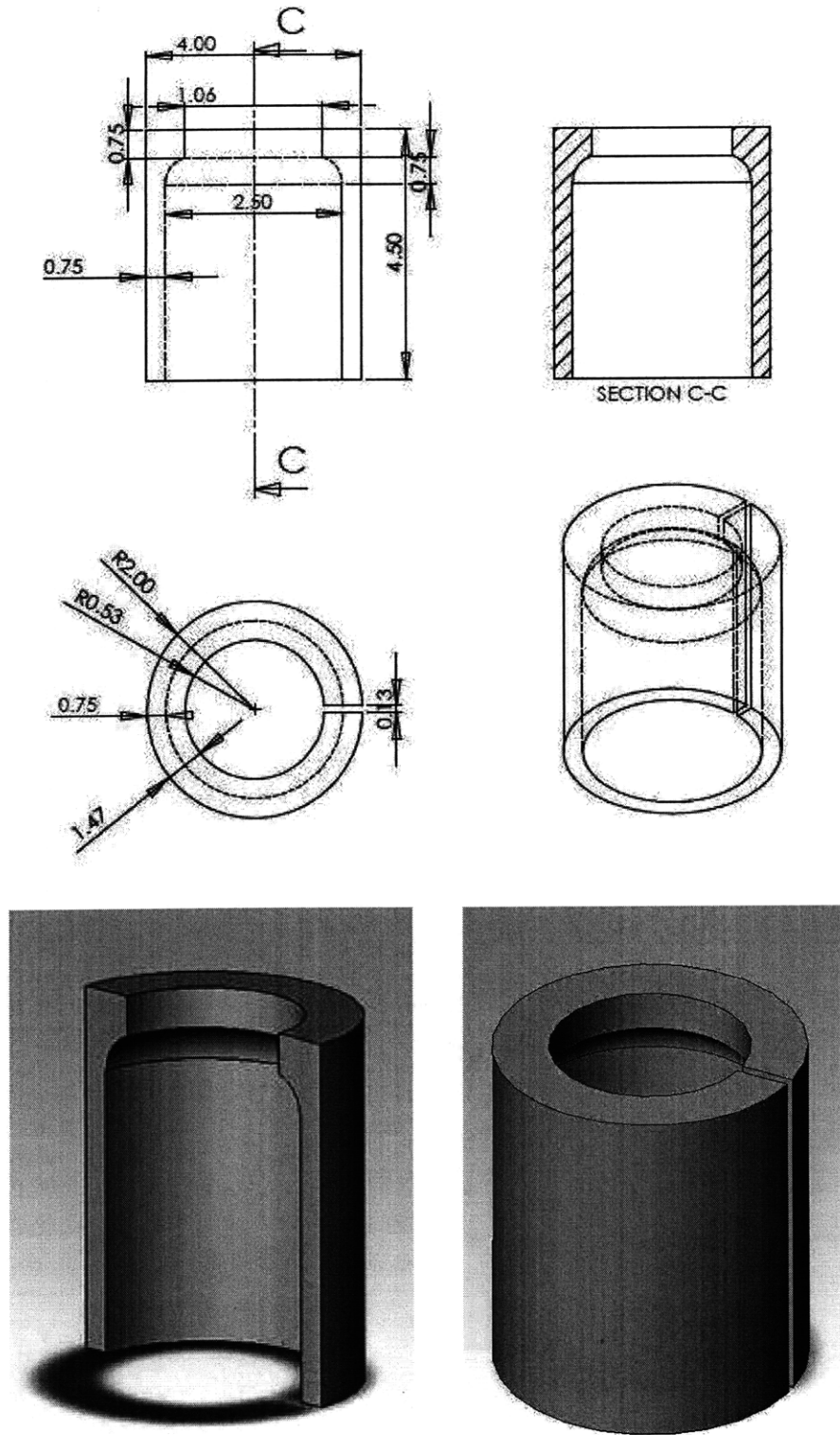


Figure 37: Solidworks Drawings of the design of the manufactured fieldshaper at MIT.

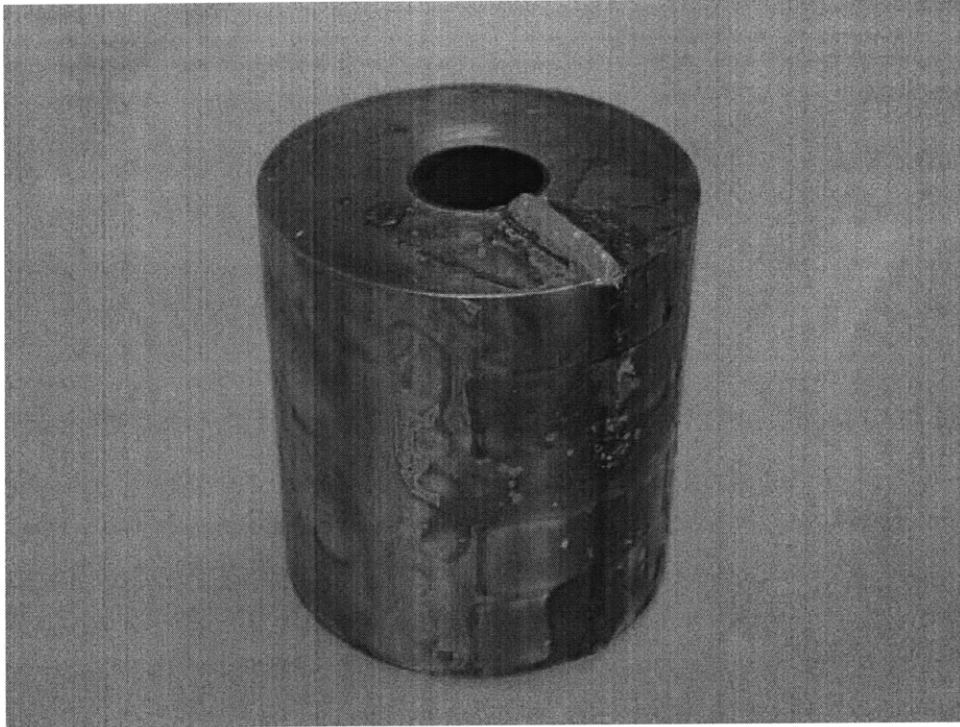


Figure 38: Photograph of the fieldshaper manufactured at MIT.

The material used for the fieldshaper was copper and the outer and inner surfaces of the cut copper were insulated with electrical insulation paste and epoxy.

During the experiments the epoxy inside the slit of the fieldshaper would crack due to the expansion of the fieldshaper. Therefore, a sheet made of Mica was then used to fit right inside the slit of the fieldshaper and to avoid any possible arcing inside the slit.

Experiment and Results

The results of the three fieldshaper experiments are presented in the Appendix B. Like stated previously, we were able to show coupling of the fieldshaper, but the EMF MAGNEFORM machine was not strong enough to create a proper EMF joint. Tensile tests on the best joints, which were also supported with adhesive proved that the joints were still rather weak.

Bibliography – Chapter 2

- [1] Johnson W, and Mamalis AG (1979), Ingenious alternatives to the press in metal forming, *Welding and metal Fabricator* (July/Aug), 375-383
- [2] Lange K (1985), *Handbook of Metal Forming*, McGraw-Hill
- [3] Daehn GS, Altynova M, Balanethiram VS, Fenton G, Padmanabhan M, Vohnout VJ, Tamhane A, and Winnard E (1995), High velocity metal forming – An old technology addresses current problems, *JOM July*, 42-45.
- [4] Mamalis AG, Manolacos DE, Kladas AG, Koumoutsos AK, Electromagnetic forming and powder processing: Trends and development, *Appl Mech Rev* **57**(4), 299-324.
- [5] Powers HG (1967), Bonding of Aluminum by the capacitor discharge magnetic forming process, *Weld. J. (Miami, FL, U. S.)* **46**(6), 507-510.
- [6] Brown WF, Banbas J, and Olson NT (1978), Pulsed magnetic welding of breeder reactor fuel pin end closures, *Weld. J. (Miami, FL, U. S.)* **57**(6), 22-26.
- [7] Masumoto I, Tamaki K, and Kojima M (1985), Electromagnetic welding of aluminum tube to aluminum or dissimilar metal cores, *Trans. Jpn. Weld. Soc.* **16**(2), 110-116.
- [8] Tamaki K, and Kojima M (1988), Factors affecting the result of electromagnetic welding of aluminum tube, *Trans. Jpn. Weld. Soc.* **19**(1), 53-59
- [9] Plum MM, and Maxwell Laboratories Inc (1996), Electromagnetic Forming, *Metals Handbook 9th Edition*, **14**, ASM, Metals Park, Ohio.
- [10] Young FJ (1973), Pulse shielding by nonferrous and ferromagnetic materials, *Proc of the IEEE* **61**(4), 404-413.
- [11] Livshitz Y, and Gafri O (1999), Technology and equipment for industrial use of pulse magnetic fields, *Digest of Tech Papers-IEEE Int Pulsed Power Conf* **1**, 475-478.
- [12] Altynova MM, Electromagnetic Metal Forming Handbook, Mat Sci and Eng Dept, Ohio State Univ, Transl of the Russian book: SMI'SOM by IV Belyy, SM Fertik, and LT Khimenko, VS available at: <http://www.er6.eng.ohio/stc.edu/~DAEHN/hyperplasticity.html>.
- [13] Ouellette RP, Ellerbusch F, and Cheremisinoff PN (1987), *Electrotechnology 2: Applications in Manufacturing*, Ann Arbor Sci.
- [14] MAGNEFORM machine manual
- [15] Padmanabhan M (1997), Wrinkling and springback in electromagnetic sheet metal forming electro magnetic ring compression, MS Thesis, Ohio State Univ, available at: <http://www.er6.eng.ohio/stc.edu/~DAEHN/hyperplasticity.html>.

- [16] Panshikar HM (2000), Computer modeling of electromagnetic forming and impact welding, MS Thesis, Ohio State Univ, available at:
<http://www.er6.eng.ohio/ste.edu/~DAEHN/hyperplasticity.html>.
- [17] Mamalis AG, Manolakos DE, Kladas AG, Koumoutsos AK, Electromagnetic forming and powder processing: Trends and development, *Appl Mech Rev* 57(4), 299-324.
- [18] S. T. S. Al-Hassan, The plastic buckling of thin-walled tubes subject to magnetomotive forces. *Journal Mechanical Engineering Science OIMechE* Vol 16 No 2 1914, 59-70.
- [19] http://repairfaq.ece.drexel.edu/sam/CORD/leot/course04_mod04/mod04-04.html
- [20] P. Zhang, Joining enabled by high velocity deformation, Thesis (2003)
- [21] I. Masumoto, K. Tamaki, M. Kojima. Electromagnetic Welding of Aluminum Tube to Aluminum or Dissimilar Metal Cores. *Transaction of the Japan Welding Society*, Vol 16, No. 2, October 1985.
- [22] <http://www.academicsuperstore.com/products/National+Instruments/Multisim>
- [23] <http://www.mathworks.com/products/matlab/>
- [24] <http://lstc.com>
- [25] P. L'Eplattenier, G. Daehn, G. Cook, M. Seth, C. Ashcraft, M. Burger, A. Shapiro. Introduction of an Electromagnetism Module in LS-DYNA for Coupled Mechanical-Thermal-Electromagnetic Simulations. 9th International LS-DYNA Users Conference.
- [26] <http://www.solidworks.com>
- [27] <http://truegrid.com/>
- [28] M. Marya and S. Marya. 'Interfacial microstructures and temperatures in aluminum-copper electromagnetic pulse welds', *Sci. Technol. Weld. Joining*, 2004, 6, 541-547.
- [29] V.A. Simonov. *Building Criterion for Metals with Explosive Welding, Combustion, Explosion, and Shock Waves*. Springer New York. Vol. 21, #1. January 1991. pgs. 1221-123.
- [30] S. Schwaigerer, G. Mühlenbeck. *Festigkeitsberechnung im Dampfkessel-, Behälter- und Rohrleitungsbau*. 5., überarb. u. erw. Aufl., 1997, XII
- [31] Wilson MN, and Srivastava KD (1965), Design of efficient flux concentrators for pulsed high magnetic fields, *Rev. Sci. Instrum.* 36(8), 1096-1100.
- [32] Y.B. Kim and E.D. Platner, *Rev. Sci. Instr.* 30, 524 (1959).
- [33] B. Howland and S. Foner, *High Magnetic Fields* (M.I.T. and Wiley, 1961) p. 249.
- [34] L. Hoffman and V. Scheuing, "Transformer Coils for High Magnetic Fields," C.E.R.N. Report 63-36

3 Fatigue Studies and Materials Selection

3.1 Introduction

Bitter coils have been shown to be capable of producing fields of 260kG, repetitively. However, their life is limited to some 1000-10000 shots. Additionally, slightly higher fields can decrease the lifetime drastically.

The single-turn coil is actually preferred over the multi-turn coil to be used as a pulsed magnet for two reasons:

- a. The single turn coil is mechanically stronger, as it does not depend on the mechanical properties of the insulating materials. Therefore, a higher peak field and longer life can be expected.
- b. By shaping the inner surface of the single turn coil fields of given configuration can easily be produced.

The field intensifier combines the single-turn secondary with a multi-turn primary coil. Therefore, any desired inductance can be presented to the external circuit. However, coupling losses between the can be relatively large in comparison to the gains of focusing the magnetic pressure using the fieldshaper. We presented the design and construction of a copper fieldshaper for the MAGNEFORM EMF machine at MIT, in Chapter 2.

PULSAR uses a cable transformer in connection with a single turn coil. Experiments with this kind of setup have been performed at PULSAR, in Israel and are presented in this study, in Chapter 4.

In this chapter, Section 3.2 will present a failure study, accompanied by a metallurgical analysis, of an Aluminum Bronze compression coil sent to MIT by FORD. After studying the failure mechanisms of an EMW tool in detail, the author was able to design a repeatable setup that mimics the crack growth and propagation observed in an electromagnetic process, see Electromagnetic Fatigue, in Section 3.3. From the detailed investigation of the failed EMW coil and the Electromagnetic Fatigue studies, a materials selection of possible coil materials is presented in Section 3.4.

3.2 Failure Study of an Aluminum Bronze Bitter Coil

FORD in Detroit, MI tested an Aluminum Bronze coil with their current EMW setup. The coil is a compression coil with a rectangular inner cross-section. Holes were drilled into the corners of the inner rectangles to reduce the stress concentration points of the geometry.

The failure study was taken on two separated samples from the Aluminum Bronze Bitter coil. A summary of the parameters of the Aluminum Bronze alloy rod C63000 (AMPCOLOY 45), from which the coil was manufactured can be found in the Appendix C. Table 1 shows a summary of the EMW process variables under which the coil was operated.

Voltage [kV]	Energy [kJ]	Peak Current [kA]	First Wave Pulse Time [μs]
15	40	800	40

Table 1: Parameters recorded during the EMW operation using the Aluminum Bronze Bitter coil at FORD, Detroit, MI.

The coil was manufactured in 2002, had 6 operating windings and a working zone of 53 mm. Figure 1 shows the first part of the fractured Aluminum Bronze Bitter coil, called Specimen I. It can be observed that the forces during the process pried the coil open and the remaining plastic deformation is still visible. Furthermore, cracks formed in the corners of the inner rectangular geometry. The cracks are longer in the middle of the axial length of the coil and have caused the coil to fracture in two parts at winding “Nr. 4”.

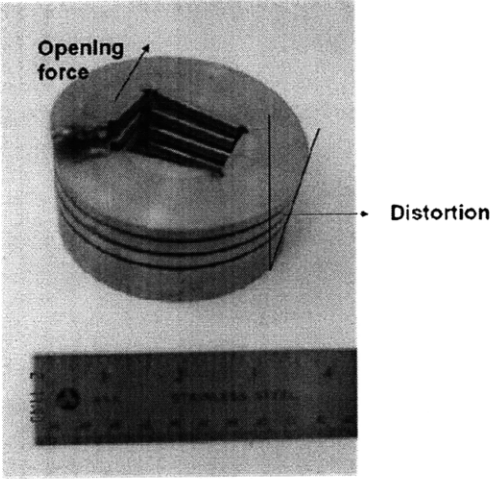


Figure 1: Digital photograph of specimen I, which was taken from the Aluminum Bronze Bitter coil. The direction of the “opening force” and the approximate angle of further distortion are shown.

The top part, which broke off the coil was named Specimen II. Figure 2 shows specimen II photographed from the side. Specimen II consists of one almost complete winding.

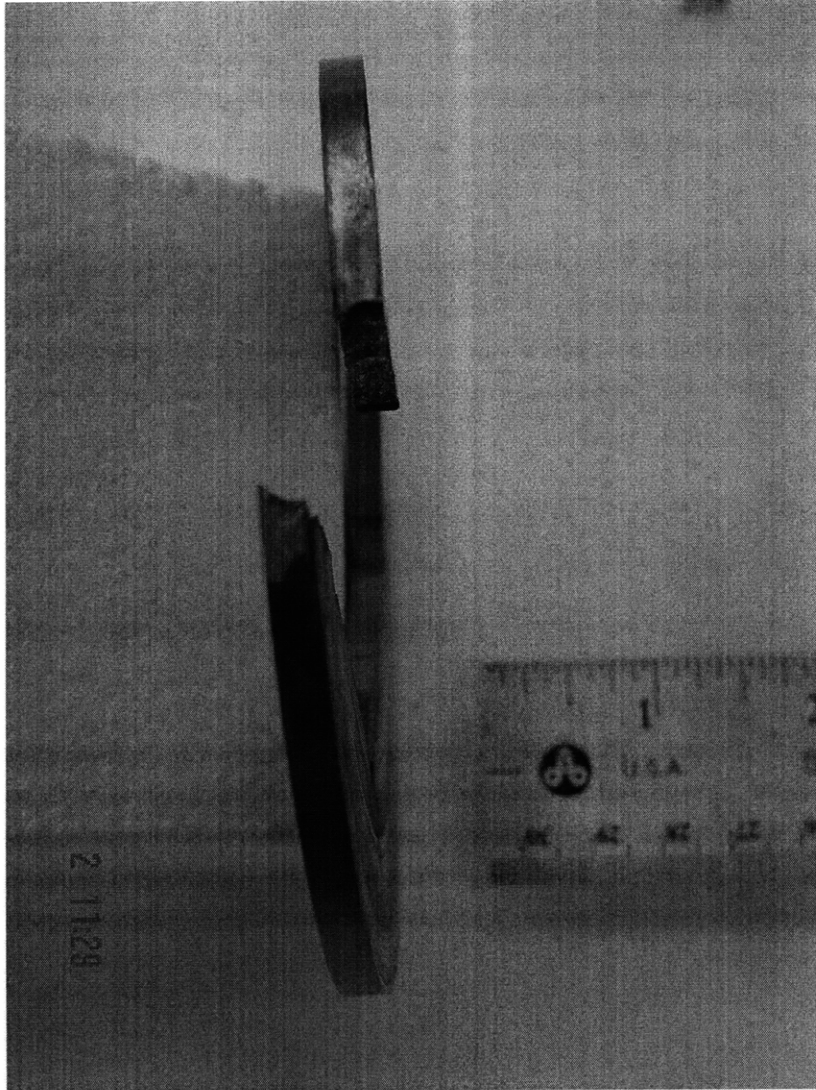


Figure 2: Digital photograph of specimen II. Specimen II is the fractured off upper part of the Aluminum Bronze Bitter coil.

The cracks were named in clockwise order. Figure 3 shows the map of cracks for Specimen I, as well as a close-up view of one of the corners of the inner rectangular geometry. Figure 4 shows the map of cracks for Specimen II, as well as a close-up view of one of the corners of the inner rectangular geometry.

The close-up views reveal a so called *Zig-Zag* geometry of the cracks. Optical microscopy was performed to get a more detailed view of this geometry, as well as of the crack interfaces.

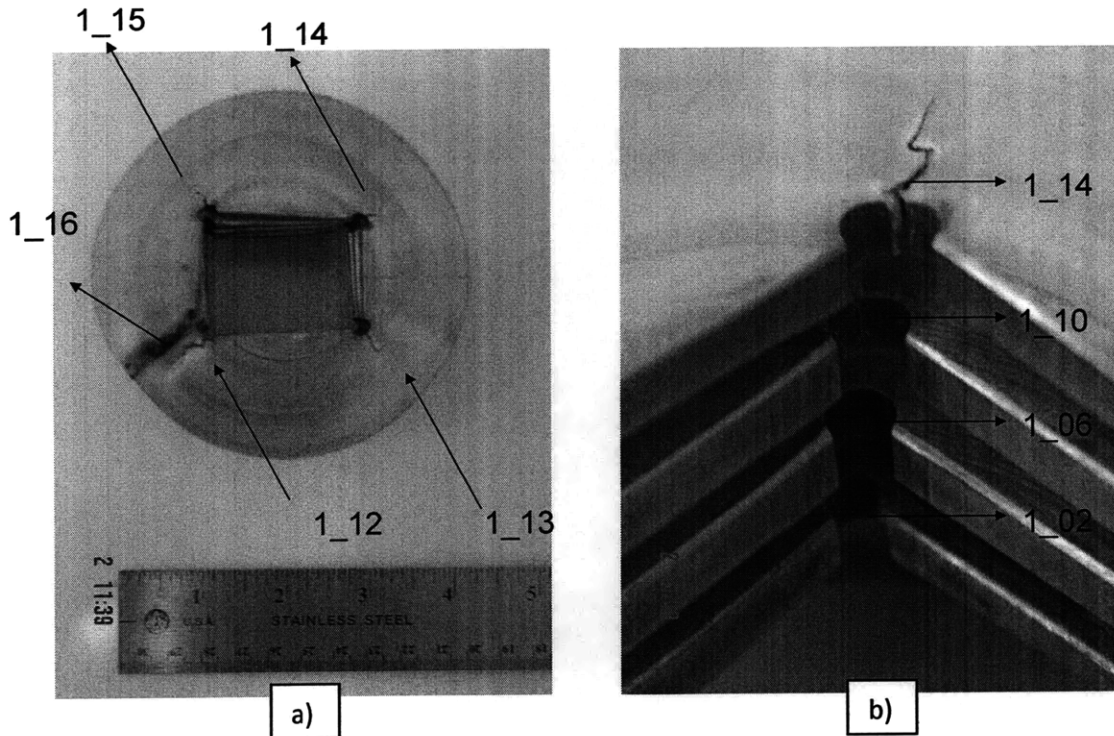


Figure 3: a) Crack map of Specimen I. Crack name: Specimen number_crack number.
 b) Upper right corner of inner rectangular geometry.

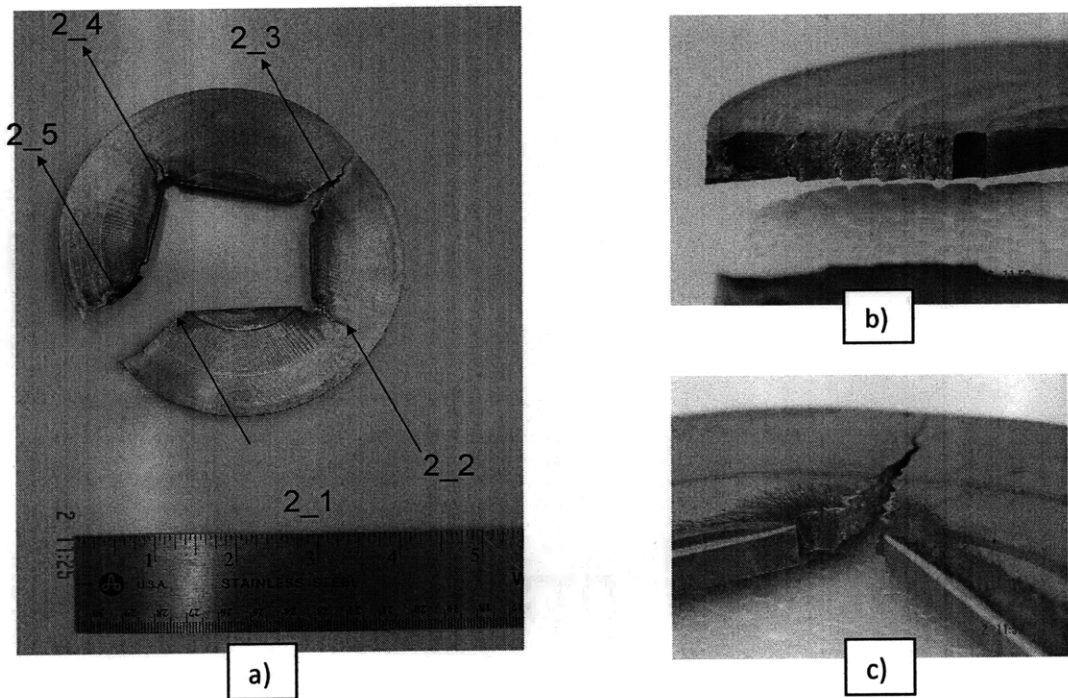


Figure 4: a) Crack map of Specimen II. Crack name: Specimen number_crack number.
 b) Close-up view of crack 2_5.
 c) Close-up view of crack 2_3.

3.2.1 A Priori Calculations

As introduced in Chapter 1, because this is an AC current operating at a high frequency, the current only penetrates to a small skin depth:

$$\delta = \sqrt{\frac{2\rho_e}{\mu\omega_d}}, \quad 3.1$$

where ρ_e is the electrical resistivity, ω is the angular frequency and $\mu = \mu_0 \times \mu_r$, where μ_0 is $4\pi \times 10^{-7}$ H/m and μ_r is the magnetic permeability of the material. This so called skin effect increases the resistance because the current has less area to flow through. Furthermore, the Joule Heating of the coil material will only occur at this skin depth. Figure 5 shows a schematic of how the current could penetrate only to a certain skin depth, in the case of the Aluminum Bronze coil:

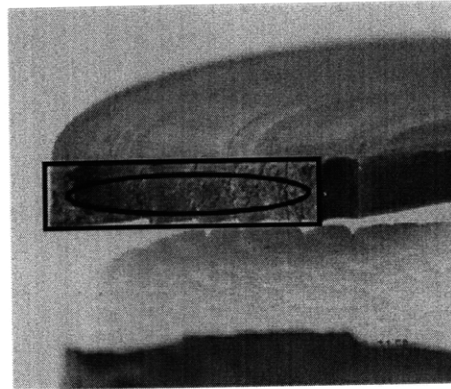


Figure 5: Cross-Section of the Aluminum Bronze Coil turn, looking at the crack interface. The area between the ellipse and the rectangle is approximately the area, where current flows.

Table 2 shows a summary of skin depth calculations made for different metallic materials.

	Relative Permeability μ_r	Permeability μ	Resistivity (micro ohm cm)	Skin Depth (mm)
Cobalt	245	3.08E-04	6.24	0.036
Nickel	1240	1.56E-03	6.4	0.016
Aluminum-Bronze	1.6	2.01E-06	1.44	0.214
Copper (pure)	1	1.26E-06	1.7	0.293
Steel	701	8.81E-04	24.8	0.042

Table 2: Different skin depths calculated for a variety of metallic materials (f = 50 kHz) [1-3].

Table 2 represents the magnetic properties of the material selection after intense research in the literature. Magnetic properties are very unique to certain materials and especially to the materials properties, such as grain size, texture and further properties [6]. The theoretical skin depth that is calculated for an Aluminum Bronze alloy at the frequency (pulse duration = 40 μ s) used for the EMW process at FORD, in Detroit is on the order of 0.3 mm.

3.2.2 Optical Microscopy (OM)

The OM was performed with the Binocular Microscope available at the MIT Welding and Joining Laboratory. Figure 6 shows a series of photographs of crack 2_3 (Specimen II, crack 3).

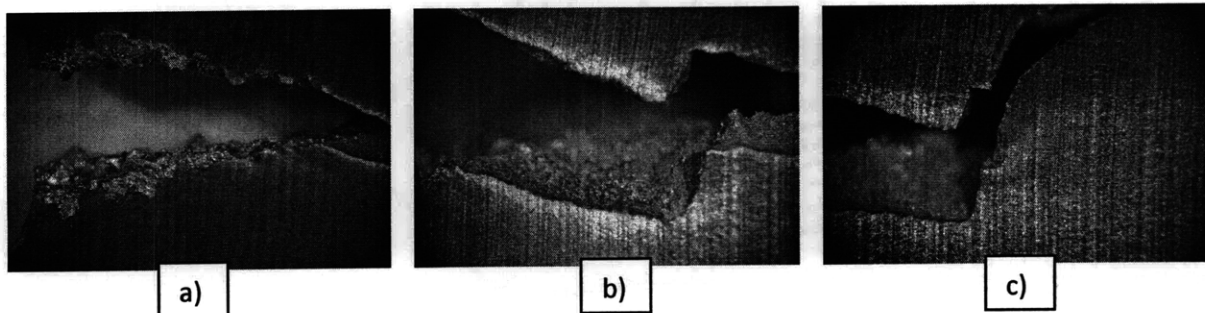


Figure 6: Series of digital photographs taken along crack 2_3 (Specimen II, 3rd Crack).

- a) Opening of the Crack showing molten surface on the sides of the crack interfaces.
- b) and c) Brittle crack interfaces resulting in shiny areas of the revealed metal surface.

The crack seems to have propagated in a brittle manner due to the observation of shiny surfaces on the crack interfaces. Furthermore, molten metal is observed over the distance of the crack length and especially at the crack opening. A close-up of the molten metal that splattered onto the sides of the crack interfaces is shown in Figure 7. Further zooming in, shows oxides in the molten Aluminum Bronze alloy.

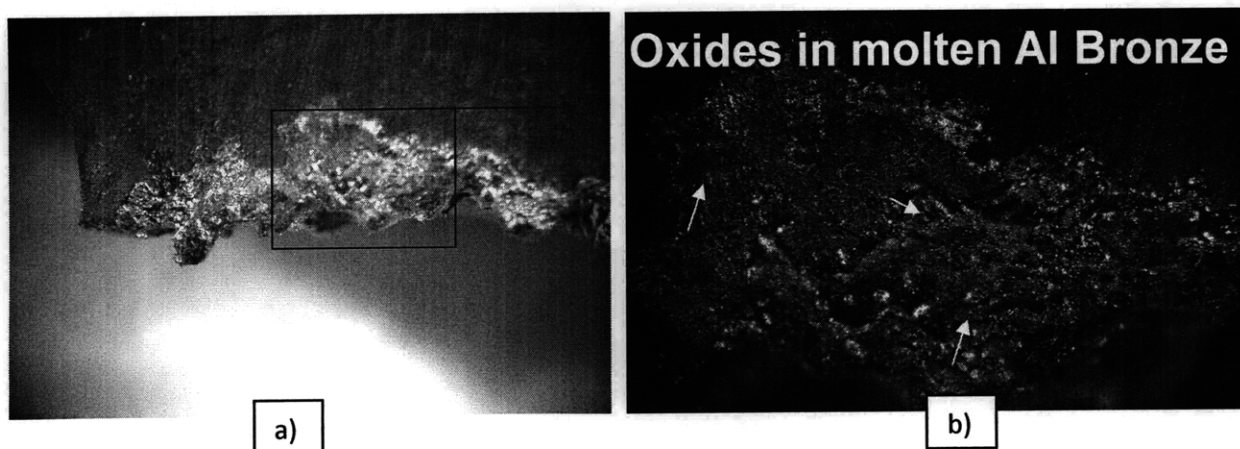


Figure 7: a) Molten surface that splattered onto the sides of the upper crack interface at the opening of crack 2_3. The red box shows the zoomed in area of Figure 6b.
b) Oxides are revealed in the molten Aluminum Bronze alloy.

3.2.3 Metallurgical Analysis

To study the effects of the thermal heating and due to the eddy currents and the arcing at the crack surfaces, a metallurgical analysis was performed.

Specimens

Crack 4 of Specimen II (2_4) was cut from Specimen II, embedded, polished and etched with 70 mL H₂O + 5g Fe(NO₃)₃ + 25 mL HCl for 20 seconds, which is a general purpose grain contrast etch for Cu and alloys and (produces a flat etch for some alloys).

Optical Microscopy

Figure 8 shows a digital photograph of the investigated section of the coil, as well an Optical Microscopy image with 5x magnification of the etched surface of crack 2_4:

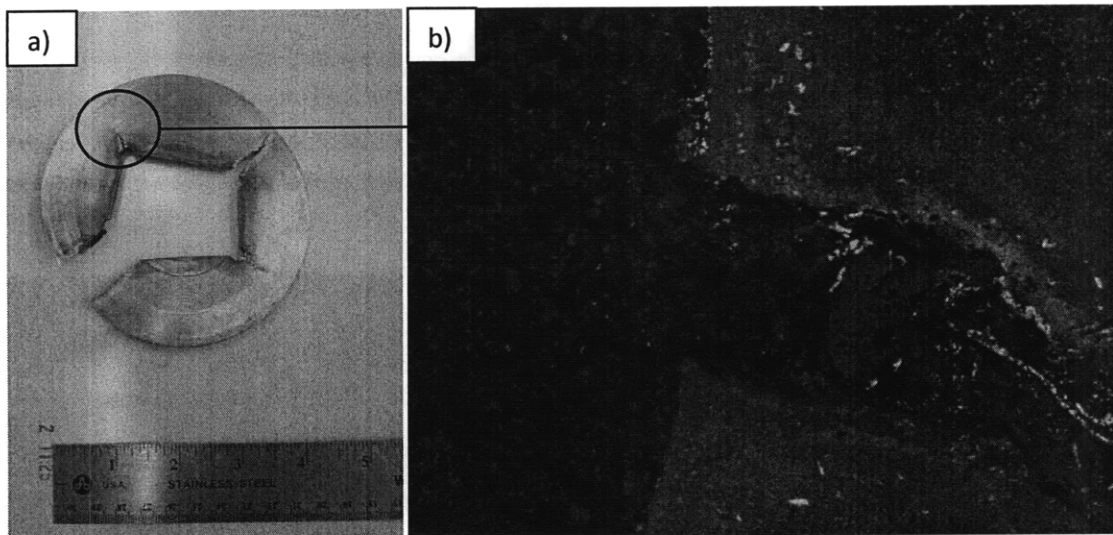


Figure 8: a) Top view of Specimen II. The black circle marks the approximate volume which was used for the metallurgical analysis.

b) Digital Photograph of the crack opening. The black area surrounding the multicolored metal is the embedding material of the microscopy specimen.

Detailed metallurgical analysis was performed on the upper interface of the crack right at the corner of the inner rectangular geometry. Figure 9 summarizes these results.

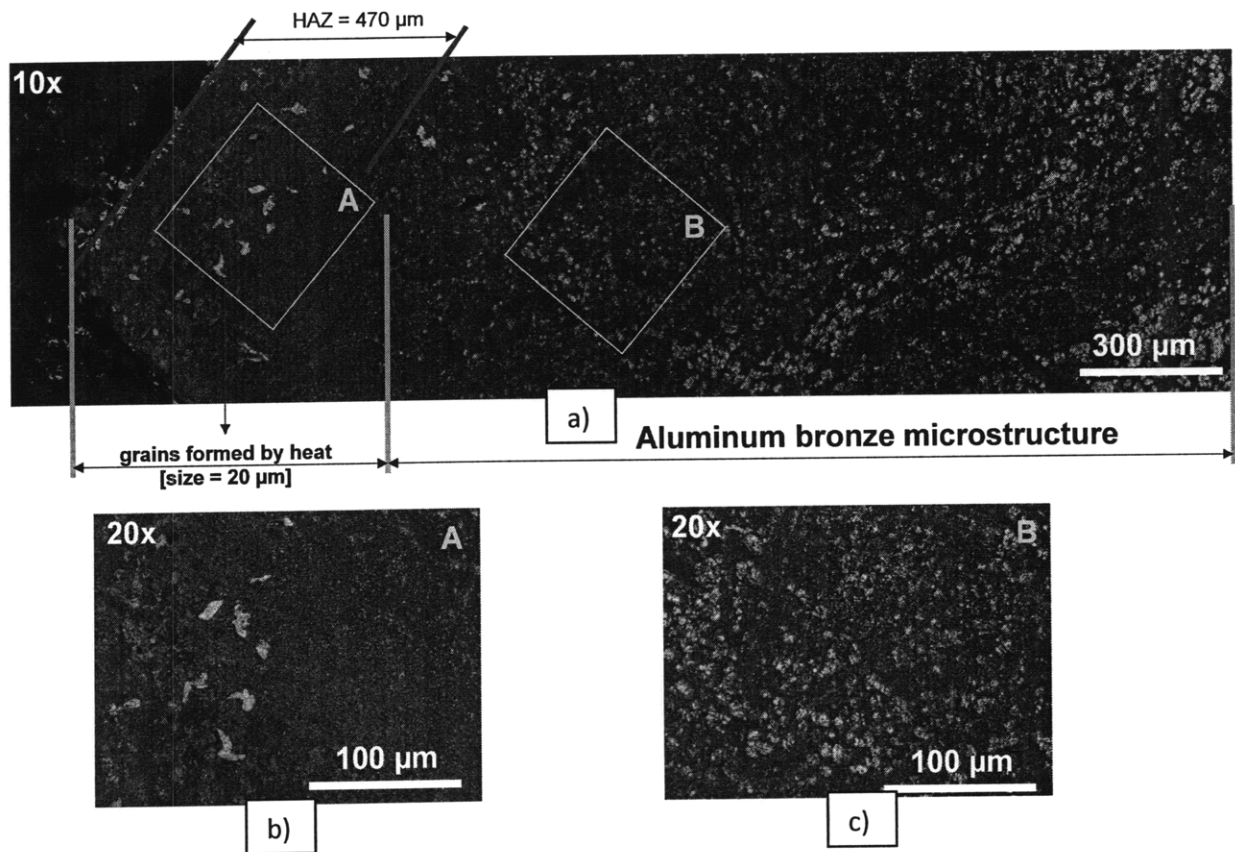


Figure 9: a) Summary of the metallurgical analysis of the Aluminum Bronze alloy at the corner of the inner rectangular geometry of the coil and the upper interface of the crack. The HAZ is marked by the red lines and measures a depth of approximately 470 micrometers
 b) Close-up view of Area A marked with a yellow box in Figure a), showing the grains that formed due to the heat-treatment in the HAZ.
 c) Close-up view of area B marked with a yellow box in Figure b), showing the typical Aluminum bronze microstructure.

It was possible to reveal the “heat-affected zone (HAZ)” that is caused by eddy currents. Furthermore, it was possible to observe grains that formed in the HAZ due to the thermal cycles. Further away from the coil surface, the normal Aluminum Bronze alloy microstructure could be observed. The HAZ has a depth of 470 micrometers, which is close to the theoretical skin depth (approximately 0.2 mm for Aluminum Bronze, see Table 2) at the calculated pulse frequency of 50 kHz (see Equ. 3.1 for the calculation of the skin depth). The remaining HAZ was created by the diffusion of the heat into the material. The grains that formed due to the heat treatment in the HAZ have an approximate size of 20 micrometers.

3.2.4 Discussion

Many factors play into the formation of the observed cracks, which are partially due to the high stresses that build up in the corners of the inner rectangular geometry, as well as the heating of the material due to the eddy currents that run along the surface. The high stresses in the corners can even be magnified by a proposed magnetic force that is created, just like in the EMW process due to opposing currents, which run along the crack interfaces. Furthermore, there is the possibility of arcing between the crack interfaces. The crack formation can be divided into four stages:

Stage I:

a) The compression force that is acting on the workpiece also acts in the opposing direction on the coil, thereby expanding the coil, which causes large stress concentration on the inner surface of the coil. These stress concentrations are magnified in the corners of the inner rectangular geometry. This harsh loading pattern can cause a crack to initiate on the inner surface of the coil.

b) The eddy currents heat up the surface of the coil. As introduced in Chapter 1 the Joule Heat can be calculated by

$$E_J = \int_0^t I^2 R dt \quad 3.2$$

Due to the difficulty of the geometry of the coil, we will not calculate its inductance. Instead we measured it at its usage frequency of 50 kHz, given by the current curve calculated in Chapter 2. The measured inductance of the fractured coil was 1 μH and was extrapolated for the entire coil (before fracture it had 6 turns and was longer) to be 1.25 μH . Now, as we know the input voltage and the inductance, as well as the resistance of the coil, which measured at its usage frequency is 0.017 Ω , we can calculate the current curve with the presented coil attached to the EMW machine at FORD, in Detroit. Now squaring the current curve and multiplying it with the resistance R of the circuit (including the coil) we get a Joule heat E_J of 34 kJ, after a time t of 500 μs . Now, using

$$\Delta T = \frac{E_J}{c_p m} \quad 3.3$$

where $c_p = 400 \text{ J/KgK}$ is the specific heat and m is the heated mass due to the skin effect of the AC current of the Aluminum Bronze alloy, respectively. Therefore, we can calculate the rise in temperature due to Joule Heating caused by the eddy currents in the calculated skin depth of the Aluminum Bronze Bitter coil to be $\Delta T \sim 291\text{K}$ (see Appendix C for the detailed MATLAB results).

This is the temperature along the inner sides of the Bitter coil. Taking into account the current and heat concentration at the corner of the inner rectangular shape of the Aluminum Bronze Bitter coil is far more complicated.

An ABAQUS model to study the behavior of cracks in electromagnetic applications is presented in Section 3.3.3. The model is also capable of calculating the heat at the surface caused by eddy currents and certainly takes into account the concentration of heat due to any kind of geometry.

Stage II:

The formation of a surface defect or even a crack is absolutely detrimental for the life of the tool:

a) Arcing: As soon as the defect is large enough, the current has the possibility to jump across the crack instead of following the outline of the defect and thereby causing a large electrical discharge right at the position of the defect.

b) The Stage I force is still acting and opens the crack further with every pulse.

c) The arcing, as well as the eddy currents, which are now confined around the small volume of the defect cause the metal to heat up very quickly and even melt, as well as causing large thermal stresses (see Section 3.3.3).

Stage III:

This Stage is believed to be happening at the same time as Stage I and Stage II, depending on the present defect size: If there are cracks or surface defects present, the currents need to run along the upper crack surface and return along the lower crack surface. Thereby, the two opposing currents create a Lorentz force. Now, this magnetic force pulls the crack apart even further. We can quantify this force and calculate the critical defect size, depending on the material's fracture toughness:

The magnetic field of an infinitely long straight wire with radius r can be obtained by applying Ampere's law. The expression for the magnetic field is

$$B = \frac{\mu_0 I}{2\pi b},$$

3.4

Where b is the distance between the wires and in our case the distance between the crack surfaces or the so-called crack opening. The force on a length Δl of a wire is

$$F = I\Delta l B \tag{3.5}$$

which setting $\Delta l = a$ (length = crack length) gives a force in terms of the current

$$F = \frac{\mu_0 I^2 a}{2\pi b} \tag{3.6}$$

For the case $a = b$ (crack length = crack opening) we get

$$F = 2 \cdot 10^{-7} I^2 \tag{3.7}$$

In the case of $a = b$, a peak current of 800 kA yields a force of 128 kN.

Aluminum Bronze has a fracture toughness K_c between 26 MPa.m^{1/2} and 68 MPa.m^{1/2} and a tensile strength between 52 ksi and 116 ksi.

The stress intensity factor can be calculated by using

$$K = \sigma \sqrt{\pi a} \tag{3.8}$$

where σ is the stress. If $K > K_c$ the crack will propagate. In our case $\sigma = 128 \text{ kN} / (\text{remaining coil width} \cdot \text{coil thickness})$, which for a remaining coil width of approximately 0.043 m (crack length of 1mm) and a coil thickness of 0.005 m yields a stress of 595 MPa and a K of 33 MPa.m^{1/2}, which is already larger than the minimum K_c .

The calculations above have been calculated for a ratio of $a/b=1$. For a ratio of $a/b=2$ cracks of lengths between 0.2 mm and 1 mm will propagate. For a ratio of $a/b=3$ cracks of lengths between 0.08mm and 0.5 mm will already propagate. So for a crack length of 80 μm and a crack opening of 80/3 μm cracks will propagate due to the magnetic force created between the crack surfaces.

Now taking into account that the current will only follow the crack shape if the skin depth is on the order of the length of the crack, we can summarize that Stage III occurs as soon as the crack-length is larger than the skin depth. Therefore, looking at Table 2, we can see that the minimal crack length, for Stage III to occur, for Aluminum Bronze is on the order of 200 μm . The minimal crack length for Steel is on the order of 40 μm .

With regards to the presented analysis one can finally get the following so-called magnetic stress intensity factor

$$K_{m,c} = \frac{\mu_0}{2\pi A} I^2 \sqrt{\pi a_c}$$

3.9

Where A is the remaining cross-sectional area and a_c is the critical crack length. When $a_c >$ skin depth δ Stage III of crack propagation is observed, if $K_{m,c}$ is $>$ K_c .

Stage IV:

The heat from the arcing and the eddy currents causes the material to expand and go into compression. Stage IV happens during the cool down of the material, which now encounters high tensile stresses that cause the crack to propagate, which is a so called thermal fatigue crack.

The thermal expansion coefficient for Aluminum Bronze is 9.5 /Fahrenheit. With a temperature rise of 291 K a strain of 0.0030 is created, which multiplied with the elastic modulus of the alloy ($18 \cdot 10^6$ psi) yields a stress of 54191 psi or 374 MPa. Certainly, far higher pressures are observed in the corners of the inside of the discussed Bitter coil. The ABAQUS model, presented in Section 3.3.3 can calculate these pressures, in future studies.

Figure 8 summarizes the crack propagation mechanisms of Stage I, Stage II and Stage III. Figure 9 shows an OM photograph of the complete crack 1_13, as well as a summary of the physical effects taking place during the EMW process (except for Stage IV).

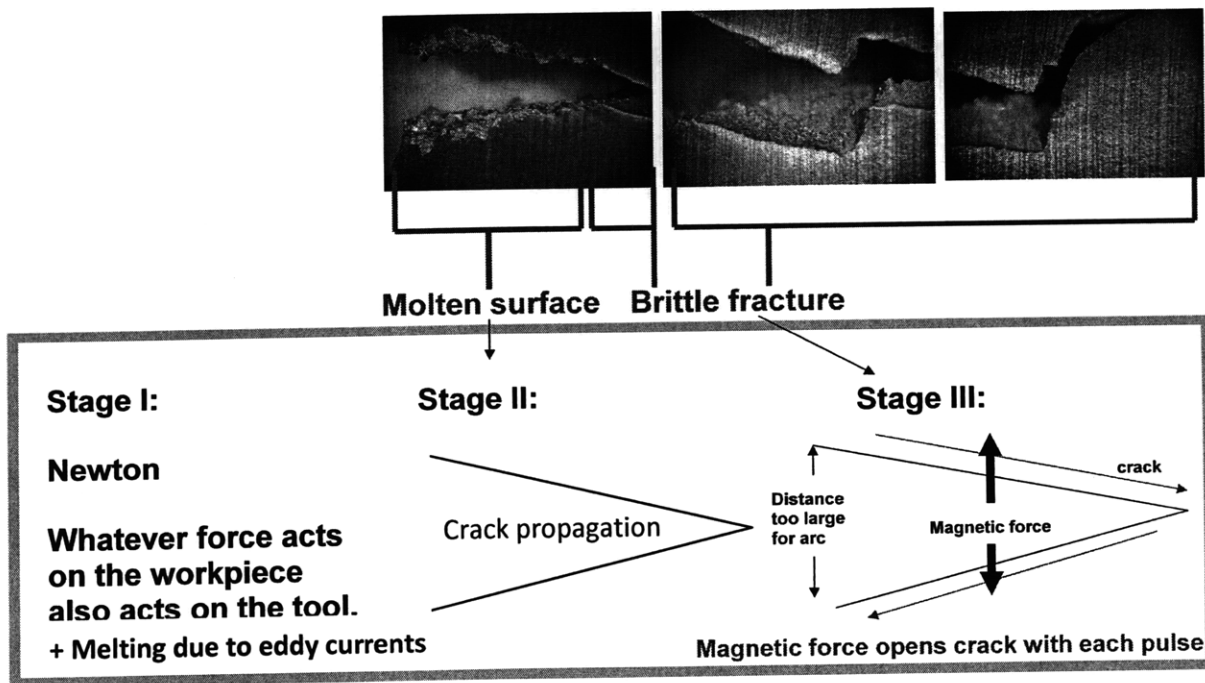


Figure 8: Summary of crack propagation effects during Stage I, Stage II and Stage III.

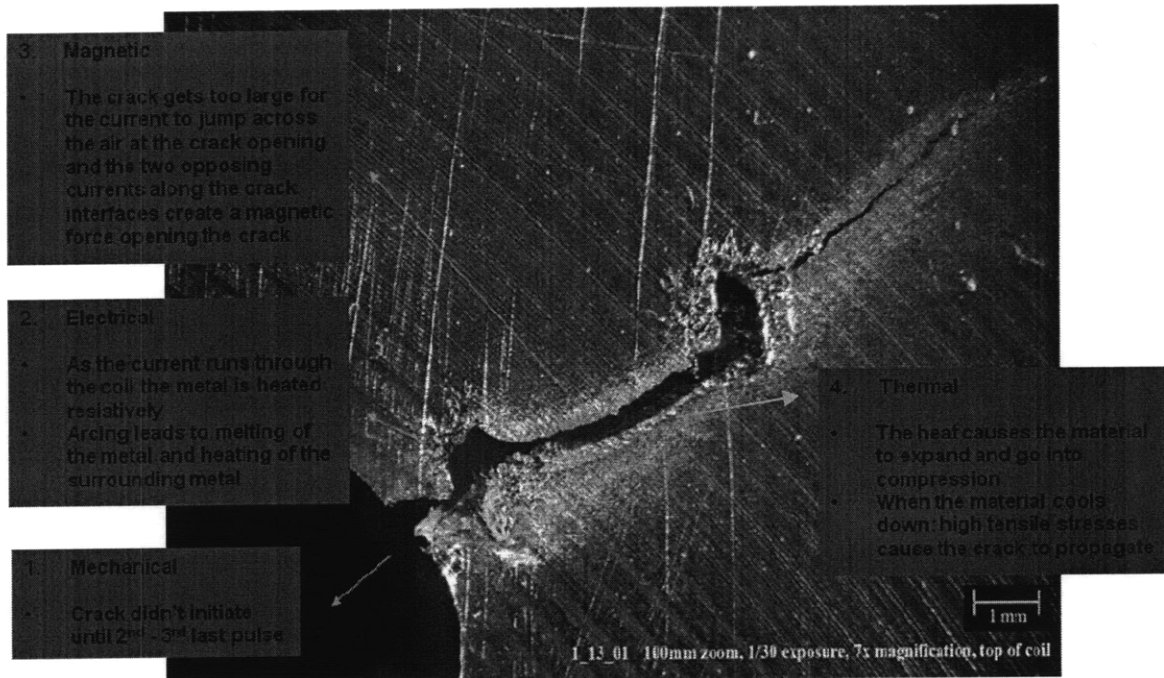


Figure 9: Digital Photograph of crack 1_13 (Specimen I, crack 13).

The design team wanted to lower these mechanical stress concentrations by drilling a hole shape into the corners of the coil, which is a good start to lower the mechanical stress concentration. However, drilling a hole into the corner of inside outline of the coil creates a Stage III scenario, as described above. Therefore, although the mechanical stress concentration is lowered, the electromagnetic stress concentration is enlarged and could be detrimental during each pulse, leading to crack initiation and propagation depending on the critical defect size.

Therefore, rather rounding the corners would have been a much better design choice for the inside of the coil. The magnetic field concentration would have been lowered in the corners, the mechanical stress concentration would have been lowered and the remaining coil cross section would have been maximized.

This will be supported by the following chapter, where we study the observed fatigue behavior of the coil and the crack formation in further detail. We call the observed behavior of the crack Electromagnetic Fatigue (EMFA).

3.3 Electromagnetic Fatigue (EMFA) or Fracture

As observed and studied in detail, by performing optical microscopy and a detailed metallurgical analysis of a failed Aluminum Bronze EMF bitter coil, one can see that many factors play into the formation of cracks in the coil during the electromagnetic process. We call the behavior of the cracks and their propagation Electromagnetic Fatigue (EMFA).

We thought, as in many other fields, it would be fundamental to study the crack formation in further detail and create a repeatable setup to observe the formation of the cracks. Thereby, one could not only study the crack formation, but also prevent it from happening through careful design of the areas of stress concentrations or other causes, such as electrical arcing and heating at defects and surfaces, respectively, that cause the coil to fail.

Materials

Three different specimens were used in our experiments: Aluminum cans were used again in preliminary EMFA tests. Aluminum cans are made of 3 different alloys. The tab and the top are made of Tab: AA5052 (Al-2.5%Mg) and AA5182 (Al-4.5%Mg), respectively, due to reasons of mechanical strength. The body is made of AA3004 (Al-1.2%Mg-1.0%Mn), which has good formability. Thereby, we had a readily available source of an Aluminum alloy. Therefore, for the first set of specimens, the material tested was the Aluminum alloy AA3004 and the tubes had an outer diameter of 2.6" and a wall thickness of 0.0047".

The next tests were performed on a high performance Aluminum alloy, Extra-Strength Aircraft-Grade Aluminum (Alloy 2024). Two kinds of specimens were tested, named Tube I and Tube II. Tube I had an outside diameter of 2.5" and a wall thickness of 0.065". Tube II had an outside diameter of 1.5" and a wall thickness of 0.035". The chosen tubing represented the thinnest wall thickness, as well as largest diameter available on the market. These dimensions were chosen, because they represent weaker mechanical strength, as when the ratio of diameter over thickness goes up, the mechanical strength of the tube decreases (this causes a decrease in P_y ; see also Chapter 1, Deformation theory).

Furthermore, a larger diameter is desirable because as the workpiece is closer to the inner surface of the coil the coupling of the opposing currents is enhanced. Further properties of the tested materials are summarized in the Appendix. Figure 12 shows a digital photograph of all sample specimens:



Figure 12: Digital Photograph of the EMFA specimens. From left to right: The preliminary Aluminum alloy specimen (AA3004) and the two Extra-Strength Aircraft-Grade Aluminum (Alloy 2024) specimens Tube I and Tube II.

Experiment

Trying to understand the mechanism of the EMFA crack growth in more detail the author went a step further and created a repeatable setup to study the formation of the same cracks observed in the compression coil.

To cause a repeatable setup of a crack opening due to the magnetic force that is created between crack interfaces, a “crack” was cut along the side of the tubular specimens. Then the tube was placed inside the MAGNEFORM machine EMF coil and an EMF shot was fired. Therefore, when the current was induced on the surfaces of the tube and it circulated around the tube circumference it needed to run down the crack length to the crack tip and run back on the other side of the crack interface.

With this setup a similar behavior is caused as observed in the mechanical theory of crack propagation, where the crack grows due to a stress concentration, because the force lines need to run along the crack interface and are concentrated at the crack tip. In the case of EMFA, however, we encounter a current concentration, as well as an electromagnetic force that is pulling the crack interfaces apart. Furthermore, if the crack is long enough, thereby increasing the amount of current, and the crack tip is too sharp the current concentration is released by causing an electronic arc right at the crack tip.

This brings a total new look upon the study of EMF and EMW tool life, as now much detail is needed to focus on a low stress concentration design, which, as we will show, already starts with the elimination of surface defects and even surface roughness.

For the specimens Tube I and II, again cracks were cut along the axial direction of the workpiece. Figure 13 shows an example of one of the samples that were then placed inside the MAGNEFORM EMF coil:

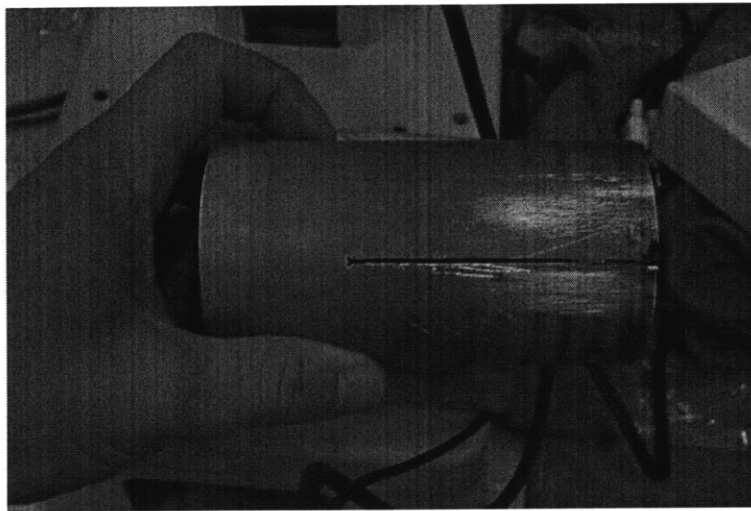


Figure 13: EMFA specimen of Tube 1 (crack length: 3", crack width: 1mm).

Furthermore, the upper ends of the crack needed to be taped to prevent arcing, so the current would run down the crack-interface, without already arcing on the top.

Results

The cut Aluminum cans were used for the preliminary EMFA tests. The tubular workpiece was mounted inside the coil with an artificial crack cut along the side parallel to the tubular axis. After the EMF process cracks were found that are similar in appearance to the *Zig-zag cracks* found at the stress concentrations of the broken Aluminum Bronze coil. A *Zig-Zag crack* produced by EMFA is shown in Figure 14.

Zig-zag cracks have also been reported in the literature by Forsyth (1962). He described the crack as a result of a single slip mechanism, also termed *Stage I crack*. When the zone of plastic deformation surrounding the crack tip, as well as the crack itself are confined within a few grain diameters, crack growth appears to be the result of single shear. This single shear takes place in the direction of the primary slip system [4].

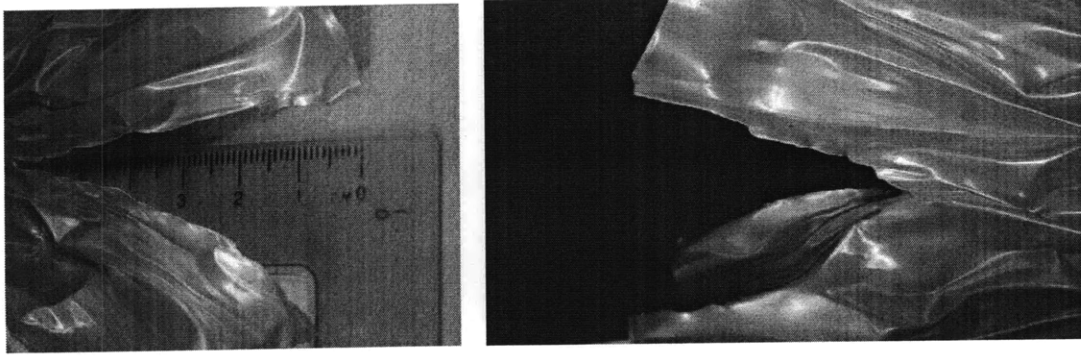


Figure 14: Two digital photographs of *Zig-Zag cracks* of the tubular aluminum alloy AA3004 workpiece that was tested in the preliminary EMFA experiments.

For the case of the AA3004 tubes the crack length was probably not long enough for arcing to occur at the crack tip. Furthermore, in this case, the deformation of the tube is the primary source of the crack opening due to the weak mechanical strength of the tubes.

For the stronger tubes I and II, the crack did not open and the eddy current created in the workpiece needed to run down the length of the precut crack interface making a sudden turn at the crack tip. This sudden turn of direction around the small radius of the crack tip instead causes an electrical discharge due to the current taking the simpler path across the air.

Figure 15 shows the results of the EMFA study for one of the Tube I specimens after 1, 3, 6, and 10 firings in the MAGNEFORMER machine at MIT. It can be seen that after one firing the current concentration heated the corner material to a temperature higher than the melting temperature. Interestingly, the created gaps form the exact shape that is also predicted for the plastic zone shape of a mechanical crack growth during plain strain loading [4]. This observation will be studied in further detail in the discussion.

After two subsequent firing, each of the two gaps formed created two further gaps, where melting occurred. After three further firings, more gaps are observed and the gaps are connected by small cracks, which come from thermal cracking after the electromagnetic process and the melting of the material.

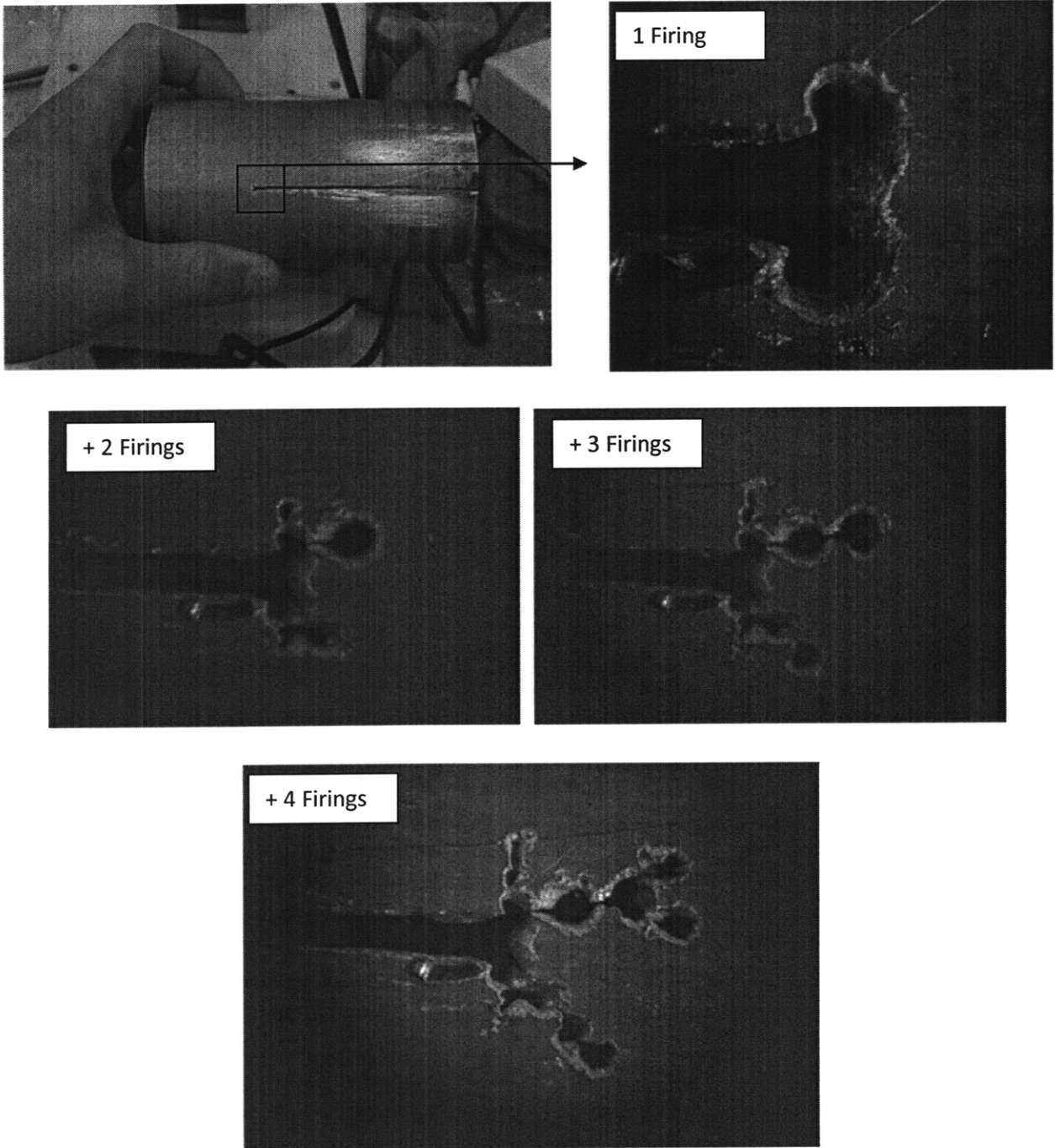


Figure 15: Summary of the EMFA experiment for one of the Tube I specimens. Crack length: 3"; Crack width: 1 mm.

We do not believe that the gaps created at the crack tip corners are from an electrical arc, because if the arc discharged, it would have to discharge at one corner, go back into the material and then discharge again at the next corner, which is highly unlikely and would not produce the two circular gaps at the crack tip corners, but rather one circular gap at the crack tip.

In the next sub-chapter we describe two ways which show design solutions to possibly overcome the problem that is caused by arcing at small defects during the electromagnetic process. After that, we show a High Speed Video Analysis of the EMFA experiments.

In the following discussion, at the end of this section we will present a summary of our observation as well as a MATLAB study of the current concentration pattern around the crack tip.

3.3.1 Design Changes of the Crack tip to weaken EMFA Effects

Having found in the fatigue study of the Aluminum Bronze bitter coil that the crack formation goes through several stages and is affected by several physical parameters, we altered the design of the crack in two ways

1. Lowering the stress concentration

The crack tip was rounded, by cutting a hole at the center of the crack tip, with a radius of approximately 3 mm (similar to the given radius for the corners of the inner rectangular geometry of the Aluminum Bronze compression coil from FORD). Figure 16 shows a Tube I specimen with a rounded crack tip, as well as a photograph of the crack tip after two pulses:

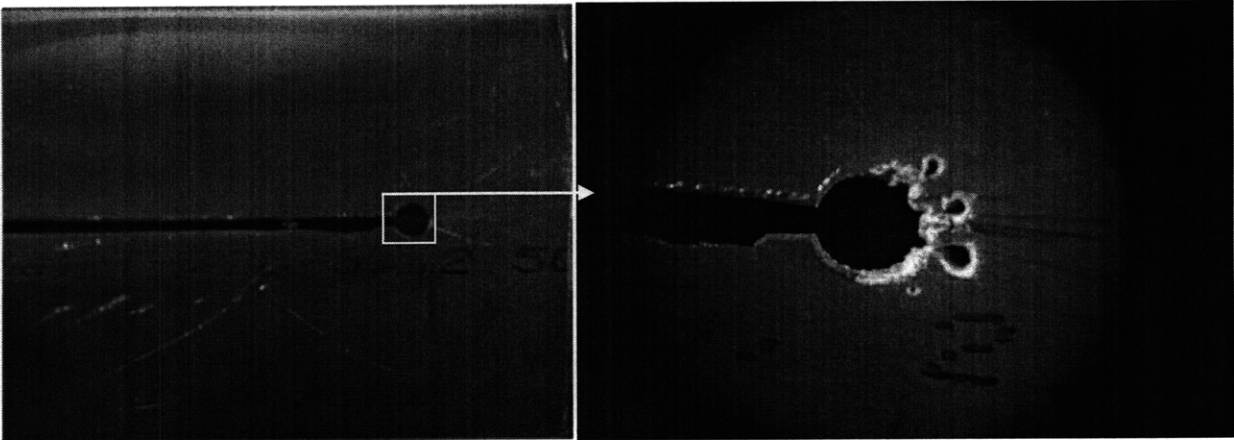


Figure 16: Summary of the EMFA experiment for one of the Tube I specimens, where a round circle was introduced instead of the crack tip (Crack length: 3.75", Crack width: 1 mm).

It can be seen that the first shot caused three small crack initiations, which must have occurred due to the surface roughness of the hole. In addition to that plain resistive heating and melting is observed again, as the second shot is followed by a crack leading into a gap as observed before for the other

experiments. Again, we observe all stages of cracking for an electromagnetic process as described before, in Section 3.2.4.

2. Insulation of the crack tip

The crack tip was covered with an insulating material, in this case cyanoacrylate, to prevent a possible electrical discharge across the air from one crack interface to the other. Figure 17 shows a Tube I specimen with an insulated crack tip after the first shot:

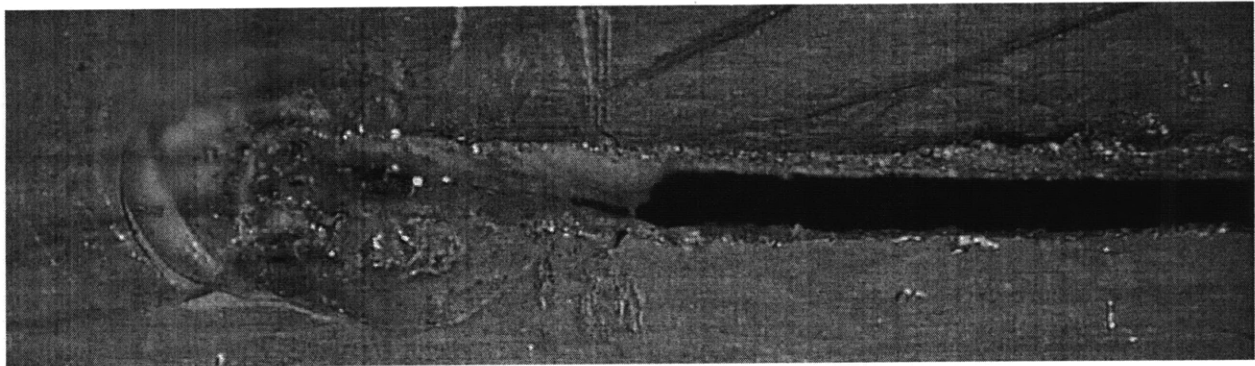


Figure 17: EMFA experiment of one of the Tube I specimens, where the crack tip was insulated with cyanoacrylate (Crack length: 3", Crack width: 1mm).

It can be seen that the cyanoacrylate cracked and it is unclear if it cracked all the way to the crack tip. Signs of an electrical discharge or melting are found, which means that the cyanoacrylate could have cracked all the way to the crack tip. However, after the melting took place the cyanoacrylate could have melted back into place at the crack tip.

We can conclude that the design steps towards preventing the crack initiation and propagation have not been effective. Furthermore, studying the design change shown in Figure 16, we can most certainly say that Stage III cracking will be enforced due to this design. The current needs to run around the circumference of the drilled hole and a concentration of flux will be created inside the hole, which was intended to lower the stress concentration. However, drilling the hole only worsens the situation, because now the remaining cross-section of the EMFA specimen or the coil is lowered and Stage III cracking will occur. Therefore, drilling a hole into the inside corners of the Aluminum Bronze Bitter coil was a bad design choice.

As stated before, rather rounding the corners than drilling a hole would have been the much better design option to lower the mechanical and electromagnetic stress concentrations, as well as enlarging the remaining cross-section of the coil.

To get better detail and a better idea of what happened during the EMFA study, we studied the cross-section of the tube during the process, using our High-Speed Video setup (described in Chapter 2).

3.3.2 High Speed Video Analysis of EMFA Experiments

The camera and lamp setup was the same as in Chapter 2. The High Speed Videos were recorded at 26,143fps, with exposure time $10\mu\text{s}$, and at a resolution of 256x256. The Nikon 50mm lens was again used, this time with an aperture f/5.6

Figure 18 shows the screenshot of the top view of the EMFA experiment recorded by the HSV setup. The video can be found on the DVD (attached).

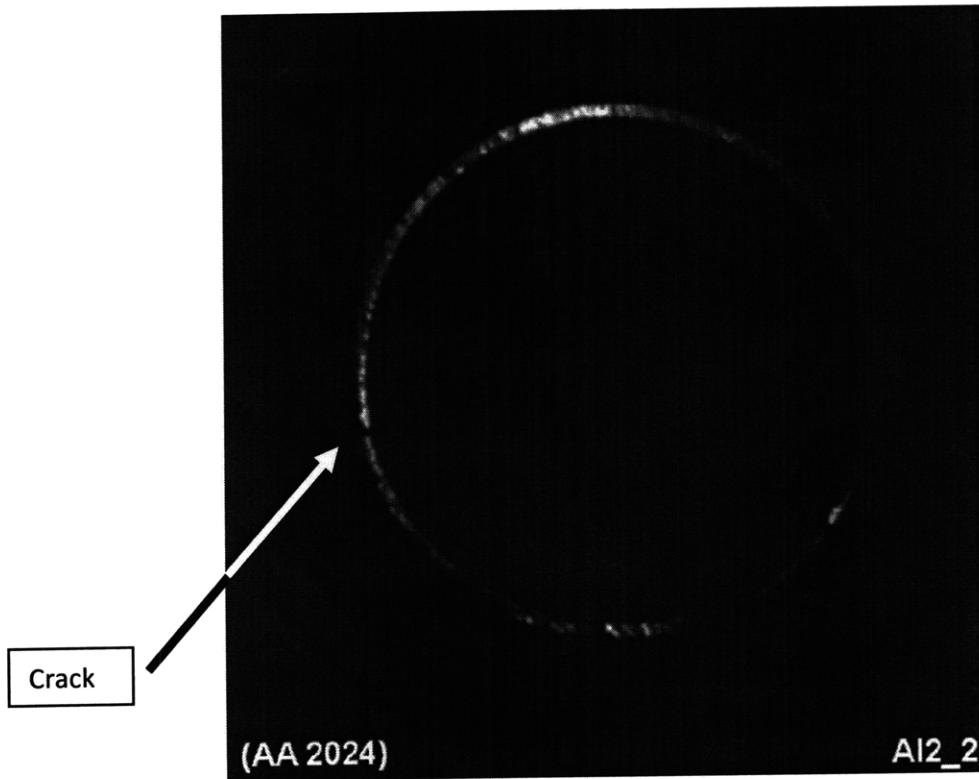


Figure 18: Screenshot from one of the HSV movies of the top view of a Tube I specimen during an EMFA experiment.

In the video, one is able to observe that the tube itself undergoes heavy, but elastic circumferential compression. Certainly, the tube also undergoes the compression forces of the coil during the EMF process, but the tube is mechanically too strong and the saw cut too narrow to be permanently deformed. Arcing is observed, which can occur due to the material surfaces touching each other, because of the circumferential compression or through the formation of an arc between the crack surfaces during the duration of the EMF pulse.

These observations compare very nicely to what has been observed for the Aluminum Bronze coil. The coil undergoes heavy stresses, but is mechanically strong enough to not be plastically deformed (until the coil broke in two, at which point residual stresses must have caused the distortion of the coil).

However, the stresses, as well as the addition of arcing, thermal heating and the electromagnetic force between the crack interfaces are constantly adding to the crack growth of defects, especially at mechanical stress and electrical current concentrations, due to bad design of the coil.

3.3.3 ABAQUS Analysis of the EMFA crack behavior

As induced current flows around the EMFA specimen, it reaches a barrier at the artificial crack, and must flow all the way around it. This means that all the current that would be flowing across the crack is forced to flow around the shape of the crack and then the tip of the crack. If the crack is long enough, there will be enough current concentrated to cause melting at the crack tip, further lengthening the crack.

Model

ABAQUS is not capable of calculating magnetic effects and calculating AC properties is tedious. Therefore a given constant surface current was used and averaged from the sinusoidal wave form that was measured during the EMFA experiment. Figure 19 shows the approximation of the discharge curve:

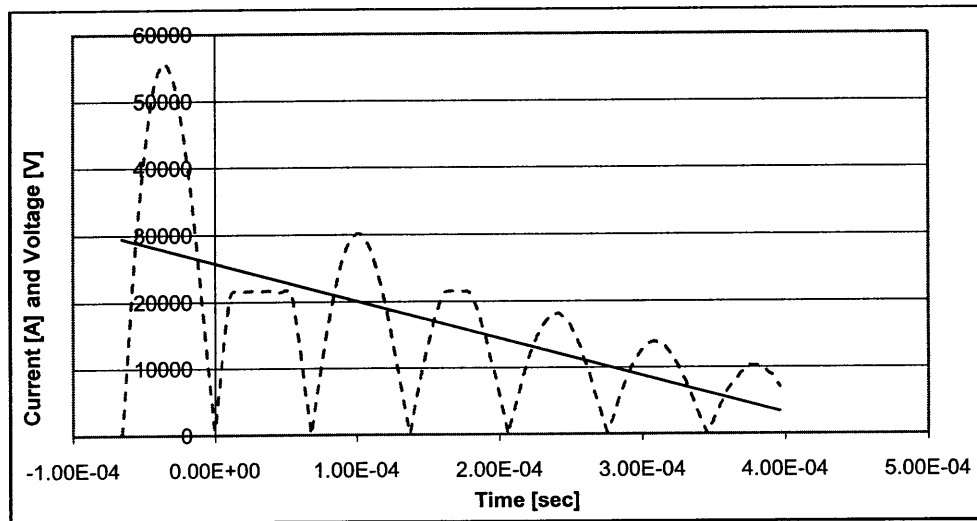


Figure 19: Approximation of the apparent discharge current (dotted line). The actual current was made positive over the entire time, as the Joule Heating is independent of the sign of the current. Furthermore, the current was averaged over the length of the measurement, giving an average current on the order of 15000 A.

From Figure 19, we can see that after squaring the actual current with an approximate average current of 15000 A over the length of the measurement, which using a coupling factor of 0.28 gives an approximate induced current of 4250 A in the workpiece, over the respective time of 450 μ s.

The coupling factor can be calculated through the following formula

$$\Psi = \sqrt{1 - \frac{L_w}{L_c}}, \quad 3.10$$

where L_w is the inductance of the coil with the workpiece inside and L_c is the inductance of the coil [8]. Having measured the coil inductance to be 25 μH , we now measured the coil inductance with the EMFA specimen inside. The new measured coil inductance L_w was 23 μH , which gives a coupling factor of 0.28.

Material

Our EMFA specimens were tubes with a certain thickness and a cut crack of a certain length. In our ABAQUA model we chose to simulate the EMFA specimen by using a plate of the same length and height that was equal to the circumference of the tube. The crack opening of 1 mm, the crack length of 80 mm and the wall-thickness of 0.65" were the same as in our EMFA specimens.

The properties for the simulated material were the same as the Al2024 for the presented EMFA experiments. Properties for the material can be found in Appendix C and [1].

Results

Figure 20 shows the ABAQUS model simulating the Joule Heating effect that is caused by the surface current running along the crack surface and turning around at the crack tip:

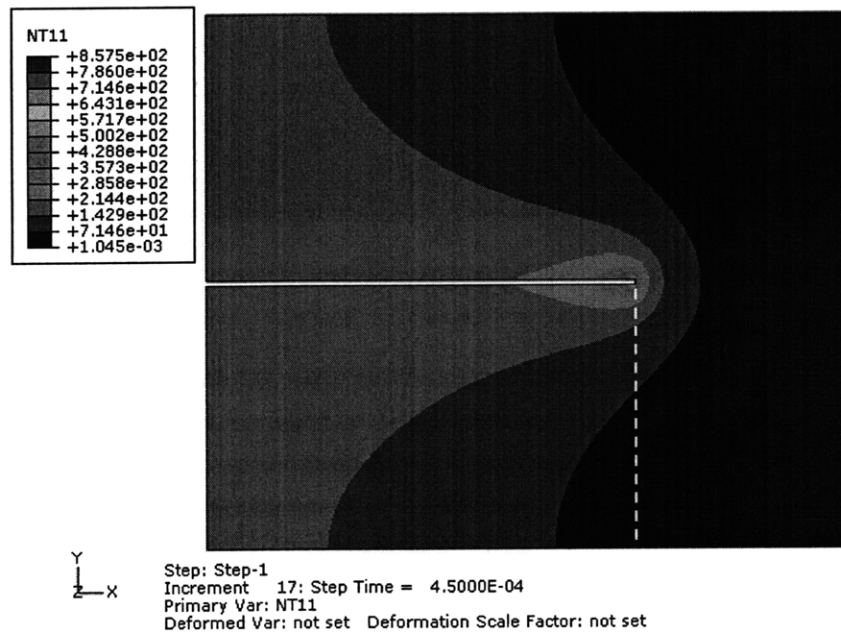


Figure 20: ABAQUS model of the Joule Heating effect causing the depicted temperature rise (in degrees Celsius), due to the surface current concentration of the EMFA specimen (Al2024). The surface current was approximated to be a constant current of 4250 A over a duration of 450 μs . The dotted line indicates the temperature profile shown in Figure 22.

From Figure 20 we can see that the crack surface are heated to a temperature of approximately 100 degrees Celsius. Figure 21 compares the result from the model with the observations made in the EMFA experiments:

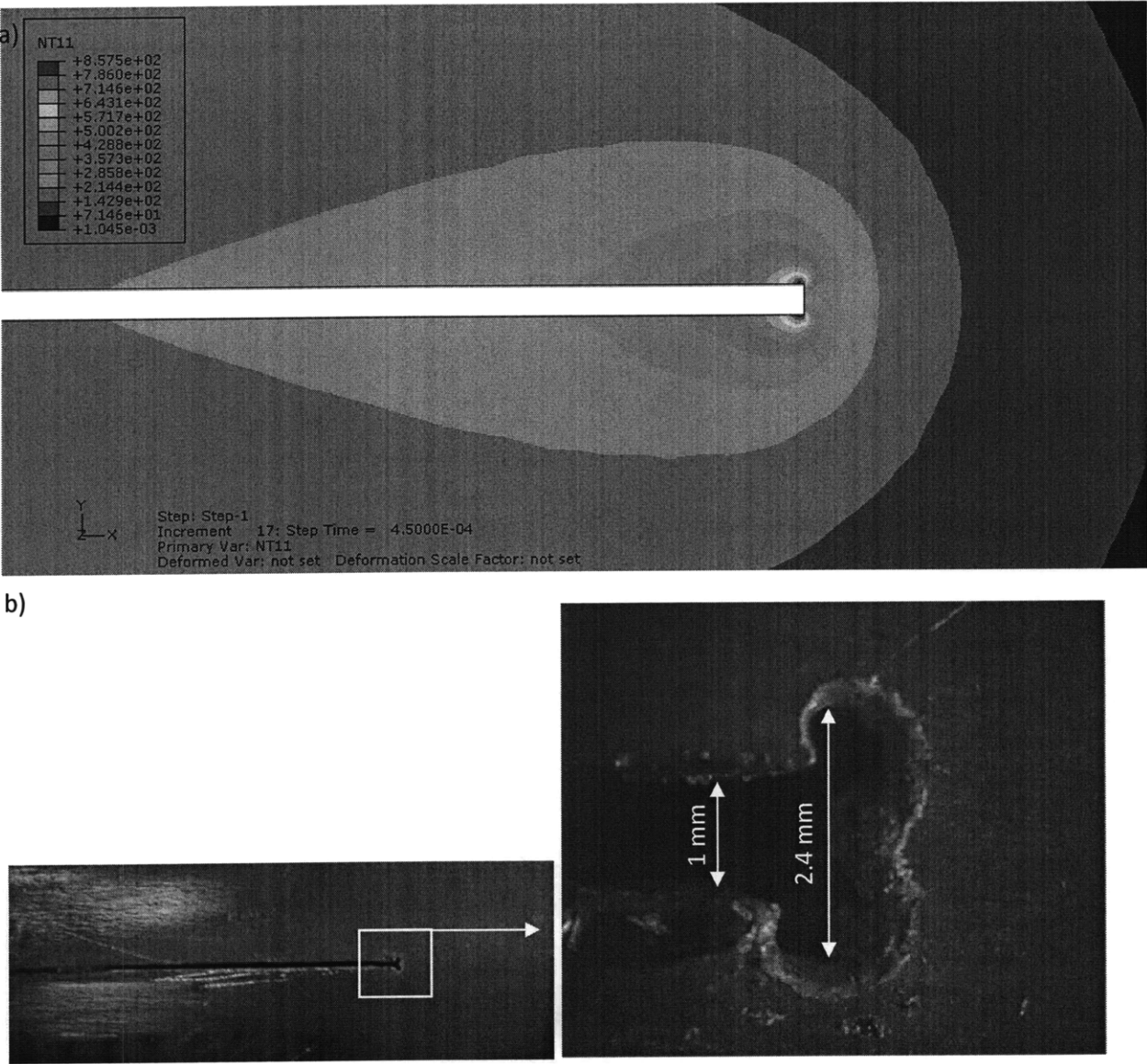


Figure 21: a) ABAQUS model of the Joule Heating effect causing the depicted temperature rise, due to the surface current concentration of the EMFA specimen (Al2024). The surface current was approximated to be a constant current of 4250 A over a duration of 450 μ s.

b) Digital Photograph of the EMFA specimen (Al2024), as well as a portion of the photograph which was zoomed in to be seen at higher detail.

For both, the simulation and the model, the temperature rise caused by the surface current concentration at the crack tip corners, reaches a temperature that is higher than the melting temperature of the presented material, which is between 502 and 638 degrees Celsius. Figure 22 shows

the temperature profile (see Figure 20) going away from the current concentration of the crack tip towards one end of the plate.

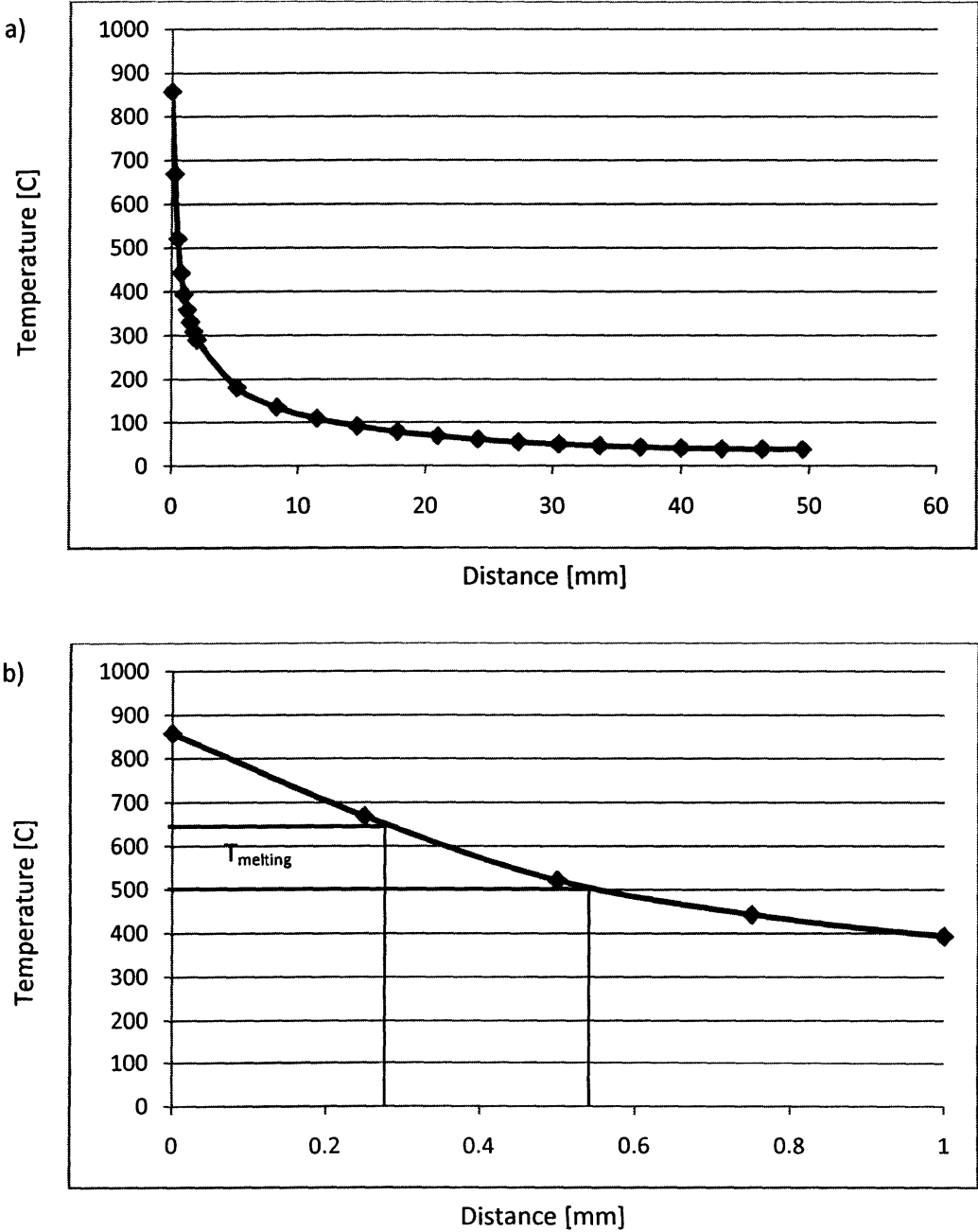


Figure 22: a) Temperature profiles over distance moving away from the crack tip of the modeled EMFA specimen. The chosen profile location can be obtained from Figure 20.
 b) Temperature profile over a distance of 1mm, near the crack tip of the modeled EMFA specimen. The melting temperature of the modeled material (Al2024) is depicted, as well as the distance, over which melting occurred.

From the measurement in Figure 21b we can obtain a distance of approximately 0.7 mm (on each side of the crack tip), over which melting occurred. From the simulation (Figure 22b) we measure an approximate distance of melting between 0.2 mm and 0.6 mm, which is very close to the observed value in the optical measurement.

Discussion

From the measurement of the optical microscopy (Figure 21b) and the modeled temperature profile we obtain a good correlation between the EMFA experiments and our presented ABAQUS model.

The presented result depends largely on the chosen coupling factor, which determines the actual induced current in the workpiece. We were able to calculate the coupling factor to be 0.28, using the measured inductance of the coil with and without a workpiece (at the operating frequency). This coupling factor might change by a factor of 2, when taking into account that the resistivity of the material changes due to a temperature change, which was not taken into account in our model. However the general outcome of the model will not change, just the current causing the end result will change, because it is now encountering a different electrical resistivity of the material.

Taking into account the thermal diffusivity α of the material, which is on the order of $8.5E-5 \text{ m}^2/\text{s}$ for Aluminum, we can calculate the distance that the heat traveled over the length of the induced current pulse of $450 \mu\text{s}$, using

$$x = \sqrt{\alpha t} . \tag{3.10}$$

This results in a distance of $380 \mu\text{m}$, which is on the order of the measured 0.2 mm to 0.6 mm for the width of the melted lobes observed for the EMFA specimens, as well as in the ABQUS model. Increasing the thermal diffusivity would lead to higher boundary of how much of the material can get heated over the short time of the current pulse and less melting would be observed. However, the design of the process and tooling material should really opt against any melting of the material at all. In section 3.4 we will present a materials selection for EMW coil materials that opts to improve the important material properties, such as the thermal diffusivity.

In the future, the model presents a great functionality to also calculate the crack-propagation due to the magnetic forces created between the crack surfaces (Stage III, see Section 3.2.4), as well as the presented stresses due to thermal heating which cause thermal fatigue (Stage IV, see Section 3.2.4).

3.3.4 Discussion

Many of the observations could only be made because of the introduction of a new kind of analysis, called Electromagnetic Fatigue Analysis. This method presents a repeatable setup to study the crack behavior and propagation of high current application materials, such as the tooling equipment for EMF or EMW.

As both the study of the Aluminum Bronze Bitter coil (Section 3.2) and the tube EMFA experiments show, cracks appear and propagate very quickly in electrical and electromagnetic applications. We can divide the observations made into two categories, short and long cracks:

Short cracks

Zig-zag cracks are observed, if the crack is still short and therefore, the current concentration is not high enough at the crack tip for melting to occur. Zig-zag cracks are normally observed in Stage I fatigue crack growth [4]. Therefore, first crack growth is due to the large stresses imposed on the tooling equipment during the EMW process. Furthermore, we were able to show an effect that would add to the crack growth, due to the magnetic force building up between the crack surfaces. Through our analysis we concluded that this effect occurs for cracks longer than the skin depth, making the skin depth an enormously important parameter for the coil life.

Long Cracks

We saw with the aluminum tubes that melting can increase the length of an already existing crack. We showed that this melting occurs because of a very high current localized at the tip of the crack (ABAQUS model, Section 3.3.3). This current concentration is magnified with increasing length of the crack, because as induced current flows around the tube, it reaches a barrier at the crack, and must flow all the way around it. This means that all the current that would be flowing across the crack is forced to flow around the tip of the crack. If the crack is long enough, there will be enough current concentrated to cause melting at the crack tip, further lengthening the crack.

Furthermore, thermal fatigue lengthens the crack even more, as during cool down of the tool and the area around the melted material at the crack tip, residual tensile stresses act on the crack tip.

Short and Long Cracks

Furthermore, crack propagation of short cracks and long cracks can occur due to the strong electromagnetic forces that pull the opposite interfaces of the crack apart. When the current flowing around a

tube is forced to flow along a crack, it creates two nearby currents in opposite directions. As we know, two opposite currents will repel each other, thereby opening the crack, see Figure 17:

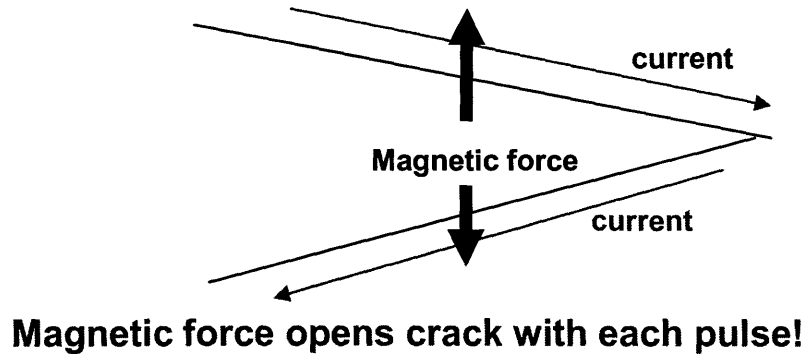


Figure 17: The magnetic force opens crack with each pulse of the electromagnetic process. The equations to determine the force are given in Section 3.2.4.

This is a particularly detrimental effect for the tool life, because it can occur at very small defects, which then grow in size. Through our analysis we determined that the critical defect size will be on the order of the skin depth.

These processes describe ways in which a crack can lengthen in electrical or electromagnetic applications. The cracks initiate during each firing and they will most likely appear at locations, where stress concentrations occur, such as in sharp corners. It is crucial for a working coil design to avoid these stress concentration, because once a short crack has formed, it can quickly grow by either of the two processes for short crack propagation described above.

We also showed two ways of possibly decreasing the stress concentrations or simply preventing the arcing at defects. First, we lowered the mechanical stress concentration by rounding the sharp corner of the crack tip. However, surface roughness still led to melting, as well as cracking, possibly due to Stage III cracking. As the surface roughness can be on the order of the skin depth of a material, it can certainly lead to Stage III cracking. Therefore, the surface roughness is a parameter that needs to be kept in mind when designing and building a tool for an electromagnetic process, such as a coil. Second, the crack tip, representing a large defect, was insulated using cyanoacrylate. This was done to prevent the possibility of arcing at the crack tip and to study the behavior of the insulator during the EMF process. However, the crack tip was still very much susceptible to the crack propagation mechanisms described above and besides preventing possible arcing at the crack tip the insulator does not fulfill any additional benefit with regards to the design and lifetime of the coil.

The next chapter (Chapter 3.4) will go into further detail about the important factors that go into the design of tooling equipment for EMF and EMW, based on the observations made in this section and Section 3.2. Based on these factors a materials selection of other possible coil materials is proposed.

3.4 Materials Selection for the EMF and EMW Tooling Equipment

As seen in the previous chapters EMW coils go through harsh conditions during their life, which can be very short and sometimes only a few cycles long. Up to now we have put some consideration into the design of a coil and how to avoid mechanical stress and electrical current concentration, which most of the time lead to failure of the tool. Also, the design and construction of a fieldshaper for the coil that is available at the MAGNEFORM EMF machine at MIT, was presented in Chapter 2.

In this chapter we focus on the coil material itself, as the rational selection of engineering materials is the ultimate goal of a materials scientist and engineer.

Materials Selection Software: Cambridge Engineering Selector

Materials selection software, such as the Cambridge Engineering Selector (CES) replaces former methods of trial and error and makes it possible to achieve reductions in component cost, enhanced product performance, better design quality, and design innovation [5]. Figure 18 shows an example of a material design selection done by the CES software.

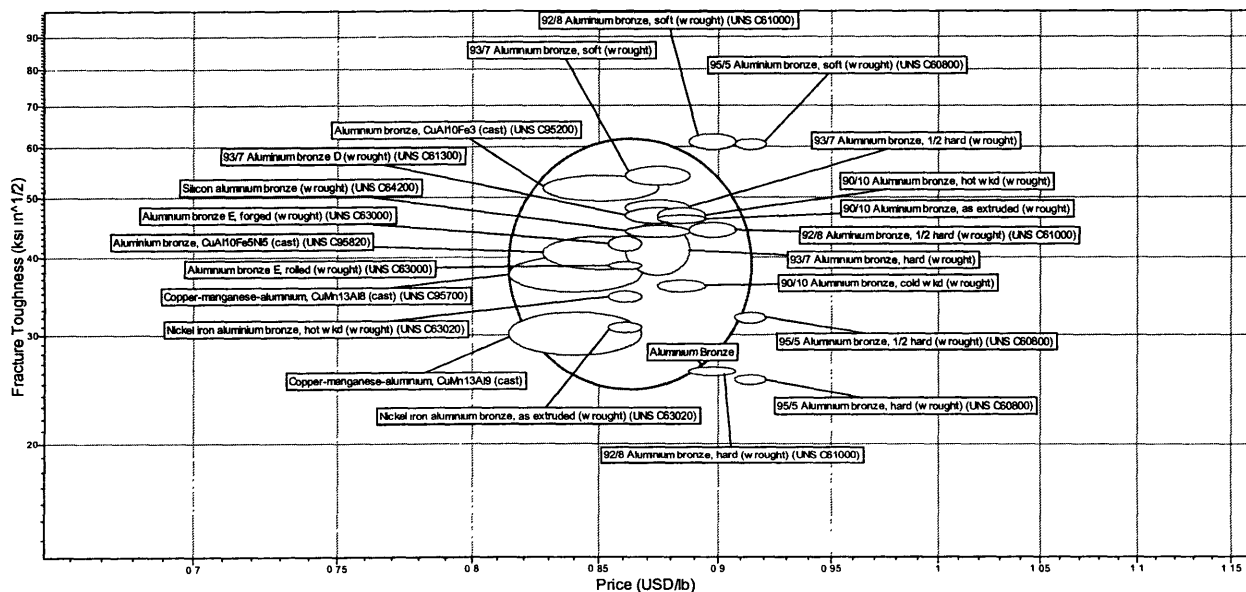


Figure 18: Example of a materials selection performed by the Cambridge Engineering Selector (CES) software. The graph shows the fracture toughness in $\text{ksi in}^{1/2}$ of all Aluminum Bronze alloys available in the database plotted against their individual price.

It is clear that a proper materials selection for the coil and the field intensifier needs to be performed which will provide materials that are able to withstand the high stresses and strains of the EMW process. The presented materials selection is based on the previous failure analysis of coils used for EMW, yielding the necessary properties of the material for this application.

Important Parameters that can be derived from the Failure Study

To make a proper materials selection, one needs to understand the physics behind the process and the important physical properties, also called “dimensions” that affect these processes (these are equal for single turn and multi-turn coil):

1. Resistivity and Permeability (Skin Depth):

The skin depth is proportional to the resistivity. A lower skin depth causes a smaller volume to be heated; however, a larger volume would lead to a lower ΔT . The permeability is inverse-proportional to the skin depth. Unfortunately, at the time of this study, the magnetic permeability parameter was not available in the CES software.

2. Thermal Conductivity:

The heat needs to be transported into the coil, away from the surface to ensure that the surface does not overheat. We calculated the distance over which heat can travel for a current pulse of 450 μs , which is on the order of 400 μm for Aluminum. The larger the distance over which that can travel during the current pulse, the lower the temperature rise over the respective distance.

3. Specific Heat:

The (remaining) heat causes the material to heat to a certain temperature, which is dependent upon the specific heat of the individual material.

4. Thermal Expansion:

The temperature difference between the surface and the bulk of the material will cause a stress depending on the expansion of the material due the temperature.

5. Maximum Service Temperature:

If the operating temperature is above the maximum service temperature, it will come to a strong decrease in the properties of the material (especially strength).

6. Fracture Toughness:

The initiation of a crack needs to be prevented at all cost. Specimen characterization showed that further electromagnetic effects can open the crack even further. Therefore, fracture toughness is a very important parameter, as it describes the toughness of a material towards resisting the initiation of cracks.

7. Tensile Strength

The coil material undergoes large deformation, which should remain in the elastic regime. Therefore, a high tensile strength is absolutely necessary.

8. Melting point:

The thermal heating of the eddy currents could cause the material to melt, for example at the surface, if the melting point was not high enough.

9. Price

In the end when all other parameters are satisfied, one should always look at the price per kilogram cost of a material, as the tool cost places a large role in the industry and especially in the automotive industry.

The Cambridge Engineering Selector (CES) software is capable of handling almost all these dimensions. Using the software one can cross compare, for example, 1818 metals that are available in the CES software database. Only one property, the magnetic permeability is not listed in the software package's databank.

Materials Selection

First of all it is clear that the material of choice must be a metal. Looking at the dimensions stated above, one could state that a good material choice could be copper, due to its magnificent electrical and thermal properties. However, the mechanical properties of copper are on the lower side in comparison with other metals. A next step is to look at certain copper alloys, which brings us to the category of Bronzes. These alloys have similar electrical and thermal properties in comparison to copper itself, but also show good mechanical behavior. One could continue here, but in this study we base our materials on the fatigue study presented previously.

The experiments with the Aluminum Bronze coils showed that Aluminum Bronze is not an optimum material for this high energy process. The author did a careful materials selection, based on the dimensions stated above and the fatigue experience from the Aluminum Bronze coils. Figure 19 shows an Ashby map that was created using the CES software of metals that are superior or equal in resistivity, thermal conductivity, specific heat, thermal expansion, fracture toughness and tensile strength, in comparison with Aluminum Bronze. 69 materials in the CES Materials Selector database made it through the selection process.

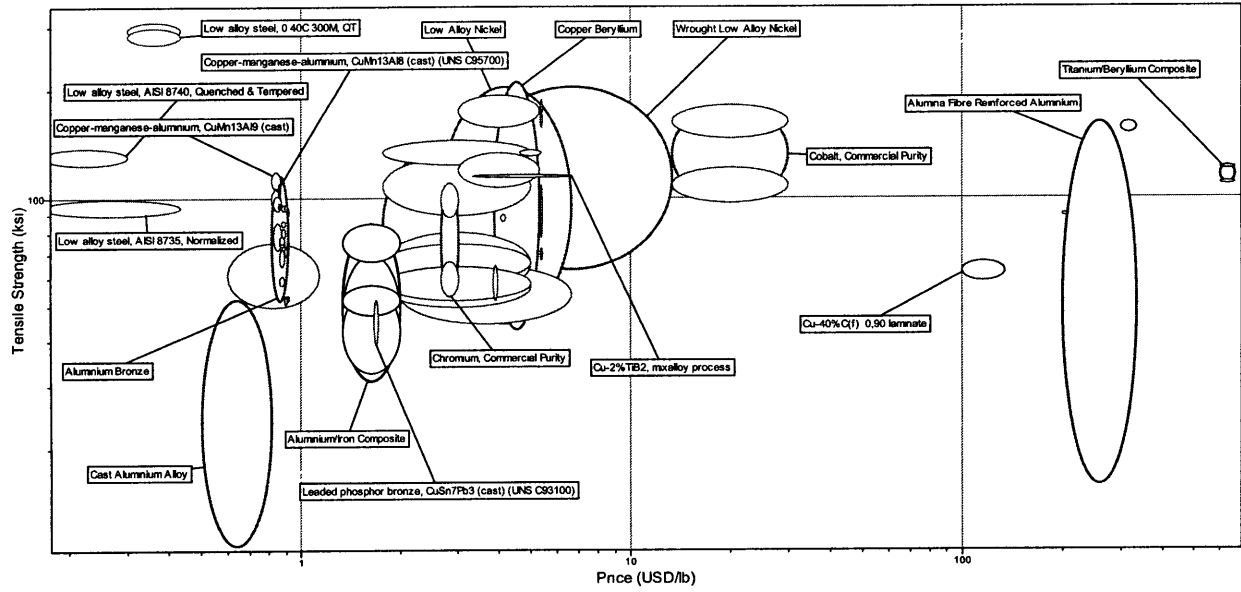


Figure 19: Ashby map of 69 materials comparing 6 important dimensions for the materials selection process. The y axis of this plot represents the materials tensile strength in ksi and the x axis represents the materials price in USD/lb.

The properties melting point and maximum service temperature have not been accounted for in the selection process, because their values are very similar for the different materials shown. A selection criterion that states, for example, “if lower don’t chose” could therefore eliminate certain materials although the temperature difference is only a few degrees Celsius. The same accounts for the price. Price was not chosen to be important as a selection criterion, because the author wanted to look at all possible choices of materials.

If melting point is taken into account as well, there are still 50 materials which are equal or superior to Aluminum Bronze. Figure 20 displays the final result, showing the materials that are superior in each dimension in comparison with Aluminum Bronze.

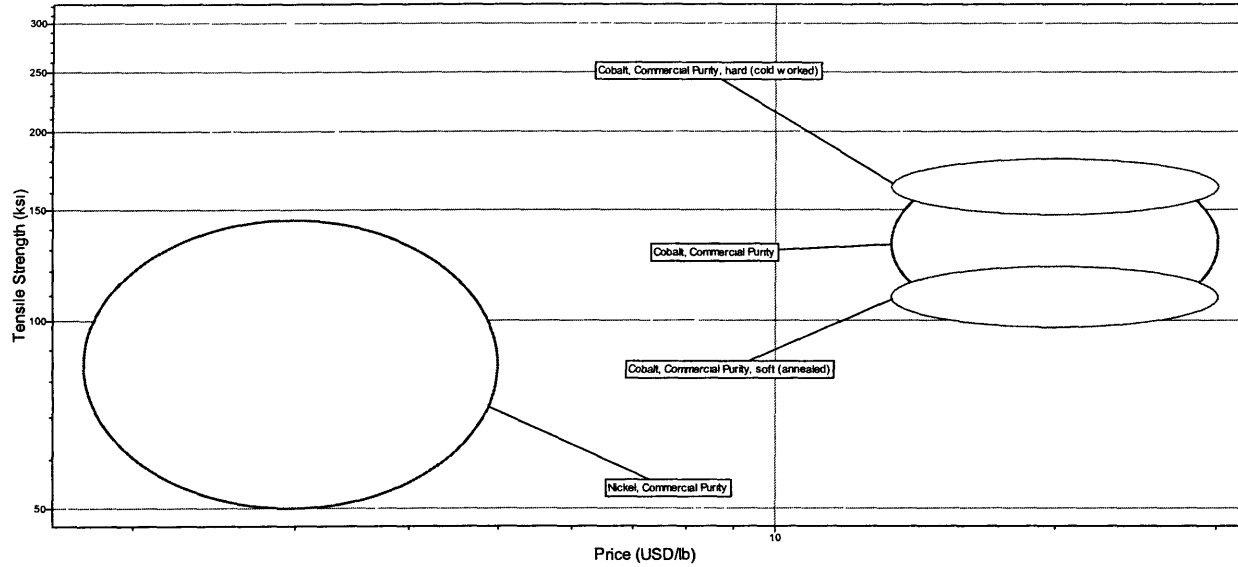


Figure 20: Ashby map of four materials comparing seven important dimensions for the materials selection process. The y axis of this plot represents the materials tensile strength in ksi and the x axis represents the materials price in USD/lb.

The results shown in Fig. 20 are already a very good first step towards finding the proper material for the application. However, so far we gave each dimension the same weight of importance in the selection process.

To complete the materials selection process, the author gave reasonable weights of importance to each dimension. Then, the cross comparison among all materials was reapplied. Table 3 shows the final results from the materials selection process, giving different significances to each dimension. Further information on the different importance given for each of the dimensions can be found in the appendix.

	RANK#0	RANK #1	RANK #2	RANK #3	RANK #4
Cobalt, Commercial Purity	2	2	1	1	1
Aluminium Bronze	6	7	8	8	9
Low Alloy Nickel	3	6	3	3	3
Copper Beryllium	5	5	5	5	5
Cu-40% C(I) 0,90 laminate	4	1	4	4	6
Chromium, Commercial Purity	1	3	2	2	2
Low alloy steel, AISI 8740, QT	4	8	7	7	8
Low alloy steel, 0.42C 300M, QT	4	9	6	6	7
Nickel, Commercial Purity	3	4	4	3	4

Table 3: Ranking of the top 9 materials comparing different significances of the important dimensions. For example, Rank#0 gave each dimension a value of 1; Rank#2 gave resistivity a value of 9, thermal conductivity a value of 8, specific heat a value of 7, ...price a value of 1 (see Appendix for all details).

Rank #2 represents the most realistic weighing of the dimensions regarding their importance for the EMW process.

The final result of the materials selection was:

1. Cobalt, Commercial Purity
2. Chromium, Commercial Purity
3. Low Alloy Nickel
4. Nickel, Commercial Purity
5. Copper Beryllium
6. Cu-40%Cr(f) 0,90 laminate
7. Low alloy steel, 0.42C 300M, QT
8. Low alloy steel, AISI 8740, QT
9. Aluminum Bronze

Further specifications about the materials and their individual strengths are given in Appendix C.

Discussion

It is unfortunate that the magnetic permeability was not an optional parameter in the materials selection process. However, one could now only look at the 9 materials chosen and compare their magnetic permeabilities. To do that we take a look at Table 2 again, where we have already shown a couple of the materials' magnetic permeabilities and calculated the resulting skin depth:

Material	Skin Depth (mm)
Cobalt	0.036
Nickel	0.016
Aluminum-Bronze	0.214
Copper (pure)	0.293
Steel	0.042

Table 3: Different skin depths calculated for a variety of possible coil materials ($f = 25$ kHz) [1-3].

As far as the magnetic properties of the materials are concerned, Cobalt, Nickel and Steel are ferromagnetic materials. Chromium is an antiferromagnetic material, Copper is a diamagnetic material and Aluminum Bronze is paramagnetic. Therefore, only Copper and Aluminum Bronze can be called non-magnetic.

As it can be seen in Table 2 the skin depth for the Aluminum Bronze alloy is a better choice in comparison to the other proposed metallic materials, as far as the low magnetic permeability of the Aluminum Bronze material is concerned, because the skin depth is increased and the area through which current can flow is maximized, just like pure Copper. Pure Copper, however, was not one of the 9 chosen materials in our materials selection, because its other properties are not high enough for the EMW process.

Furthermore, at such high currents the saturation magnetization of the other materials (except for Copper, which like Aluminum Bronze is non-magnetic) would lead to a drop of the relative magnetic permeability μ_r , leading to a skin depth on the order of the skin depth observed the non-magnetic materials times a factor of

$$\sqrt{\frac{\rho_{e,non-magnetic}}{\rho_{e,magnetic}}}, \quad 3.4$$

where $\rho_{e,non-magnetic}$ and $\rho_{e,magnetic}$ would be the electrical resistivity of the non-magnetic material and the magnetic material, respectively.

The short time over which the skin depth is lower due to the higher relative permeability leads to a decrease in rise time of the current, but already at a current of a few tens of Ampere the metal will have reached full magnetic saturation, which will reduce the magnetic permeability to a value on the order of the magnetic permeability of a non-magnetic material, such as copper. As the time is very short to reach a couple of tens of Amperes in the EMW process, this effect can be neglected [6]. Furthermore, through annealing and other materials treatments the relative permeability can be tailored to a desired value [7].

To summarize, Aluminum Bronze is a good choice for a Bitter coil, because the area through which current can flow is maximized, but like we said after a short amount of time the skin depth will also increase in the other proposed materials, because the relative permeability will decrease, because of the saturation magnetization of the materials.

PULSAR has developed a software package based on the EMW calculations presented in the Literature that can calculate the necessary coil material and machine with regards to their database. The capabilities of this software are presented in Appendix C by calculating and studying three different cases.

Bibliography – Chapter 3

[1] <http://www.matweb.com>

[2] <http://hyperphysics.phy-astr.gsu.edu/hbase/solids/ferro.html>

[3] <http://www.ee.surrey.ac.uk/Workshop/advice/coils/mu/>

[4] S. Suresh. Fatigue of Materials; Cambridge University Press

[5] <http://www.grantadesign.com/products/ces/>

[6] J.P. Schaffer, A. Saxena, S.D. Antolovich, T.H. Sanders, S. B. Warner. The Science and Design of Engineering Materials. Book, McGraw-Hill (1999)

[7] R. C. O’Handley. Modern Magnetic Materials. Book, John Wiley (2000)

[8] I. V. Belyy, S.M. Fertik, L.T. Khimenko. „Electromagnetic Metal Forming Handbook”, English Version of Russian book Translated by M.M. Altynova, Dept. of Materials Science and Engineering, The Ohio State University, 1996.

4 Pulsed Electromagnetic Welding

4.1 Introduction

The explosive welding process is one of the most useful and widely employed applications of the high energy rate methods to the fabrication of materials. Nowadays, the automotive industry seeks to find the same value in the EMW process, by being able to weld mechanically and physically dissimilar materials. In comparison, in fusion welding melting of the two metals is essential at the interface, and in pressure welding large plastic deformation is required. Therefore, only metals which have similar melting points and plastic flow stresses are joinable through these processes, respectively. EMW can join dissimilar metals; the use of an electromagnetic process imposes nevertheless a limitation from the view point of cost and can be detrimental on the life of the tooling equipment, as we have seen in Chapter 3.

4.2 Background

So far we have said that the EMF and the EMW processes are very similar as far as the individual necessary components are concerned. However, in Chapter 2 we showed that the time-scales, due to the necessity of a much lower inductance in the RLC circuit in the EMW case are very different. Through the study of EMF (Chapter 2) we measured and calculated deformation velocities and explained how certain materials are more easily deformed than others, due to their low strain rate sensitivity (see Chapter 1) and better formability, such as Al6061-T6. Other materials are less easily deformable with increasing strain rate.

The literature states that the welded length ratio R (see Chapter 1) is an important final parameter for measuring the strength of a weld. In Chapter 1, we also discussed several additional process parameters that affect the final product, such as the design of the coil and the possibility of introducing a fieldshaper between the coil and the outer workpiece. These fall into the category of circuit theory and also include the number of turns or the inductance of the coil, which is very important to achieve EMW, as stated above.

We then mentioned several process parameters which fall into the category of deformation theory, such as the tapered angle of the inner workpiece, the gap between the outer and inner workpiece (sometimes also referred to as the *core*, if it is a solid rod, usually), the diameter and wall-thickness of the workpieces and the weld length. Certainly many of these parameters are interrelated, for example, as the diameter of the outer workpiece is increased, the inner radius of the coil needs to be increased, which in turn, increases the inductance of the coil (see Equ. 1.20, Chapter 1).

So far we only said that the necessary time-scales need to be very different to achieve the critical threshold velocities of the outer workpiece to go from EMF to EMW, thereby forming a solid state joint between the inner and the outer workpiece. We have stated that due to the high strain rates during the

EMW process the materials behave like a highly viscous fluid. As a result, a small surface layer, called “jet” is extruded. This causes the contaminated layers of the core and workpiece surfaces to be removed and upon further pressure on each other are welded together (see Chapter 1).

With the observations made to this point the author would like to present a couple of steps and further conditions (in addition to the conditions named in Chapter 1) to optimize the EMW process.

4.3 Hypothesis to Optimize the EMW Process using a Threshold Kinetic Energy Approach

The author would like to present a new formula derived from the critical threshold velocity equations, which makes it simple to create approximate energy calculations and graphs displaying welding windows for certain materials.

The literature shows that the threshold velocity necessary to achieve EMW is strongly dependent upon the Vickers hardness of the material. The author has derived a formula which makes it very simple to create *threshold kinetic energy* vs. Vickers Hardness plots.

Using Equ. 1.17 and setting $k'=1$ to receive

$$v_c' = \sqrt{\frac{2 \cdot H_v}{\rho}} \quad 4.4$$

Now a *threshold kinetic energy* can be calculated by saying

$$E_k(v = v_c') = E_{crit} = \frac{1}{2} \cdot m \cdot v_c'^2 \quad 4.5$$

Inserting Equ. 4.4 into 4.5 gives

$$E_{crit} = V \cdot H_v \quad 4.6$$

where V is the volume of the deformed metal section during the EMW process. One can see by Equ. 4.6 that the critical necessary kinetic energy that is needed to accelerate the mass over which the EMW process takes place is largely affected by the deformed volume, as well as the Vicker's Hardness of the material. The author believes that is a quite important observation as it gives a good way of creating welding windows for many materials.

The following examples will provide such welding windows using the formula presented for the critical kinetic energy.

Example A:

A6061-O electromagnetically welded in the annealed temper before it is heat-treated to produce the T6 temper could decrease the necessary energy of the process by a factor of 3. Figure 9 shows the kinetic energy calculations, based on the critical velocity necessary for welding (see Chapter 1) and the masses for several workpiece dimensions.

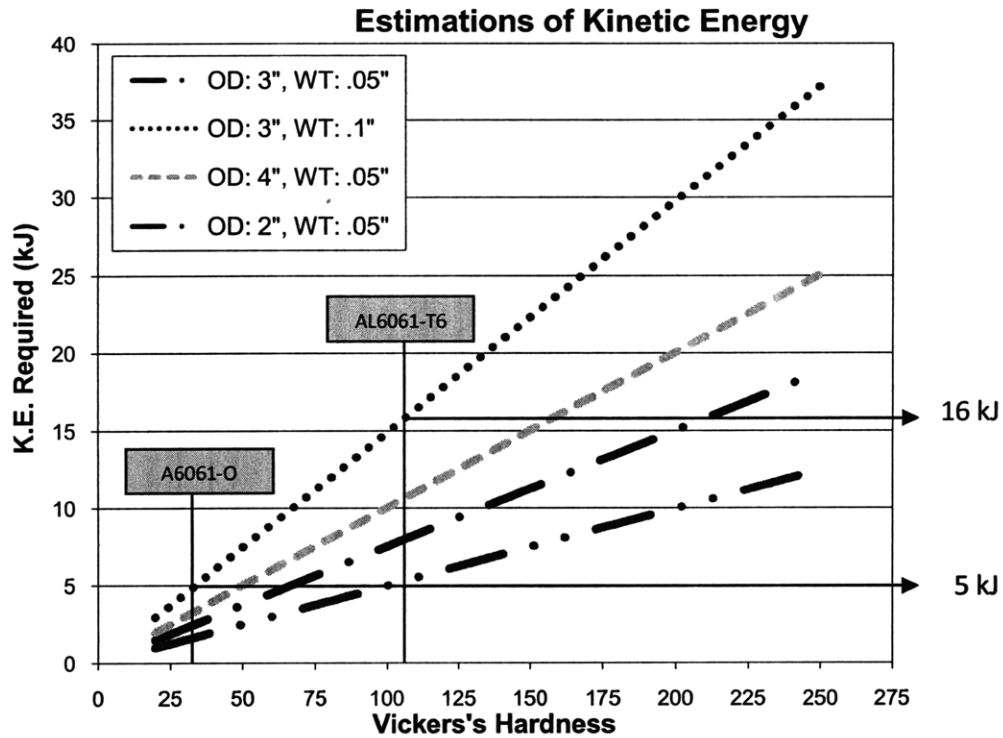


Figure 9: Threshold kinetic Energy necessary to perform EMW on A6061-O and AL6061-T6, for several workpiece dimensions. The deformed length is 0.5”.

It can be seen in Figure 9 that just due to the increase of hardness of Al 6061 T6, due to the T6 heat-treatment of Al 6061, the necessary theoretical threshold kinetic energy that needs to be supplied increases from approximately 5 kJ to 16 kJ.

Example B:

Now, one can also compare the change in the threshold kinetic energy, when changing the workpiece dimensions. In this example we look at doubling either the outer diameter or the wall-thickness of an AL6061-T6 tube. Figure 10 shows the change in necessary energy when changing the dimensions of the workpiece materials.

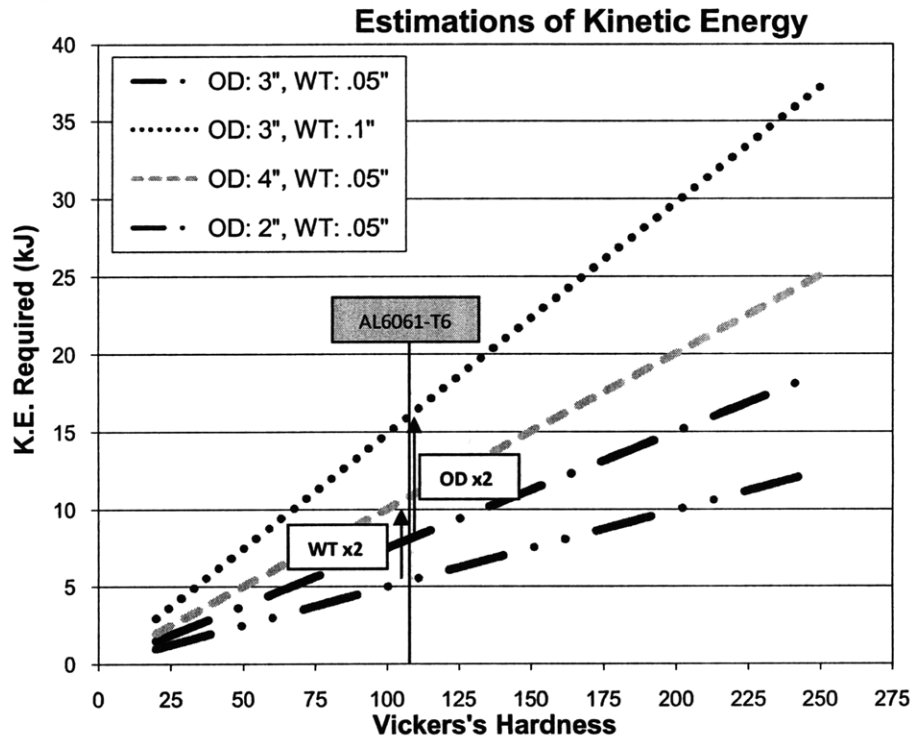


Figure 10: Threshold kinetic energy necessary to perform EMW on Al6061-T6 and several workpiece dimensions. The change in necessary energy by changing a certain dimension of the workpiece is shown for two cases. The deformed length is 0.5”.

From Figure 10, we can see that changing the dimensions, such as the outer diameter or the wallthickness of the material can be quite detrimental for the critical threshold kinetic energy needed for the EMW process.

Example C:

In the last example, we show the welding windows and necessary critical threshold kinetic energies for the two material families of Aluminum alloys and stainless Steels. Figure 11 shows this example by displaying the welding windows across the range of Vicker’s Hardness for each material family, respectively.

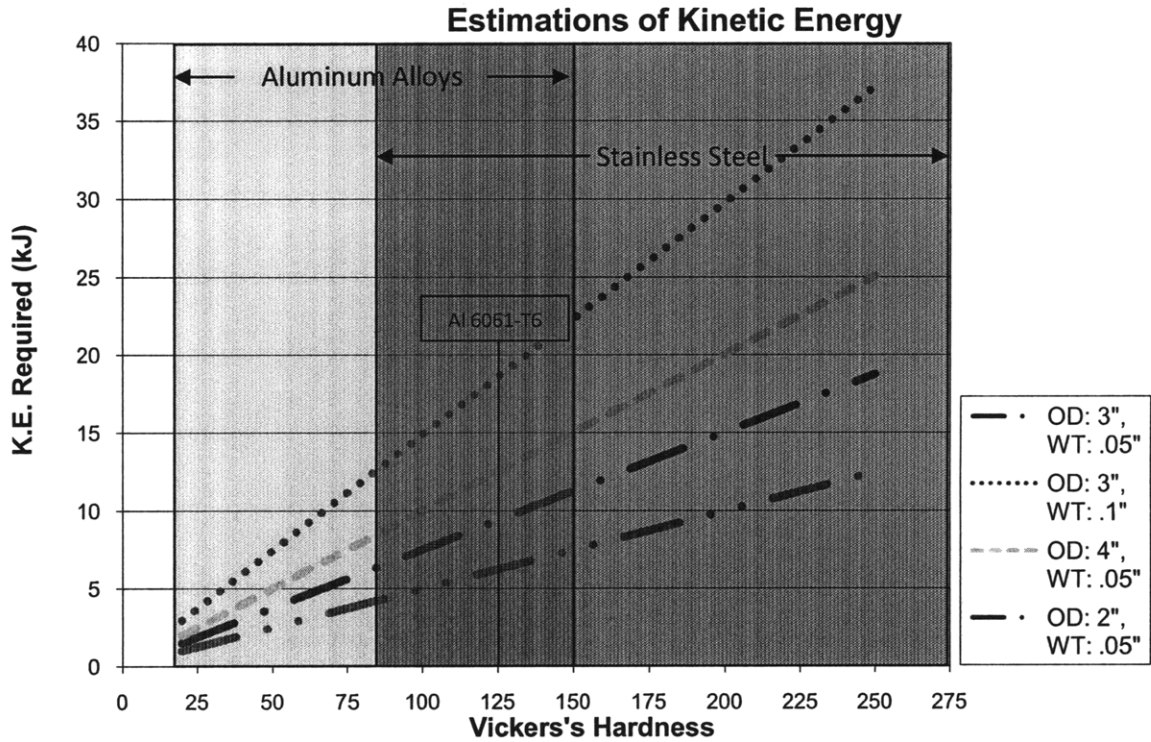


Figure 11: Threshold kinetic energy necessary to perform EMW on Al6061-T6 and several workpiece dimensions. The welding windows for the material families of Aluminum alloys and stainless Steels are displayed, over their range of Vicker's Hardness, respectively.

From *Example C* and Figure 11 we can observe that it should be possible for workpiece materials made of stainless Steel, which have a Vickers's Hardness that is lower than 150, to be more weldedable through the EMW process than some Aluminum alloys, with a Vicker's Hardness that is higher than 110.

On the other hand, similar threshold kinetic Energies can be adjusted for two materials of similar Vicker's Hardness, while adjusting the dimensions of the workpiece (for example the wall-thickness; not the diameter, as a change in diameter would change the workpiece-coil coupling or the necessary inner diameter of the EMW coil and therefore its inductance).

4.4 EMW Experiments

Through the course of the study, the author came across the company PULSAR, which already has been described in detail (see Chapter 1). A collaboration between MIT and PULSAR (Yoav Tomar , Victor Shribman) was established and initiated by the author starting in the fall of 2006. This collaboration was based on FORD employing PULSAR to develop their current EMW machinery in Detroit and PULSAR was very eager to collaborate again.

As stated, in Section 1.3.2, FORD would provide MIT with EMW samples manufactured with their machine, in Detroit, which should then be studied in detail. However, the machine at Detroit was never available for any EMW experiments and no specimens were delivered to MIT. Therefore, the author decided to partner with PULSAR and go to Israel to perform the experiments himself.

A design of experiment (DOE) was suggested by the author and approved by FORD to be performed at PULSAR. The following section introduces the tested materials in the DOE.

4.4.1 Design of Experiment

Due to the vast amount of parameters that affect the quality of the final EMW joint a design of experiment (DOE) was suggested by the author to minimize the amount of necessary experiments.

Introduction

We want to determine what factors most affect the quality of the final EMW joint. The primary factor to be investigated is the strength of the resulting weld. Secondary factors are the weld area or the percentage of the actual joint circumference. The affecting factors are:

- Outer Workpiece Material
- Taper angle
 - Positive/Negative Taper
- Gap between workpiece and core
- Diameter of Tube
- Tube Wall Thickness
- Cleanliness of Material
- Capacitor Charge

To make the experiment manageable, one may want to eliminate one or more factors in the DOE. Dropped factors can be saved for future optimization experiments if deemed necessary. After some

consideration we decided to drop the factors capacitor charge, which would just be set to the highest value allowed for the EMW coil. Furthermore, changes to the capacitor charge could be easily addressable in subsequent experiments.

Next, “high” and “low” values for all parameters needed to be picked, in accordance with what material is available (diameter of tube, wall-thickness), as well as the experimental side (inner diameter of the coil). A general rule for choosing the upper and lower boundaries for the DOE parameters is to set the parameters as far apart as possible, but not exceed the operating boundaries.

Then, certain constants need to be chosen, which will always remain the same, such as:

- Core should always be of same material, which we chose to be Al6061-T6
- At least two trials should be done on each setting for “noise” factors
 - Air Conditions
 - Operator Differences
 - Machine Inconsistencies
- Groups of samples should be done in batches, again to account for “noise” factors
- Energy used
 - 10 kJ for the first DOE Study (August 2007)
 - 12 kJ for the second DOE Study (November 2007)

A *Full Factorial Design of Experiment* would require 2^8 (256) samples (2^7 for every design set up and two trials on every setup). This would certainly not prove to be economical with respect to time or money. A *Fractional Factorial Design of Experiment* can be employed as long as third degree interactions can be ruled insignificant [1,2].

For our experiments we chose to do a half factorial DOE, which would mean the following:

- Required Experimental Setups: 16
- Total Samples: 32 – 48 (Each Setup still has to be done 2-3 times to verify results)
- Assumes no strong three-factor interactions
- Gives a good indication of important factors

Finally, after the weld strength tests on the samples are performed, a data analysis can be done using statistical software to create interaction plots and statistical graphs. This analysis will show which parameters need to be focused on most to optimize the weld strength.

Following are the chosen DOE parameters for two DOE studies that were performed at PULSAR, in August and November 2007, respectively.

Parameters in the first DOE Study (August 2007)

Table 2 shows a summary of the DOE parameters, which were decided upon in consent with FORD, Detroit and PULSAR (Batch #1, August 2007).

DOE Parameter	Phys. Parameter	High Value (+)	Low Value (-)
A	Taper Angle [°]	2.5	0
B	Tube Wall-Thickness [mm]	1.5	1
C	Diameter [inch]	1.5 (Coil A)	1 (Coil B)
D	Gap [mm]	2	1
E	Cleanliness	Alcohol	Layer of Oil

Table 2: Summary of the DOE parameters, which were decided upon in consent with FORD, in Detroit and PULSAR, in Israel (Batch #1, August 2007).

Parameter A represents the tapered angle of the inner workpiece. PULSAR mentioned that their experiments were usually done with no taper angle. According to the literature, however, a taper angle can be beneficial to the final EMW joint, therefore it was one of the definite DOE parameters chosen [3]. Parameter B and C, tube wall-thickness and diameter, were agreed upon to give good starting values for the experimental setup (inner diameter of the coil), as well as from the industrial point of view. PULSAR had two coils available with the proper inner diameters and therefore, no new coils had to be fabricated. Parameter D, the gap, was decided upon from values from the literature and experience from PULSAR with their EMW coils, regarding the proposed sample size. Finally, parameter E, the cleanliness of the surface of the inner workpiece was chosen to be the last important DOE parameter. From what was presented before about the importance of the surface treatment this was an obvious choice to be made. As a side note, the upper (+) and lower boundary (-) of parameter E is calculated by multiplying the values (+/-) of A, B, C and D. Table 3 shows the variation of the parameters used in the DOE study.

Run	A Taper Angle	B Wall- Thickness	C Diameter	D Gap	E=ABCD Cleanliness
1	-	-	-	-	+
2	-	-	-	+	-
3	-	-	+	-	-
4	-	-	+	+	+
5	-	+	-	-	-
6	-	+	-	+	+
7	-	+	+	-	+
8	-	+	+	+	-
9	+	-	-	-	-
10	+	-	-	+	+
11	+	-	+	-	+
12	+	-	+	+	-
13	+	+	-	-	+
14	+	+	-	+	-
15	+	+	+	-	-
16	+	+	+	+	+

Table 3: Variation of the DOE parameters, in the first DOE study, yielding 16 different experimental setups and samples.

The setups (“Runs”) in Table 3 were tested twice, rendering a total of 32 experiments. All 32 samples were shipped to MIT for further investigations. We performed tensile tests on the first half of samples and Optical Microscopy, as well as a metallurgical analysis on the 2nd half.

Parameters in the second DOE Study (November 2007)

After the results from the first DOE study we chose to include another DOE parameter in the study and perform another set of 32 experiments, again with a half factorial DOE.

The parameters A, B, C, D and E were the same as in Table 3. Parameter F was the additional parameter that was added in this study and represented the scratch-brushing of the inner workpiece surface in the direction of the longitudinal axis of the sample. As stated above scratch-brushing was one of the most effective methods to decrease the necessary deformation to achieve a good joint in cold-welding and was therefore chosen to be a parameter of interest for our second trial of EMW experiments. Table 4 shows the new DOE parameters and Figure 12 shows an example of the scratch-brushed inner workpiece.

Basic Design						
Run	A	B	C	D	E = ABC	F = BCD
1	-	-	-	-	-	-
2	-	-	-	+	-	+
3	-	-	+	-	+	+
4	-	-	+	+	+	-
5	-	+	-	-	+	+
6	-	+	-	+	+	-
7	-	+	+	-	-	-
8	-	+	+	+	-	+
9	+	-	-	-	+	-
10	+	-	-	+	+	+
11	+	-	+	-	-	+
12	+	-	+	+	-	-
13	+	+	-	-	-	+
14	+	+	-	+	-	-
15	+	+	+	-	+	-
16	+	+	+	+	+	+

Table 4: Variation of the DOE parameters in the second DOE study, again yielding 16 different experimental setups and samples.

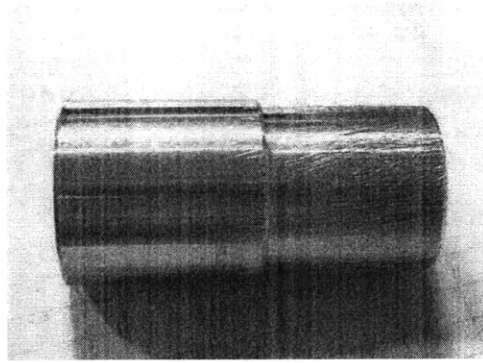


Figure 12: Photograph of the scratch-brushed inner workpiece (DOE parameter F = +).

4.4.2 Experimental Setup

Materials and Specimens

The material chosen for the outer and inner workpiece was Al6061-T6. The rods and tubes were machined and prepared at PULSAR, in Israel.

The inner workpiece rods were turned down to the appropriate outer diameter over the distance, where the EMW joint would be placed. The appropriate outer diameter was determined by the respective gap for the DOE run (parameter D).

The outer workpiece tube was turned down on the inside to reduce the wall thickness over the distance where the EMW joint would be placed. The wall-thickness of the entire tube was 1.5 mm, but would be turned down to 1 mm, for the DOE run (low value of the wall-thickness, parameter B).

The inner workpiece was either cleaned with alcohol or covered with a fine layer of oil, applied with a Q-tip, depending on the DOE parameter E. Furthermore, the inner workpiece was scratch-brushed using a steel brush or left in its original state, depending on the DOE parameter F.

Experimental Setup at PULSAR

All EMW experiments were performed at PULSAR in Israel. As stated above, the first DOE study was done in August 2007 and the second DOE study was done in November 2007. I was present during the experiments of the second study. Figure 13 shows the setup with close-up views of the capacitor bank, the transforming station, the oscilloscope and the coil (clockwise, starting on the top left). This setup was used to for EMW experiments at PULSAR, in November 2007.

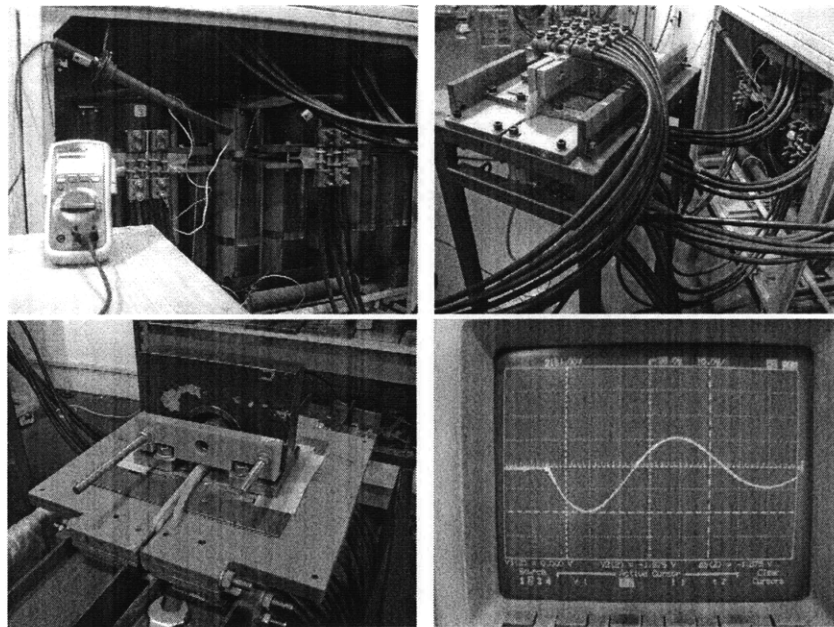


Figure 13: Close-up photographs (of the experimental setup at PULSAR, in November 2007) of the capacitor bank, the cable transformer station, the oscilloscope and the coil (clockwise, starting on the top left).

The machine properties of the EMW machine at PULSAR are shown in Table 5:

Capacitance	320	μF
Working voltage, max	25	kV
Self inductance	25	nH
Energy storage, max	100	kJ
Peak current, max	1200	kA

Table D.5: Properties of the pulse current generator.

A cable pulse transformer was used in order to increase the discharge system's efficiency with the following properties, see Table 6:

Number of windings	3
Number of lines	8
Transformation ratio	$k = 2.7$

Table 6: Properties of the cable pulse transformer.

A magnetic field measurement of the coils used at PULSAR was performed and the report can be found in the Appendix D along with a schematic drawing of the EMW coil used by PULSAR. We measured the magnetic field to be between 6 T and 14 T and between 5 T and 9T, along the working zone of the 1.5" specimen coil and the 1" specimen coil, respectively.

EMW Process

The energy used was 10 kJ and 12 kJ in the first DOE and second DOE, respectively. The EMW process is similar to the EMF process studied previously. First, the sample is inserted into the coil. It is fixed appropriately with a stage and insulating material to avoid shorts. Second, the investigators move to a safe area and the machine is fired remotely. The capacitor bank discharges and the process can be observed very visually and audibly by a large spark coming out of the outer workpiece. Ear-protection should be worn at the time of the process, under all circumstances. The current and voltage are recorded and the sample can be removed after the process has finished.

In the following Section 4.4.3, we present an analysis of the welded EMW specimens from both DOE studies. Tensile tests were performed for both studies. Weld length measurements, Optical Microscopy and a metallurgical analysis were performed for the specimens from the first DOE study.

4.4.3 EMW Specimen Evaluation

In this section we present Optical Microscopy, as well as a metallurgical analysis and SEM analysis of half of the welded EMW joints of the first DOE study. Then we show the tensile test results of both DOE studies. Figure 14 shows a photograph of one of the 1" EMW specimens after being welded.

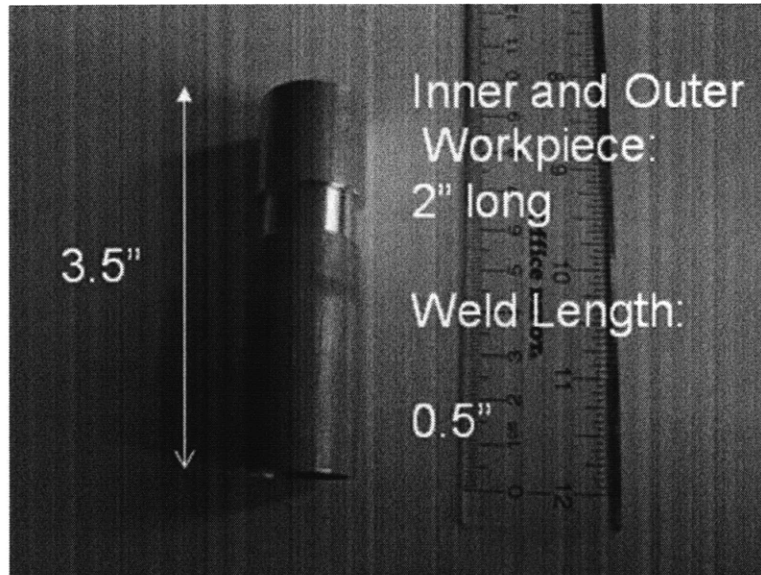


Figure 14: Digital photograph showing one of the 1" diameter samples.

The outer workpiece is well formed around the inner workpiece. The EMW weld presents a very clean weld. The overall final sample length was 3.5" with a weld length of approximately 0.5". Figure 15a shows the outer workpiece after being heavily deformed and even destroyed, because no inner workpiece was inserted. In comparison Figure 15b shows the final deformation of the outer workpiece after being fired in the EMF MAGENFORM machine, at MIT.

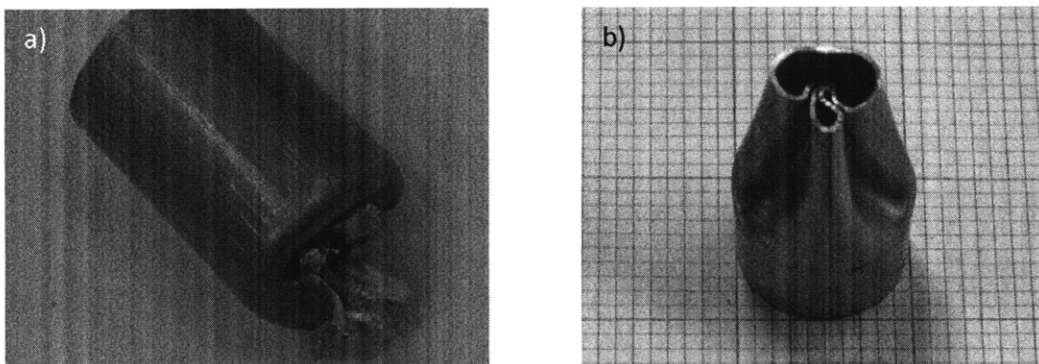


Figure 15: a) Outer workpiece deformation without inner workpiece, tested with the EMW machine at PULSAR, in Israel.

b) Comparison of the outer workpiece deformation without an inner workpiece, tested at the EMF MAGNEFORM machine setup (with the addition of the manufactured fieldshaper), at MIT.

From Figure 15a, one can see that the deformation of the outer workpiece through the EMW coil is very heavy, when there is no inner workpiece in the way of the deformation. The sides of the outer workpiece slam into each other and burst under heavy deformation, as well as during the deformation process. On the other hand, the EMF outer workpiece gets deformed nicely until the surfaces are in contact (see Figure 15b).

First, we will now present the metallurgical analysis of the 1" (see Figure 14) and 1.5" EMW samples. Then we will show the analysis of the Optical Microscopy and SEM observations (Section 4.4.3.2) and then we will study the wavy interface of the EMW joint using the EDS setup at the Materials Joining and Welding Laboratory. These tests are performed for the first batch of the DOE (August 2007). Finally, we present the tensile test analysis, as well as the results from the DOE for both batches (August and November 2007).

4.4.3.1 Metallurgical Analysis

Sample Preparation

A metallurgical analysis was prepared and performed by the author and Victor Shribman at PULSAR. The samples were cut on a Metkon METACUT CUT-OFF MACHINE. Then they were molded and polished using the following:

- 220, 320, 400, 1000 (360 rot/min) and
- 3 micron diamond paste (185 rot/min).

The cut samples were cleaned with water and acetone and dried with an electric dryer. After that the following chemistry was used to etch the surface:

- 1ml HF (48% conc.) and 200 ml Water
- Or 45 ml HCl, 15 ml HNO₃, 15 ml HF (48%), 5 ml H₂O

The solution was applied with a swab stick until the grain structure appeared. Unfortunately, ten of the samples broke during sectioning, due to not overcoming the residual stress during the EMW process. Samples R3, R4, R11, R12, R15, R16 from the first DOE were cut and prepared accordingly (see Table 3).

Results and Discussion

In the following we show the Optical Microscopy (OM) results for sample R4. The OM was performed with an OPTIPHOT-100 (Camera 5x, 10x, 20x and Video Camera: additional 10x). Figure 17 shows the optical microscopy images of sample R4. In Figure 17a the deformation of the grains in the outer tube (upper part in the image) can be observed.

In Figure 17b a crack can be observed. These cracks form in the interface and stop where the weld has occurred. It is not clear if the cracks form during or after the joining process.

The weld length is measured between the tips of the cracks coming from both sides in the interface. The weld length for sample R4 was 3.5 mm. Figure 17c depicts the interface with a magnification of 500x.

The measured interface width was approximately 16 μm . This is very large in comparison to the usual thickness of oxides in Al alloys around 50nm. Therefore the hypothesis arises that melting of the base metal has occurred during the joining process, which is now part of the interface shown in Figure 17c. Reported wave amplitude values for other materials from the explosive welding literature are shown in Table 7.

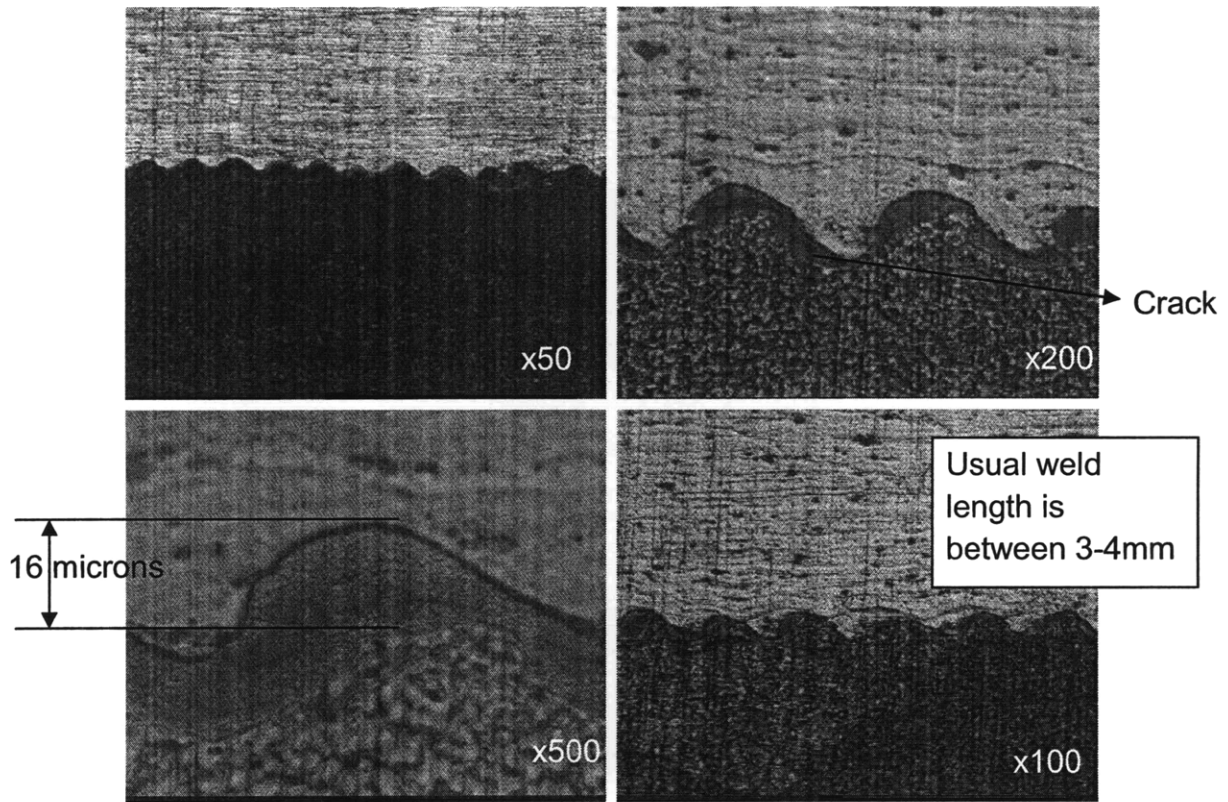


Figure 17: Metallurgical analysis of sample R4. a) OM photograph of the wavy EMW interface (magnification of 50x). b) Larger magnification (200x) showing 2 full humps of the wave and a crack in the first. c) OM photograph of one wave hump (magnification of 500x). d) OM photograph with lower magnification (100x).

Outer Workpiece	Inner Workpiece	Initial angle of incidence	Amplitude [inches]	[mm]
Stainless Steel	Stainless Steel	5	0.006	0.1524
Copper	Stainless Steel	5	0.009	0.2286
Stainless Steel	Copper	5	0.009	0.2286
Copper	Copper	5	0.012	0.3048
Stainless Steel	Stainless Steel	10	0.012	0.3048
Copper	Stainless Steel	10	0.016	0.4064
Stainless Steel	Copper	10	0.015	0.381
Copper	Copper	10	0.022	0.5588

Table 7: Summary of reported wave amplitude values for other materials from the Explosive Welding literature.

Scanning Electron Microscopy (SEM) was performed to study the interface in higher detail and will be described in the following Section 4.4.3.3.

4.4.3.2 Optical Microscopy and SEM

In this section we characterize the EMW joint using Optical Microscopy (OM) and Secondary Electron Microscopy (SEM). Weld length ratio measurements are performed using OM and SEM and the wavy interface is studied in further detail with the SEM.

As stated in Chapter 1, the calculation of the weld length ratio R is calculated with the following formula:

$$R = l/l_0 * 100\%, \quad 4.1$$

where l_0 is the total length of circumference at the tube-core interface after welding and l is the length of the welded portion along the circumference of the interface. Figure 18 gives an example from the EMW literature.

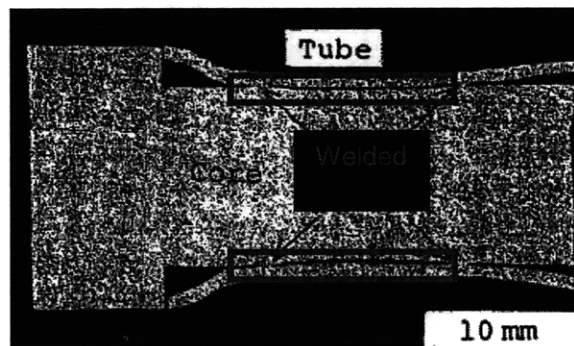


Figure 18: Example of the actual welded length (red box), from which the welded length ratio is calculated [18].

Specimens

The following Optical Microscopy (OM) and SEM analyses were performed at MIT. The OM samples were cut on the BUEHLER samplmet2 abrasive cutter with a BUEHLER 10-4120 blade. Unfortunately, during cutting, five of the eight welds broke, as shown in Table 8, which summarizes the OM specimens. Table 8 shows that five of the OM specimens failed during the preparation:

- Part of the welds in samples 2/1 and 13/1 opened during cutting.
- Weld 5/1 broke completely in the saw.
- Sample 9/1 overheated in the saw and opened as well.
- Then, sample 14/1 was cut in the EDM to avoid high mechanical forces during cutting, but opened during cutting as well.

Run	A	B	C	D	E=ABCD	during cutting, weld broke:	
	Taper Angle	Wall-Thickness	Diameter	Gap	Cleanliness	completely	on one side
1	-	-	-	-	+		
2	-	-	-	+	-		x
5	-	+	-	-	-	x	
6	-	+	-	+	+		
9	+	-	-	-	-		x
10	+	-	-	+	+		
13	+	+	-	-	+		x
14	+	+	-	+	-	x	

Table 8: Summary of OM specimens, which were investigated to measure the weld length. The table also shows which of the specimens broke during cutting. Five out of eight specimens broke on at least one side of the joint during preparation.

Furthermore, from Table 8 we can see that four of the five broken samples were uncleaned inner workpiece specimens. We will discuss the importance of the cleaning of the surface further in the discussion of this chapter.

Correct clamping, symmetric to the sample axis, turned out to be essential for a successful cut, since stress releases that occur after cutting through the welded region can displace the sample away from the center position. However, there seemed to be an elastic spring-back, which was responsible for the opening of the welds after having cut through the sample. Appendix D shows calculations made with an EMW calculation package provided by PULSAR, where we will show that residual stresses are still apparent in the sample after the EMW process, when using a process energy of 10 kJ.

For the SEM specimens, polishing was realized on the Handimet II Roll Grinder with grits of 240, 320, 400 and 600, at MIT. Further specimen preparation included grinding with grits of 800, 1200 and 2400 with subsequent polishing with ChemoMET PSA backed with grits of 9, 3 and 0.5 μm .

OM Results and Discussion

OM pictures have been taken on the stereo microscope, available at MIT and the corresponding R values have been calculated from the measured weld lengths of the 1" samples. An example of the OM photographs from which the actual welded length was measured is given in Figure 19.

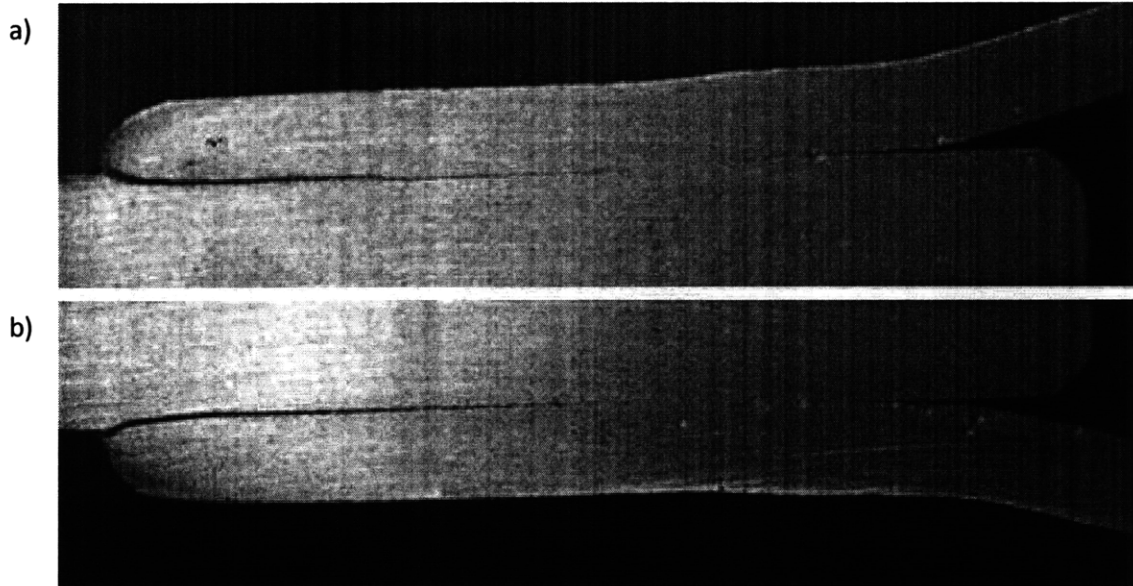


Figure 19: OM photograph of the cross section that was used to measure the welded length to calculate the welded length ratio of the corresponding specimen. a) Top section of the cut specimen. b) Bottom section of the cut specimen.

Table 9 shows the summary from the welded length ratio measurements for the OM study. Two R values were calculated for each side of the specimen (see Figure 19). An average for l_0 of 10.5 mm was used to calculate R for all the samples. Furthermore, it was impossible to measure the welded length for some specimens, being zero due to the breaking of the joint during cutting.

From Table 9 it can be seen that the weld length ratio measurements are very different depending on which side of the cut specimen (see Figure 19 for an example) the weld length was measured. This can be due to differences of the magnetic pressure around the outer workpiece during the EMW process. For example at the slit of the coil a much lower magnetic pressure will be induced upon the workpiece.

	A	B	C	D	E=ABCD	during cutting, weld broke:			
Run	Tapered Angle	Wall-Thickness	Diameter	Gap	Cleanliness	completely	on one side	R ₁	R ₂
1	-	-	-	-	+			20.0	19.0
2	-	-	-	+	-		x	0	38.5
5	-	+	-	-	-	x		-	-
6	-	+	-	+	+			66.7	49.5
9	+	-	-	-	-		x	29.5	0
10	+	-	-	+	+			40.0	76.1
13	+	+	-	-	+		x	61.8	0
14	+	+	-	+	-	x		-	-

Table 9: R values for the 1" samples, measured on the light microscope, for both sides of the cross section

Furthermore, another weld length ratio study using the SEM is presented in the Appendix D. There, we also compare the welded length ratios to the measured maximum loads from the tensile test experiments, presented in Section 4.4.3.4. Again, no conclusive results could be drawn from the welded length ratio measurements, because the measurement only takes place at one or two points along the circumference of the EMW joint. In the future, the author would suggest to do non-destructive ultrasonic testing of the EMW joints to measure the welded length ratios around the entire circumference.

Unfortunately, many of the specimens could also not be investigated at all, because of failure during the sample preparation. We will now present the results from the study of the samples in the SEM.

SEM Results and Discussion

The following SEM images show the polished un-etched samples. Figure 20 shows the outer end of the weld with a large notch at the weld interface.

Comparing the previously shown metallurgical analysis of the etched specimens with the SEM specimens, one can see that without etching of the surface, the EMW interface is not visible in the SEM. Furthermore, without etching no differentiation between the inner and outer tube is possible in regions

where bonding occurs. Figure 21 shows an SEM image of the weld interface at twice the magnification as in Figure 20.

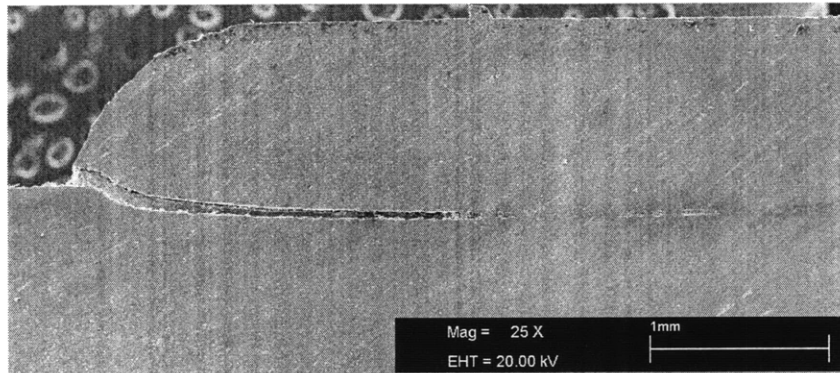


Figure 20: SEM image of the outer end of the EMW joint. Magnification = 25x.

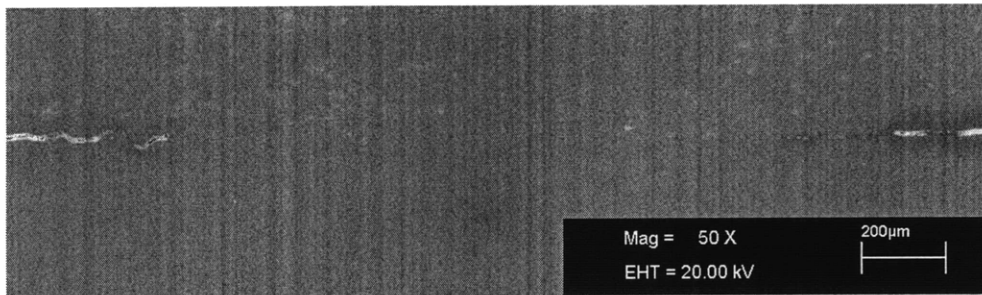


Figure 21: SEM image of the EMW joint after polishing. Magnification = 50x.

Again, from Figure 21, we can say that the weld interface is not visible and that only the end of the weld can be seen in the SEM. However, a bit of a wavy interface can be observed at the ends of the weld. Figure 22 shows an SEM image of the wavy interface with a magnification of 200x.

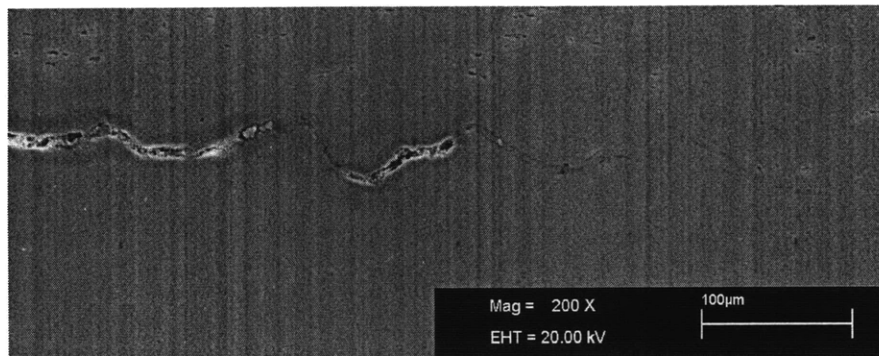


Figure 22: SEM image of the wavy interface showing the amplitude of the wavy interface of the EMW joint. The image was taken at the end of the weld. Magnification = 200x.

The SEM image in Figure 22 makes a wavy interface visible, which could have been welded, but cracked during the process or at a later time.

The next SEM pictures, show the samples being etched with the exact same preparations steps as described in the metallurgical analysis section. Figure 23 shows an SEM image of sample R4. The image depicts a region near the left notch of the weld length.

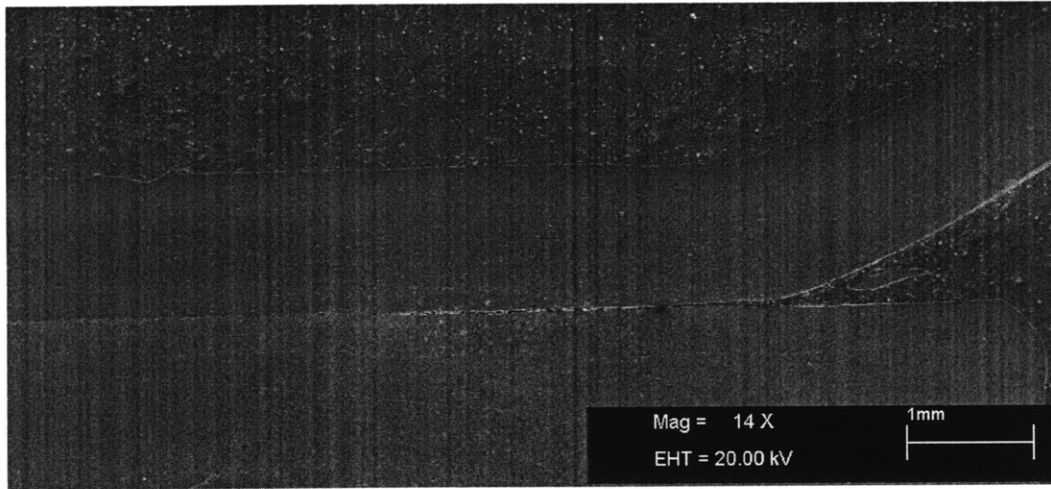


Figure 23: SEM image of an etched sample (R4). The image shows the right region of specimen.

From Figure 23 we can see that the etching of the sample as has made the wavy interface visible, in comparison to the un-etched sample (see Figure 20). The following SEM image in Figure 24 is an SEM image of the wavy interface, while moving a bit to the left and doubling the magnification, with respect to Figure 23.

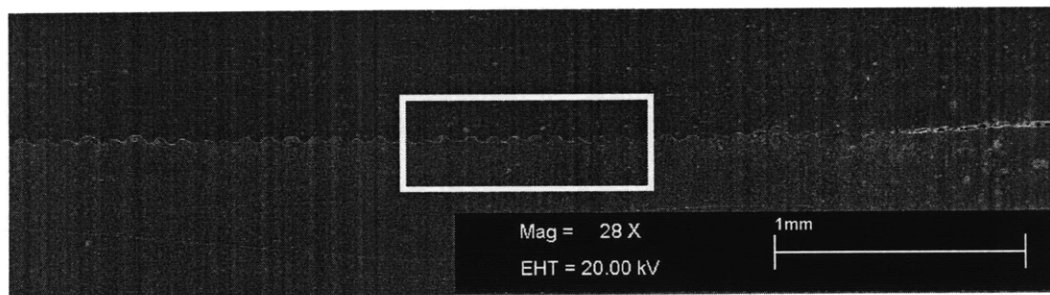


Figure 24: SEM image of an etched sample (R4) depicting the wavy EMW interface (28x magnification). The image shows the right region of the specimen. The white square marks the region that was observed in the following SEM image (Figure 25).

The following SEM image depicted in Figure 25a shows approximately the area that is marked with the white square, in Figure 24.

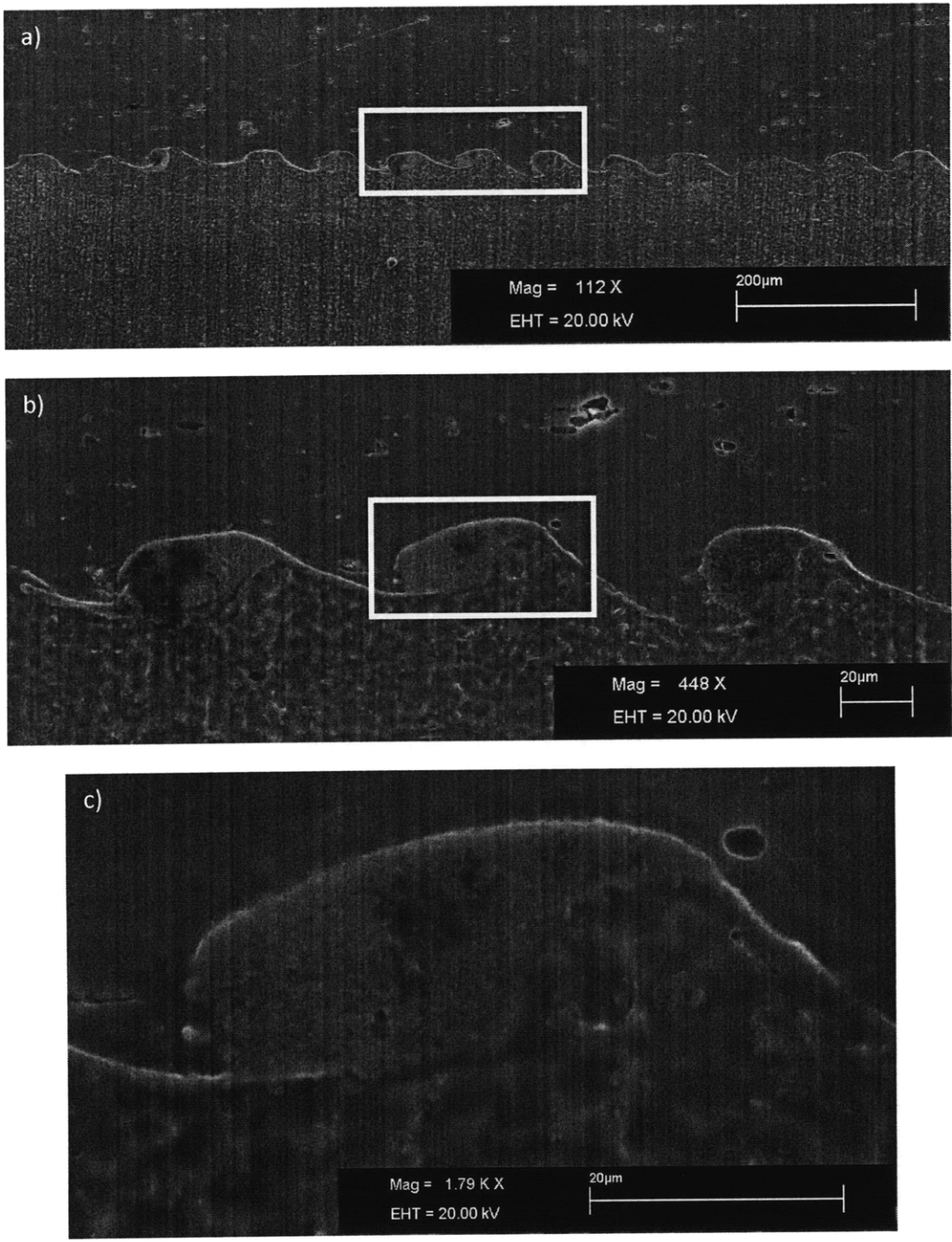


Figure 25: SEM image of an etched sample (R4) depicting the wavy EMW interface.
a) 112x magnification. The white square marks the region from the following SEM image (Figure 25b).
b) 448x magnification. The white square marks the region from the following SEM image (Figure 25c).
c) 1790x magnification.

Figure 25c shows the approximate view that we have already been able to observe through the OM study, see Figure 17. Again the hump size of the wavy interface is on the order of 20 µm.

In Appendix D we present another study of the weld length ratio of the un-etched specimens, however using SEM. Next, an Energy Dispersive Spectrometer analysis was performed to study the wavy interface and its chemical composition in more detail.

4.4.3.3 Chemical analysis– EDS

Energy Dispersive Spectrometer (EDS) micro-analysis is performed by measuring the energy and intensity distribution of X-ray signals generated by a focused electron beam on the specimen (EDS). With the attachment of the energy dispersive spectrometer, the elemental composition of materials can be obtained.

Measurement

In this section we present the chemical analysis of the wavy interface using the EDS setup at the Materials Welding and Joining Laboratory, at MIT. The samples were mounted in the SEM, which was used to image the EMW joint presented in the previous section. Then the SEM was turned into EDS mode and a chemical analysis of the wavy EMW joint interface was performed.

Results and Discussion

Figure 26 shows an SEM image of sample R4, but on the left side of the weld interface. The white squares marked (1) and (2) show the areas that were studied using EDS.

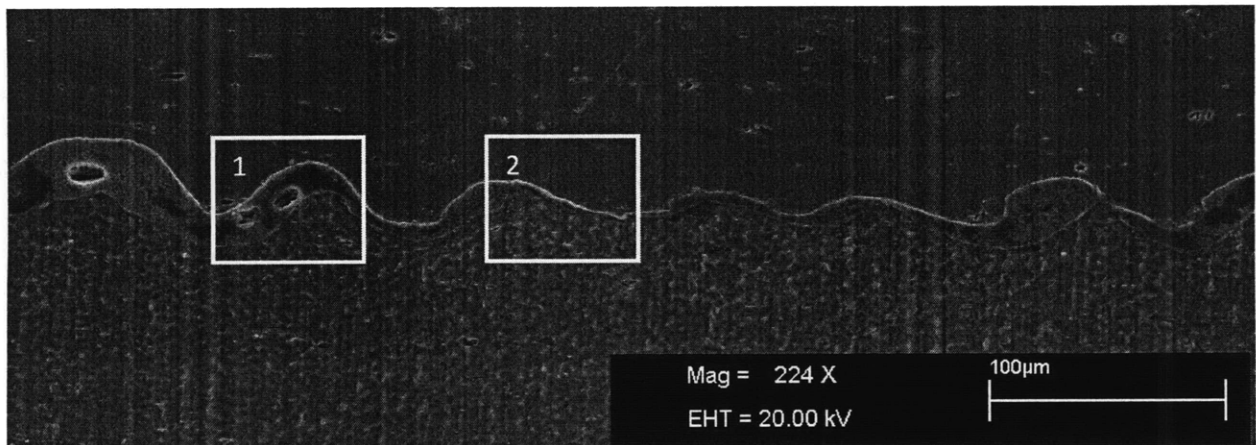


Figure 26: SEM image of an etched sample (R4) depicting the wavy EMW interface (224x magnification). The image was taken in the left region of the weld near the fringe.

Figure 27 shows an EDS study of an etched EMW sample and its wavy interface (sample R4). The area which was studied is marked in Figure 26 by square (1). Figure 28 shows an EDS study of the same

sample, as in Figure 27, but in a region of the weld where the humps of the wavy interface are not that pronounced. The studied area for this case is marked in Figure 26 by square (2).

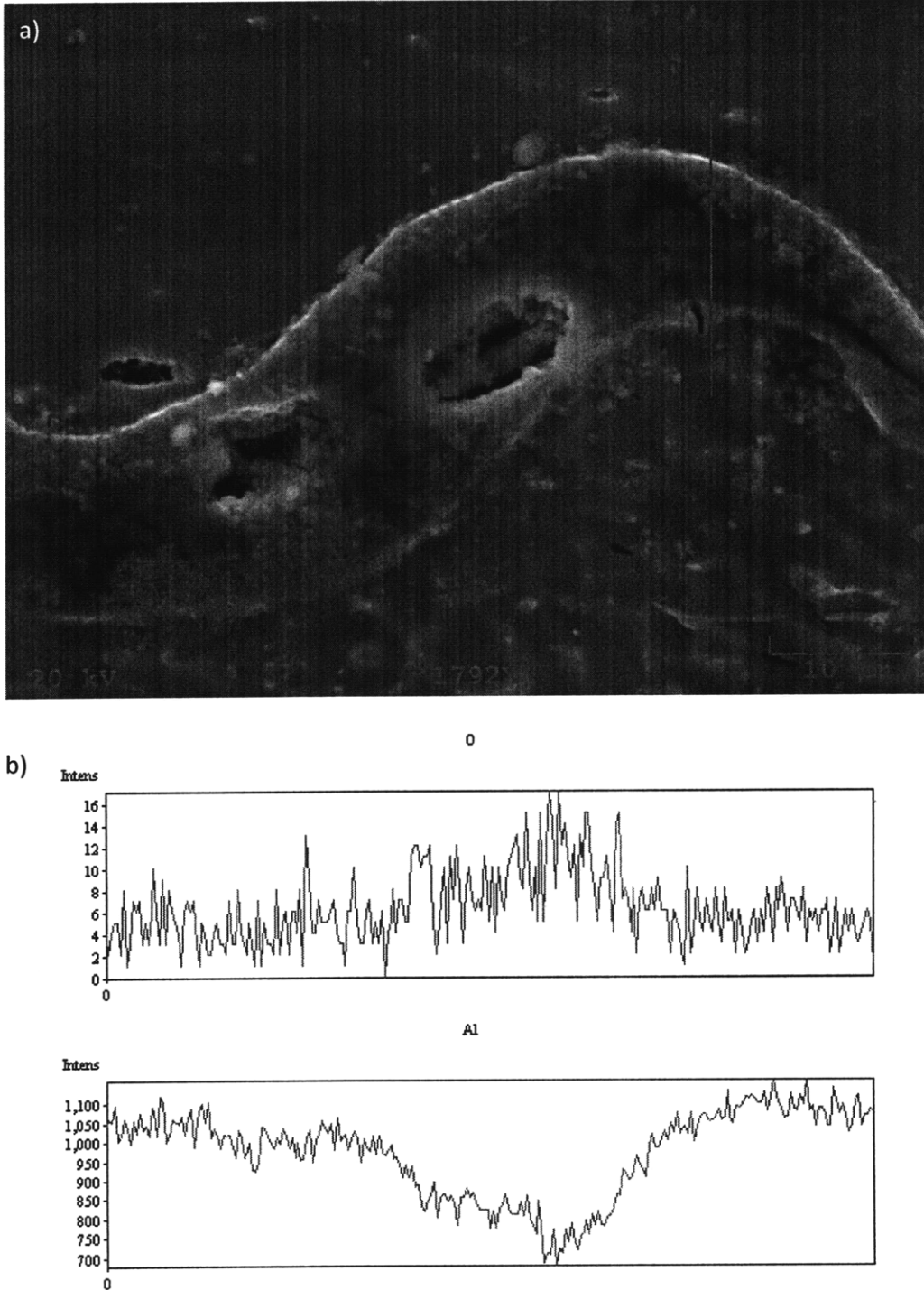
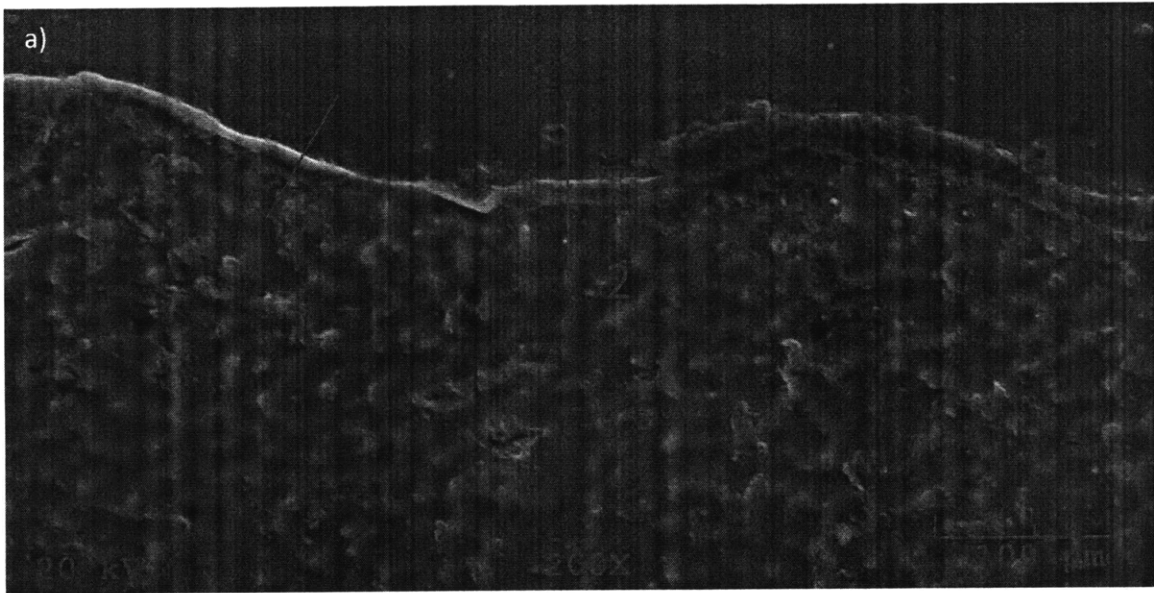


Figure 27: a) 8x Zoom of the left region shown in Figure 26. The red line is an EDS line-scan.

b) EDS analysis of the line-scan



b)

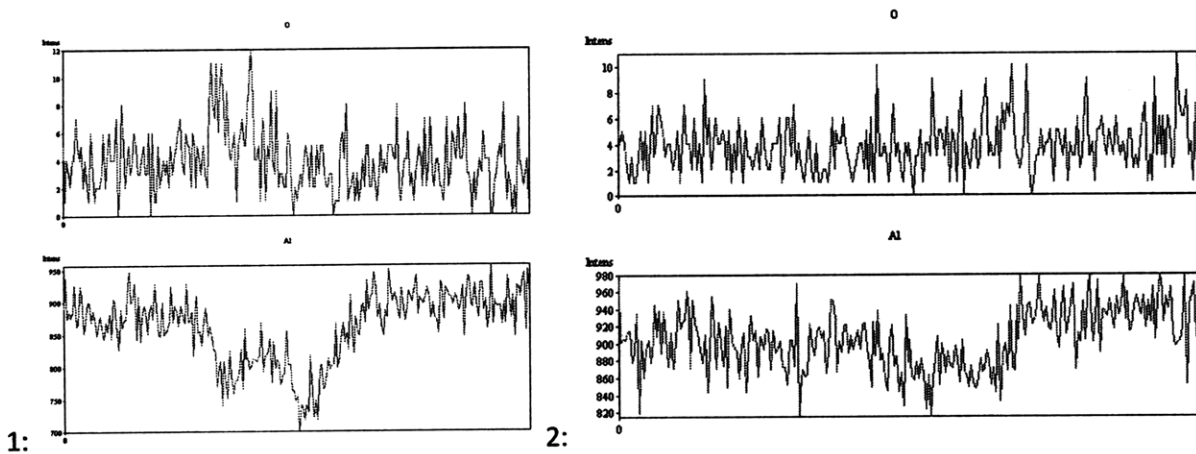


Figure 28: a) 4x Zoom of the middle region shown in Figure 26. The red lines are EDS line-scans.

b) EDS analysis of the EDS line-scans 1 and 2.

The intensity of the oxygen content in Figure 28 for the EDS line scan 1 and 2 is approximately 5. The intensity of the aluminum content always drops right at the interface. This could be due to the mismatch of the crystal lattices, which therefore are not as closely packed as in the bulk.

In Figure 27, where the humps of the wavy interface are far more developed, we observe a definite spike in oxygen content and again a drop in aluminum content. The rise in oxygen content at the joint interface must be due to trapped oxygen and, therefore trapped oxide, which was not fully ejected during the EMW process.

Summary of Optical Evaluation

We were able to show the wavy interface through Optical Microscopy, as well as SEM. The SEM study was accompanied by an EDS study, which was used to study the chemical structure across the wavy EMW joint interface. We were able to observe a low bulk material content right across the interface, as well as an increase in oxygen content. We interpret this observation as the trapping of left oxide in between the two material surfaces at the new interface. The focus, however in this study was not the metallurgical analysis of the EMW joint, as other authors have already studied the importance of the metallurgical aspect, in the past. This was also done for dissimilar metals which prove to be a more interesting field as far as the metallurgical study is concerned. For example, the following features have been reported (summarized by M. Marya and S. Marya in Interfacial microstructures and temperatures in aluminum-copper electromagnetic pulse welds):

- 1) Extensive grain elongation in the welding direction [4, 5]
- 2) Residual dislocation densities of the order of 10^{11} cm^{-2} near the bond interface [5]
- 3) Recrystallisation and recovery in bands on both sides of the high dislocation density regions [6,7]
- 4) Limited diffusion across the weld interface [5]
- 5) Submicroscopic interfacial melting ($< 5\mu\text{m}$) [6,7], etc.

The major interest, also through the scientific objectives of this FORD-MIT alliance project (see Chapter 1) was the study of the circuit parameters (covered in Chapter 2) and the importance of several welding parameters, which have been investigated by the proposed DOE, in the following section. The parameters influence on the final result, the measured maximum load on the specimens in a tensile test, was studied and the DOE was helpful to give directions for the second batch of experiments and will certainly be helpful for future parameter studies.

4.4.3.4 Tensile Tests and DOE Results

Tensile tests performed on the specimens of the first DOE batch (August 2007)

Experimental

The tensile tests were performed on an MTS, model number 311.21. The used load cell had a rating of 50kN. The tests were performed at a strain rate of 0.02 min^{-1} . Inserts were placed inside the cylinders of the welded parts, so the grips of the tensile testing machine would not crush them. The diameters of the inserts were 35.1 mm and 36.1mm in diameter, for the 1.5" diameter with 1.5mm and 1 mm wall-thickness samples, respectively. The diameters of the inserts were 22.4mm and 23.4 mm in diameter, for the 1" diameter with 1.5mm and 1 mm wall-thickness samples, respectively.

Results and Discussion

Table 9 shows the results of the tensile test for the first DOE study. When comparing the strength of the EMW joints with the base material strength of the Al6061-T6 tubes we can make the following observations, for the first batch of the DOE:

The strength of tubular base material Al 6061 T6 can be calculated, multiplying its ultimate tensile strength of 310 MPa with the cross-section of the tube (which will change depending on the wall-thickness). Using these values we get the following base material strength, displayed by the maximum force in Newton, for the 1.5" and 1" tubing:

- 1.5" diameter with a wall-thickness of
 - 1.5 mm: 53.5 kN
 - 1.0 mm: 36.01 kN
- 1" diameter with a wall-thickness of
 - 1.5 mm: 34.9 kN
 - 1 mm: 23.8 kN

Now, looking at the maximum measured strengths of the tested EMW joints we get the following results:

- 1.5" diameter, cleaned with a wall-thickness of
 - 1.5 mm. : 31.3 kN
 - 1 mm: 32.3 kN
- and un-cleaned with a wall-thickness of
 - 1.5 mm. : 28.4kN
 - 1 mm: 24.5 kN
- 1" diameter, cleaned with a wall-thickness of
 - 1.5 mm. : 34.3 kN
 - 1 mm: 21.5 kN
- and un-cleaned with a wall-thickness of
 - 1.5 mm. : 11.3 kN
 - 1 mm: 16.6 kN (2 mm gap)

When comparing the values of the base material of the Al6061-T6 tubing with the presented EMW joints, we observe the strongest EMW joint with a maximum force of 34.3 kN for the 1" diameter case (C=-), which was also cleaned (E=+), had a gap of 2 mm (D=+), a wall thickness of 1.5 mm (B=+) and a taper angle of 0 degrees (A=-). This EMW joint is almost as strong as the base material for the 1" diameter and 1.5 mm wall-thickness case, which has a maximum force 34.9 kN.

The second strongest EMW joint with a maximum force of 32.3 kN was observed for the 1.5" diameter (C=+) case, which was also cleaned (E=+), had a gap of 2mm (D=+), a wall thickness of 1mm (B=-), and a taper angle of 0 degrees. (A=-). However, the base material has maximum force of 36.01 kN.

DOE Results and Discussion

Three DOE plots were analyzed from the presented DOE and are described in Appendix D. The outcome of the DOE study is similar to what has been found above and states that the gap and cleanliness are the most important parameters to affect the final tensile strength of the EMW joint, with a probability of 90% (see Appendix D).

Furthermore, it could be found that a taper angle of 2.5 degrees has a negative effect with increasing wall-thickness. It could be possible that the taper angle increases the gap between the inner and outer workpiece beyond a distance after which the velocity of the outer workpiece is not high enough anymore to create a proper EMW joint. Therefore, the tensile strength decreases for the larger wall-thickness and larger taper angle. So, in the case of our setup, we are observing stronger joints for lower taper angles.

	A	B	C	D	E=ABCD		
Run	Taper Angle	Wall-Thickness	Diameter	Gap	Cleanliness	max force [kg]	Displacement at max force [mm]
1	-	-	-	-	+	303	0.813
2	-	-	-	+	-	1709	0.692
3	-	-	+	-	-	701	1.642
4	-	-	+	+	+	3356	1.551
5	-	+	-	-	-	1162	3.01
6	-	+	-	+	+	3523	1.332
7	-	+	+	-	+	2679	1.123
8	-	+	+	+	-	2917	0.784
9	+	-	-	-	-	837	0.461
10	+	-	-	+	+	2223	1.065
11	+	-	+	-	+	-	-
12	+	-	+	+	-	2454	1.058
13	+	+	-	-	+	1404	0.434
14	+	+	-	+	-	619	0.365
15	+	+	+	-	-	423	0.362
16	+	+	+	+	+	3267	1.759

Table 9: Tensile test results (bold letters used for samples of 1.5" in diameter). Specimen R11 was not tested during the tensile tests of the first DOE.

Figure 29 and Figure 30 summarize all tensile test experiments that were performed for the first DOE study.

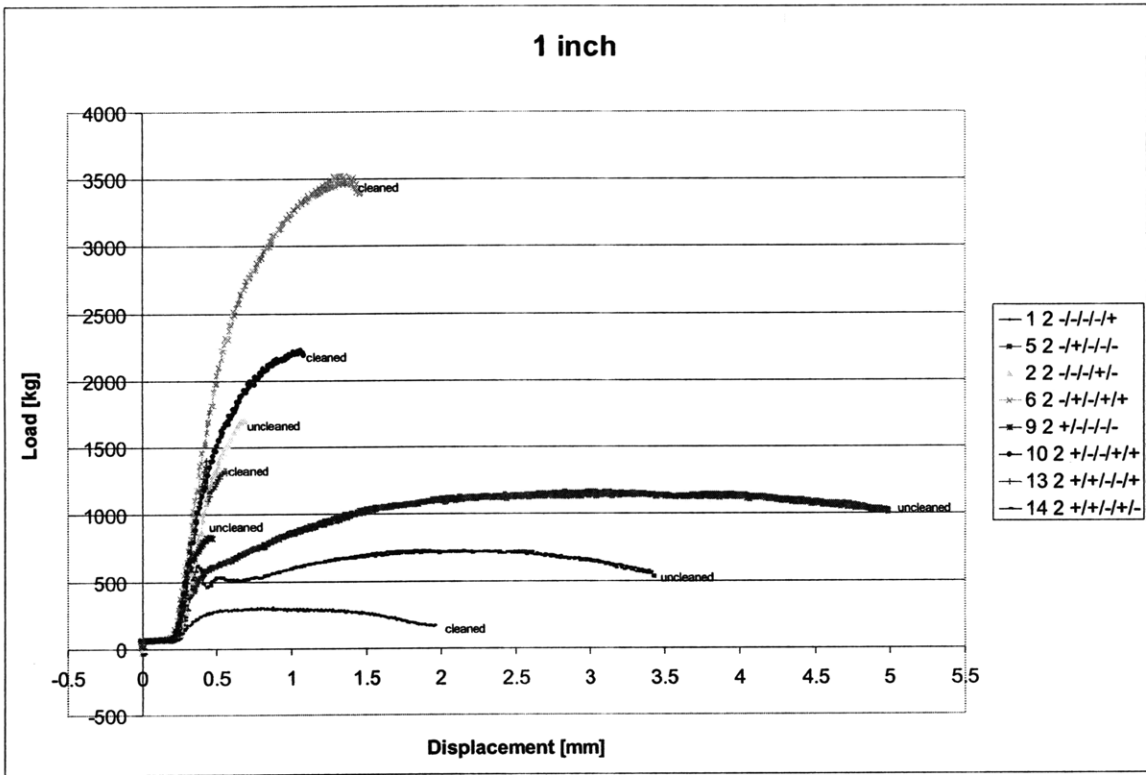


Figure 29: Tensile test results for the 1" EMW specimens of the first DOE batch (August 2007).

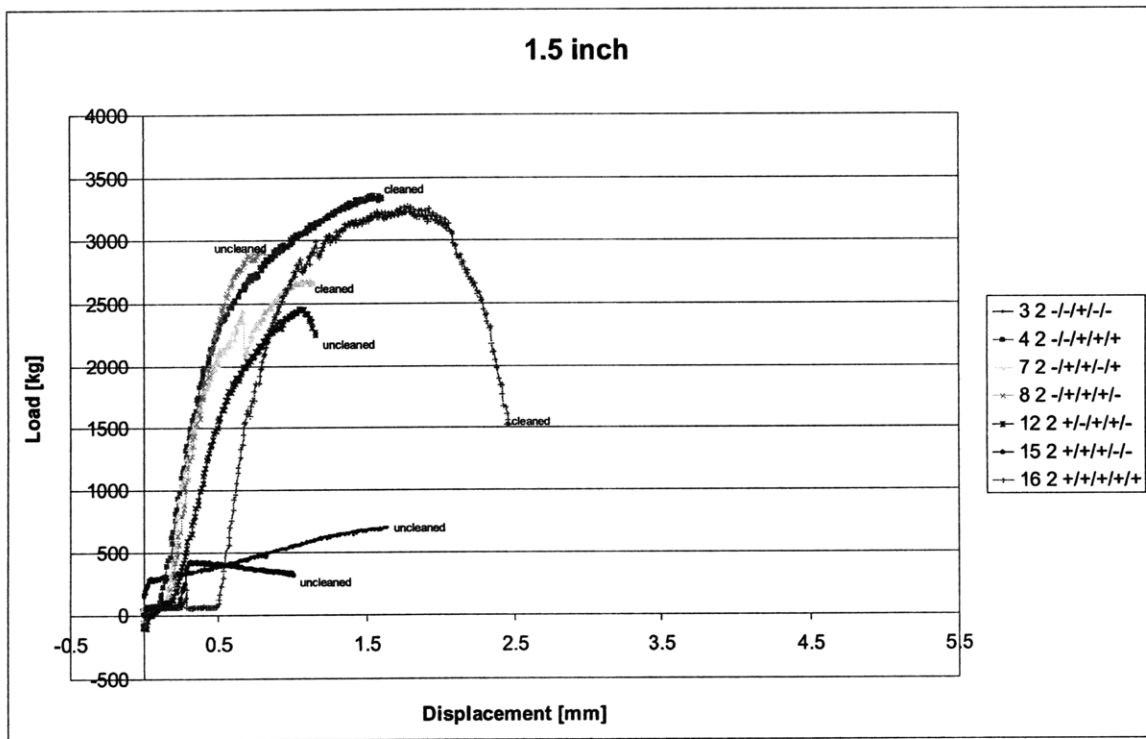


Figure 30: Tensile test results for the 1.5" EMW specimens of the first DOE batch (August 2007).

In general, cleaned samples seem to perform better in tensile tests than samples that haven't been cleaned before welding. Another essential parameter seemed to be the gap size. Samples with a bigger initial gap between the workpieces (2 mm) tended to show considerably higher strengths in the tensile tests than samples welded with the smaller gap (1 mm). The two strongest welds within both the 1" and the 1.5" sample runs are the ones that had a big gap size and were cleaned before welding.

Surprisingly, weld 13 and 14 that had the highest measured R-values did not perform best in the tensile tests, and the descending order in R-values did not match the maximum forces applied in the tensile test. This was probably due to the fact that the weld was not continuous along the circumference and the measured R-values, which are only measured at one (if the specimen broke on one side during cutting) or two points along the circumference, are not representative for the average weld length.

Appendix D shows the results from the DOE proving the observed statements that the gap and cleanliness were the parameters which affected the final strength of the weld the most and should be optimized primarily in the future.

Tensile tests performed on the specimens of the second DOE batch (November 2007)

Experimental

The tensile tests for the second batch of EMW specimens were performed on an INSTRON 4206. The used load cell had a rating of 150 kN. The tests were performed at a strain rate of $0.02'' \text{ min}^{-1}$, same as for the first batch.

This time, to fix the EMW joints to the tensile machine, Al6061-T6 rods were inserted into the Al tubes and welded together. The rods welded into the 1'' and 1.5'' samples were $7/8''$ and $1\ 3/8''$ in diameter respectively.

Then, holes with a diameter of 0.5'' were drilled into each end (the new attached rod, as well as the inner workpiece, in order to attach the samples to the tensile testing machine. Figure 31 shows the new kind of tensile specimen for the 1'' EMW joint, as well its setup in the INSTRON machine.

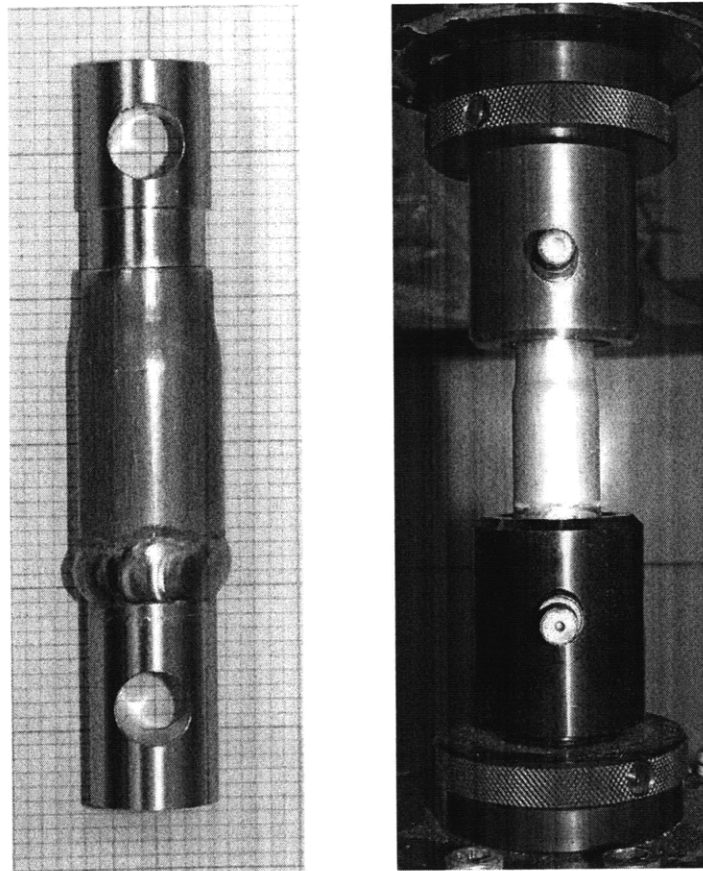


Figure 31: a) Photograph of the 1'' tensile specimen. The background of the photograph shows the scale of the image, where one little square is a tenth of an inch in size.
b) Photograph of the tensile test setup for the second batch of EMW specimens. The setup shows the pins that go through the drilled holes of the specimen and the holding fixture of the machine, thereby connecting the two.

The schematic drawings of the new samples for the 1'' and 1.5'' specimens can be found in the Appendix D.

Furthermore, it was possible to perform each tensile test twice for each DOE experiment, because this time the other half of the 32 specimens was not used for SEM or OM evaluation.

Results

Table 9 and Table 10 show the maximum measured loads for the 1” and 1.5” specimens, respectively. The maximum load was calculated from the average of the two tensile tests performed on two specimens with the same DOE parameters. The values for all the tests can be found in the Appendix D.

	A	B	C	D	E=ABC	F=BCD	
Run	Taper Angle	Wall-Thickness	Diameter	Gap	Cleanliness	Surface Condition	maximum load (kg)
1	-	-	-	-	-	-	524
2	-	-	-	+	-	+	648
5	-	+	-	-	+	+	1696
6	+	-	-	-	+	-	1896
9	+	-	-	-	+	-	1543
10	+	-	-	+	+	+	1465
13	+	+	-	-	-	+	361
14	+	+	-	+	-	-	278

Table 9: Maximum measured loads for the 1” specimens.

	A	B	C	D	E=ABCD	F=BCD	
Run	Taper Angle	Wall-Thickness	Diameter	Gap	Cleanliness	Surface Condition	maximum load (kg)
3	-	-	+	-	+	+	840
4	-	-	+	+	+	+	847
7	-	+	+	-	-	-	782
8	-	+	+	+	-	+	1055
11	+	-	+	-	-	+	112
12	+	-	+	+	-	-	159
15	+	+	+	-	+	-	2051
16	+	+	+	+	+	+	3546

Table 10: Maximum measured loads for the 1.5” specimens.

As stated before, the maximum load values were calculated through the average of the two maximum loads for the two tensile tests performed per DOE run. However, a second test was not performed for the 1” specimens R1 and R5 and therefore one value had to be used in the DOE analysis. The same was the case for the 1.5” specimens R3, R4, R7 and R16. In the case of the R3 and R7 the

wrong surface condition (DOE parameter F) was applied to the specimens the tests and they were therefore not taken into account in the DOE analysis. R4 was also only tested once and R16 showed a rupture in the specimen fixture at the weld, which cause a very low maximum load during the tensile tests and was therefore also removed from the DOE analysis. All tensile test data and failure modes of the individual samples can be found in the Appendix D.

From the results presented in Table 9 and Table 10, it can be clearly seen that cleanliness is one of the most important parameters for the final strength of the EMW joints. In fact, for the 1" specimens all cleaned specimens showed the highest maximum loads during the tensile tests. For these specimens, failure in the base material of the specimen was observed. Also, for the two 1.5" specimens (R15 and R16; see Table 10) failure in the base material could be observed. They were specimens, for which the inner workpiece was cleaned prior to the EMW process and they showed the highest maximum loads.

However, it needs to be stated that the values of the maximum loads were larger on average for the first DOE, when comparing the values from the first DOE (August 2007) to the values of the second DOE (November 2007). There was only one specimen (R16) which showed a high maximum load of 3546 kg, which compared to the theoretical strength of 5460 kg, for this case, still seems small. On the other hand, all the specimens with the highest maximum loads that also were cleaned before the EMW process, as stated above, showed failure in the base material of the tensile specimen, which is usually a sign for a good weld.

The decrease in strength in comparison to the first DOE could be due to the fact that the new DOE parameter of surface condition could actually be harmful to the final strength of the EMW joint. Another cause could be the increase in energy for the second DOE from 10 kJ to 12kJ. This value was not tested in the DOE and can therefore not be shown to be significant for the observed decrease in overall strength of the joints. Another value could be the application of oil (DOE parameter E = +), which was then equally for each DOE, but could have differed between the two DOEs (August and November 2007). Possibly, for the second DOE, more oil was applied to the surface of the inner workpiece causing a part of the observed decrease in strength.

DOE Results and Discussion

In our first DOE analysis of the measured tensile strength presented in we showed that the gap and the cleanliness were strong DOE parameters, which would affect the tensile strength the most, besides the obvious parameters such a diameter and wall-thickness.

For the second batch of DOE experiments, the results were very inconclusive, at first sight. The DOE would help clarify the data. Figure 32 shows the cube plot of the second DOE giving a good overview of the importance of the different parameters on the final strength of the EMW joint.

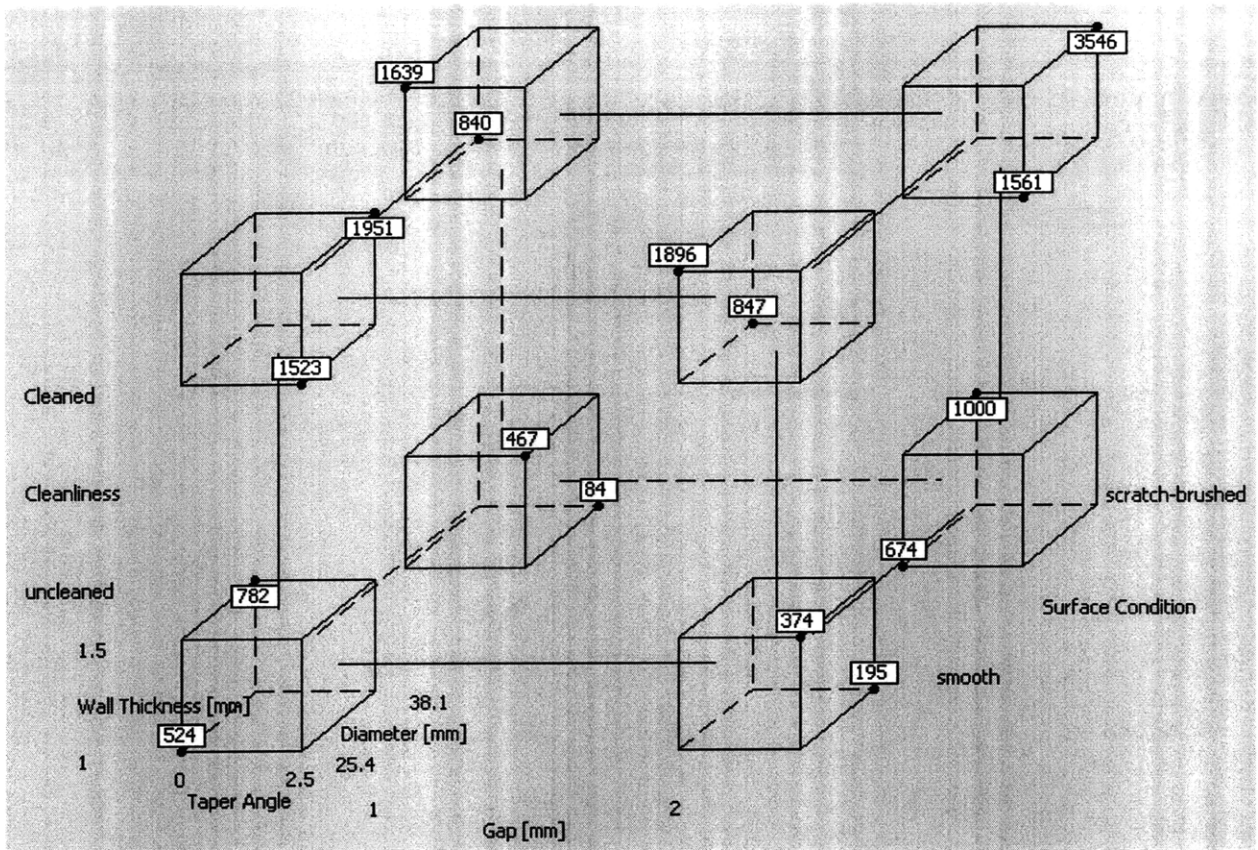


Figure 32: Cube plot of the DOE analysis for the first batch of EMW specimens. The values at the corners of the cubes show the values of the measured maximum loads in kg. The x-axis, the y-axis and the z-axis, of the entire plot, show the parameter gap, surface condition and cleanliness respectively.

From Figure 32 we can see right away that again cleanliness has the strongest effect on the final strength of the EMW joint. The other parameters do not seem to have an effect that can clearly be identified.

Through further DOE analysis, which is presented in Appendix D, we were able to find two further effects that had a strong effect on the final strength of the EMW joint: the wall-thickness and the interaction of the taper angle with cleanliness.

The first finding that the wall-thickness affects the final strength of the EMW joint is obvious, but it is still important, because in the case of the EMW process a larger wall-thickness will also mean a larger mass that needs to be accelerated. Therefore, it is very good that we can show that this wall-thickness clearly increases the strength of the final joint.

The second observation is very interesting, because it has a connection to the actual formation of the jet-stream, which removes the oxide of the outer and inner workpiece, during the EMW process and could be affected by an interaction of the taper angle and cleanliness of the surface.

Two EMW Designs of Experiments were performed in this study. The first batch was done with 10 kJ and the second batch was done with 12 kJ, which would be the upper limit of the possible energy for the coils provided by PULSAR.

The EMW process calculations package, provided by PULSAR during the experiments in November 2007, states that with 10 kJ as well as with 12 kJ one still gets residual stresses in the final EMW joints. This was observed for some of the samples during cutting, for the preparation of the weld length ratio measurement. As far as the observed weld lengths are concerned, however, which were observed through a metallurgical analysis performed on the first batch of DOE specimens, an appropriate weld length was observed.

On the other hand, we could not get conclusive results from the weld length ratio measurements, which were performed at MIT. Future non-destructive analysis such as ultrasonic testing would be a better choice to get better results for the weld length ratio measurement around the entire circumference of the EMW joint.

Bibliography – Chapter 4

[1] Antony, Jiju. Design of Experiments for Engineers and Scientists. Oxford: Butterworth-Heinemann, 2003.

[2] Montgomery, Douglas C. Design and Analysis of Experiments. 6th ed. Hoboken: John Wiley & Sons, Inc, 2005.

[3] Pulsar Ltd.

[4] ASM Handbook. Welding Brazing and Soldering. Vol. 6, American Society for Materials (1993).

[5] L.F. Trueb. J. Appl. Phys., (1986), 40, 2976-2987.

[6] L.I. Markashova, Y.U.A. Sergeeva, V.V. Statsenko, V.A. Chudakov. Paton Weld. J., (1991) ,187-191.

[7] A. Stern, M. Aizenshtein. Sci. Technol. Weld. Joining, (2002), 7, 339-342.

5 Conclusions and Future Work

The EMF and EMW processes are examples of multidisciplinary research as the phenomena associated with them fall under the several branches of engineering sciences. The goal of my research during this FORD-MIT Alliance project (Section 1.3) became the study of EMF and EMW, their parameters and outcome, which affect the final joint and the energy needed to achieve a proper EMW joint.

Using the observations made in this study, we propose several methodologies to study and optimize the process, thereby lowering the necessary process energy and lengthening the life-time of the tooling and equipment. The hope is that EMW can be verified as a high volume automotive welding process which will enable greater use of aluminum in low to moderate price vehicles, thereby improving fuel economy and other customer-perceived characteristics, such as performance, handling and corrosion resistance.

In Chapter 1 we presented a literature search on Cold-Welding, EMF, Explosive Welding and EMW. Important observations that have been made in the past are presented by categorizing them into deformation theory, circuit theory and energy theory. Finally, limiting conditions observed for explosive welding to achieve a proper joint are presented and combined with findings from the EMW and Cold-Welding literature.

Findings of particular importance are the effect of surface preparation, as well as the surface hardness of the workpieces. This becomes especially important later on, when looking at welding windows displaying the possibility of creating an EMW joint based on the threshold velocity (and in our presentation threshold kinetic energy) and the surface hardness of the material of the outer workpiece (presented in Chapter 4).

It is not an easy task in the field of EMW to study the process, because there are only a few providers of EMW machinery in the world, PULSAR and MAGNEFORM. Through the FORD-MIT Alliance it was difficult to obtain a source of EMW specimens, because FORD owns an EMW machine constructed by PULSAR, in Detroit, however, the machine was tied up for the entire length of this study and the promised experiments could never be performed.

The author was able to create a collaboration with PULSAR in Israel through the course of this study and also with LSTC, in California. LSTC, in California is currently working on a very sophisticated LS-DYNA model for the EMF process and is on the verge to convert it to an EMW process model. However, due to the lack of EMW data in the literature it was not yet possible to prove the model. Through the collaboration we provided LSTC with Solidworks drawings of the EMF coil accompanied by

measurements of the EMF process at MIT (see Section 2.4.4 LS-DYNA Simulation Effort). LSTC would provide the meshing of the coil drawing, which would make the model ready to simulate the EMF process, at MIT. In the future the same process could be used to study and simulate the EMW process, for example at PULSAR. The author hopes that the presented data will add to the optimization of the LS-DYNA model and make it possible to create simulations, without the difficult efforts necessary to create a good setup for EMW and test the many parameters that affect the process.

In Chapter 2 we studied the EMF process in detail and showed that the theorem of a critically damped RLC circuit is of great importance to create the energy necessary to achieve an EMW joint. Through the proposed theorem of a critically damped circuit the RLC parameters can be tuned so that a short and maximized discharge current pulse can be achieved. This optimization is observed and necessary for good EMW machinery, such as provided by PULSAR.

Furthermore, we created a MultiSIM model that lets the user of such RLC circuit machinery, be it EMF or EMW, simulate the process to a certain point. It is possible with the current MultiSIM model to extrapolate the inductance of the machine, as well as the resistance of the machine. These are important parameters, which also need to be taken into account to fulfill the conditions for a critically damped circuit. Furthermore, it is possible to observe any changes in voltage or current, by changing the circuit parameters in the model and study their effects. For example, it can be studied how a very low inductance on the order of nanoHenries (with the appropriate R and C parameters) suddenly can change the circuit from a normal RLC circuit into a critically damped circuit.

By comparison of the MultiSIM model and our experimental data, we were able to determine the unknown machine inductance and resistance of the MAGNEFORM machine that was used for the EMF experiments presented in Chapter 2, at MIT. The measured inductance and resistance were $0.001 \mu\text{H}$ and 0.001Ω , respectively. Therefore, the machine inductance and resistance represent very good values, but the measured maximum input voltage and inductance of the coil ($V = 10 \text{ kV}$ and $L_c = 23 \mu\text{H}$, respectively) will always keep the discharge current levels and behavior limited to an EMF process.

Next, we present a MATLAB model of the RLC circuit consisting of the current and deformation equations presented in Chapter 1 and it was possible to calculate the discharge current curves, as well as the magnetic pressure curves for the EMF setup at MIT and compare them to the measured data curves. It was then possible to use the machine data from the EMW machine at FORD, in Detroit and calculate the machine's current curves and magnetic pressure curves. By comparing the two calculations we could show that the chosen inductance of 38 nH was a very good value to observe a critically-damped behavior for the EMW machine at FORD. On the other hand, as stated above, the measured coil and machine inductance means the machine at MIT will only perform EMF. Furthermore, it was possible to calculate the velocity and acceleration curves of the following EMF experiments and even propose an optimal gap of 1 mm between an outer and inner workpiece (if used in the EMF setup) to achieve a maximum velocity of about 50 m/s , in the case of our tested Aluminum tubing (Aluminum cans material: AA3004).

The MAGNEFORM machine, at MIT was modified intensely and several additional measurement devices were added to the setup to study the EMF process in detail. The observations made were then used to prepare for the EMW experiments. Current and voltage was measured through a Pearson current monitor, as well as through a self built voltage probe. From the measured curves it was possible to calculate the power that was apparent during each firing of the machine, as well as the energy created.

High-Speed Videography studies would add further data points to the observations and equipment was loaned from the Edgerton Center. High-Speed Videos were taken of several experiments, at MIT. It was possible to compare the calculated workpiece velocity to the measured velocity and get maximum values on the order between 50 m/s and 100 m/s.

Furthermore, the observations that have been made with the High-Speed Video equipment are of great importance to improve the LS-DYNA EMF model from LSTC. With regard to the EMF model and the comparison of the simulation to the data observed in the experiments, X-rays of the coil were taken and a Solidworks model of the MAGNEFORM EMF coil, at MIT, was created. This Solidworks model is an accurate representation of the compression coil and can provide a good base for future EMF simulations using the LS-DYNA EMF model and the data provided from the High-Speed Videos.

Not only velocity measurements, but also power measurements were performed, as stated above. The deformation of the individual workpieces was noted and compared to the power that was injected into the EMF process. For the Aluminum tubing (AA3004) a decrease of up to 50% in outer diameter was observed.

With this background it was then possible to study the change in mechanical strength of metallic tubing being subjected to an outer pressure, while introducing wrinkles in the circumference of the tubing. The literature presents the buckling of tubular parts as a large problem, as their mechanical strength is decreased, through the introduction of wrinkles. In the case of this study, however, we propose to use the decrease in mechanical strength of the tubing as an advantage. We propose that through a two step process, where first wrinkles are introduced into the outer workpiece through an EMF compression step onto a mandrel the mechanical properties are reduced and a following EMW step will only require a reduced energy to deform the workpiece onto the inner workpiece, creating an EMW joint far more efficiently. We presented the theoretical background of the deformation of tubular workpiece through an outer pressure, as well as the dependence of the necessary collapse pressure on the number of wrinkles. Then we tested the proposed strategy in the EMF MAGNEFORM machine, at MIT. A workpiece was deformed several times onto a mechanically much stronger mandrel, thereby creating a controlled deformation of the workpiece and introducing a controlled number of wrinkles. After that the mandrel was removed and the change in diameter was measured and compared to the change in diameter of a workpiece that was compressed without any prior buckling. We were able to show a critical number of wrinkles n , between 7 and 9, for our setup dimensions at which point a much larger deformation of the workpiece could be observed at the same level of energy. In the future, an optimal mandrel design could be proposed, thereby, creating good coupling when the EMW process step is performed. Furthermore, experiments should be performed to observe the effect and measure

the amount of energy that can be saved during the EMW process step. Possibly, the total energy could be larger than during the usual process, but the maximum energy for the individual steps will be lower, thereby, increasing the life of the tooling equipment.

Finally, to complete the study of EMF and its possibilities we manufactured a fieldshaper for the EMF setup at MIT. We were able to prove the concept of the fieldshaper, as well as point out interesting facts about the design such as the necessity of a flexible insulation material in the slit of the fieldshaper. The tested samples were chosen to have no tapered angle, a tapered angle and a groove with adhesive inside, respectively. Only the specimens with the groove inside the inner workpiece were proper joints. The strengths of the joints were tested in tensile tests, but the results were not very promising, due to the lack of energy of the MAGNEFORM machine. In any case, we were able to show the concept of a fieldshaper, as well as some first steps towards studying the effect of an adhesive in an EMF joint, which could be beneficial against corrosion problems.

In Chapter 3 we present a failure study of an Aluminum Bronze Bitter coil, tested at FORD, in Detroit and sent to MIT. This chapter covers some of the most important findings for the EMW process, in this study. Bitter coils, as intended to be used in the automotive industries for the EMW process, have very short life expectancies. A tendency to move towards single-turn coils, which show far better mechanical properties, should be suggested, at this point. Furthermore, many aspects with regards to the materials selection, as well as the surface and material preparation to avoid preliminary defects in the tooling equipment must be accounted for to secure its long life-time.

Through the failure analysis of the Aluminum Bronze Bitter coil, the failure mechanisms were carefully studied through optical microscopy and metallurgical analysis. We were able to deduct four reasons for the initiation and propagation of cracks in EMW and electromagnetic process with high currents, in general. The first cause and so-called first stage (Stage I) of crack initiation and propagation, which has usually mainly been accounted for the low life-time of the coils, is the magnetic pressure acting on the workpiece, which in turn also acts upon the tool. Furthermore, the high eddy currents cause Joule Heating of the material and can cause temperatures, close to the operating temperature or even to the melting temperature of the material. In the case of the Aluminum Bronze Bitter coil the temperature rise, due to the current of 800 kA, was calculated to be 291 K. Furthermore, we were able to observe the heat-affected zone (HAZ) caused by the eddy currents through the metallurgical analysis. Measurements of the HAZ showed a thickness of 470 μm , which is on the order of the theoretical skin depth for the presented Aluminum Bronze alloy of approximately 200 μm .

We found another three factors that play into the decrease of life-time for tooling equipment in high-current electromagnetic processes. The second factor, also called Stage II, accounts for the existence of a crack, defect or stress concentration due to the tool design. This defect will cause a multiplication of the inherit problems already observed in Stage I. Especially, the current concentration at such defects causes a much higher rise in temperature than usually observed along the tool surface. Furthermore, Stage I and II, depending on the defect size can be accompanied by a very detrimental effect, which we

call Electromagnetic Fatigue (EMFA). At this point, if the defect size is larger than the skin depth of the surface eddy current, the current will follow the shape of the defect and a magnetic field is build up between the defect surfaces. Now, the same effect occurs as used in the EMW process to accelerate the outer workpiece onto the inner workpiece: The two defect surfaces, which now encounter opposing currents, create a magnetic pressure which pulls them apart from each other, thereby opening the crack with each pulse. The crack will then propagate if the critical electromagnetic fracture toughness (see Chapter 3) is larger than the fracture toughness of the present tool material. We have calculated several scenarios and were able to determine that the ratio a/b of the length of the crack opening b to the crack length a is largely important. The longer the crack length and the smaller the crack opening the larger the resulting force and the stress on the remaining tool cross-section.

Again, as far as defects are concerned, it is important to repeat that the small skin depth plays a large role for this effect to occur. This means that materials with a lower resistivity and a higher relative magnetic permeability are more susceptible to Stage III crack initiation and propagation. Thereby, we can create a relationship between the material properties, the inherit material's defect size and the resulting strength of the material in electromagnetic high-current applications.

On the other hand, if bad design of the tool already leads to current concentrations, as well as opposing currents Stage III crack initiation and propagation will be observed immediately, if the fracture toughness of the material is not high enough. This bad choice of the design was observed for the coil sent to MIT by FORD. The mechanical stress concentrations were intended to be lowered on the inside of the Bitter coil, by drilling holes into the corners of the rectangular inner shape. However, through this design Stage III crack initiation and propagation is promoted and will cause an opening force, depending on the current, between the inner surfaces of the drilled holes, already beginning with the first pulse.

Therefore, the correct design for the inner shape of a Bitter coil for compressing rectangular shapes, instead of the drilling of holes in the corners, is the rounding of the corners, which would decrease the Stage III force, maximize the remaining cross-section of the coil at the corner and optimize the mechanical stress concentration. Future studies could look into optimizing the balance between necessary roundness of the corners to create enough force for the EMW process, as well as keep the coil from failing at these locations. One could begin by looking at Maxwell's equations, such as

$$\oint H dl = \int j dA, \quad 6.1$$

Where H is the magnetic field, integrated over the length and j is the current density integrated over the area [1]. Now we can simplify Equ. 6.1 to

$$H = \frac{Ih\delta}{l}, \quad 6.2$$

where I is the discharge current in the coil, h is the thickness of the coil, δ is the skin depth and l is the length of the current path. Looking at Equ. 6.2, we can see that the magnetic field is increased when

increasing the current I , the thickness of the coil h and the skin depth δ . Increasing the length l of the current path will decrease the magnetic field. These changes to increase or decrease H relate precisely to the changes in the design of the corners. An increase in H increases the magnetic force acting on the surfaces, which is caused by an increase in the area ($h \times \delta$), through which the current runs. The length l can be seen as the roundness of the corners, which means that a sharper corner (smaller l) will cause a larger magnetic field concentration.

To study the process of crack initiation and propagation in detail the author developed a repeatable method to analyze electromagnetic fatigue accompanied by High-Speed Video Analysis. Through this method a workpiece is mounted inside an EMF coil and an artificial crack is introduced along the side of the tube parallel to the length axis. Then, the EMF machine is fired and a current is induced on the surface of the EMFA specimen, inside the coil. This current runs to the edge of the crack, where it cannot continue its path, but must run down the crack, turn around at the crack tip and run back up on the other side of the crack. This causes the exact behavior observed at cracks, defects and electromagnetic stress concentrations in electromagnetic applications. The effect of length a and opening b of the crack can be studied, as well as effects of the shape of the crack tip or introduced defect. The study was accompanied by a High-Speed Video analysis and we were able to observe arcing across the crack, as well as heavy elastic deformation of the EMFA specimen during the experiment. The outcome of the experiment compares very well to the fatigue study of the Aluminum Bronze Bitter coil. We can observe the creation of cracks (caused by the deformation, the electromagnetic force and thermal fatigue), as well as localized melting at the crack tip, due to the concentration of the current.

In addition we created an ABAQUS model comparing the observed melting at the crack tip of the EMFA specimen to the temperature rise being simulated in the model. Using the coupling factor between the EMF coil and the EMFA specimen, one can relate the discharge current in the coil to the induced current in the workpiece, resulting in a current of 4250 A in the workpiece. This in turn results in a temperature rise of 170 K along the crack surface and up to 860 K at the crack tip, at which point melting is observed. Comparing the size of the lobes observed for the EMFA specimens, caused by the localized melting, to the results from the model we can show good agreement and a distance of melting of approximately 0.2 mm to 0.7 mm.

In the future, the EMFA experiments accompanied with the ABAQUS model can be used to calculate the stresses at cracks, defects, current- and stress-concentrations to optimize the design of a tool used in high-current electromagnetic applications.

At the end of Chapter 3, we present an optimized material selection for the EMF and EMW tooling equipment, through the findings of the failure study, using CES Materials Selector software. We were able to find a collection of materials with better mechanical and thermal properties than the chosen Aluminum Bronze alloy. In the future, a new materials selection with a new materials database including the magnetic properties of the materials (which in this study have been studied for the individually selected materials, after their selection from the database) should be performed. It is important to mention that we believe that the choice of a magnetic material can have a small disadvantage in the first few microseconds of the process, during which the material is magnetized to its

saturation magnetization, after which it behaves like a non-magnetic material. This can cause an increase in the rise time of the discharge current in the coil. Furthermore, magnetic materials usually observe a higher electrical resistivity, which is also not beneficial for the EMW process. Quantitative comparisons of the chosen materials should be performed, in future studies.

In Chapter 4, we start to look at the EMW process by proposing a new formula to optimize the process, study the necessary kinetic energy to achieve EMW and create welding windows for EMW, depending on the volume of the accelerated material, as well as its hardness.

We were able to show that by decreasing the hardness of the outer workpiece material, far lower energies would be necessary to achieve EMW. The author believes that it would be a large step in the optimization of the Aluminum EMW process, to weld an outer workpiece made from A6061-O to an inner workpiece made from A6061-T6, thereby saving a large amount of energy necessary to accelerate the outer workpiece. In fact, through the proposed method, one can easily see that for the same EMW joint dimensions (outer diameter of 3", wall-thickness of 0.1" and a deformed length of 0.5") the necessary critical kinetic energy can be decreased by a factor of three, from 16 kJ to 5 kJ. Having proposed, in Chapter 1, through the study of Cold-Welding that post-heat treatment can be beneficial to the joint, the A6061-O alloy can then be heat-treated to receive comparable strength to the inner workpiece made of A6061-T6. Furthermore, work-hardening of the outer workpiece during the deformation will have already increased its strength. Other material combinations could be, for example, Aluminum to Steel, which is a very close setup to the applications, asked to be studied from FORD for this FORD-MIT alliance study.

Finally, in Chapter 4, we present the EMW experiments, which were performed in August and November 2007, at PULSAR, in Israel. Two EMW Design of Experiments were performed in this study. The first batch was done with 10 kJ and the second batch was done with 12 kJ, which would be the upper limit of the possible energy for the coils provided by PULSAR.

The EMW process calculations package, provided by PULSAR during the experiments in November 2007, states that with 10 kJ as well as with 12 kJ one still gets residual stresses in the final EMW joints. This was observed for some of the samples during cutting, for the preparation of the weld length ratio measurement. As far as the observed weld lengths are concerned, however, which were observed through a metallurgical analysis performed on the first batch of DOE specimens, an appropriate weld length was observed.

On the other hand, we could not get conclusive results from the weld length ratio measurements, which were performed at MIT. Future non-destructive analysis such as ultrasonic testing would be a better choice to get better results for the weld length ratio measurement around the entire circumference of the EMW joint.

We were able to show the wavy interface through Optical Microscopy, as well as SEM. The SEM study was accompanied by an EDS study, which was used to study the chemical structure across the wavy

EMW joint interface. We were able to observe a low bulk material content right across the interface, as well as an increase in oxygen content. We interpret this observation as the trapping of oxide in between the two material surfaces at the new interface. The focus, however in this study was not the metallurgical analysis of the EMW joint, as other authors have already studied the importance of the metallurgical aspect, in the past. This was also done for dissimilar metals which prove to be a more interesting field as far as the metallurgical study is concerned.

The major interest of this investigation of EMW, also through the scientific objectives of this FORD-MIT alliance project (see Chapter 1) was the study of the circuit parameters (covered in Chapter 2), of the fatigue of the tooling equipment (covered in Chapter 3) and the welding parameters (introduced in Chapter 1), which have been investigated by the proposed DOE, in Chapter 4. The parameter influence on the final result, the measured maximum load of the specimens during a tensile test, was studied and the DOE was helpful to give directions for the second batch of experiments and will certainly be helpful for future parameter studies.

EMW joints that were stronger than the base material could be produced and it was possible to filter out the most important EMW process parameters, which affected the final strength of the joint. These were gap and cleanliness of the inner workpiece specimen, for the first DOE. The cleanliness is a parameter in which the automotive industry shows a lot of interest. In a factory setting, parts are usually not cleaned with alcohol and have a small layer of oil on their surface. For our tests, however, the importance of cleaning the specimens proved to be very significant for the final strength of the EMW joint.

Furthermore, we could also show that the interaction between the taper angle and the wall-thickness plays a role on the final EMW joint strength. This is certainly the case as they affect each other during the collision of the two workpieces.

For the second DOE, again EMW joints that were stronger than the base material could be produced however, it needs to be stated that the values of the maximum loads were larger on average for the first DOE, when comparing the values from the first DOE (August 2007) to the values of the second DOE (November 2007). There was only one specimen (R16) which showed a high maximum load of 3546 kg, which compared to the theoretical strength of 5460 kg.

We thought that possibly the additionally introduced surface condition of a scratch-brushed inner workpiece could be harmful to the final strength of the EMW joint, but the DOE showed no such effect. Another cause could be the increase in energy for the second DOE from 10 kJ to 12kJ. This value was not tested in the DOE and can therefore not be shown to be significant for the observed decrease in overall strength of the joints. Another value could be the application of oil (DOE parameter E = +), which was then equally for each DOE, but could have differed between the two DOEs (August and November 2007). Possibly, for the second DOE, more oil was applied to the surface of the inner workpiece causing a part of the observed decrease in strength.

Through the second DOE we were able to find the important EMW parameters, which were cleanliness, the wall-thickness and the interaction between the taper angle and the cleanliness.

To summarize the findings from both batches of EMW experiments, we were able to find that an increase in gap, an increase in wall-thickness (although it increases the accelerated mass), an increase in cleanliness, the interaction between the taper angle and the cleanliness, as well as the interaction between the taper angle and the wall-thickness play an important role on increasing the strength of the final EMW joint.

For the latter two interactions we can certainly state that they are clearly interrelated through the important process of jet formation, during the EMW process. Quantification of the interaction of these parameters could be the field of study of future investigations.

Furthermore, we were able to show that scratch-brushing the inner workpiece parallel to the length axis showed no significant improvement in strength of the final EMW joint. Possibly, another study could be performed to compare the observed strengths for the case of a scratch-brushed inner workpiece normal to the length axis. However, parameters such as the application and oil, as well as the process energy should be kept the same for future studies to avoid other effects on the final strength of the joint.

Future of EMW

We have stated before that EMW has incomparable benefits over other joining methods, such as the lack of a heat-affected zone, the possibility to join dissimilar metals and its speed (see also Chapter 1 and then the presented literature). We would now like to present briefly where we conclude that EMW could find its place between the present welding methods.

Clearly, there is a large workpiece size dependence and we have presented a method to create welding windows for EMW depending on computing the critical necessary kinetic energy and the volume and hardness of the chosen material to be joined using EMW.

With the proposed steps for optimization, such as the RLC circuit parameters, the controlled introduction of designed wrinkles using EMF to the outer workpiece to lower its mechanical strength prior to the EMW step, the use of single-turn coils in connection with a cable transformer (as successfully used by PULSAR), the proper choice of the material of the outer and inner workpiece, the proper deformation theory parameters, such as the gap, the tapered angle, etc., the proper surface preparation, involving the right amount of cleaning, and so forth, the author could see EMW being introduced to the automotive industry as a prototype of a new joining technology. The possibility of joining the proposed material cross-sections by FORD would have to be studied through the introduction of new coil designs, using the presented methodologies to increase the life-time of the coils at the same time. Finally, the joints and their resulting fatigue strength and corrosion behavior would have to be studied, in the future.

Figure 1 shows a comparison graph between different welding techniques and EMW displaying the capital equipment cost over the productivity of the process.

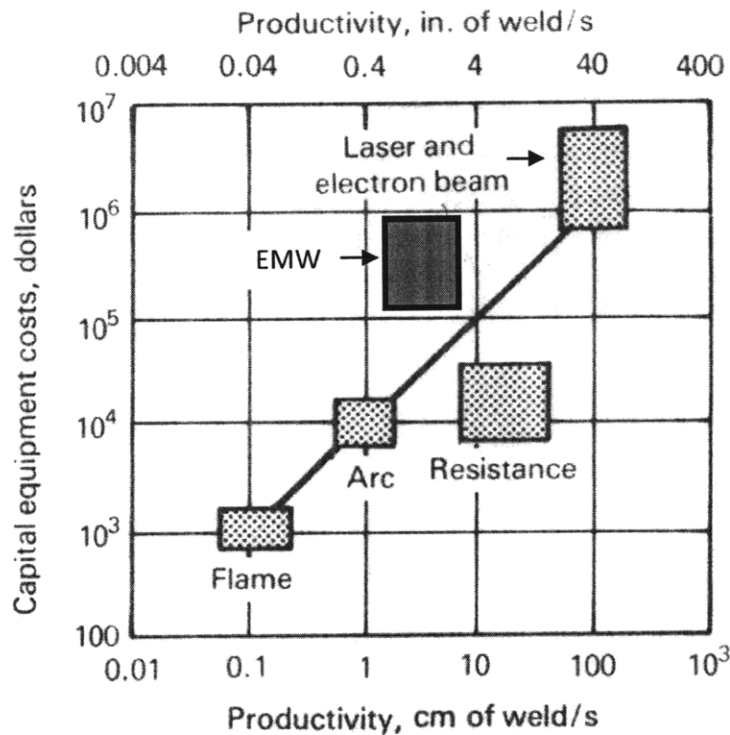


Figure 1: Approximate relationship between capital cost of welding equipment and speed at which sheet metal joints can be produced in comparison to the welding of tube using EMW.

The productivity for EMW, in Figure 1 was calculated for welding the circumference of ten 3" and 5" diameter tubes, over the total time of one minute, yielding a length between 40 mm/s and 70 mm/s, approximately. We can see that EMW could compare to resistance welding, as far as its productivity is concerned, however the capital equipment cost of EMW is two orders of magnitude larger. Laser and electron beam welding have similar capital equipment costs, but have a far higher productivity in comparison to EMW.

It needs to be stated that the other welding productivities are calculated for the joining of sheet metal instead of tubular joints for EMW. The ability of EMW to produce a weld in less than a second for a round or rectangular tube is still extraordinary. Still, EMW cannot outperform other present welding techniques as far as the productivity or capital cost are concerned and it will have to rely on its other presented strengths.

Also, there are already applications, where EMW shows benefits over other welding techniques, such as the welding of HVAC parts, introduced in Chapter 1.

Another possibility for EMW to gain market size in the industry could be the venturing into another market first, before the automotive market. An EMW joint is clearly also something very aesthetic in comparison to the joints produced using other welding techniques. Possibly, EMW could be introduced

into the bicycle market, where prices are very high to produce an aesthetic and high-tech final product, see Figure 2.

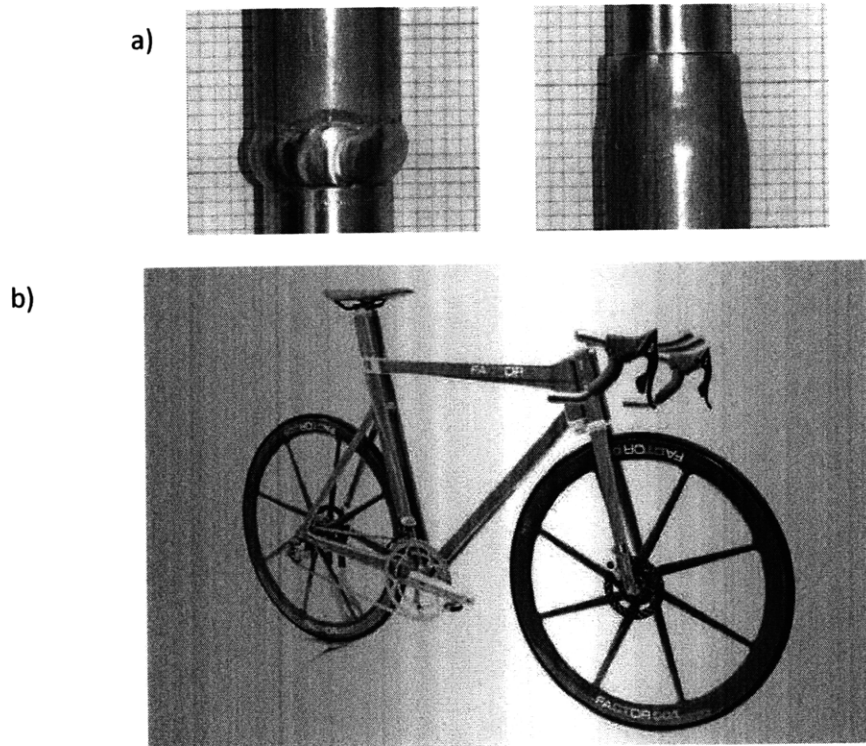


Figure 2: a) Comparison of an EMW weld to a commercial weld.
b) One of the world's most expensive bicycles [3].

Figure 2a shows the comparison of aesthetics between an EMW weld (left) and a commercial weld (right). Figure 2b shows one of the world's most expensive bicycles, the BERU f1 Systems Factor 001 Bicycle. It costs more than a standard family-sized sedan and actually retails around GBP20,000. This bike is made of carbon fiber and comes with an on-board computer.

To summarize, my work intended to address some of the most important issues by investigating the EMF and the EMW process in detail, resulting in a proposed selection of EMW tool materials that will withstand the high stresses and strains of the process. Furthermore, EMF and EMW experiments accompanied by theoretical calculations were performed, where deformation, mechanical properties etc. were measured and windows for EMW with structurally sufficient welds were established. Finally, through a clear understanding of the EMW process parameters, a theoretical set of parameters is presented to optimize the EMW process, reducing the high stresses that are induced on the welding tools and lengthening their life-time.

The hope is that the presented observations and theoretical models to calculate the process parameters and their result on the EMW final joint and tooling equipment should be able to propel the study of EMW to become a possible joining process of the future.

Bibliography – Chapter 5

[1] P.A. Tipler. Physik, Book (1994).

[2] T. W. Eagar. Challenges in joining emerging materials. Proc. Of Int. Conf. on Advances in Joining Newer Structural Materials, Montreal, Canada (1990).

[3] <http://www.besportier.com>

APPENDIX

APPENDIX A (see the bibliography of Chapter 1 for the according references)

Further Possible Limiting Conditions for the EMW process

As stated in Chapter 1, for EMW to take place a jet-stream removes the oxide from the metal, during the impact of the two workpieces. Then the two materials are joined, due to the ongoing compression force and kinetic energy acting upon the outer workpiece. This is, in general, very similar to what is observed in the process of Cold-Welding. Here, also the oxide and contaminants at the surface are removed. Second, under ongoing pressure the two material surfaces are joined at the new interface [35,37,38].

The author believes that just like for other Cold-Welding processes the similarity of the two materials joint during the welding process could be of great importance, such as similar crystal structure or crystal orientation. On the other hand, it is observed in the Cold-Welding literature that it is sometimes beneficial to join two materials with two very different base characteristics, such as the surface hardness of the materials and their oxides. Additionally, we can show that other parameters, like the surface roughness, pre-heat-treatment and post-heat-treatment can play an important role for the strength of the final joint.

In this section of the Appendix, the author looks at a few of these material properties and how they interact with the properties of the final joint, based on observations from the EMW and Cold-welding literature. Then a possibly optimal theoretical set of parameters is presented for EMW and future EMW experiments.

1. Study of Material Combinations observed in EMW

Table A.1 (see also Chapter 1) shows the materials database of material combinations, of which it has been reported that Electromagnetic Welding could be observed:

		Inner tube-rod												
		Alumi. 1xxx	Alumi. 3xxx	Alumi. 5xxx	Alumi. 6xxx	Alumi. 7xxx	Cast Alumi.	Cu	Brass (C360)	Steel 10xx	SS (304)	Ni	Mg	Ti
O u t e r t u b e	Alumi. 1xxx	U	U	U	U	U	U	U	U	U	U		U	
	Alumi. 3xxx	U	U	U	U	U	U	U	U	U	U			
	Alumi. 5xxx	U	U	U	U	U	U	U	U	U	U		U	
	Alumi. 6xxx		U	U	U	U	U	U	U	U	U			
	Alumi. 7xxx				U	U	U							
	Cast Alumi.													
	Copper						U	U	U	U	U			
	Brass (C360)						U			U				
	Steel 10xx									U	U			
	SS (304)										U			
	Ni										U	U		U
	Mg													
	Ti													

Table A.1: Metal combinations that have been successfully welded [34].

One can see that the metals can almost in all cases be welded to themselves. In a few cases one metal can be welded to many other materials (like Aluminum), in other cases to just one additional material.

The analysis in this study shows that if the crystal structures are close or similar it is more probable that a weld can be observed at achievable EMW process energies. Table A.2 shows the material combinations presented in Table A.1 plus further EMW material combinations found in the literature. Instead of just showing the possibility of a successful EMW joint, at the cross-section of the rows and columns we display the crystal structures that the EMW joint now shares.

Metal		Zr	Mo	Mg	S.Steel	Ni	Ti	Steel	Brass	Cu	Al
	Crystal Structure	hex	bcc	hex	fcc/bcc (α/γ)	fcc	Hex	fcc/bcc (α/γ)	fcc/bcc (α/β)	fcc	fcc
Al	fcc			fcc-hex	fcc/bcc-fcc			fcc/bcc-fcc	fcc/bcc-fcc	fcc-fcc	fcc-fcc
Cu	fcc				fcc/bcc-fcc	fcc-fcc		fcc/bcc-fcc	fcc/bcc-fcc	fcc-fcc	
Brass	fcc/bcc (α/β)								fcc/bcc-fcc/bcc		
Steel	fcc/bcc (α/γ)							fcc/bcc-fcc/bcc			
Ti	hex					hex-fcc					
Ni	fcc					fcc-fcc					
S.Steel	fcc/bcc (α/γ)				fcc/bcc-fcc/bcc						
Mg	hex			hex-hex							
Mo	bcc		bcc-bcc								
Zr	hex	hex-hex									

Table: A.2: Summary of all successful EMW metal combinations with their respective crystal structures [34, 41].

From Table A.2 it can be seen that almost all of the successfully welded EMW metal combinations to this date are autogeneous or have a hexagonal (hex) to face-centered cubic (fcc) crystal structure combination. Additionally, it can be seen that no fcc to body-centered cubic (bcc) or hex to bcc combinations can be successfully welded.

It is well known that the crystal lattices of fcc and hex are very similar [37], so up to this point the hypothesis that similar crystal structures seem to have a positive effect on the possibility to create an EMW joint holds.

Now, we are studying some of the “good” crystal structure combinations haven’t been successfully welded yet. Table A.3 gives an overview, of the possible combinations, which would share a “good” set of combined crystal structures (Brass and Steel have been left out of this comparison).

Metal	Crystal Structure	Zr	Mo	Mg	S.Steel	Ni	Ti	Steel	Brass	Cu	Al
		hex	bcc	hex	fcc/bcc (α/γ)	fcc	Hex	fcc/bcc (α/γ)	fcc/bcc (α/β)	fcc	fcc
Al	fcc			fcc-hex	fcc/bcc-fcc			fcc/bcc-fcc	fcc/bcc-fcc	fcc-fcc	fcc-fcc
Cu	fcc				fcc/bcc-fcc	fcc-fcc		fcc/bcc-fcc	fcc/bcc-fcc	fcc-fcc	
Brass	fcc/bcc (α/β)								fcc/bcc-fcc/bcc		
Steel	fcc/bcc (α/γ)							fcc/bcc-fcc/bcc			
Ti	hex					hex-fcc					
Ni	fcc					fcc-fcc					
S.Steel	fcc/bcc (α/γ)				fcc/bcc-fcc/bcc						
Mg	hex			hex-hex							
Mo	bcc		bcc-bcc								
Zr	hex	hex-hex									

Table A.3: Colored material combinations cannot be welded, although their crystal structures are similar. Orange is fcc-hex, red is same structure-same structure. Brass and Steel have been left out of this comparison.

Table A.3 opens the following questions:

Why can the following hex-hex metal combination not be welded?

Ti-Ti: As reported in the Cold-Welding literature hexagonal metals are difficult to cold-weld [40]. Furthermore, Ti is only weldable to Ni, when using EMW.

Why can the following fcc-fcc metal combination not be welded?

Al-Ni

Why can the following hex-fcc metal combinations not be welded?:

Al-Zr, Al-Ti, Cu-Zr, Cu-Mg, Cu-Ti, Ti-Zr, Ti-Mg, , Ni-Zr, Ni-Mg, Mg-Zr: Overall, Ti and Ni seem to be not very joinable as far as the EMW process is concerned. Leaving these out of the known not joint material combinations leaves the following:

Al-Zr, Cu-Zr, Cu-Mg, Mg-Zr: Again, Mg and Zr have a hexagonal crystal structure and are therefore not very easily welded, according to the Explosive Welding literature [40].

2.b. Effect of Crystal Orientation

The most preferred slip systems are bcc: $\{110\}\langle 111\rangle$ and fcc: $\{111\}\langle 110\rangle$ with a total number of 36 and 12 slip systems, respectively. Studying the Cold-Welding literature the author found that there is a tendency for trans-interfacial grain growth more readily in butt welding of bars than with lap welding of sheet:

a) Extruded and heavily-drawn rods of fcc metals tend to develop a texture with the $\langle 111\rangle$ axis in parallel to the direction of drawing and extrusion. Therefore, butt welding welds (111) planes.

b) Sheet rolled from fcc metals with large deformations (<50%) usually has the (110) plane in the plane of rolling. Therefore, lap welding welds (110) planes. After recrystallisation however, this heavily deformed sheet has the (100) plane in the plane of rolling.

To summarize, in cold-welding polycrystalline specimens the (111) planes are a better match. Experiments for single-crystal specimens, however, show a tendency of better joints being observed for the welding of (110) to (110) planes. Therefore, the difference between the strength superiority of butt welds over lap welds is due to another cause.

Still, it is observed that during the cold-welding of (100) planes, slip would readily occur along the (111) plane at comparatively low pressures. On the other hand, when welding (111) to (110) planes, conditions would not be so favorable for slip, resulting in a greater pressure being applied normal to the interface. This would be expected to lead to a better general breakdown of the oxide film, which would assist later grain growth across the interface [36].

In conclusion, the texture of the outer and inner workpiece can be a very important factor to consider in future EMW experiments. The findings, from the cold-welding literature, regarding the advantage of welding (111) to (110) planes could be studied in the future, by drawing the outer workpiece and extruding the inner workpiece with the optimum texture orientations.

2. Effect of Material Surface Hypothesis

2.a. Workpiece Material Hardness

Based on the formulas presented in the literature for the critical threshold velocity to achieve EMW and the new formula for a so-called critical threshold kinetic energy (Chapter 4), it is clear that the hardness of the materials is of great importance.

2.b. Metal and Metal-Oxide Hardness Ratio

From Table A.1, one can see that it is possible to weld Aluminum to a lot of different metals: Steel, Stainless Steel, Brass, Copper and Magnesium. Figure A.1 shows a graph of the metal-oxide to metal hardness ratio versus the necessary deformation to achieve a weld through Cold-Welding, at room temperature.

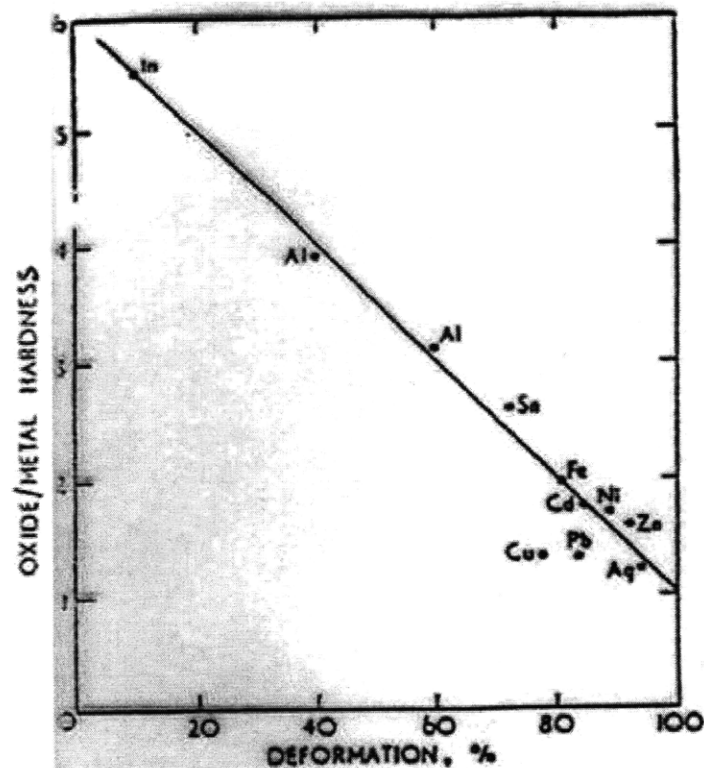


Figure A.1: Effect of hardness ratio on minimum deformation required for welding at room temperature [36].

From Figure A.1, one can see that Al only needs 40% deformation to be welded at room temperature. Therefore, Aluminum can be easily welded at low temperatures with the right amount of deformation. This is also observed in EMW.

1.c. Effect of Surface Condition

If the harder metal in dissimilar metal welds is acting as the penetrating element, variation in the surface roughness of the harder element would be expected to affect the weld strength more than variation of the roughness of the softer component.

In the case of welds between iron and Aluminum, leaving the iron in the clean pickled condition and scratch-brushing the Aluminum failed to produce welds if less than 65% deformation were applied. On the other hand, if iron was scratch-brushed and the Aluminum was merely degreased, welds could be made with 43% and 60% deformation [36]. Figure A.2 shows the mechanism of a hard metal being welded to Aluminum:

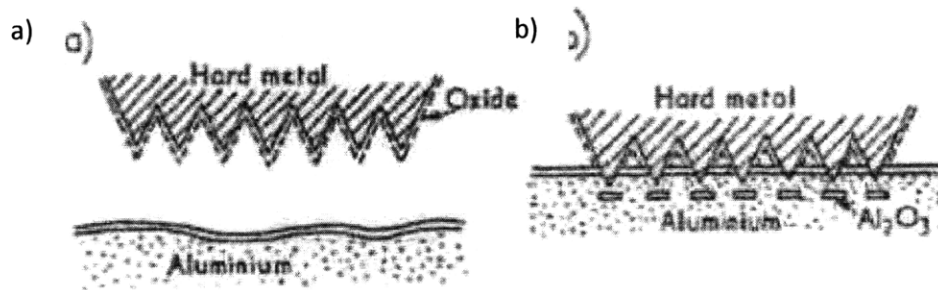


Figure A.2: Mechanism of welding a hard metal to Aluminum [36].

Figure A.2a displays the two surfaces before contact, where the hard metal was scratch-brushed. Figure A.2b shows the two metals after contact, where the scratch-brushed hard metal has successfully penetrated the Aluminum-oxide layer, which is now moved to the inside of the bulk Aluminum [36].

Table A.5 shows a summary of other surface treatments and their affect on the deformation required to cold-weld Aluminum.

Surface Preparation	Deformation [%]
Scratch-brushed	58.0
Heptane	63.7
Vaseline (non-polar)	69.8
Vaseline + 10 % oleic acid	85.3
Oleic acid	91.0
Water	78.2
Ethyl alcohol	82.5

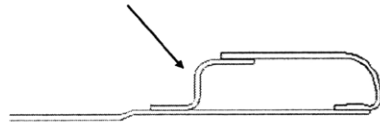
Table A.5: Summary of surface treatments and there affect on the deformation required to cold-weld Aluminum [35].

An example of an optimized EMW materials combination could be the joining of Aluminum 6061 (outer workpiece) to Steel or Al6061-T6 (inner workpiece) with the following argumentation and considerations:

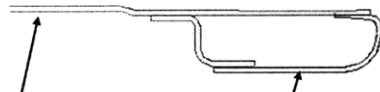
- Welding of harder metal to softer metal:
 - Necessary critical kinetic energy to deform the outer workpiece and achieve EMW can be lowered by factors of 3
 - Oxide/metal hardness ratio between the outer and inner workpieces would be beneficial
- Dissimilar metals:
 - + Further preparation:
 - Inner workpiece material should be scratch brushed (Surface Condition could be optimized – to be shown in Chapter 4)
 - Optional: Both materials cleaned with Heptane
 - + Post heat-treatment:
 - Al 6061 → T6
 - Beneficial against intermetallic compounds
- Texture orientation
 - Tubing should be prepared to optimize the texture orientation so that the right set of crystal orientations are joined on impact during the EMW process
- Electrical properties
 - Due to the higher electrical resistivity of steel compared to Al6061-T6, the so-called “cushioning effect” that can be created by the inner workpiece (see Chapter 1) can be lowered

Applications at FORD

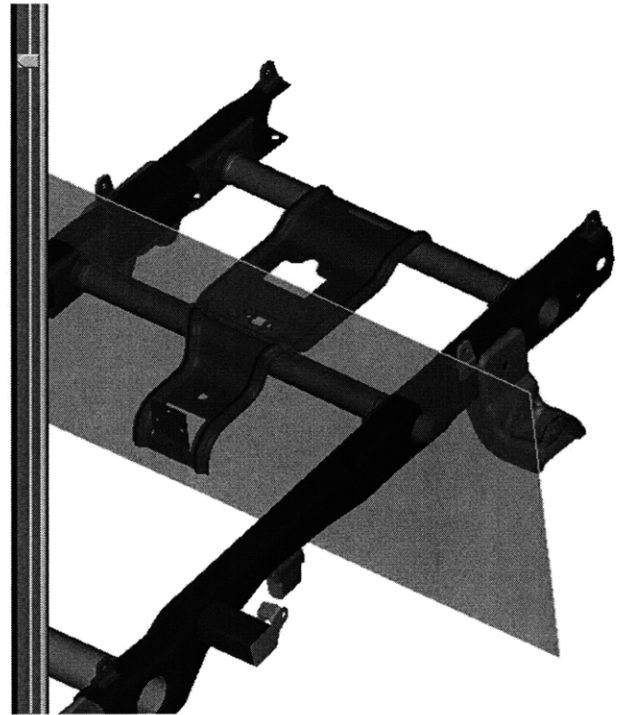
RAIL INR (LOCAL)



ALUMINUM

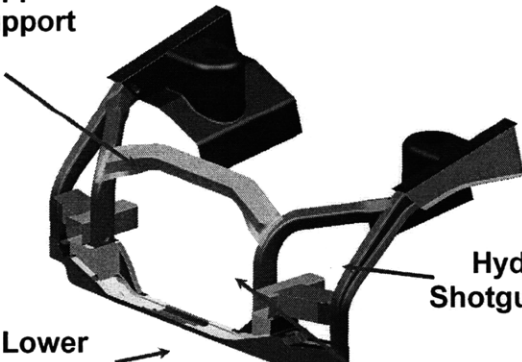


RAIL OTR



Hybrid Hydroform and Stampings

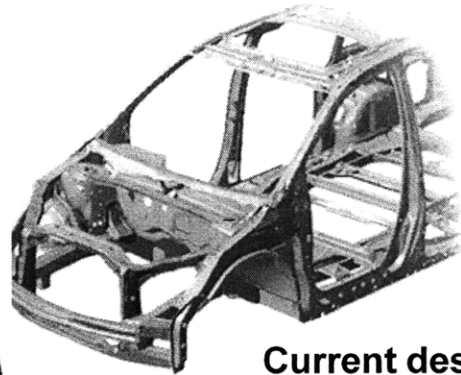
Stamped Upper Radiator Support Assy.



Stamped Lower Radiator Support Assy.

Hydroformed Shotgun Extension

Hydroformed Inner Radiator Support



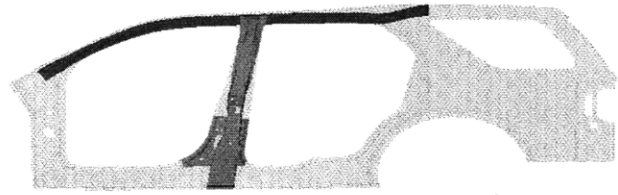
**Current design
All stampings**

EMW could be used to join hydroformed structural elements

- Component Comparison

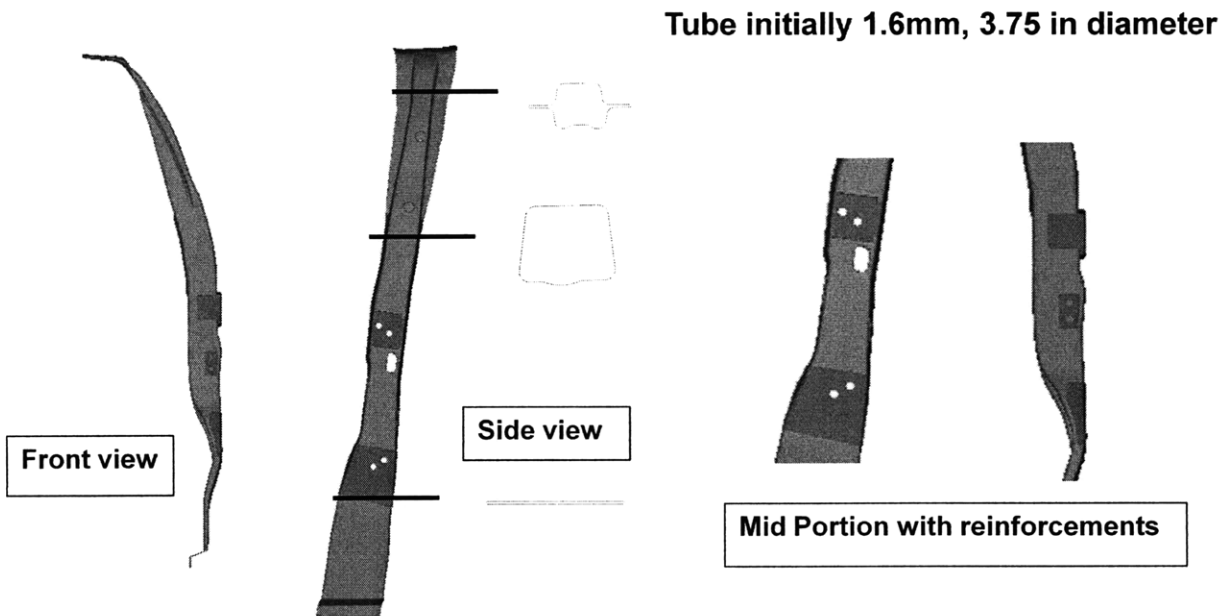


Conventional Design



Hydro formed design

EMW could be used to join hydroformed structural elements and reinforcements



EMW could be used to attach reinforcements or join pillar to roof rail

Appendix B (see Chapter 2 for the according references)

Safety and Operation of MAGNEFORMER

General

The Safety Precautions section can be found in the user manual of the MAGNEFORMER machine, at MIT [14].

CAUTION

DURING MACHINE OPERATION OR IN THE EVENT OF MALFUNCTION, THE VOLTAGES WHICH APPEAR ON CAPACITORS, IGNITRONS, VACUUM SWITCHES RESISTORS AND ASSOCIATED WIRING ARE LETHAL.

MAGNEFORMER Machine Operation

The MAGNEFORMER machine must never be operated without the safety shield in place. When the shield is in the down position it will actuate interlock switch S-102 before the operational sequence can begin.

Furthermore, the MAGNEFORMER machine must never be cycled without a work coil in place. Without the work coil in the discharge circuit, the principal current will not be transferred through the ignitrons but will flow through series resistors R-111, R-112, R-113 and R-109 and R-110 in parallel to ground. At the higher power-level settings these resistors will burn out and must then be replaced before further operation is possible. For further information on the operation of the MAGNEFORMER machine consult section VI in [14].

Workpiece materials used in the experiments:

I. Aluminum Cans

Figure B.1 shows the mechanical properties of an Aluminum can. In our experiments only the tubular body was used for the experiments. Therefore, only the material AA3004 was tested.

Mechanical Properties

Tab: AA5052 (Al-2.5%Mg)

Top: AA5182 (Al-4.5%Mg)

**Body: AA3004
(Al-1.2%Mg-1.0%Mn)**

**E = 10E7 psi ... Young's Mod.
v = 0.35 ... Poisson's Ratio**

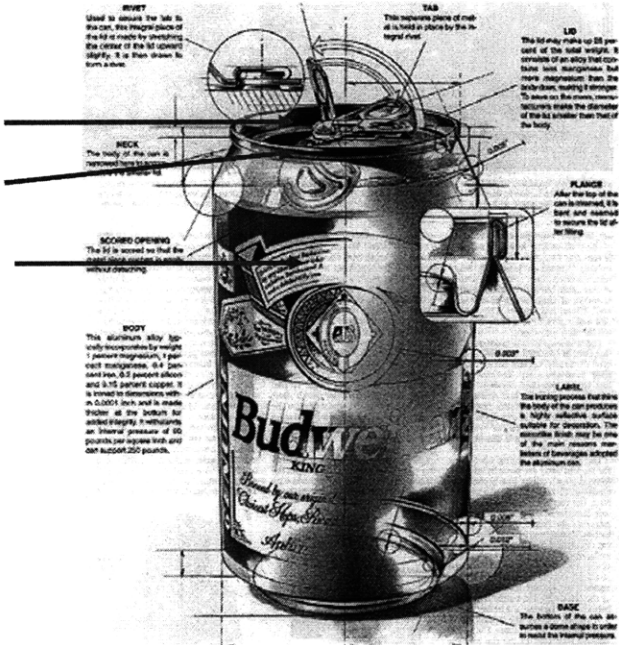


Figure B.1: Mechanical properties of an Aluminum can.

II. Tube 2.5" diameter

Shape	Tubes
Tube Type	Round
Wall Thickness	.065"
Wall Thickness Tolerance	±.007"
Length	6'
Length Tolerance	+1"
Inside Diameter	2.37"
Outside Diameter	2.5"
Outside Diameter Tolerance	±.015"
Material	Extra-Strength Aircraft-Grade Aluminum (Alloy 2024)
Finish/Coating	Unpolished (Mill)
Tolerance	Oversize
Temper	T3
Hardness	120 Brinell
Yield Strength	42,000 psi
Straightness Tolerance	.01" per foot
Temperature to Maintain Strength	-320° to +300° F
Specifications Met	American Society for Testing and Materials (ASTM)
ASTM Specification	ASTM B210

Table B.1: Mechanical properties of the 2.5" tubing used in the EMF experiments presented in this chapter.

III. Tube 1.5" diameter

Shape	Tubes
Tube Type	Round
Wall Thickness	.035"
Wall Thickness Tolerance	±.004
Length	6'
Length Tolerance	+1"
Inside Diameter	1.43"
Outside Diameter	1.5"
Outside Diameter Tolerance	±.015"
Material	Extra-Strength Aircraft-Grade Aluminum (Alloy 2024)
Finish/Coating	Unpolished (Mill)
Tolerance	Oversize
Temper	T3
Hardness	120 Brinell
Yield Strength	42,000 psi
Straightness Tolerance	.01" per foot
Temperature to Maintain Strength	-320° to +300° F
Specifications Met	American Society for Testing and Materials (ASTM)
ASTM Specification	ASTM B210

Table B.1: Mechanical properties of the 1.5" tubing used in the EMF experiments presented in this chapter.

Frame by frame measurements to measure speed of the compression of the tubes

New tubes were cut for further velocity measurements and named #6, #8, #9 (#7 failed). Table B.3 shows the results of the High-Speed Videography study and the study and measurements of the individual frames, with the resulting speeds of the individual points.

tube	frame0	frame1	T	x_0	y_0	x_1	y_1	dx	dy	v	v-real
6	-14881	-14867	0.00005	98	198	110	140	12	58	84612.	29.3
6	-14881	-14867	0.00005	136	-38	137	-73	1	-35	50020.4	17.3
6	-14881	-14867	0.00005	56	147	101	145	45	2	64349.2	22.3
6	-14881	-14870	0.00005	221	131	196	136	-25	-5	46354.7	16.1
8	-13194	-13181	0.00005	63	150	124	124	61	26	102015.2	35.4
8	-13194	-13183	0.00005	226	170	195	152	-31	18	65176.2	22.6
8	-13194	-13181	0.00005	97	-39	175	121	78	-82	174111.4	60.4
9	-15256	-15243	0.00005	57	-80	150	106	93	-26	148563.1	51.5
9	-15256	-15251	0.00005	139	-12	144	-48	5	-36	145382.3	50.4
9	-15256	-15255	0.00005	202	-33	198	-39	-4	-6	144222.1	50.0

Table B.3: Linear velocities of points on the deformed tubes.

MATLAB code for calculating the Magnetic Pressure, Tube Acceleration, Tube Velocity and Tube Displacement

```

% Constants
muo = pi*4e-7;           % permeability of free space
sigma = (86.9e6)         % average yield stress of AA3004 (Pa)
gamma = 2720;           % density of Aluminum (kg/m^3)
ro = 3.99e-8;           % resistivity of AA3004 (ohms-m)
t = linspace(0,0.6*1e-4,1000);

% Using soda can geometry
a = 0.03175;            % radius of tube (m)
c = 0.0508;            % inside radius of coil (m)
lo = 0.1016;           % coil length
l = .089;              % tube length (m)
D = .066;              % tube diameter (m)
h = .00012;           % tube thickness (m)
m = 0.005;

% Electrical Circuit Properties

T = 6;                 % number of coil windings
Eo = 7300;             % initial charge voltage (V)
C = 220e-6;           % capacitance of bank (F)

Lc = 2.5e-6;           % coil inductance (H)
Li = 0.001e-6;        % internal inductance (H)
L = Lc+Li

Rc = .017;             % coil resistance (ohms)
Ri = .001;            % internal resistance (ohms)
R = Rc+Ri %+(2*pi*a*T^2*ro)/sd; % equivalent resistance (ohms)

beta = R/(2*L);
omega = sqrt(1/(L*C)-beta^2) % angular frequency of discharge

Jo = .5*C*Eo^2;
py = h*sigma/a
po = (muo*T^2*Jo)/L

i = (Eo/(L*omega)).*exp(-beta*t).*sin(omega*t);

%it=subs(i,tt);
%subplot(4,1,1)
%plot(tt,it)

%p = .5*muo*T^2*i.^2;
p= 10*po*exp(2*t*-beta).*sin(t.*omega).*sin(t.*omega); %Factor of 10 (losses
in strength, effect of fieldshaper)
pd=p-py;

%Plot real magnetic pressure

```

```

%pt=subs(p,tt);
subplot(4,1,1)
plot(t,p,'b',t,py,'--b')
title('Underdamped Magnetic Pressure')
xlabel('Time (s)')
ylabel('Pressure (Pa)')

%Plot magnetic Deformation pressure pd

%pdt=subs(pd,tt);
% subplot(4,1,2)
% plot(t,pd)
% title('Underdamped Magnetic Deformation Pressure')
% xlabel('Time (s)')
% ylabel('Pressure (Pa)')

% Critically damped case

%ic = V/L*t.*exp(-R.*t/(2.*L));
%pc = (mueo*N^2*ic.^2)/2;

%
%acceleration
f=zeros(length(t),1);
for i=1:length(t)
    if p(i)>py
        f(i)=2*pi*a*1.*pd(i);
    end
end
acc = f./m;

% Plot tube acceleration

%acct=subs(acc,tt);
Subplot(4,1,2)
plot(t,acc,'g:');
title('Tube Acceleration')
xlabel('Time (s)')
ylabel('Acceleration (m/s^2)')

%
%velocity

velt=zeros(length(t)-1,1);
timv=zeros(length(t)-1,1);
i=1;
ac(1)=acc(i); ac(2)=acc(i+1);
tim(1)=t(i); tim(2)=t(i+1);
timv(i)=t(i)+(t(i+1)-t(i))/2;
velt(i)=trapz(tim,ac);

```

```

for i=2:length(t)-1
    ac(1)=acc(i); ac(2)=acc(i+1);
    tim(1)=t(i); tim(2)=t(i+1);
    timv(i)=t(i)+(t(i+1)-t(i))/2;
    velt(i)=velt(i-1)+trapz(tim,ac);
end

% vel=-1/2*pi*a*1*(exp(-2*t*beta)*po*beta^2+exp(-2*t*beta)*po*omega^2-
po*exp(-2*t*beta)*beta^2*cos(2*t*omega)+po*exp(-
2*t*beta)*beta*omega*sin(2*t*omega)+4*py*t*beta^3+4*py*t*beta*omega^2)/m/beta
/ (beta^2+omega^2);
% velt=subs(vel,tt);

subplot(4,1,3)
plot(timv,velt,'Color','red','LineWidth',1)
title('Tube Velocity')
xlabel('Time (s)')
ylabel('Velocity (m/s)')

%
%postion

x_pos=zeros(length(timv)-1,1);
timv_x=zeros(length(timv)-1,1);
i=1;
veloc(1)=velt(i); veloc(2)=velt(i+1);
timx(1)=timv(i); timx(2)=timv(i+1);
timvx(i)=timv(i)+(timv(i+1)-timv(i))/2;
x_pos(i)=trapz(timx,veloc);

for i=2:length(timv)-1
    veloc(1)=velt(i); veloc(2)=velt(i+1);
    timx(1)=timv(i); timx(2)=timv(i+1);
    timvx(i)=timv(i)+(timv(i+1)-timv(i))/2;
    x_pos(i)=x_pos(i-1)+trapz(timx,veloc);
end

subplot(4,1,4)
plot(timvx,x_pos,'r:')
title('Tube Displacement')
xlabel('Time (s)')
ylabel('Displacement (m)')

```

MATLAB Code to calculate the Tube Velocity using the Impulse

```
% Constants
muo = pi*4e-7;           % permeability of free space
sigma = (86.9e6)         % average yield stress of AA3004 (Pa)
gamma = 2720;           % density of Aluminum (kg/m^3)
ro = 3.99e-8;          % resistivity of AA3004 (ohms-m)
t = linspace(0,0.2e-3,1000);

% Using soda can geometry
a = 0.03175;           % radius of tube (m)
c = 0.0508;           % inside radius of coil (m)
lo = 0.1016;          % coil length
l = .089;             % tube length (m)
D = .066;            % tube diameter (m)
h = .00012;          % tube thickness (m)
m = 0.005;

% Electrical Circuit Properties

T = 6;                % number of coil windings
Eo = 7300;           % initial charge voltage (V)
C = 220e-6;          % capacitance of bank (F)

Lc = 2.5e-6;         % coil inductance (H)
Li = 0.001e-6;       % internal inductance (H)
L = Lc+Li

Rc = .017;           % coil resistance (ohms)
Ri = .001;           % internal resistance (ohms)
R = Rc+Ri %+(2*pi*a*T^2*ro)/sd; % equivalent resistance (ohms)

beta = R/(2*L);
omega = sqrt(1/(L*C)-beta^2) % angular frequency of discharge

Jo = .5*C*Eo^2;
py = h*sigma/a
po = (muo*T^2*Jo)/L

i = (Eo/(L*omega)).*exp(-beta*t).*sin(omega*t);

%it=subs(i,tt);
%subplot(4,1,1)
%plot(tt,it)

%p = .5*muo*T^2*i.^2;
p= 10*po*exp(2*t*-beta).*sin(t.*omega).*sin(t.*omega); %Factor of 10 (losses
in strength, effect of fieldshaper)
pd=p-py;

%Plot real magnetic pressure

%pt=subs(p,tt);
```

```

subplot(3,1,1)
plot(t,p,'b',t,py,'--b')
title('Underdamped Magnetic Pressure')
xlabel('Time (s)')
ylabel('Pressure (Pa)')

%Plot magnetic Deformation pressure pd

%pdt=subs(pd,tt);
% subplot(4,1,2)
% plot(t,pd)
% title('Underdamped Magnetic Deformation Pressure')
% xlabel('Time (s)')
% ylabel('Pressure (Pa)')

% Critically damped case

%ic = V/L*t.*exp(-R.*t/(2.*L));
%pc = (mueo*N^2*ic.^2)/2;

%
%-----
%acceleration
f=zeros(length(t),1);
for i=1:length(t)
    if p(i)>py
        f(i)=2*pi*a*1.*pd(i);
    end
end
acc = f./m;

% Plot tube acceleration

%acct=subs(acc,tt);
Subplot(3,1,2)
plot(t,acc,'g:');
title('Tube Acceleration')
xlabel('Time (s)')
ylabel('Acceleration (m/s^2)')

%
%-----
%velocity (IMPULSE)

pressure= 10*po*exp(2*t*-beta).*sin(t.*omega).*sin(t.*omega);

%integration imp
velt=zeros(length(t)-1,1);
timv=zeros(length(t)-1,1);
imp=zeros(length(t)-1,1);
i=1;
pressu(1)=pressure(i); pressu(2)=pressure(i+1);
tim(1)=t(i); tim(2)=t(i+1);
timv(i)=t(i)+(t(i+1)-t(i))/2;

```

```

imp(i)=trapz(tim,pressu);

for i=2:length(t)-1
    pressu(1)=pressure(i); pressu(2)=pressure(i+1);
    tim(1)=t(i); tim(2)=t(i+1);
    timv(i)=t(i)+(t(i+1)-t(i))/2;
    imp(i)=imp(i-1)+trapz(tim,pressu);
end

% %rearrange of pressure vector
% pressurev=zeros(length(t)-1,1);
% for i=1:length(t)-1
%     pressurev(i)=(pressure(i)+pressure(i+1))/2;
% end

velocity = (imp-py*timv)./(gamma*h); %p=m*v

subplot(3,1,3)
plot(timv,velocity,'Color','red','LineWidth',1)
title('Tube Velocity')
xlabel('Time (s)')
ylabel('Velocity (m/s)')

```


MATLAB Code for calculating the Discharge Current, the Temperature and the Magnetic Pressure

```
mueo=4*3.14*10^-7;
N=6;
t =[0:10^-8:10^-3];
syms tt;

Li = 38*10^-9;
Lc = 1.25*10^-6;
L = Lc + Li;
% L=38*10^-9; % Critically damped case

V=15000;
C = 320*10^-6;

Jo=0.5*V^2*C;

po = (mueo*N^2*Jo)/L;

Rm=0.01;
Rc=0.017;
R=Rm + Rc;
% R=(4*L/C)^0.5 % Critically damped case

beta = R/(2*L);

w = (1/(L*C)-(R/2/L)^2)^.5;

i = V/(w*L).*exp(-beta.*tt).*sin(w.*tt);
pf= po*exp(2*tt*-beta).*sin(tt.*w).*sin(tt.*w);

% Critically damped case

% ic = V/L*t.*exp(-R.*t/(2.*L));
% pc = (mueo*N^2*ic.^2)/2;

% Temperature

i2=(V/(w*L).*exp(-beta.*tt).*sin(w.*tt)).*(V./(w*L).*exp(-
beta.*tt).*sin(w.*tt));
i2_int=int(i2,'tt');

i2t =subs (i2_int, t);

Ej= R*i2t;

m = .309; % (kg)
cp = 400; % (J/KgK)

T_1=Ej./(cp*m);
T_1=T_1-min(T_1);
```

```
% plot(t,pf)
it=subs(i,t);
plot(t,it);
figure(2);
plot (t, T_1);
```

EMF with the Introduction of a Fieldshaper - Experiments and Results

1. Workpiece Without Tapered Angle

We showed in the EMW literature research that a tapered angle is beneficial to the formation of a jet-stream, as well as the forming of a successful EMW joint (see Chapter 1). In this experiment an inner workpiece with no tapered angle was used.

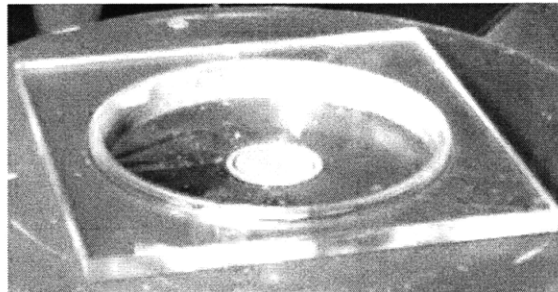
Specimens

The tested material was Al6061-T6. The outer workpiece tubing consisted of 1" long outer tubes with an outer diameter of 1" and a wall-thickness of 0.035". The inner workpiece were 2.5" long rods with an outer diameter of 0.875".

Experiment

The inner workpiece was placed inside the sample holder, as was the outer workpiece, yielding a gap of 0.045". The MAGNEFORM machine was fired at a power level of 80. Figure B.2 shows photographs of the setup for the fieldshaper experiments with the sample holder, the sample, the inner and outer workpiece in place.

a)



b)



Figure B.2: Front and top view of the fieldshaper experiment setup with an inner workpiece without a tapered angle.

Discussion and Results

Unfortunately for none of the tested samples a proper joined could be created. The team therefore, moved on to a different design for the inner workpiece, one with a tapered angle and one with a turned down diameter towards the end of the workpiece.

The electromagnetic coupling of the fieldshaper took place, however, as the outer workpiece was certainly deformed upon the inner workpiece, but not sufficiently to create a permanent joint.

2. Workpiece With tapered Angle

Specimens

The tested material was Al6061-T6. The outer workpiece tubing consisted of 1" long outer tubes with an outer diameter of 1" and a wall-thickness of 0.035". The inner workpiece were 2.5" long rods with an outer diameter of 0.875". Now the inner workpiece was turned down over a length of 1" to reduce the diameter from 0.875" to 0.75" resulting in a tapered angle of 4 degrees. Figure B.3 shows the new design for the inner workpiece with a tapered angle of 4 degrees over a length of 1", opting for an optimal tapered angle, as described by the literature:

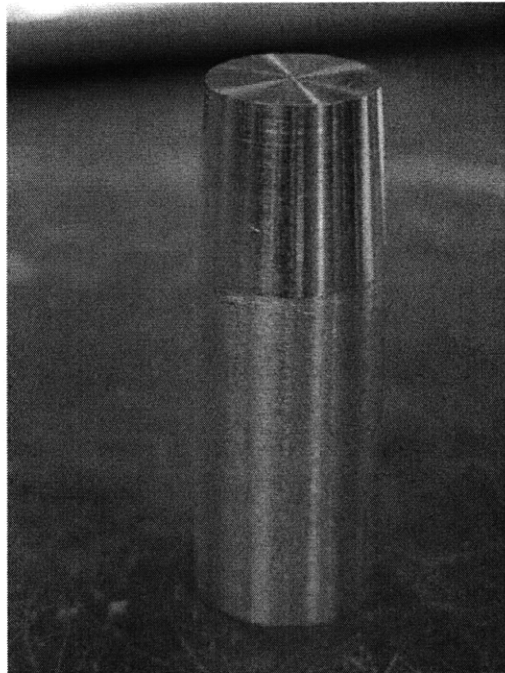
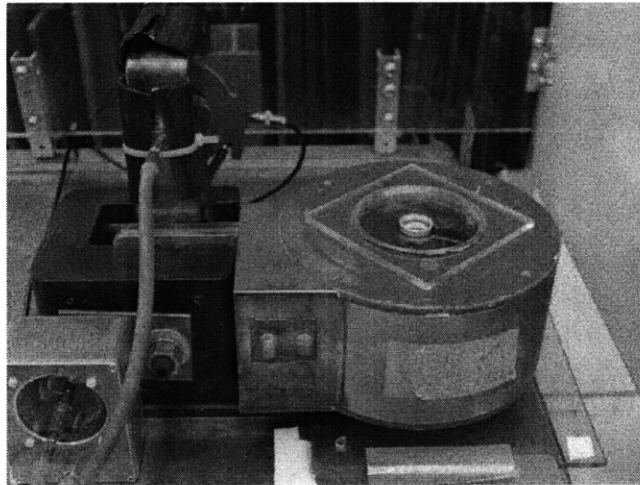


Figure B.3: Tapered inner workpiece specimen

Experiment

Again, the inner workpiece was placed inside the sample holder, as was the outer workpiece, yielding a gap of 0.045" on the bottom of the outer workpiece and a gap of 0.1" on the top of the outer workpiece. The MAGNEFORM machine was fired at a power level of 80. Figure B.4 shows the setup of the fieldshaper experiments with an inner workpiece with a tapered angle of 4 degrees:

a)



b)



Figure B.4: a) Setup for Tapered Inner Workpiece Experiment with Fieldshaper
b) Tapered inner workpiece inside the tubular outer workpiece.

Results

Unfortunately, again, the outer workpiece could not be formed permanently onto the inner workpiece. Figure B.5 shows a photograph of the electromagnetically formed outer workpiece on top of the inner workpiece, which had a tapered angle of 4 degrees.

Figure B.5: Photograph of the deformed outer workpiece on top of the inner workpiece.

Of course, the deformation of the outer workpiece was larger than compared to the inner workpiece without a tapered angle experiments.

Discussion

Again, the energy of the MAGNEFORM machine was not large enough to overcome the necessary force to create a permanent joint. One could also say that the available gap between the inner and outer workpiece was not large enough for the outer workpiece to reach the maximum possible velocity. At this point, the author is certainly agreeing to the fact that EMF experiments are material- and time-consuming, without much outcome in the end. That is why another specimen design for the inner workpiece was chosen, to make sure of a proper forming joint, even without too large available energy.

3. Workpiece With turned down diameter and supported by adhesive

In this last set of experiments with the fieldshaper strong measures were taken to achieve a final permanent joint, after the deformation of the outer workpiece upon the inner workpiece. The previous experiments showed that a new design of the inner workpiece needed to be manufactured. Furthermore, the joint was reinforced by adhesive.

Specimens

Figure B.6 shows the design of the new inner workpiece specimen:

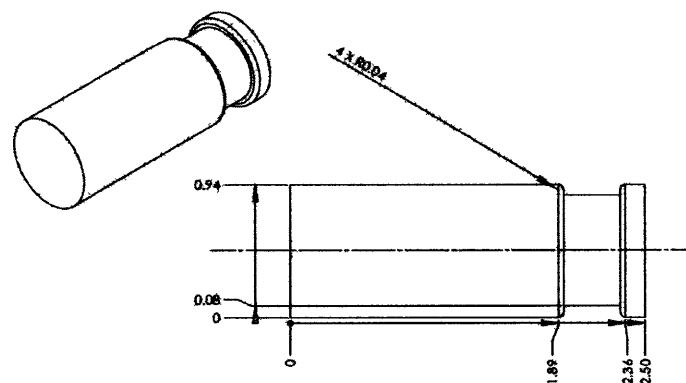


Figure B.6: Inner workpiece specimen for the last series of experiments with the fieldshaper.

The tested material was Al6061-T6. The outer workpiece tubing consisted of 2.5" long tubes with an outer diameter of 1" and a wall-thickness of 0.035". The inner workpiece were 2.5" long rods with an outer diameter of 0.875". As shown in Figure B.6, a groove was cut around the circumference of the inner workpiece.

Furthermore, three of the manufactured specimens were further prepared for the joining process by inserting epoxy inside the groove of the inner workpiece, in which the outer workpiece would be formed into. The data sheet for the adhesive can be found at the end of this section of Appendix B.

Experiment

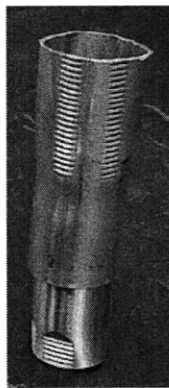
Again, the MAGNEFORM machine was fired at a power level of 80. Three specimens with no epoxy and three without were produced in this set of experiments. Furthermore, first tensile tests of the specimens were performed. For the outer workpiece not to shatter underneath the gripping force of the tensile machine grips, metallic rods were inserted into the tube, where the grip force applied.

Tensile tests were performed on the resulting joints on an MTS, model number 311.21. The used load cell has a rating of 50kN. The tests were performed at a strain rate of 0.02''min^{-1} .

Discussion and Results

It was possible to obtain a proper joint for the epoxy specimens. One out of three of the non-epoxy specimens was only a joint in the axial direction but would move in the radial direction. Figure B.7a shows a photograph of the no-epoxy specimen and Figure B.7b shows the epoxy specimen after it had been treated with red dye and torn apart by the tensile test. The red dye was used to see, where the epoxy was attached to the surfaces after the forming experiment and after the tensile test was performed:

a)



b)

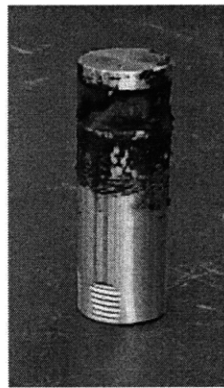


Figure B.7: a) Photograph of the tensile tested specimen without epoxy.

b) Photograph of the tensile test specimen with epoxy, after it had been treated with dye.

Figure B.8 shows a summary of the tensile tests for the specimens that were electromagnetically formed (epoxy and no-epoxy) with the addition of a fieldshaper:

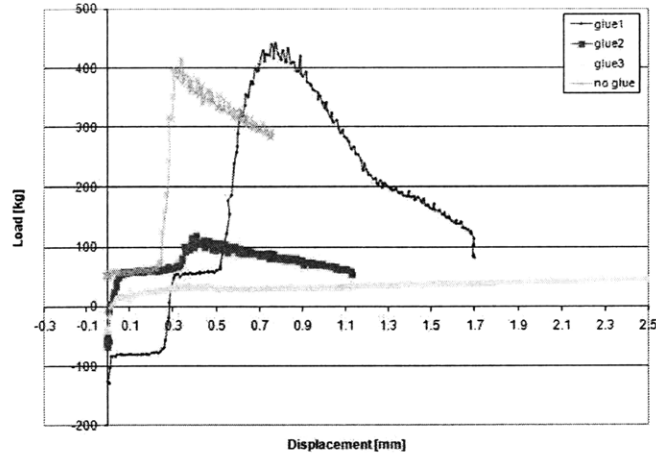


Figure B.8: Tensile test data of one non-glued specimen and three glued specimens.

Out of the specimens with epoxy specimen 3 failed right away and specimen 2 failed at a very low load of only 100 kg. Specimen 1, which was the third specimen with epoxy inside the groove of the inner workpiece showed the best strength, with a maximum strength of approximately 425 kg at a displacement of approximately 0.8 mm. The specimen with no epoxy showed a maximum strength of 400 kg at a displacement of approximately 0.3 mm.

Clearly, the epoxy did not add to the maximum strength of the joint, but would lead to a larger necessary displacement to pull the joint apart. However, the joint was not weakened by the additional epoxy. This is good, because EMF joints could benefit from having an epoxy between the joint parts to prevent corrosion.

Finally, Figure B.9 shows the effect of the slit of the fieldshaper, which causes the magnetic pressures to be much lower at the position of the slit, next to the outer workpiece.

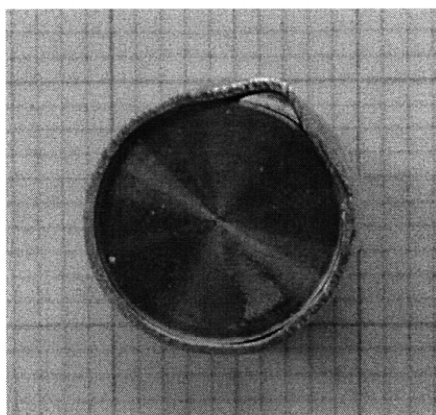


Figure B.9: Effect of slit of fieldshaper, which lowers the magnetic pressure acting on the outer workpiece at the position of the slit.

From Figure B.9 we can clearly see that there is a large effect of the slit of the fieldshaper and the deformation at this position is much lower. Again, this can be detrimental for the final strength of the specimen. The proposed sealing using the adhesive could counter-act this zone of enlarged corrosion weakness. Furthermore, in EMW joints we propose to always study a percentage of the produced joints using non-destructive testing, such as ultrasonic testing, prior to destructive testing.

Data Sheet for Epoxy

LOCTITE

1001 Trout Brook Crossing
Rocky Hill, CT 06067-3910
Telephone: (860) 571-5100
FAX: (860) 571-5465

Product Description Sheet Speedbonder® Product H8000

Industrial Products, May 2002

Description

Loctite® Speedbonder H8000 is a non-sag, two component, room temperature curing, 10:1 mix ratio, methacrylate adhesive system. H8000 is designed to have fast fixture time and excellent bond strength on multiple substrates including metals and composites. The product also has high elongation and excellent cold temperature impact strength. This adhesive forms resilient bonds and maintains its strength over a wide range of temperatures.

Recommended Substrates: Steel, Aluminum, Stainless Steel, FRP, Xenoy, RTM, Gelcoat, and ABS.

Features

- Non-sagging gaps filled to 1/2 inch
- Superior impact and peel strength
- Little or no surface preparation
- Offers excellent tolerance to off-ratio mixing
- Rapid room temperature cure
- 100% reactive
- Excellent environmental resistance

Typical Cured Properties	Typical Value
Tensile Strength, psi, ASTM D 638	2300 to 2500
Elongation, %, ASTM D 638	50 to 100
Young's Modulus (psi)	70,000 to 90,000
Shear Strength @ 180°F, psi, ASTM D 1002	1900 to 2100

Typical Uncured Properties	Part A	Part B	Mixed
Open Time @ 70°F, mins	-	-	10 to 15
Open Time @ 40°F, mins	-	-	60 to 75
Exotherm Time @ 70°F, mins	-	-	18 to 25
Fixture Time, 3 kg weight, @ 70°F, mins	-	-	15 to 20
Color	yellow	Blue	Green
Viscosity, cP Brookfield HBT Spindle #6, 10 Rpm	160,000 to 220,000	40,000 to 70,000	-
Specific Gravity	0.94	1.15	0.96
Weight per Gallon, Lbs	7.83	9.58	-
Mix Ratio			
By weight	8.17	1	-
By volume	10	1	-

Typical Cured Properties	Typical Value
Shear Strength, psi, ASTM D1002 @ 70°F	
Aluminum	3000 to 3500
Steel	3000 to 3500
Stainless Steel	2800 to 3100
FRP	>1200 to 1600
Gelcoat	>1000 to 1500

Typical Cured Properties	Typical Value
Shear Strength, psi, ASTM D1002 @ 180 °F	
Aluminum	1100 to 1300
Etched Aluminum	800 to 1000
Ground Steel	1000 to 1200

Side Impact Strength, kJ/m ² , GMS751P test	Typical value	
	@70°F	@-40°F
Aluminum	>42	>42
FRP	>15	16
Ground Steel	24	30

T-Peel, psi, ASTM D1876	Typical Value
Steel	35 to 45
Aluminum	50 to 60

GENERAL INFORMATION

This product is not recommended for use in pure oxygen and/or oxygen rich systems and should not be selected as a sealant for chlorine or other strong oxidizing materials.

For safe handling information on this product, consult the Material Safety Data Sheet, (MSDS).

Handling and Application

Mixing: It is highly recommended that either meter mix equipment or cartridges with static mix nozzles be used to properly ratio and dispense the adhesive. For optimum mixing, the Loctite static mixer, item 985545 is recommended. Once mixed, H8000 should achieve a uniform green color. Heat buildup during and after mixing is normal. To reduce the likelihood of exothermic reaction or excessive heat buildup, mix less than 100 grams at a time. Mixing smaller amounts will minimize heat buildup.

Applying: Bonding surfaces should be clean, dry, and free of contamination. Extensive surface preparation is not required for H8000, and good bonds can be formed on most substrates after a solvent wipe. To assure maximum bond strength, surfaces must be mated within the adhesive's open time. Use enough material to completely fill the joint when parts are clamped.

Curing: Parts should remain undisturbed during the interval of time between the material's open time and fixture time. After the fixture time is achieved the material has reached handling strength. Temperature below 55°F will slow the cure; above 85°F will accelerate cure rate.

Clean Up: It is important to clean up excess adhesive from work area and application equipment before it hardens. Denatured alcohol and many common industrial solvents are suitable for removing uncured adhesive. H8000 is flammable. Keep containers tightly closed after use. Keep away from heat, sparks, and open flame.

Storage

Speedbonder adhesives should be stored in unopened containers in a dry location at 40°F +/- 5 F. For further specific shelf life information, contact your local Technical Service Center.

NOT FOR PRODUCT SPECIFICATIONS.
THE TECHNICAL DATA CONTAINED HEREIN ARE INTENDED AS REFERENCE ONLY.
PLEASE CONTACT LOCTITE CORPORATION QUALITY DEPARTMENT FOR ASSISTANCE AND RECOMMENDATIONS ON SPECIFICATIONS FOR THIS PRODUCT.
ROCKY HILL, CT FAX: +1 (860)-571-5473 DUBLIN, IRELAND FAX: +353 (1)-481-8988

Loctite is a Trademark of Loctite Corporation, U.S.A.

Packaging
490ml EPS cartridges
5 Gallon Pails
55 Gallon Drums

Note

The data contained herein are furnished for information only and are believed to be reliable. We cannot assume responsibility for the results obtained by others over whose methods we have no control. It is the user's responsibility to determine suitability for the user's purpose of any production methods mentioned herein and to adopt such precautions as may be advisable for the protection of property and of persons against any hazards that may be involved in the handling and use thereof. In light of the foregoing, Loctite Corporation specifically disclaims all warranties expressed or implied, including warranties of merchantability or fitness for a particular purpose, arising from sale or use of Loctite Corporation's products. Loctite Corporation specifically disclaims any liability for consequential or incidental damages of any kind, including lost profits. The discussion herein of various processes or compositions is not to be interpreted as representation that they are free from domination of patents owned by others or as a license under any Loctite Corporation patents that may cover such processes or compositions. We recommend that each prospective user test his proposed application before repetitive use, using this data as a guide. This product may be covered by one or more United States or foreign patents or patent applications.

Appendix C (see the bibliography of Chapter 3 for the according references)

Aluminum Bronze alloy rod C63000 (AMPCOLOY 45)

Material details from Copper and Brass Co:

- *Ultimate Tensile Strength - 118,000 psi*
- *Yield Strength (Tensile) - 75,000 psi*
- *Elongation in 2" - 15%*
- *Brinell Hardness (3000kg) - 228*
- *Density - 0.271 Lbs/In³*
- *Thermal Conductivity - 0.09 CGS*
- *Proportional Limit - 48,000psi*
- *Fatigue (100,000,000 cycles) - 38,000psi Aluminum bronze rod C63000 (AMPCOLOY 45)*

Details from FORD:

- *Coils were manufactured 3+ years ago!*
- *Number of turns: 6*
- *Working zone of about 53 mm*
- *Process:*
 - *15 kV (of max. 25kV)*
 - *Up to 40 kJ of energy*
 - *Peak current = 800 kA*
 - *First wave pulse time = 40 microseconds*

Temperature Profile Calculation of the Aluminum Bronze Bitter Coil

Figure C.1 shows the calculated discharge current for the case of the Aluminum Bronze Bitter Coil. Figure C. 2 shows the calculated temperature profile. The respective MATLAB code can be found in Appendix B.

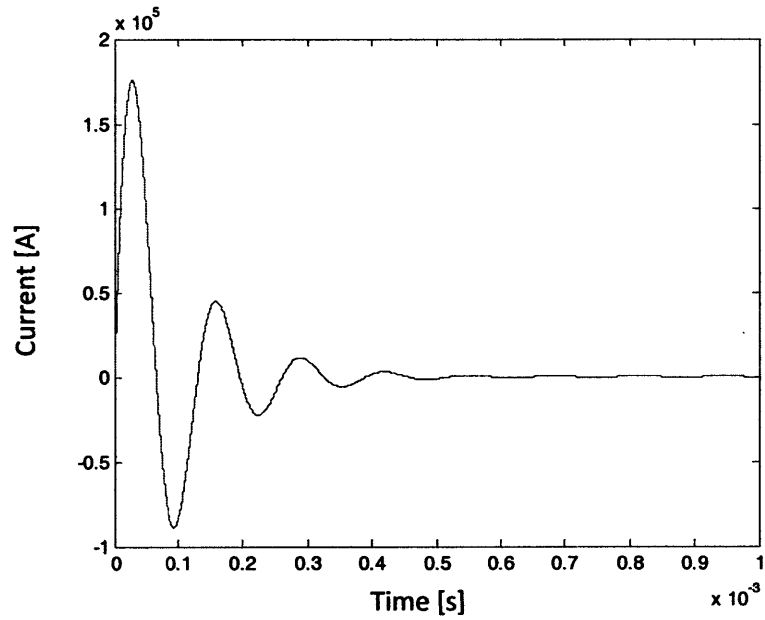


Figure C.1: Calculated discharge current for the case of the Aluminum Bronze Bitter Coil.

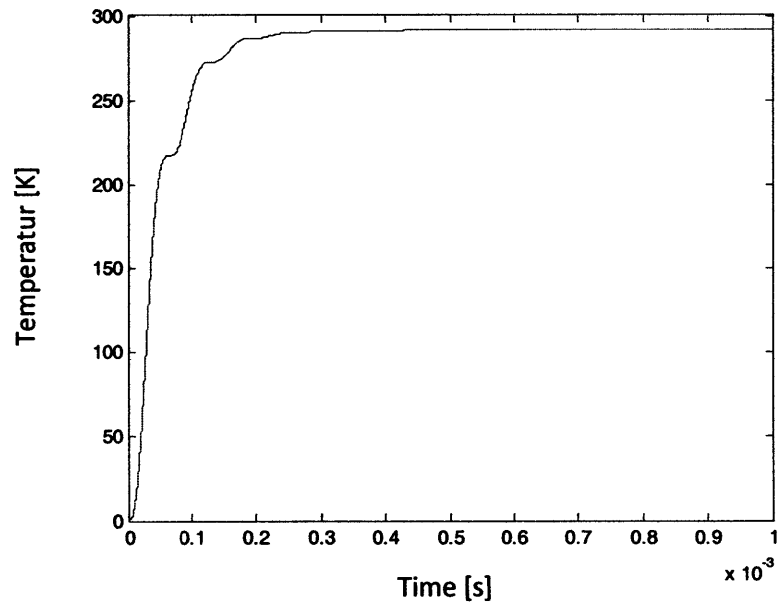


Figure C.2: Temperature profile over time along the surface of the Aluminum Bronze Bitter coil.

Materials Selection

Figure C.3 shows the ranking values of the individual materials selection dimensions:

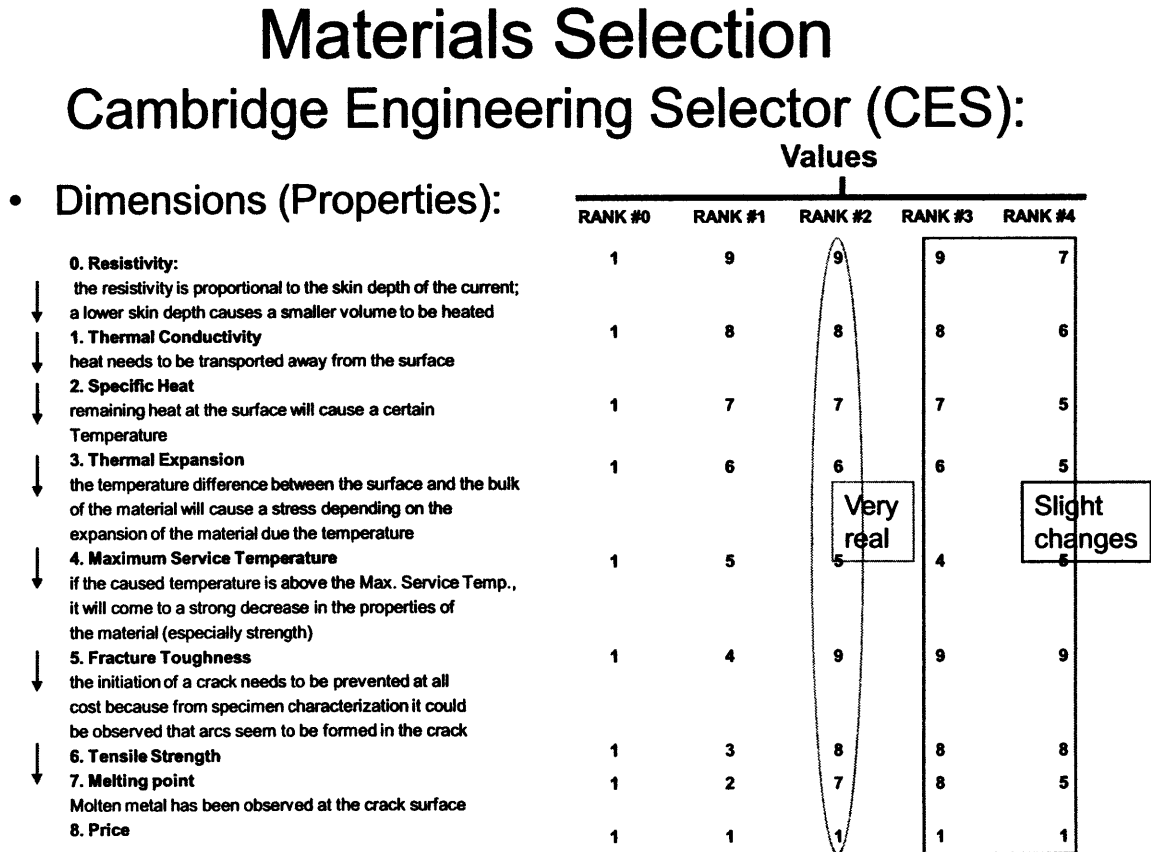


Figure C.3.: Values of the dimensions of the materials selection study for several cases giving different importance to different dimensions depending on the scenario (rank).

Figure C.4 to Figure C.14 give the materials properties from the CES materials selection database for the chosen materials in the presented materials selection study.

Designation				
MMC: C10100/C(f) copper-graphite composite				
Composition				
Cu-40%C(f)				
Density *	0.2191	-	0.2223	lb/in ³
Energy Content *	4.875e+004	-	5.417e+004	kcal/lb
Price *	100.1	-	133.4	USD/lb
Recycle Fraction	0	-		
Mechanical				
Bulk Modulus *	20.31	-	22.48	10 ⁶ psi
Compressive Strength*	58.02	-	65.27	ksi
Elongation *	0.5	-	1	%
Elastic Limit *	58.02	-	65.27	ksi
Endurance Limit*	29.73	-	33.36	ksi
Fatigue Strength Model*	27.65	-	35.62	ksi
Fracture Toughness*	42.77	-	50.05	ksi.in ^{1/2}
Hardness - Vickers*	120	-	135	HV
Loss Coefficient*	1e-003	-	2e-003	
Modulus of Rupture*	59.47	-	66.72	ksi
Poisson's Ratio *	0.2	-	0.29	
Shape Factor	26	-		
Shear Modulus *	10.01	-	11.46	10 ⁶ psi
Tensile Strength*	59.47	-	66.72	ksi
Young's Modulus*	20.74	-	23.44	10 ⁶ psi
Thermal				
Maximum Service Temp. *	1026	-	1116	*R
Melting Point *	2441	-	2461	*R
Minimum Service Temperature	0	-		
Specific Heat *	0.117	-	0.1231	BTU/lb.F
Temp. Dep. of Resistivity*	2.917	-	2.972	/R
Thermal Conductivity	147.3	-	150.8	BTU./h.ft ² .F
Thermal Expansion	1.667	-	1.722	µstrain/F
Electrical				
Resistivity *	1.91	-	2	µohm.cm
Typical Uses				
Electronic packaging				

→ 2 – 4 pound coil:
230 – 460 \$

→ 20 % less than
Al Bronze

→ 40 % less than
Al Bronze

→ outstanding el.
th. conductivity

1

Figure C.4: Material properties with some notes for the selection of the material, regarding the important dimensions of the materials selection, for the Cu-40% laminate.

Chromium, Commercial Purity				
Designation				
Chromium Metal				
Composition				
>99%Cr, typically				
Density	0.2565	-	0.2601	lb/in ³
Energy Content *	2167	-	1.3e+004	kcal/lb
Price	2.669	-	3.003	USD/lb
Recycle Fraction*	0.2	-	0.3	
Mechanical				
Bulk Modulus	19.73	-	24.66	10 ⁶ psi
Compressive Strength*	26.83	-	62.37	ksi
Elongation	2	-	55	%
Elastic Limit *	26.83	-	62.37	ksi
Endurance Limit*	21.03	-	55.11	ksi
Fracture Toughness*	109.2	-	136.5	ksi.in ^{1/2}
Hardness - Vickers	200	-	270	HV
Loss Coefficient*	2e-004	-	7e-004	
Modulus of Rupture*	26.83	-	62.37	ksi
Poisson's Ratio	0.2	-	0.22	
Shape Factor	28	-		
Shear Modulus	14.5	-	17.4	10 ⁶ psi
Tensile Strength	53.66	-	110.2	ksi
Young's Modulus	35.53	-	41.34	10 ⁶ psi
Thermal				
Maximum Service Temperature	1152	-	1404	*R
Melting Point	3780	-	3870	*R
Minimum Service Temperature	0	-		*R
Specific Heat	0.1051	-	0.1242	BTU/lb.F
Thermal Conductivity	48.53	-	54.31	BTU./h.ft ² .F
Thermal Expansion	3.333	-	3.889	µstrain/F
Electrical				
Resistivity	12.7	-	15	µohm.cm
Typical Uses				
Protective coatings; electro-deposits; alloying element in steels, superalloys; used to give glass an emerald green colour; Catalyst; Used for anodising aluminium; Tanning leather;				
Warning				
All chromium compounds should be regarded as highly toxic. Chromium(VI) compounds are highly toxic and carcinogenic. Chromium(III) compounds are less toxic. Chromium compounds are important pollutants.				
Other Notes				
Chromium is steel-grey, lustrous, hard, metallic, and takes a high polish.				

→ 36 % higher than
Al Bronze

39

Figure C.5: Material properties with some notes for the selection of the material, regarding the important dimensions of the materials selection, for Chromium of commercial purity.

Low Alloy Nickel

Designation				
Nickel alloys with 90% or more Nickel content				
Composition				
>90Ni				
Density	0.2962	-	0.3251	lb/in ³
Energy Content *	4334	-	2.492e+004	kcal/lb
Price	2.669	-	6.672	USD/lb
Recycle Fraction*	0.7	-	0.9	
Mechanical				
Bulk Modulus *	15.23	-	29.01	10 ⁶ psi
Compressive Strength*	20.31	-	155.2	ksi
Elongation	4	-	50	%
Elastic Limit	14.5	-	155.2	ksi
Endurance Limit*	17.4	-	102.3	ksi
Fracture Toughness*	95.56	-	136.5	ksi.in ^{1/2}
Hardness - Vickers	75	-	370	HV
Loss Coefficient*	1e-004	-	2.6e-003	
Modulus of Rupture*	14.5	-	155.2	ksi
Poisson's Ratio *	0.3	-	0.32	
Shape Factor	30	-		
Shear Modulus *	6.527	-	12.47	10 ⁶ psi
Tensile Strength	44.96	-	204.5	ksi
Young's Modulus	18.85	-	31.91	10 ⁶ psi
Thermal				
Maximum Service Temperature* ⁹	918	-	1152	*R
Melting Point	2939	-	3119	*R
Minimum Service Temperature	0	-		*R
Specific Heat	0.1015	-	0.1338	BTU/lb.F
Thermal Conductivity	12.71	-	36.4	BTU.ft/h.ft ² .F
Thermal Expansion	6.389	-	8.333	µstrain/F
Electrical				
Resistivity	10	-	46	µohm.cm
Typical Uses				
Chemical and food processing; Electronic parts; Aerospace; Gas turbine components; High temperature tensile testing apparatus; Furnaces; Heating elements; Springs; Clips; Press components for extruding plastics; Moulds for glass production;				
Warning				
All nickel compounds should be regarded as toxic. Some can cause cancer and/or foetal abnormalities.				
Other Notes				
Registered tradenames include "DURANICKEL" & "PERMANICKEL" (INCO).				

Best sp. heat
 30 % less than
 Al Bronze

Figure C.6: Material properties with some notes for the selection of the material, regarding the important dimensions of the materials selection, for Chromium of commercial purity.

Cobalt, Commercial Purity

Designation				
Cobalt Metal				
Composition				
>99.3%Co - typical impurities: Ni,Fe,Cu				
Density	0.3179	-	0.3215	lb/in ³
Energy Content *	1.192e+004	-	3.684e+004	kcal/lb
Price	13.34	-	30.03	USD/lb
Recycle Fraction*	0.9	-	0.95	
Mechanical				
Bulk Modulus	25.24	-	30.75	10 ⁶ psi
Compressive Strength*	42.79	-	134.2	ksi
Elongation	2	-	20	%
Elastic Limit *	42.79	-	134.2	ksi
Endurance Limit*	39.16	-	90.65	ksi
Fracture Toughness*	109.2	-	136.5	ksi.in ^{1/2}
Hardness - Vickers	160	-	370	HV
Loss Coefficient*	2e-004	-	8e-004	
Modulus of Rupture*	42.79	-	134.2	ksi
Poisson's Ratio	0.31	-	0.33	
Shape Factor	18	-		
Shear Modulus	10.73	-	12.18	10 ⁶ psi
Tensile Strength	97.9	-	181.3	ksi
Young's Modulus	28.86	-	31.18	10 ⁶ psi
Thermal				
Maximum Service Temperature* ⁹	954	-	1170	*R
Melting Point	3150	-	3182	*R
Minimum Service Temperature	0	-		*R
Specific Heat	0.1003	-	0.1099	BTU/lb.F
Thermal Conductivity	53.16	-	57.78	BTU.ft/h.ft ² .F
Thermal Expansion	6.389	-	7.778	µstrain/F
Electrical				
Resistivity	5.5	-	8	µohm.cm
Typical Uses				
Radiation sources; anodes; catalytic uses; medical implants; cermet composites; alloying of steels; high-temperature alloys; alloys for magnets; catalysts; paints;				
Warning				
Cobalt is a suspected carcinogen.				
Other Notes				
Cobalt has magnetic properties similar to those of iron.				

23 times more
 expensive than
 Al Bronze
 per cubic inch

Figure C.7: Material properties with some notes for the selection of the material, regarding the important dimensions of the materials selection, for Cobalt of commercial purity.

Low alloy steel, 0.42C 300M, QT

Designation				
Low alloy steel, 0.42C 300M, Quenched and Tempered				
Composition				
Fe/ 42C/1.8Ni/1.6Si/ 82Cr/ 4Mo/ 08V				
Density	0.2816	-	0.2844	lb/in ³
Energy Content *	6500	-	8992	kcal/lb
Price	0.3003	-	0.4337	USD/lb
Recycle Fraction*	0.7	-	0.8	
Mechanical				
Bulk Modulus	26.85	-	28.22	10 ⁶ psi
Compressive Strength	247	-	273	ksi
Elongation	7	-	8.135	%
Elastic Limit	230	-	254.2	ksi
Endurance Limit	116	-	128	ksi
Fatigue Strength Model*	108.9	-	135.7	ksi
Fracture Toughness	45	-	52	ksi.in ^{1/2}
Hardness - Vickers	551	-	609	HV
Loss Coefficient*	2e-004	-	5e-004	
Modulus of Rupture	230	-	254.2	ksi
Poisson's Ratio	0.32	-	0.3331	
Shape Factor	14	-		
Shear Modulus	11.02	-	11.59	10 ⁶ psi
Tensile Strength	280.1	-	309.5	ksi
Young's Modulus	29.01	-	30.5	10 ⁶ psi
Young's Modulus with Temp.*	29.01	-	30.5	10 ⁶ psi
Thermal				
Maximum Service Temperature	887.4	-	934.2	*R
Melting Point	3071	-	3200	*R
Minimum Service Temperature	*360	-	414	*R
Specific Heat	0.1101	-	0.1146	BTU/lb.F
Thermal Conductivity	31.78	-	34.43	BTU.ft/h.ft ² .F
Thermal Expansion	6.9	-	7.254	µstrain/°F
Electrical				
Resistivity *	18	-	27	µohm.cm
Similar Standards				
USA (UNS): K44220				
Typical Uses				
General construction; general mechanical engineering; automotive; Pressure vessels; pipework;				
Warning				
Some rare heat treatments of certain alloys may produce values for mechanical properties outside the given ranges, eg AISI 9255. tempered at 205C				

245.85 Celsius

42

Figure C.8: Material properties with some notes for the selection of the material, regarding the important dimensions of the materials selection, for Low Alloy Steel (0.42C 300M, QT).

Low alloy steel, AISI 8740, QT

Tradenames				
P11, Pelton Casteel, Inc. (USA); A-1204, AFORA (Aceros Afora S.A.) (SPAIN);				
Designation				
Low alloy steel, AISI 8740, Air-melted, Quenched and Tempered				
UNS Number G87400				
Composition				
Fe/ 38. 43C/ 4. 6Cr/ 4. 7Ni/ 75-11Mn/ 15- 3Si/ 2- 3Mo/ < 035P/ < 04S				
Density	0.2816	-	0.2844	lb/in ³
Energy Content *	6500	-	7800	kcal/lb
Price	0.1668	-	0.3003	USD/lb
Recycle Fraction*	0.7	-	0.8	
Mechanical				
Bulk Modulus	26.85	-	28.22	10 ⁶ psi
Compressive Strength	108.1	-	119.4	ksi
Elongation	17	-	19.76	%
Elastic Limit	100.1	-	110.6	ksi
Endurance Limit*	73.97	-	85.57	ksi
Fatigue Strength Model*	70	-	89.68	ksi
Fracture Toughness*	27.3	-	49.14	ksi.in ^{1/2}
Hardness - Vickers	370	-	460	HV
Loss Coefficient*	2e-004	-	5e-004	
Modulus of Rupture	100.1	-	110.6	ksi
Poisson's Ratio	0.32	-	0.3331	
Shape Factor	35	-		
Shear Modulus	11.02	-	11.59	10 ⁶ psi
Tensile Strength	125	-	138.2	ksi
Young's Modulus	29.01	-	30.5	10 ⁶ psi
Young's Modulus with Temp.	29.01	-	30.5	10 ⁶ psi
Thermal				
Maximum Service Temperature	1382	-	1485	*R
Melting Point	3069	-	3202	*R
Minimum Service Temperature*	387	-	441	*R
Specific Heat	0.1101	-	0.1146	BTU/lb.F
Thermal Conductivity	31.78	-	34.43	BTU.ft/h.ft ² .F
Thermal Expansion	6.9	-	7.254	µstrain/°F
Electrical				
Resistivity *	23	-	35	µohm.cm
Typical Uses				
General construction; general mechanical engineering; automotive; Pressure vessels; pipework;				
Warning				
Some rare heat treatments of certain alloys may produce values for mechanical properties outside the given ranges, eg AISI 9255. tempered at 205C ⁴³				

Lower end of all 69 materials

Figure C.9: Material properties with some notes for the selection of the material, regarding the important dimensions of the materials selection, for Low Alloy Steel (AISI 8740, QT).

Nickel, Commercial Purity

Designation				
Nickel 200 series grades (UNS Nos. of form N022xx)				
Composition				
>99%Ni or better				
Density	0.319	-	0.3233	lb/in ³
Energy Content	2.492e+004	-	7.475e+004	kcal/lb
Price	1.772	-	4.989	USD/lb
Recycle Fraction*	0.7	-	0.9	
Mechanical				
Bulk Modulus	23.5	-	29.01	10 ⁶ psi
Compressive Strength*	10.15	-	135.6	ksi
Elongation	2	-	60	%
Elastic Limit	10.15	-	135.6	ksi
Endurance Limit*	19.58	-	72.52	ksi
Fracture Toughness	91	-	136.5	ksi.in ^{1/2}
Hardness - Vickers	80	-	300	HV
Loss Coefficient*	2e-004	-	3.2e-003	
Modulus of Rupture*	10.15	-	135.6	ksi
Poisson's Ratio	0.305	-	0.315	
Shape Factor	30	-		
Shear Modulus	10.44	-	12.47	10 ⁶ psi
Tensile Strength	50.04	-	145	ksi
Young's Modulus	27.56	-	31.91	10 ⁶ psi
Thermal				
Maximum Service Temperature	*918	-	1152	*R
Melting Point	3074	-	3130	*R
Minimum Service Temperature	0	-		*R
Specific Heat	0.108	-	0.1099	BTU/lb.F
Thermal Conductivity	38.71	-	52.58	BTU.R/h.ft ² .F
Thermal Expansion	6.667	-	7.5	µstrain/*F
Electrical				
Resistivity	8	-	10	µohm.cm
Typical Uses				
Chemical and food processing; Electronic parts; Aerospace; Caustic evaporators; Combustion boats; Plater bars; Cathode shanks; Fluorescent lamps; Hydrogen thyratons; Electrodes; Heat exchangers; Heat shields;				
Warning				
All nickel compounds should be regarded as toxic. Some can cause cancer and/or foetal abnormalities.				

•Similar to Cobalt
•all properties higher than for Al Bronze
•But 7 times cheaper than Co

→ **20 % and 10 % lower than Cobalt**

44

Figure C.10: Material properties with some notes for the selection of the material, regarding the important dimensions of the materials selection, for Nickel of commercial purity.

Copper Beryllium

General				
Designation				
Copper Alloy: Copper Beryllium				
Composition				
Cu/0-2 Be/0-2 Co				
Density	0.2981	-	0.3161	lb/in ³
Energy Content *	1.3e+004	-	1.733e+004	kcal/lb
Price	3.87	-	5.338	USD/lb
Recycle Fraction*	0.4	-	0.5	
Mechanical				
Bulk Modulus	18.85	-	21.76	10 ⁶ psi
Compressive Strength	15.95	-	174	ksi
Elongation	1	-	45	%
Elastic Limit	15.95	-	174	ksi
Endurance Limit	13.05	-	44.96	ksi
Fracture Toughness	13.65	-	63.7	ksi.in ^{1/2}
Hardness - Vickers	60	-	400	HV
Loss Coefficient*	1e-005	-	2e-004	
Modulus of Rupture	15.95	-	174	ksi
Poisson's Ratio	0.34	-	0.35	
Shape Factor	30	-		
Shear Modulus	6.527	-	7.542	10 ⁶ psi
Tensile Strength	43.51	-	210.3	ksi
Young's Modulus	17.4	-	20.02	10 ⁶ psi
Thermal				
Maximum Service Temperature	594	-	846	*R
Melting Point	2061	-	2425	*R
Minimum Service Temperature	0	-		*R
Specific Heat	0.09315	-	0.09864	BTU/lb.F
Thermal Conductivity	49.11	-	121.3	BTU.R/h.ft ² .F
Thermal Expansion	9.167	-	10.28	µstrain/*F
Electrical				
Resistivity	3.31	-	10	µohm.cm
Typical Uses				
High conductivity, high strength electrical components, springs, clips, fasteners, moulds, dies				

→ **196.85 Celsius**

→ **outstanding el. th. conductivity**

45

Figure C.11: Material properties with some notes for the selection of the material, regarding the important dimensions of the materials selection, for Copper Beryllium

Designation				
Copper Alloy: Aluminium Bronze				
Composition				
Cu/5-20 Al				
Density	0.2637	-	0.2962	lb/in ³
Energy Content *	1.192e+004	-	1.398e+004	kcal/lb
Price	0.814	-	0.9141	USD/lb
Recycle Fraction*	0.4	-	0.5	
Mechanical				
Bulk Modulus	15.81	-	21.03	10 ⁶ psi
Compressive Strength	18.56	-	76.87	ksi
Elongation	8	-	65	%
Elastic Limit	18.56	-	76.87	ksi
Endurance Limit	23.93	-	39.89	ksi
Fracture Toughness	24.57	-	61.88	ksi.in ^{1/2}
Hardness - Vickers	87.5	-	250	HV
Loss Coefficient*	1.5e-005	-	2.5e-004	
Modulus of Rupture	18.56	-	76.87	ksi
Poisson's Ratio	0.34	-	0.35	
Shape Factor	30	-		
Shear Modulus	5.366	-	7.252	10 ⁶ psi
Tensile Strength	52.21	-	116	ksi
Young's Modulus	14.5	-	19.44	10 ⁶ psi
Thermal				
Maximum Service Temperature	936	-	1197	°R
Melting Point	2356	-	2410	°R
Minimum Service Temperature	0	-	198	°R
Specific Heat	0.09315	-	0.09602	BTU/lb.F
Thermal Conductivity	34.67	-	49.69	BTU.ft/h.ft ² .F
Thermal Expansion	8.056	-	10.83	µstrain/°F
Electrical				
Resistivity	9.33	-	52.5	µohm.cm
Typical Uses				
High strength corrosion-resistant parts for marine and chemical use, pumps, valve gears, chains die-cast components for autos, condensers, heat exchangers for brine, acid and salts, coins, jewellery				

46

Figure C.12: Material properties with some notes for the selection of the material, regarding the important dimensions of the materials selection, for Aluminum Bronze.

EMW Tool Materials Selection Software by PULSAR

PULSAR has created an excel software with theoretical calculations to calculate the important dimensions depending on the input parameters of the process. Furthermore, the in-house software gives a materials choice suggestion for the particular case. Figure C.13 shows an example of the software front view (calculations and database are in the back and proprietary).

MP-Sim for MP-Weld simulation

Click to Select from List in blue cells Enter values in Green cells

Outer Tube		Inner Tube	
Units:	mm		
Material	SSt 303	Material	SSt 303
Outer diameter	260	Outer diameter	260
		diameter 2 (if angled)	
Wall thickness	1.2	Wall thickness (enter 0 for a full)	1.2
Weld area Geometry	Simple-Flare		

Load Information		Load Allowed (for recommended dimensions)	
Load Type	Tear, kg pull	Outer tube	34,110.487
Load Value	34,000.00	Flare (if used)	34,110.487
Strength/Load =	100.32%	Transition	34,110.487
		Inner tube	218,702.004
		Weld	34,126.347

Simulation Results			
	Coil allowed: Any		
	Recommended dimensions [mm]		
	Outer tube	Flare	Inner tube
Outer Diameter	260.00	260.08	252.4
Wall thickness	1.20	1.20	8.15
Lap Length	18.00	Worked length	11.00
Weld length	Minimum Required	1.23 [mm]	6/128"
	Recommended	1.23 [mm]	6/128"
Required gap		63.20 [mm]	2 63/128"
	Actual gap:	2.64 [mm]	13/128"

Process Feasibility:


Not Feasible: Requires too much Ene

Required energy (kJ)	N/A	0.000 [TJ]
Recommended machine	N/A	

Figure C.13: Example of the Excel Software used at PULSAR to calculate the necessary EMW machine and coil equipment for specific input parameters. In this case the software is asked to weld Stainless Steel 303 to Stainless Steel 303.

In the case of Figure C.13 the software is asked to weld Stainless Steel 303 to Stainless Steel 303. The software states that the process is not feasible because there is no machine or coil available that could perform the necessary weld, due to the excessive energy requirements.

Figure C.14 gives an example of the software stating that the process is feasible; in this case Al6061-T6 is calculated to be welded to Al6061-T6.



MP-Sim for MP-Weld simulation

Click to Select from List in blue cells Enter values in Green cells

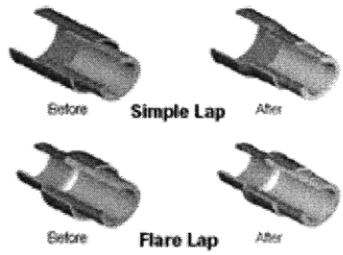
Outer Tube		Inner Tube	
Units:	mm		
Material	AL 6061-T6	Material	AL 6061-T6
Outer diameter	260	Outer diameter	260
		diameter 2 {if angled}	
Wall thickness	1.2	Wall thickness (enter 0 for a full	1.2
Weld area Geometry	Simple-Flare		
Load Information		Load Allowed {for recommended dimensions	
Load Type	Tear, kg pull	Outer tube	30,841.565
Load Value	34,000.00	Flare {if used}	30,841.565
Strength/Load =	90.71%	Transition	30,841.565
		Inner tube	146,321.558
		Weld	34,014.187
Simulation Results		Coil allowed: Any	
	Recommended dimensions [mm]		
	Outer tube	Flare	Inner tube
Outer Diameter	260.00	260.08	252.4
Wall thickness	1.20	1.20	5.98
Lap Length	18.00	Worked length	11.00
Weld length	Minimum Required	1.36 [mm]	7/128"
	Recommended	1.36 [mm]	7/128"
Required gap		14.26 [mm]	72/128"
	Actual gap:	2.64 [mm]	13/128"
Process Feasibility:	88.82%		
Process is Feasible			
Required energy (kJ)	13.268		
Recommended machine	MP35-25 (A)		
		19.128 (TI)	

Figure C.14: Example of the Excel Software used at PULSAR to calculate the necessary EMW machine and coil equipment for specific input parameters. In this case the software is asked to weld Al6061-T6 to Al6061-T6.

The PULSAR software states that the process is feasible and that the required energy will be about 13.268 kJ. Therefore, the recommend machine MP35-25 (A) and coil are suggested.

Figure C.15 shows the calculation of the same material combination as in Figure 22, but now the outer diameter of the inner and outer workpiece have been changed to 3 inch and the wall-thickness has been changed to 0.1 inch, which is similar to some of our dimensions shown previously.

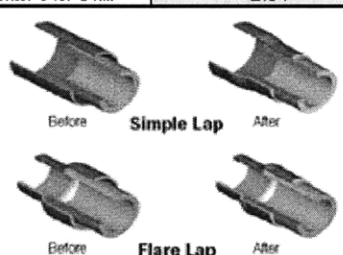
Outer Tube		Inner Tube	
Units:	mm		
Material	AL 6061-T6	Material	AL 6061-T6
Outer diameter	76.2	Outer diameter	76.2
Wall thickness	2.54	Wall thickness (enter 0 for a full angled)	2.54
Weld area Geometry	Simple+Flare		
Load Information		Load Allowed (for recommended dimensions)	
Load Type	Tear, kg pull	Outer tube	18,580.454
Load Value	34,000.00	Flare (if used)	18,580.454
Strength/Load =	54.65%	Transition	18,580.454
		Inner tube	61,383.431
		Weld	34,005.765
Simulation Results		Coil allowed: Any	
	Recommended dimensions [mm]		
	Outer tube	Flare	Inner tube
Outer Diameter	76.20	78.37	62.6
Wall thickness	2.54	2.46	12.28
Lap Length	38.00	Worked length	24.00
Weld length	Minimum Required	5.47 [mm]	28/128"
	Recommended	5.47 [mm]	28/128"
Required gap		1.73 [mm]	9/128"
	Actual gap:	5.42 [mm]	27/128"
Process Feasibility:	84.03%		
Process is Feasible			
Required energy (kJ)	4.190		
	20.602 [TJ]		
Recommended machine	MP12-9 {H}		

Figure C.15: Example of the Excel Software used at PULSAR to calculate the necessary EMW machine and coil equipment for specific input parameters. In this case the software is asked to weld Al6061-T6 to Al6061-T6, like in Figure 8, but now the dimensions of the workpieces have been changed.

Again the process is feasible and the required energy is 4.19 kJ and the recommended PULSAR machine is MP12-9 {H}.

All in all, the PULSAR software seems to be a very strong solution for quick answers to what coil and machine is necessary for the needed input parameters. Furthermore, PULSAR is (besides MAGNEFORM) the only provider of EMW machinery. Therefore, although only machinery and coils from PULSAR are used in the database, this software is really the only software that is available and useful on the market.

Appendix D (see bibliography of Chapter 4 for the according references)

Magnetic Field Measurements of the EMW coil at PULSAR (November 2007)

This report contains the results of magnetic field measurement made for two types of working coils for pulse magnetic welding of MIT samples. The coils used were for welding of 1" and 1.5" dia Aluminum tubes

Equipment: Pulse Current Generator

The Pulse Current Generator data is shown in Table D.1:

Capacitance	320	μF
Working voltage, max	25	kV
Self inductance	25	nH
Energy storage, max	100	kJ
Peak current, max	1200	kA

Table D.1: Properties of the pulse current generator.

A cable pulse transformer was used in order to increase the discharge system's efficiency with the following data, see Table D.2:

Number of winds	3
Number of lines	8
Transformation ratio	$k= 2,7$

Table D.2: Properties of the cable pulse transformer.

Working Coil and Special Devices

Two one turn coils with two different working zone dimensions ($D=1''$ and $D=1.5''$, respectively) were used for this study, see Figure D.1. Figure D.1 also shows a photograph of the front-view of the EMW coil.

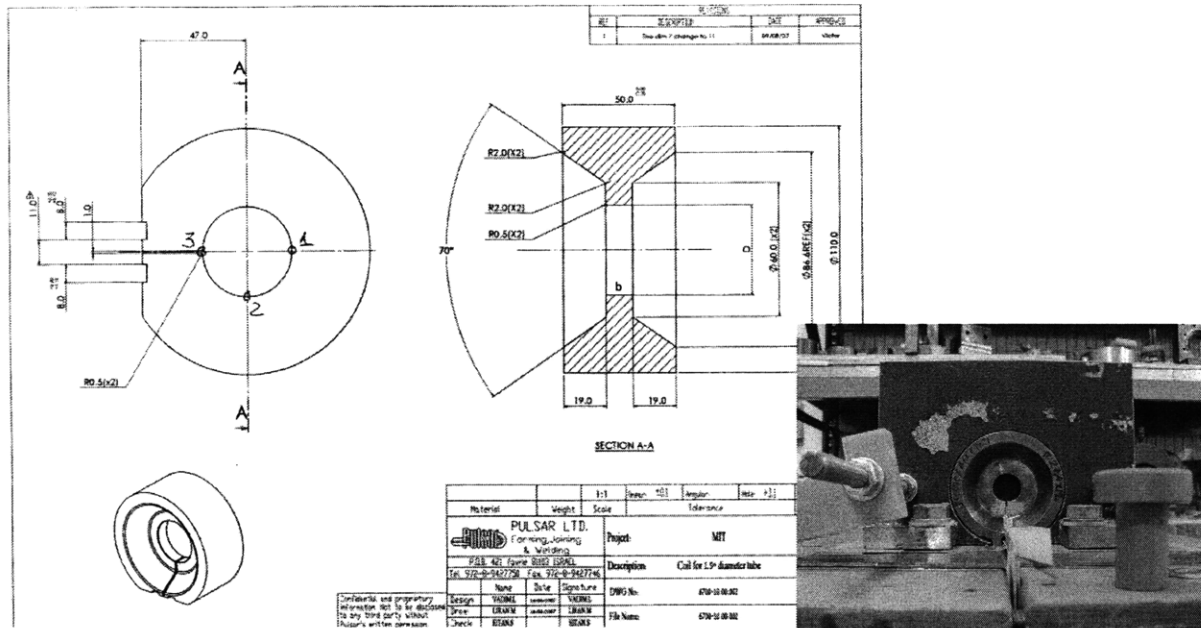


Figure D.1: Schematic drawing and photograph of the front-view of the EMW coil used in the study for the 1.5" diameter samples.

Measuring Devices

The measuring devices included:

- A Rogovsky Coil for current measuring together with an integrator. The Rogovsky coil scale was $M_i = 126 \text{ kA/Volt}$, where M_i is current amplitude measured on oscilloscope.
- A magnetic field induction probe, also with an integrator. The magnetic field probe scale was $M_B = 14 \text{ Tesla/Volt}$, where M_B is magnetic force measured on the oscilloscope.
- A TEXTRONIX TDS 202 4B Oscilloscope was used for the signal registration

Magnetic Field Measurement

A schematic of the measuring device and a digital photograph with the measuring probe in place are shown in Figure D.2. A measuring probe was inserted along the indents of the measuring device at different displacements shown in Figure D.3.

Measurements were carried out at 9 points for each coil - three at positions in the tangential direction at points 1, 2, 3 (see Figure D.1) and further three in the axial direction at points 5, 6, 7 (see Figure D.1 and Figure D.2).

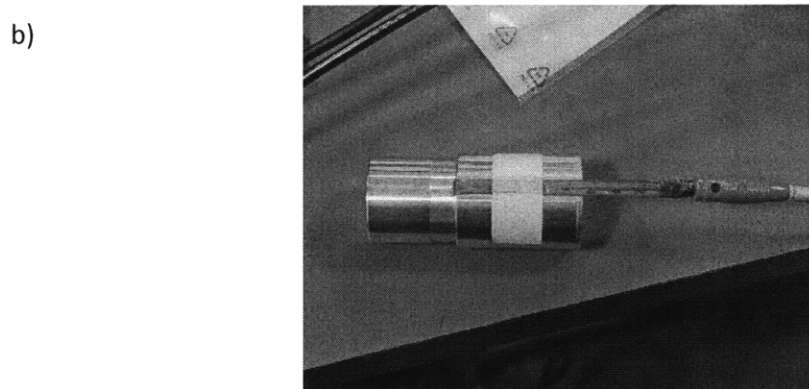
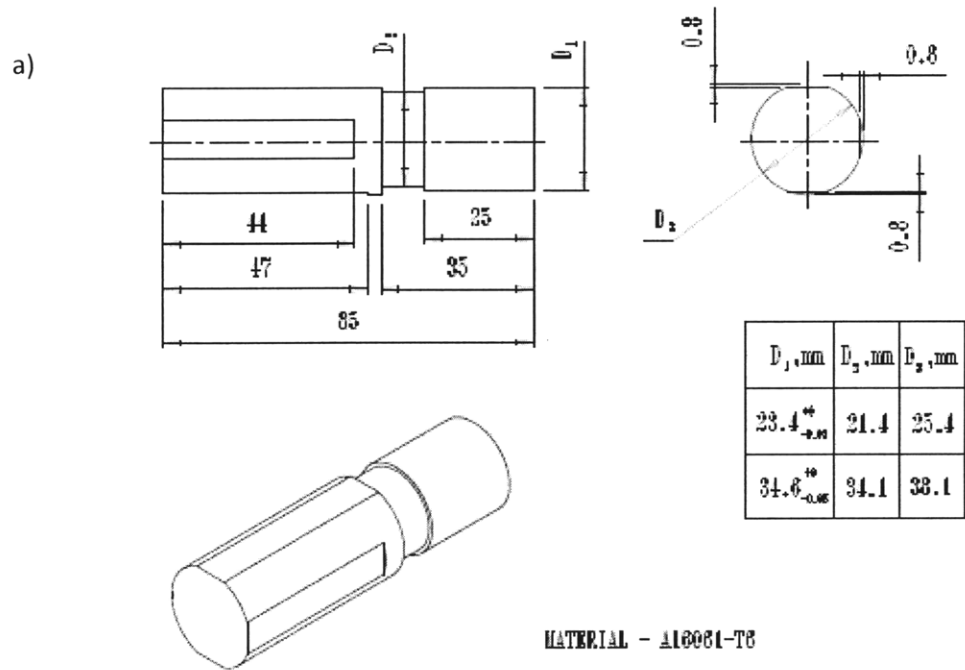


Figure D.2.: a) Schematic of the measuring rod for the magnetic field measurements.
 b) Photograph of the measuring device with the measuring probe in place.

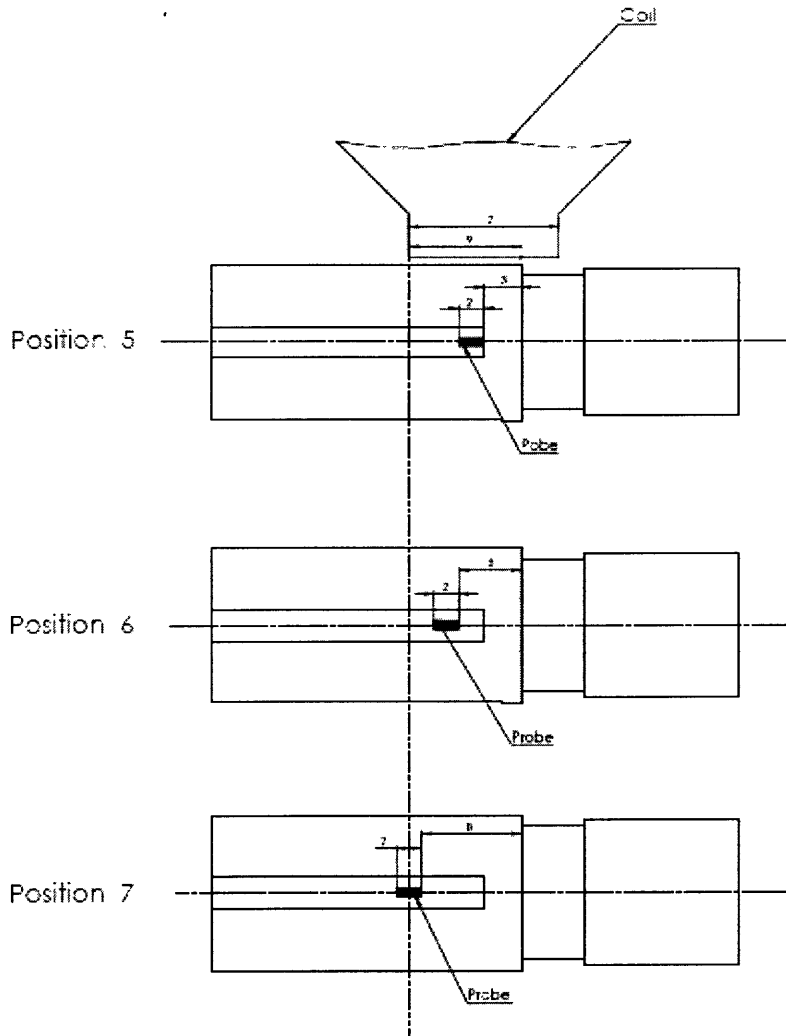


Figure D.3: Position map of the magnetic field measurement probe being inserted into the measuring rod (see Figure D.2).

This means that each point number in the presented Tables below has the following number designation eg point #1-5 means that the probe was in Position 1 in the tangential direction and Position 5 in the axial direction, etc

Results

The measured data from the experiment was $I_{1, \text{measured}}$ [V] and B_{measured} [V]. The data was then converted as follows:

$$I_1 [\text{kA}] = I_{1, \text{measured}} [\text{V}] * 126,$$

$$I_2 [\text{kA}] = I_1 [\text{kA}] * k, \text{ where } k=2, 7 \text{ and}$$

$$B [\text{T}] = B_{\text{measured}} [\text{V}] * 14.$$

The measurements for the 27,4 mm ID coil are shown in Table D.7. The charge voltage for all experiments in Table D.3 was 3,0 kV, which means that the energy was $W= 1, 44$ kJ. The results are shown graphically in Figure D.4.

#	Point #	$I_{1, \text{measured}}$ [V]	I_1 [kA]	I_2 [kA]	B_{measured} [V]	B [T]	$B/12$
1	1-5	0,687	86,56	233,7	0,656	9,184	0,0392
2	1-6	0,687	86,56	233,7	0,584	8,176	0,0349
3	1-7	0,686	86,43	233,36	0,448	6,272	0,0268
4	2-5	0,687	86,56	233,7	0,64	8,96	0,0383
5	2-6	0,691	87,07	235,0	0,584	8,176	0,0348
6	2-7	0,686	86,43	233,36	0,384	5,376	0,023
7	3-5	0,687	86,56	233,7	0,6	8,4	0,0359
8	3-6	0,687	86,56	233,7	0,496	6,944	0,0297
9	3-7	0,695	87,57	236,44	0,376	5,18	0,0219

Table D.3: Experimental results for the magnetic field measurements of the 1.5" EMW specimen coil, performed at PULSAR (November, 2007).

The measurements for the $ID=40$, 1 mm coil (1.5" OD EMW specimen coil) are shown in the Table D.4. The charge voltage in all experiments in Table D.3 was 5,0 kV, which means that the energy was $W=4kJ$. The results are shown graphically in Figure D.5.

#	Point #	$I_{1, \text{measured}}$ [V]	I_1 [kA]	I_2 [kA]	B_{measured} [V]	B [T]	$B/12$
1	1-5	1,04	131	353,8	1,0	14,0	0,0396
2	1-6	1,04	131	353,8	0,82	11,48	0,0325
3	1-7	1,04	131	353,8	0,4	5,6	0,0158
4	2-5	1,04	131	353,8	0,98	13,72	0,0387
5	2-6	1,04	131	353,8	0,82	11,48	0,0325
6	2-7	1,04	131	353,8	0,4	5,6	0,0158
7	3-5	1,04	131	353,8	0,84	11,76	0,0333
8	3-6	1,04	131	353,8	0,66	9,24	0,0261
9	3-7	1,04	131	353,8	0,4	5,6	0,0158

Table D.4: Experimental results for the magnetic field measurements of the 1" EMW specimen coil, performed at PULSAR (November, 2007).

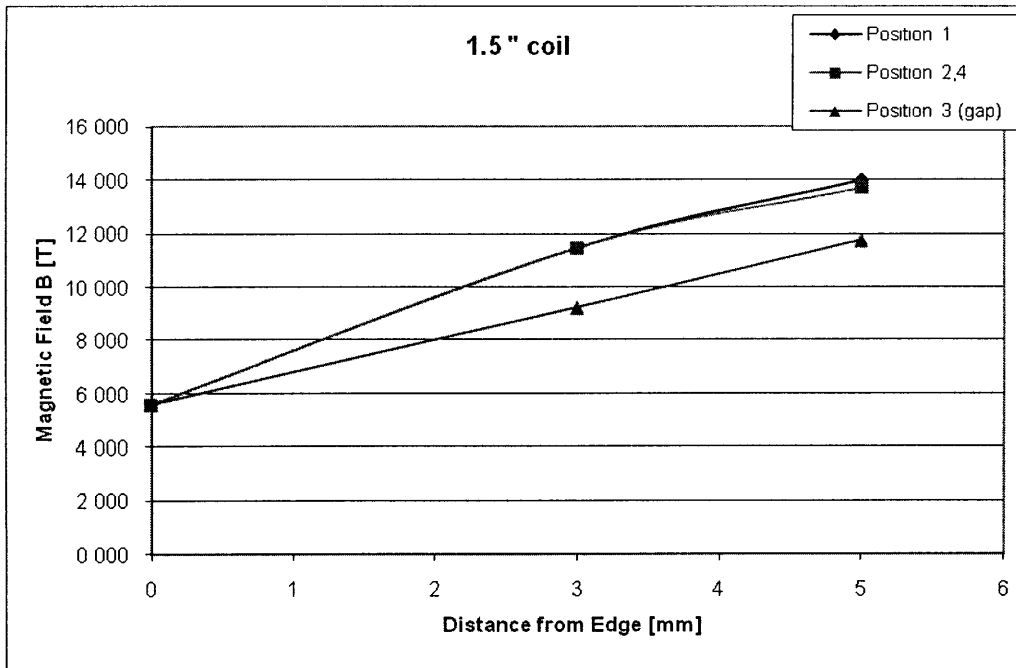


Figure D.4: Graphic representation of the magnetic field measurement results, for the 1.5" specimen coil, performed at PULSAR (November, 2007).

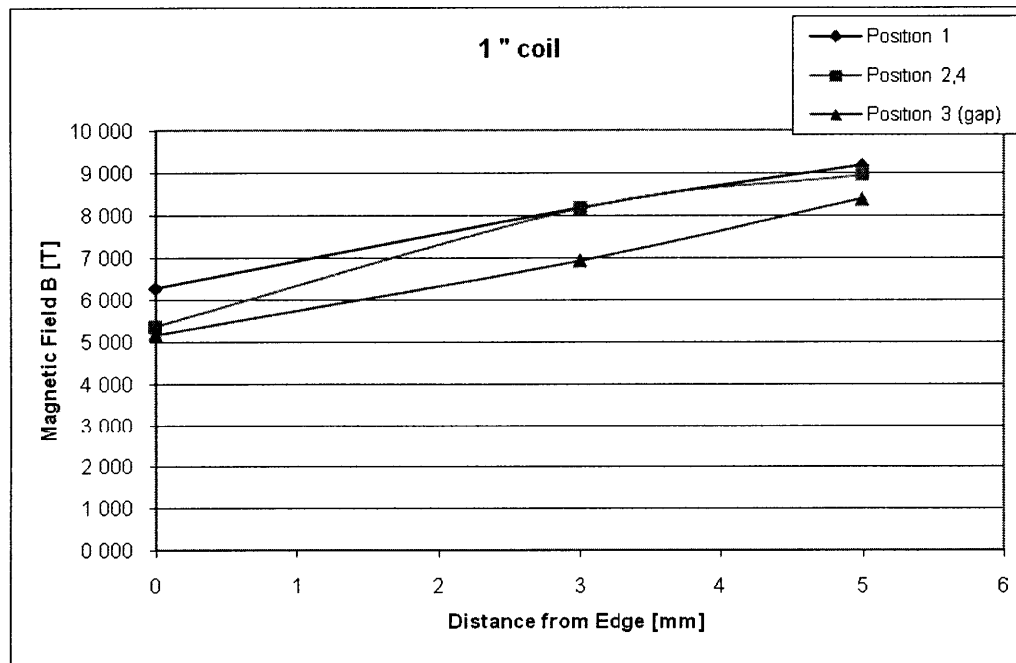


Figure D.5: Graphic representation of the magnetic field measurement results, for the 1" specimen coil, performed at PULSAR (November, 2007).

Discussions

The position and displacement of the magnetic field measuring device in the working coil are shown in Figure D.1 and Figure D.3, respectively. The device was placed in the same way as the real work-piece, which means that it was placed 9 mm inside the coil. Accordingly, point 5 was 2 mm from the edge of the workpiece, point 6 was 5 mm from edge of work-piece and point 7 was 8 mm from edge of work-piece.

The length of the magnetic field probe in the axial direction is 2 mm. Therefore, the variation of the magnetic field over the length of 7 mm- 9mm was in the range of 18% for coil of $ID = 1,5$ inch and 10% for coil of $ID = 1$ inch.

It is very important that at the end of the working zone, the magnetic field distribution in the tangential direction is independent of the angle, as shown in Figure D.4 and Figure D.5.

Finally, equating B/I calculates the coil efficiency. The theoretical B/I must be in the range of μ_0/b , where $\mu_0 = 4\pi \cdot 10^{-7} = 1.256 \cdot 10^{-6}$ H/m and b is the length of coil working zone in meters (see Figure D.1 for the working zone b). For the coil's 12 mm working zone, the theoretical B/I is 0.10466 T/kA.

The measured B/I max is in the range 0.0396 -0.0392 T/kA or about 37% of the theoretical value. This is in agreement with other results for one turn coil experiments in which about 1/3 of the theoretical value of the magnetic field is applied [3].

Weld length ratio measurement using SEM

Two different weld lengths have been measured using the SEM. A minimum weld length for the part of the weld that was completely welded and no material contrast could be detected. From this measurement we calculated a minimum weld length ratio R_{min} . Then, a maximum weld length ratio R_{max} was calculated by measuring a maximum weld length including the fringe of the weld. Again, an average for l_0 of 10.5 mm was used to calculate R for all the samples (same as for the R measurements for the optical microscopy study). The amplitude of the weld at its fringe was measured as well. For the SEM analysis only one side of the specimen was studied. Table D.5 shows the summary of the SEM measurements.

	A	B	C	D	E=ABCD			
Run	Tapered Angle	Wall-Thickness	Diameter	Gap	Cleanliness	R_{max}	R_{min}	Amplitude [μm]
1	-	-	-	-	+		10.9	35.47
2	-	-	-	+	-	15.4	7.4	42.01
3	-	-	+	-	-			
4	-	-	+	+	+	33.2	16.9	29.38
5	-	+	-	-	-			
6	-	+	-	+	+	51.8	45.5	15.15
7	-	+	+	-	+	24.4	14.7	41.97
8	-	+	+	+	-	35.3	23.3	26.12
9	+	-	-	-	-	22.4	12.6	18.28
10	+	-	-	+	+	22.1	22.1	20.92
11	+	-	+	-	+	52.1	46.9	23.97
12	+	-	+	+	-	0	0	35.13
13	+	+	-	-	+	48.6	43.7	13.62
14	+	+	-	+	-	53.6	43.7	41.38
15	+	+	+	-	-	23.8	9.1	13.77
16	+	+	+	+	+	40.0	38.6	23.24

Table D.5: R values weld interface wave amplitudes measured on the SEM (specimens with the larger diameter are in bold font).

Comparison of Maximum Tensile Force to the measured Welded Length Ratio

Figure D.6 shows the comparison of the measured maximum loads during the tensile tests of the first DOE batch (August 2007) with the measured welded length ratio.

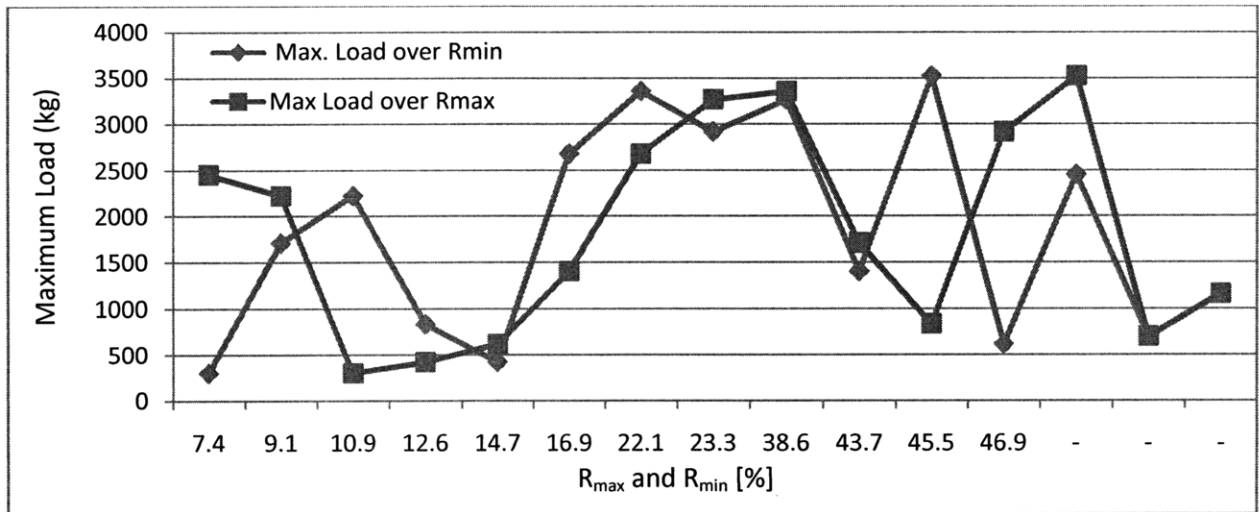


Figure D.6: Comparison of the measured maximum loads during the tensile tests of the first DOE batch (August 2007) with the measured welded length ratio.

As stated before, the measured welded length ratios are not accurate as they are only measured at one point of the circumference of the EMW joint. Therefore, we have to agree that the results in Figure D.6 are not very conclusive, with the exception of measured maximum welded length ratios R_{max} between 10.9% and 38.6%.

Schematic drawings for the tensile test specimens of the second DOE batch:

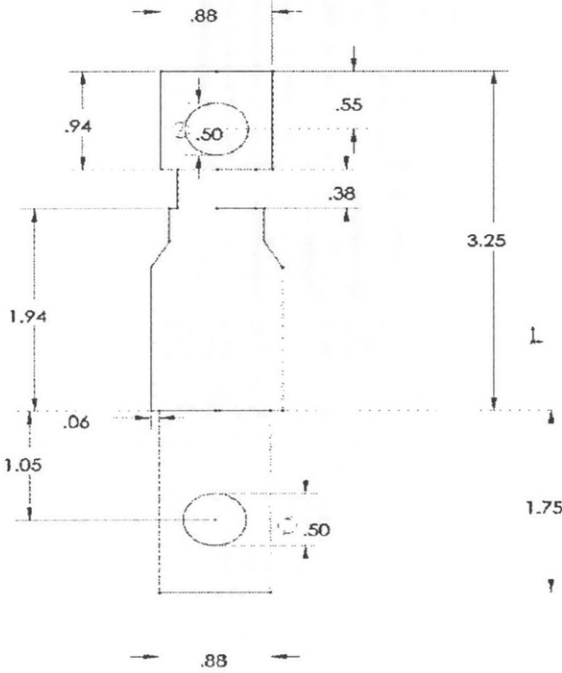


Figure D.7: Schematic drawing of the tensile test specimen for the 1" EMW joint.

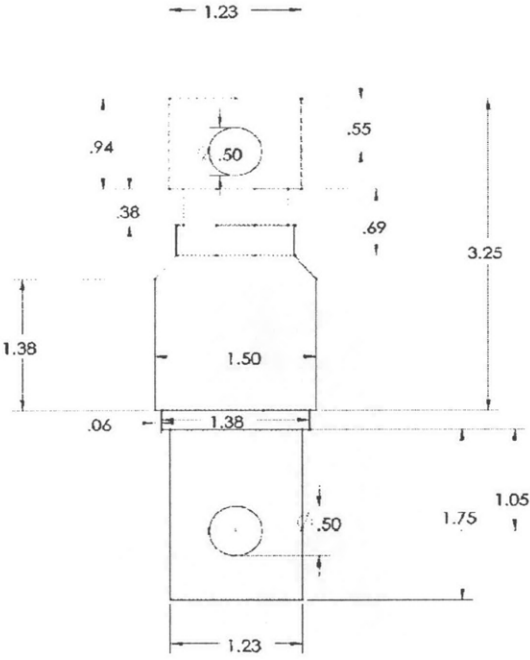


Figure D.8: Schematic drawing of the tensile test specimen for the 1.5" EMW joint.

DOE of the first EMW specimens batch from PULSAR (August 2007)

In our analysis of the measured tensile strength presented in Chapter 4 we showed that the gap and the cleanliness were strong DOE parameters, which would affect the tensile strength the most, besides the obvious parameters such a diameter and wall-thickness. Table D.6 summarizes the strongest EMW joints, with their respective DOE parameters:

	angl	wall	diam	gap	clean.		
Run	A	B	C	D	E=ABCD	max load [kg]	Displacement at max force [mm]
4	-	-	+	+	+	3356	1.551
6	-	+	-	+	+	3523	1.332
10	+	-	-	+	+	2223	1.065
16	+	+	+	+	+	3267	1.759

Table D.6: Summary of the strongest EMW joint specimens with the respective DOE parameters and the resulting max tensile load and displacement at failure.

Figure D.9 from the DOE analysis shows a cube plot, which simplifies the analysis to find the most important parameters presented in Chapter 4:

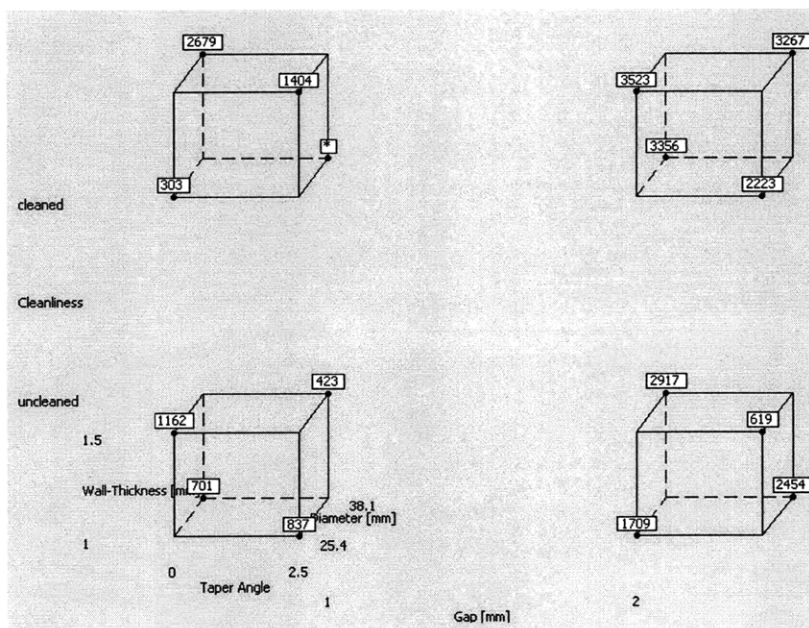


Figure D.9: Cube plot of the DOE analysis for the first batch of EMW specimens. The values at the corners of the cubes show the values of the measured maximum loads in kg. The x-axis of the entire plot and the y-axis show the parameter cleanliness and gap, respectively.

From Figure D.9 one can see that for a larger gap as well as a cleaned inner workpiece the highest tensile strengths can be observed. This can also be shown in a so-called Pareto Diagram, which is shown in Figure D.10:

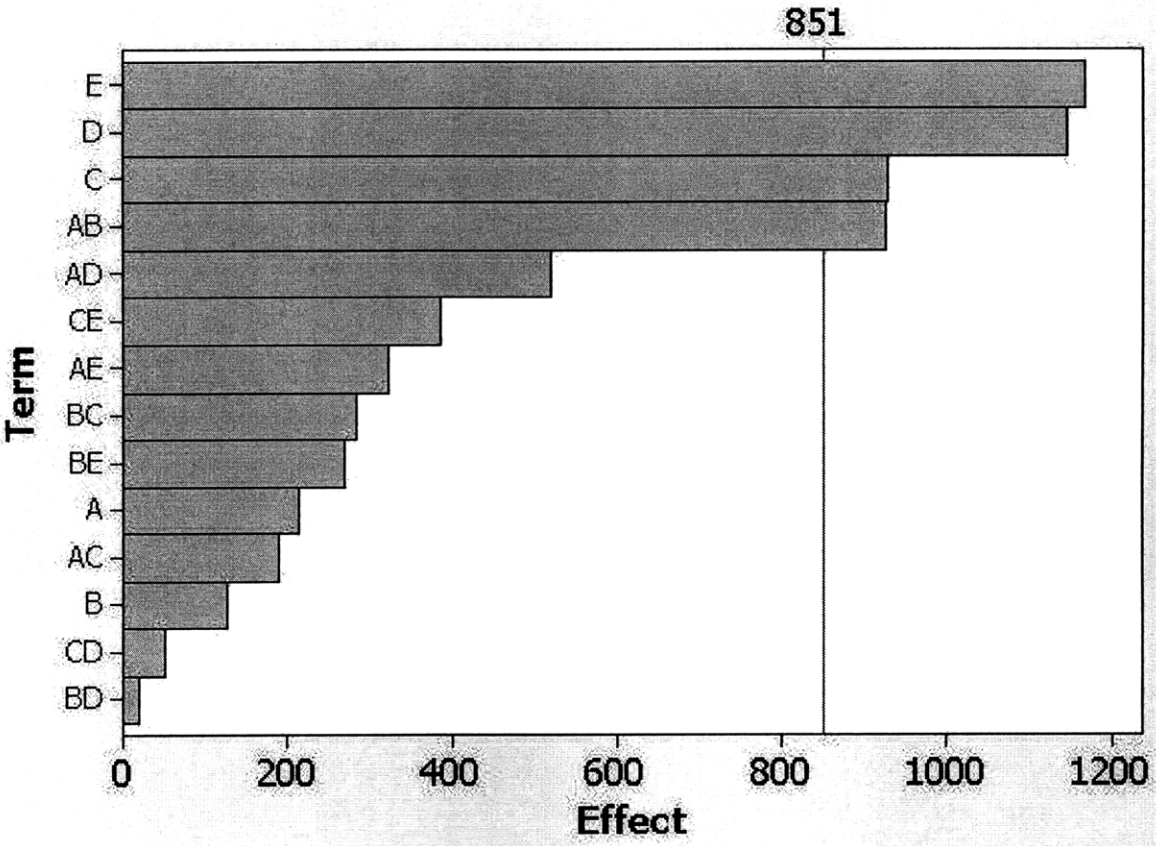


Figure D.10: Pareto Diagram of the all DOE parameters of the first DOE study. The red line displays the limit above which parameters become significant for the chosen α of 0.1.

The Pareto diagram shown in Figure D.10 shows that all parameters of the first DOE and their significance with regards to their effect on the resulting tensile strength. A Pareto diagram can also show interactions such as the interaction between two or three parameters (AB, see Figure D.10). Therefore, also the interaction between the parameters A (Taper Angle) and B (Wall-Thickness) is significant.

The value of α reflects the probability to find an effect that is non-existent, which would mean that one is making a wrong hypothesis. The value of α was chosen to be 0.1 in this case, which means that there is a 10% probability of making a wrong prediction, based on the presented DOE analysis.

Another plot that can show interaction between the different parameters is a so-called interaction plot, shown in Figure D.11.

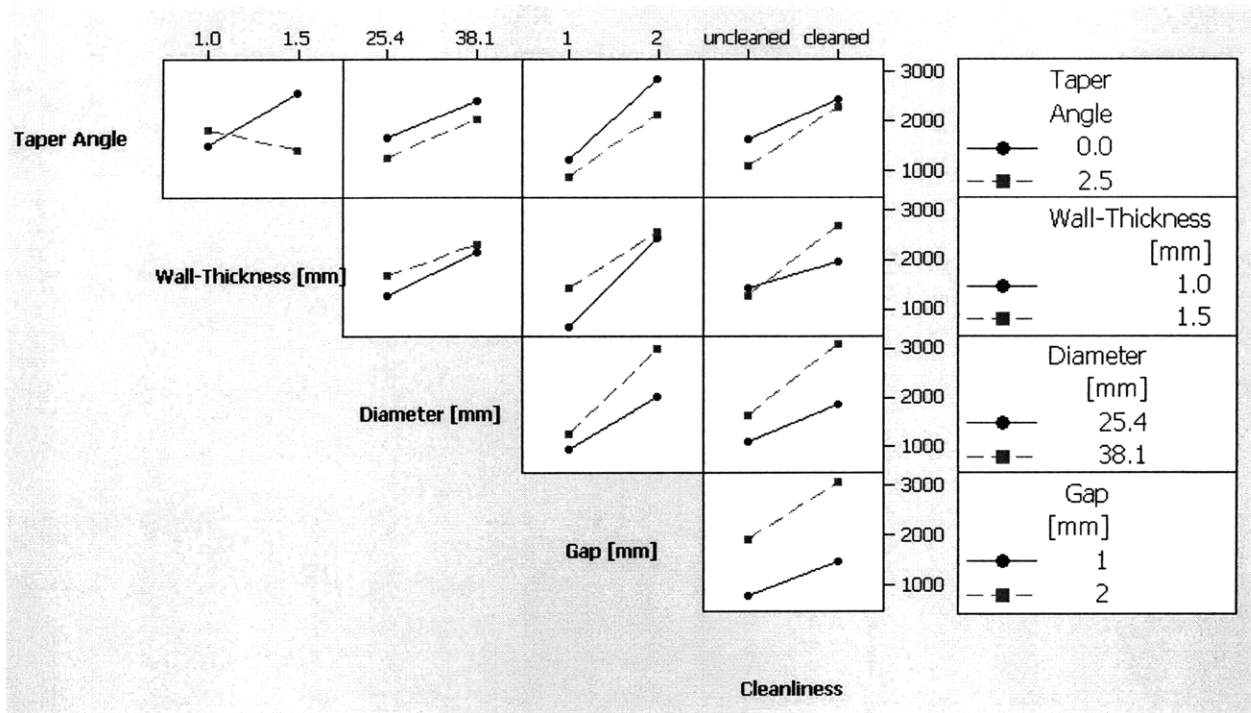


Figure D.11: Interaction plot for all parameters with the effect on the mean tensile strength of the EMW joints.

Analyzing Figure D.11, we find that our observations match the presented interactions shown, with the exception of the tapered angle and its change in effect, due to a change in wall thickness. We can see that for a taper angle of zero degrees the tensile strength increases with increasing wall-thickness, as expected. However, if a taper angle of 2.5 degrees is chosen the tensile strength decreases with increasing wall thickness.

DOE of the second EMW specimens batch from PULSAR (November 2007)

Table D.7 and Table D.8 show the maximum measured loads for the 1" and 1.5" specimens, respectively. The maximum load was calculated from the average of the two tensile tests performed on two specimens with the same DOE parameters.

	A	B	C	D	E=ABC	F=BCD	T1		T2		
Run	Taper Angle	Wall-Thickness	Diameter	Gap	Cleanliness	Surface Condition	maximum load (kg)	Displacement at max force [mm]	maximum load (kg)	Displacement at max force [mm]	Failure Mode
1	-	-	-	-	-	-	524	4.359	-	-	s
2	-	-	-	+	-	+	674	4.043	623	4.552	s-s-s
5	-	+	-	-	+	+	1639	1.437	1752	2.311	s-b
6	+	-	-	-	+	-	1896	4.33	-	-	sp
9	+	-	-	-	+	-	1523	2.174	1564	2.054	b-b
10	+	-	-	+	+	+	1561	2.431	1369	2.339	b-b
13	+	+	-	-	-	+	467	3.149	255	3.117	s-s
14	+	+	-	+	-	-	374	3.592	182	3.276	s-s

Table D.7: Maximum measured average loads and individual maximum forces and respective displacement at failure for the two performed tensile tests per DOE run, for the 1" specimens. The column Failure Mode shows the way in which the specimen failed during the test (sp...specimen fixture failure , s...outer workpiece slipped off the inner workpiece, b...failure in the base material of the outer workpiece).

	A	B	C	D	E=ABCD	F=BCD	T1		T2		
Sample	Taper Angle	Wall-Thickness	Diameter	Gap	Cleanliness	Surface Condition	maximum load (kg)	Displacement at max force [mm]	maximum load (kg)	Displacement at max force [mm]	Failure
3	-	-	+	-	+	+	840	0.508	-	-	sp
4	-	-	+	+	+	+	847	0.399	-	-	sp
7	-	+	+	-	-	-	782	3.882	-	-	s
8	-	+	+	+	-	+	1000	5.669	1109	5.342	s-s
11	+	-	+	-	-	+	84	1.685	140	1.797	s-s
12	+	-	+	+	-	-	195	0.179	122	0.229	s-s
15	+	+	+	-	+	-	1951	1.773	2151	0.886	b-b
16	+	+	+	+	+	+	3546	3.526	808	1.074	b-sp

Table D.8 : Maximum measured average loads and respective displacement at failure for the two performed tensile tests per DOE run, for the 1.5" specimens. The column Failure Mode shows the way in which the specimen failed during the test (sp...specimen fixture failure , s...outer workpiece slipped off the inner workpiece, b...failure in the base material of the outer workpiece).

From Table D.7 we can see that the 1" specimens failed in different modes. Figure D.12 shows photographs of the 1" specimens and their different failure modes. It can be seen that (from left to right) the specimens failed in three modes:

- 1) Slip off of the outer workpiece off the inner workpiece, due to a non-complete EMW joint.
- 2) The two samples in the middle of Figure D.12 depict the optimal failure mode of the EMW joint specimen, where the base material of the tube is weaker than the EMW joint.
- 3) Failure of the specimen itself. This only happened for one of the specimens, sample R6 T1, which showed the strongest mechanical properties, with a maximum load of 1896 kg, which was the closed to the theoretical strength of the material of 2438 kg.

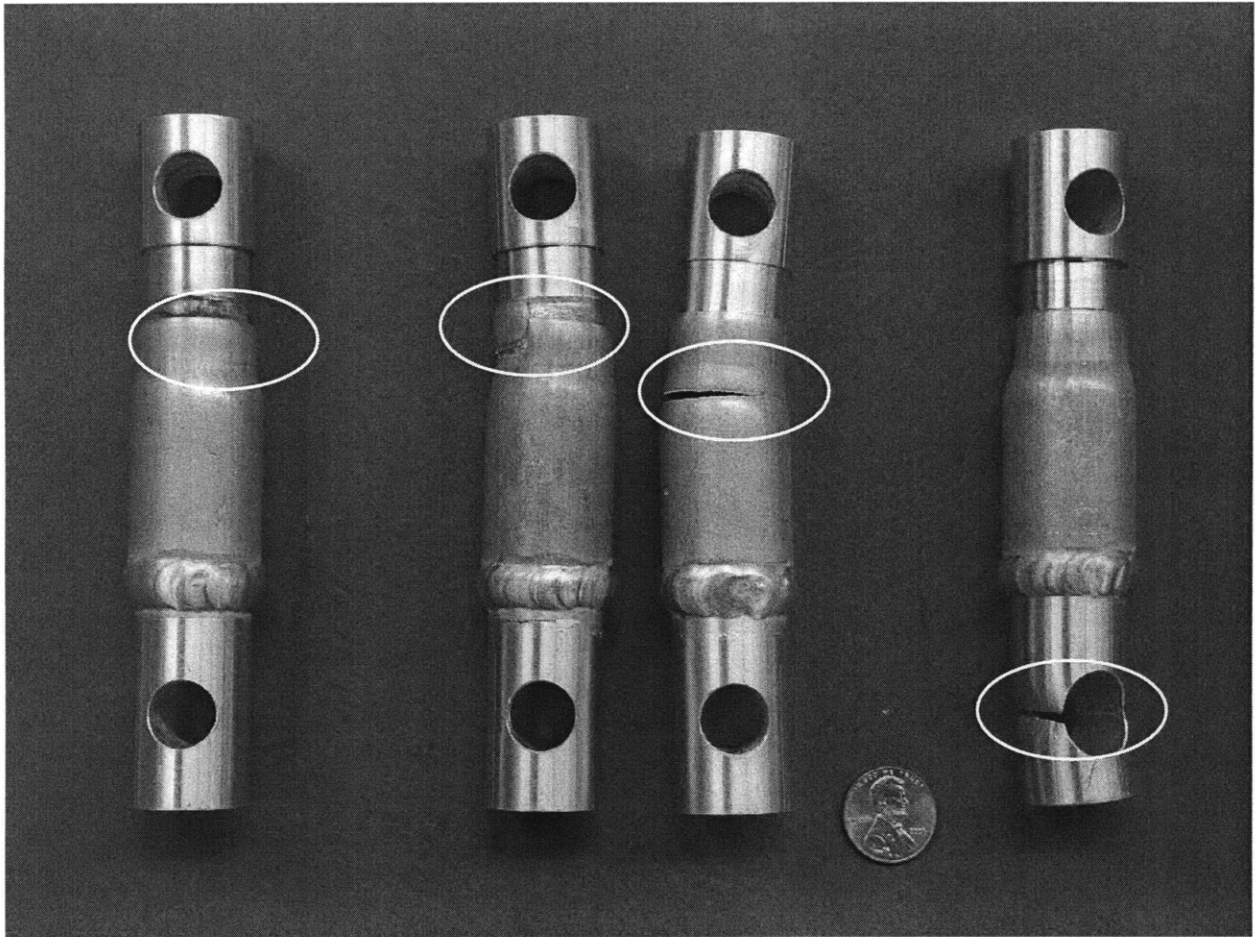


Figure D.12: Photograph of the 1" specimens and their different failure modes marked by the white circles.

From Table D.9 we can see that the 1.5" specimens failed in different modes. Figure D.13 shows photographs of the 1.5" specimens and their different failure modes. It can be seen that (from left to right) the specimens failed in three modes:

- 1) Slip off of the outer workpiece off the inner workpiece, due to a non-complete EMW joint.
- 2) The two samples in the middle of Figure D.12 depict the optimal failure mode of the EMW joint specimen, where the base material of the tube is weaker than the EMW joint.
- 3) Failure of the specimen itself. This only happened for three of the specimens: sample R3 T2, R4 T1 and R16 T1.

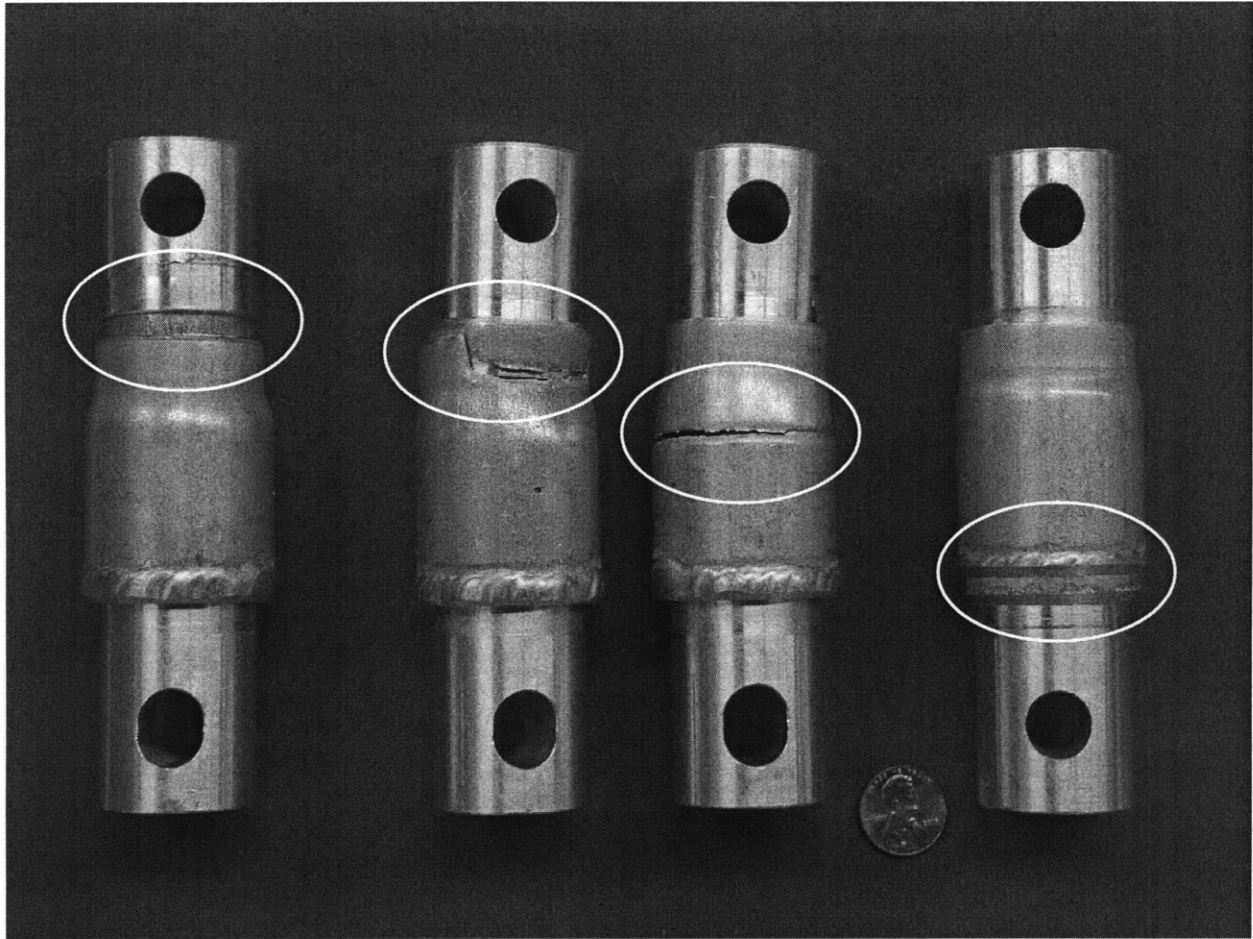


Figure D.13: Photograph of the 1.5" specimens and their different failure modes marked by the white circles.

DOE Graphs

From the cube plot of the second DOE, presented in Chapter 4, one can see that for a cleaned inner workpiece the maximum loads can be observed during the tensile tests. Further effects can be found in the following Pareto Diagram, which is shown in Figure D.14.

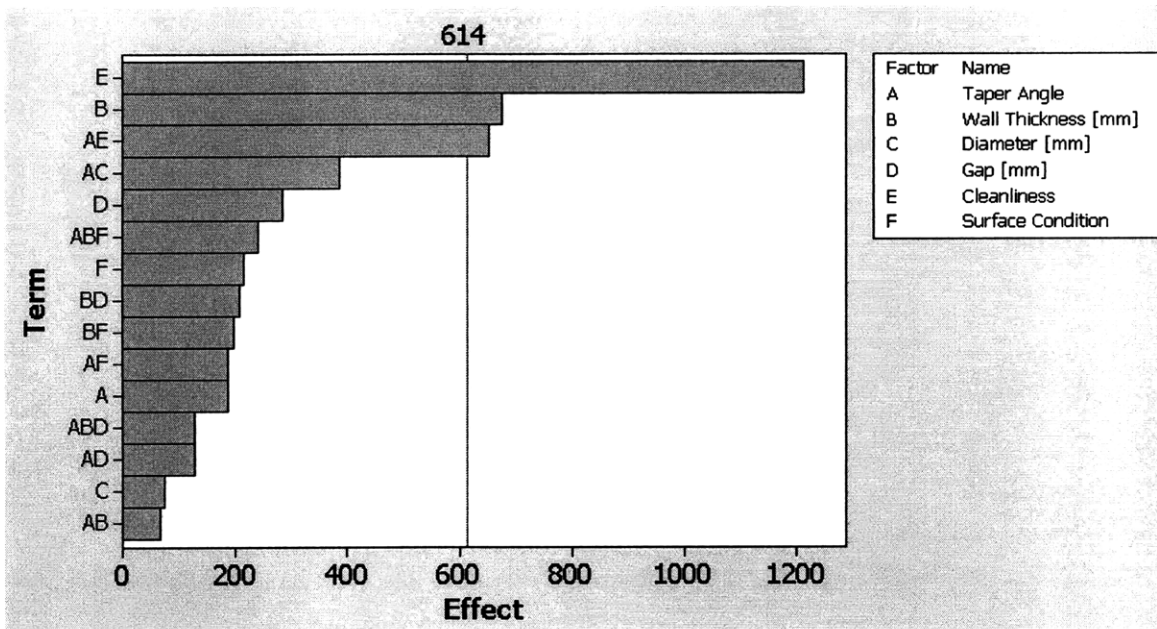


Figure D.14: Pareto Diagram of all DOE parameters of the second DOE. The red line displays the limit above which parameters become significant for the chosen α of 0.1.

The Pareto diagram in Figure D.14 shows that the all DOE parameters of the second DOE. The parameters E, B and AE, which are cleanliness, wall-thickness and the interaction of the taper angle with the cleanliness have significance with regards to their effect on the resulting tensile strength.

Another plot which can show the significance of certain parameters in a DOE study is the so-called normal plot of effects, shown in Figure D.15:

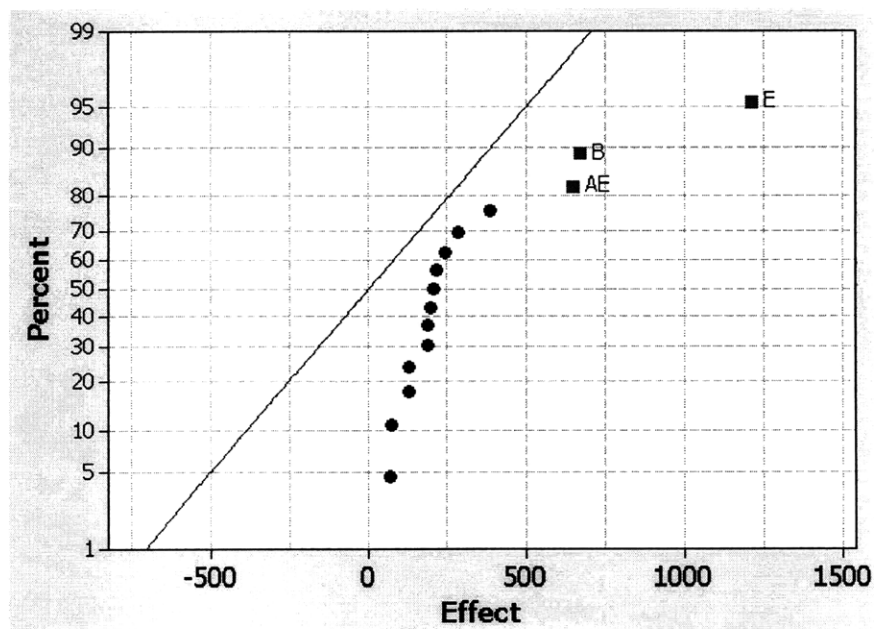


Figure D.15: Normal plot of effects for the parameters of the second DOE ($\alpha = 0.1$).

The plot of effects shows the same result as the Pareto diagram in Figure D.14. The parameters, which are marked by red squares are now the significant parameters, whereas the other parameters which are close to the straight line have an average effect and are therefore not significant. Figure D.16 shows the interaction plot of the second DOE and its parameters:

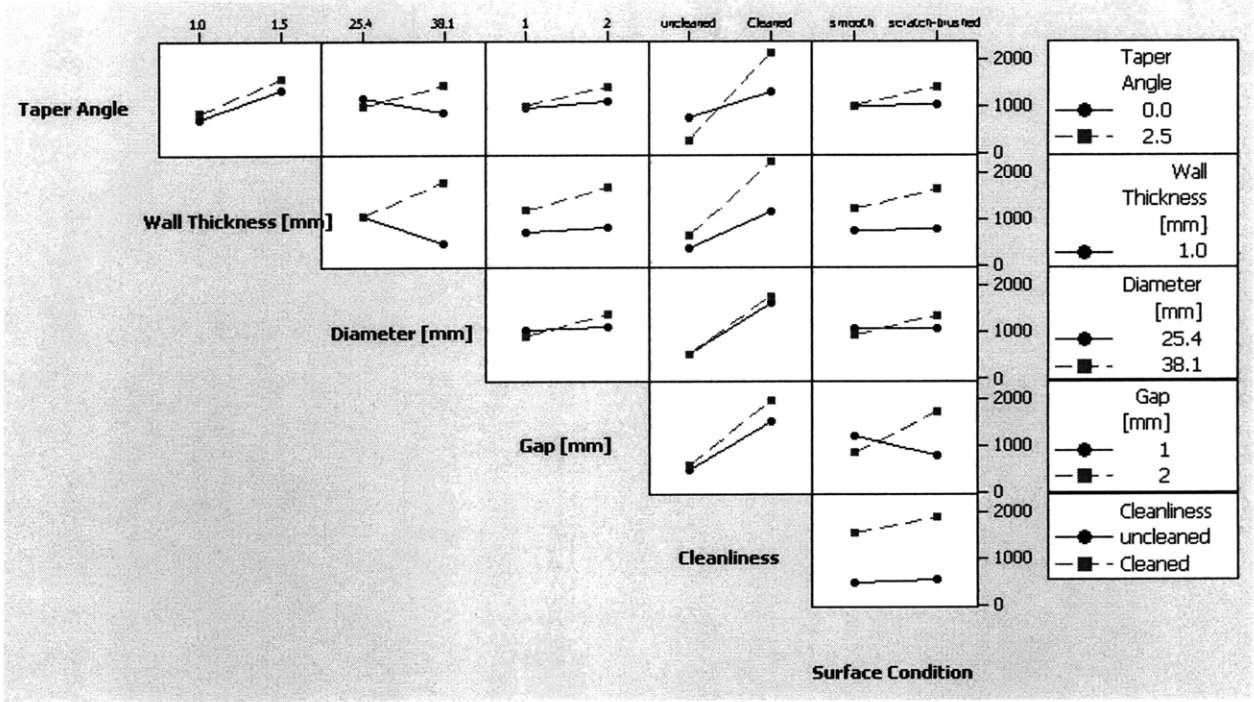


Figure D.16: Interaction plot for all parameters of the second DOE, with the effect on the mean maximum load observed during the tensile tests of the EMW joints.

Analyzing Figure D.16, we find that our observations match the observed significant parameters, to this point, as well as the strong interaction between the tapered angle and the cleanliness.

EMW Process Calculations Package provided by PULSAR

Figure D.17 shows an example of the calculation package provided by PULSAR, in Israel, during our DOE experiments, in November 2007.

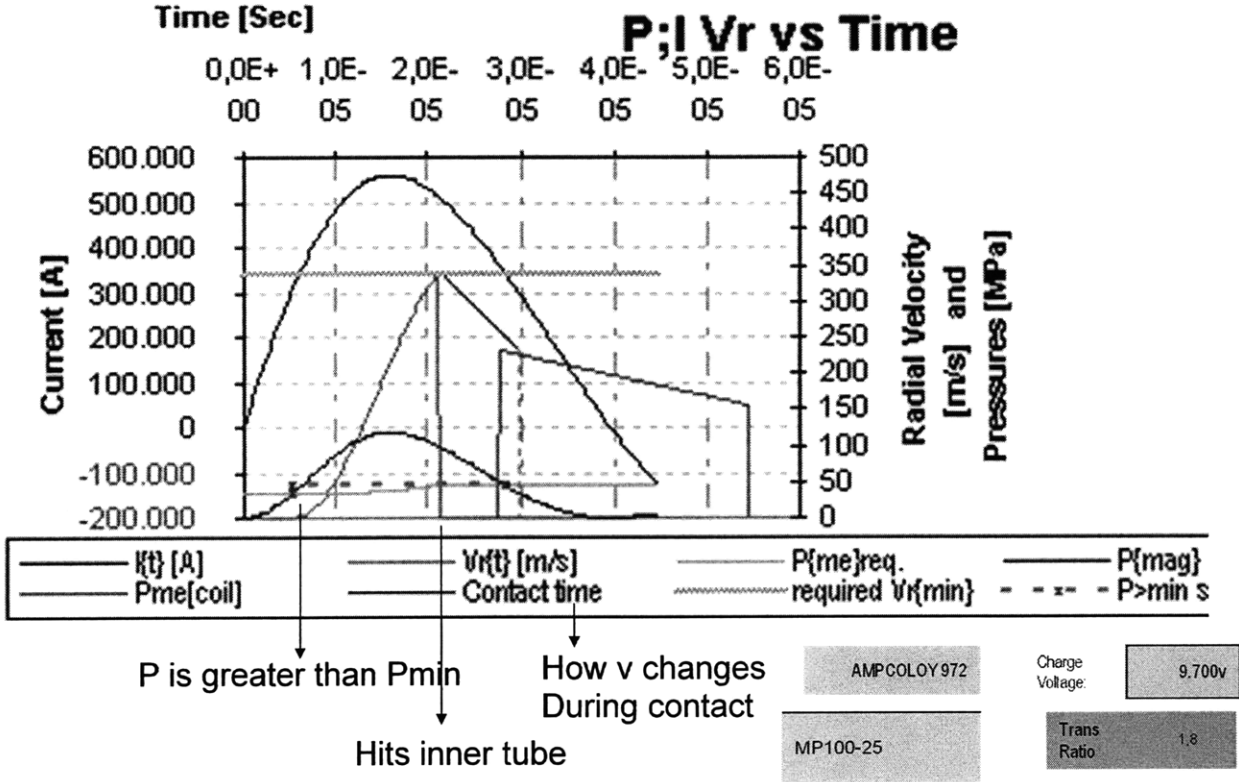


Figure D.17 : Example of the end result of the calculations from the EMW process software package from PULSAR.

Figure D.17 shows a bit more sophisticated result than was already presented in Chapter 2 through our MATLAB model. In the PULSAR software also the moment of impact is taken into account, which then results in a certain contact time over which the outer and inner workpiece are colliding.

Furthermore, it is possible to calculate residual stresses, which can remain in the outer workpiece after the EMW process. We observed such residual stresses during cutting of the samples provided by PULSAR for the first DOE batch (August 2007). The outer workpiece would spring open after a certain length of it had been cut. Basically, during the cutting the remaining cross-section was reduced to a point after which the residual stress would tear open the outer workpiece trying to deform it back to its original state. Table D.9 shows the calculation of the impact speed, the necessary velocity and the

residual stress with the input parameters outer diameter (OD), wall-thickness (WT) and the input voltage for the individual DOE batches at 10 kJ and 12kJ of process energy:

Inputs				Outputs		
Materials	OD [inch]	WT [mm]	Input Voltage [V]	Impact Speed [m/s]	Necessary Speed [m/s]	Overcoming Residual Stress [%]
T6 to T6	1.5	1.5	8700	117	338.84	26.3
T6 to T6	1.5	1.5	9800	204	338.84	101.1
T6 to T6	1.5	1.5	11000	273.15	338.84	244.5
T6 to T6	1.5	1.5	13000	350.93	338.84	461.2
T4 to T6	1.5	1.5	9800	269.91	338.84	471.3
T6 to T6	1.5	1	9700	340.78	338.84	296.2
T6 to T6	1.5	1	10000	356.32	338.84	337.9
T6 to T6	1	1	8700	150.82	338.84	91.4
T6 to T6	1	1	16500	342.91	338.84	675.5

Table D.9: Summary of the calculations made using the EMW process software package provided by PULSAR.

From Table D.9 we can make several conclusions.

First, the first DOE which was performed at an energy of 10 kJ (Input voltage ~ 8700 V), produced several samples with remaining residual stresses. This is due to the fact the impact velocities are sometimes too high due to the low input voltage and then high mechanical strength of the outer workpiece. Then, the residual stress is not overcome (value below 100%, but to be on the safe side it should be below ~ 200%).

Second, switching the outer workpiece to T4, instead of T6 (middle example of Table D.9) changes the overcoming of the residual stress by a factor of four.

Third, some of the samples do not overcome the necessary critical velocity, although they overcome the residual stress barrier. This is not the case for any of the samples, which are produced with an input voltage higher than 10000 V (approximate case for 12 kJ), but the 1.5" OD and 1.5 mm WT sample, which has an impact speed that is still lower than the critical velocity.